

# **Light-magnetism coupling: towards the manipulation of magnetic domain walls and domains**

**Paul-Iulian Gavriloaea**

Programa de Doctorado en Física de la Materia  
Condensada, Nanociencia y Biofísica

Instituto de Ciencia de Materiales de Madrid

Facultad de Ciencias

Dirección:

dr. Oksana Fesenko Morozova (Chubykalo-Fesenko)  
dr. Rubén Otxoa de Zuazola

**Madrid, 2025**

---

# Light-magnetism coupling: towards the manipulation of magnetic domain-walls and domains

---

Doctoral student: Paul-Iulian Gavriloaea

Supervisors: dr. Oksana Fesenko Morozova  
(Chubykalo-Fesenko)  
dr. Rubén Otxoa de Zuazola

Tutor: prof. dr. Farkhad Aliev

*PhD thesis*

Host institution: Materials Science Institute of Madrid

Awarding institution: Autonomous University of Madrid

2025



# Abstract

Magnetic domain walls (DWs) and domains (MDs) represent fundamental units of data in spintronics, one of the competing technologies in the race towards the future electronics industry beyond CMOS. At the other end, the light-matter coupling holds significant potential in the migration towards unprecedently fast and energy efficient magnetic memory and logic devices, in contrast with conventional current driving schemes. This thesis investigates from a numerical and theoretical point of view the interaction between ultrashort fs-ps laser excitations and magnetic textures primarily in the shape of DWs with a supplementary focus on MDs. While the integration of all-optically controlled spintronic devices in the current data industry remains a major technological challenge, numerical and analytical calculations provide an alternative route in advancing and exploring the laser manipulation of MDs/DWs. Distinguishing between classes of thermal and non-thermal phenomena in the context of conventional thermodynamics, we explore distinct laser-matter coupling routes in three types of magnetic systems:

(I) We first demonstrate a novel driving mechanism analysing a  $180^\circ$  DW in a generic ferromagnet (FM) with perpendicular magnetisation. It is shown that a fs longitudinal deformation of the magnetic texture leads to a magnetisation gradient across the DW which can promote a transverse wall displacement up to the longer ps-ns time-scale towards the region of decreased magnetisation length. Compared to the well-known spin-Seebeck effect, this mechanism is purely non-thermal as it does not rely on the generation of heat gradients. The calculations are carried out using the high-temperature micromagnetic formalism of the Landau-Lifshitz-Bloch (LLB) equation.

(II) Making use of atomistic spin dynamics (ASD) simulations and an analytical  $\sigma$ -model, we demonstrate antiferromagnetic (AFM) DW dynamics in  $\text{Mn}_2\text{Au}$  via a non-thermal laser optical torque (LOT), originating as a second order light induced response. Taking into account the symmetry of the torque and the local Néel vector orientation with respect to the laser polarisation direction, we arrive at the remarkable conclusion that LOT can efficiently drive Lorentz invariant  $90^\circ$  DW dynamics but does not promote the displacement of  $180^\circ$  wall configurations. This is in direct contrast with the established, first-order response commonly known in the literature as the Néel Spin Orbit Torque (NSOT), which is dominant in  $\text{Mn}_2\text{Au}$  at THz frequencies but less effective in visible light in relation to LOT. Our investigation highlights the conditions in which this mechanism could be verified experimentally, contributing towards the potential observation of ultra-fast AFM DW dynamics.

(III) Lastly, we attempt at filling an existing gap in the theoretical description of the helicity-independent, all-optical switching (HI-AOS) mechanism recently demonstrated in various synthetic ferrimagnetic (FiM) layered systems based on Tb or Dy. The reversal is believed to occur due to an in-plane precession stimulated by the heat-induced loss of the perpendicular order and granular irregularities which naturally tilt the out-of-plane easy-direction. Based on a set of AFM coupled LLB equations, we construct a micromagnetic model to verify this hypothesis in a test Tb/Co bilayer.

While this conjecture could not be confirmed, we recover important experimental conclusions reaching a near-demagnetised state which triggers precessional dynamics and leads to incoherent reversal via a ring-domain pattern independent of laser pulse duration.

**Key words:** magnetic domain-walls, magnetic domains, ultra-fast magnetisation dynamics, thermal/non-thermal opto-magnetism.



## Resumen

Las paredes de dominio magnético (DWs) y los dominios magnéticos (MDs) son elementos fundamentales en espintrónica, una de las tecnologías emergentes que compiten en la carrera por la electrónica más allá del CMOS. A su vez, el acoplamiento luz-materia ofrece una vía prometedora para desarrollar dispositivos magnéticos de memoria y lógica ultrarrápidos y energéticamente eficientes, en contraste con los métodos convencionales basados en corriente. Esta tesis investiga, desde un punto de vista numérico y teórico, la interacción entre excitaciones láser de fs-ps y texturas magnéticas, centrándose principalmente en las DWs y, en menor medida, en los MDs. Aunque la integración de dispositivos espintrónicos controlados ópticamente en la industria de datos sigue siendo un desafío tecnológico, los cálculos numéricos y analíticos ofrecen una alternativa para avanzar en la manipulación láser de MDs/DWs. Distinguiendo entre fenómenos térmicos y no térmicos dentro del marco de la termodinámica convencional, exploramos distintos mecanismos de acoplamiento láser-materia en tres tipos de sistemas magnéticos:

(I) Demostramos un mecanismo novedoso de desplazamiento de una pared de  $180^\circ$  en un ferromagneto (FM) genérico con imanación perpendicular. Mostramos que una deformación longitudinal de la textura magnética en fs genera un gradiente de imanación a través de la DW, promoviendo su desplazamiento transversal a escalas temporales más largas (ps-ns) hacia la región de menor imanación. A diferencia del conocido efecto spin-Seebeck, este mecanismo es puramente no térmico, ya que no se basa en la generación de gradientes de temperatura. Los cálculos se realizan utilizando el formalismo micromagnético de alta temperatura de la ecuación de Landau-Lifshitz-Bloch (LLB).

(II) Mediante simulaciones ASD y un modelo analítico  $\sigma$ , examinamos la dinámica de DWs en  $Mn_2Au$ , inducida por un torque óptico de láser (LOT) no térmico, generado como una respuesta de segundo orden a la excitación luminosa. Teniendo en cuenta que la simetría del LOT depende de la orientación local del vector de Néel respecto a la dirección de polarización del láser, observamos la propagación de DWs de  $90^\circ$  con invarianza de Lorentz, pero no de configuraciones de  $180^\circ$ . Esto contrasta con el torque de primer orden conocido como Néel Spin-Orbit Torque (NSOT), dominante en  $Mn_2Au$  a frecuencias de THz, pero menos eficiente en el régimen de luz visible en comparación con el LOT. Nuestro análisis establece las condiciones experimentales para la observación de esta dinámica ultrarrápida de DWs en AFMs.

(III) Finalmente, abordamos la falta de un modelo teórico que explique el mecanismo HI-AOS recientemente observado en múltiples ferrimagnéticos (FiM) sintéticos y basados en Tb o Dy. Se cree que la inversión ocurre debido a una precesión en el plano inducida por la pérdida del orden perpendicular, debido a excitaciones térmicas y la presencia de irregularidades granulares que inclinan naturalmente la dirección fácil fuera del plano. Utilizando un modelo micromagnético basado en ecuaciones LLB con acople AFM, analizamos este fenómeno en una bicapa de Tb/Co.

Aunque no se logró confirmar esta hipótesis, recuperamos resultados experimentales clave, mostrando un estado cercano a la desimánación que genera posteriormente dinámicas precesionales y conduce a una inversión incoherente mediante un patrón de dominios tipo anillos, independiente de la duración del pulso.

**Palabras clave:** paredes de dominio magnético, dominios magnéticos, dinámica de imanación ultrarrápida, optomagnetismo térmico/no térmico.



# Contents

<b>Abstract</b>	<b>iv</b>
<b>Resumen</b>	<b>vii</b>
<b>Acknowledgements</b>	<b>xx</b>
<b>1 Introduction</b>	<b>1</b>
1.1 Motivation . . . . .	1
1.2 Thermal and non-thermal light-matter coupling: a general perspective of ultra-fast phenomena . . . . .	3
1.2.1 Thermal mechanisms . . . . .	3
1.2.2 Non-thermal mechanisms . . . . .	4
1.3 Magnetic domain-walls and domains: assembling the future digital world . . . . .	5
1.3.1 A discussion in the context of conventional spintronics . . . . .	6
1.3.2 Opto-magnetism towards the next-generation of memory and logic devices . . . . .	8
1.4 The aims of this thesis and its outline . . . . .	11
<b>2 Theoretical background and numerical models</b>	<b>14</b>
2.1 Magnetic interactions in solid-state systems . . . . .	14
2.1.1 The exchange interaction . . . . .	15
2.1.2 The spin-orbit interaction, magnetocrystalline anisotropy and anisotropic exchange . . . . .	16
2.1.3 The Zeeman interaction . . . . .	17
2.1.4 The dipolar interaction . . . . .	18
2.2 Magnetic domains and domain-walls . . . . .	18
2.3 Models of magnetisation dynamics . . . . .	20
2.3.1 Atomistic spin dynamics . . . . .	21
2.3.2 High temperature micromagnetics: the classical Landau-Lifshitz-Bloch equation . . . . .	23
2.3.3 The two-temperature model . . . . .	26
2.4 Summary . . . . .	27
<b>3 Domain wall dynamics via a laser-induced transient magnetisation</b>	<b>29</b>
3.1 Introduction . . . . .	29
3.2 Numerical model and material parameters of a generic ferromagnet . . . . .	31
3.3 Results . . . . .	32
3.3.1 Domain-wall dynamics in a 1D model following an instant magnetisation change of non-thermal origin . . . . .	32
3.3.2 Domain-wall displacement in a stripe system with heat and transient magnetisation . . . . .	38
3.4 Conclusions . . . . .	43

<b>4 Efficient 90° domain wall motion in Mn<sub>2</sub>Au via pure optical torques</b>	<b>47</b>
4.1 Introduction . . . . .	47
4.2 Extended Heisenberg Hamiltonian of Mn <sub>2</sub> Au . . . . .	49
4.3 Antiferromagnetic order control via non-thermal laser-induced torques . . . . .	50
4.4 Analytic description of laser-driven antiferromagnetic domain wall dynamics . . . . .	53
4.4.1 Two-sublattice based energy density of the Mn <sub>2</sub> Au crystal . . . . .	54
4.4.2 The antiferromagnetic Landau-Lifshitz-Gilbert equations of motion . . . . .	57
4.5 Special relativity signatures in antiferromagnetic domain-wall kinematics . . . . .	59
4.6 Optical torque driving mechanism: a comparison between 90° and 180° domain-walls . . . . .	61
4.7 Magnetic texture proliferation nearing the supermagnonic limit . . . . .	62
4.8 Spin texture chirality analysis in optically driven 90° wall geometries . . . . .	63
4.9 Driving periodic ultra-fast domain-wall contraction and expansion . . . . .	65
4.10 Conclusions and discussions . . . . .	66
<b>5 Domain nucleation and domain-wall kinematics in the all-optical switching of a Tb/Co bilayer</b>	<b>68</b>
5.1 Introduction . . . . .	68
5.2 Studying a Tb/Co bilayer in a two macrospin picture . . . . .	70
5.2.1 Basis of the TMspin model . . . . .	71
5.2.2 Temperature scaling of the Tb/Co magnetisation. The effect of the interlayer coupling . . . . .	72
5.2.3 Static hysteresis cycles for in-plane and tilted external field . . . . .	74
5.2.4 Easy-axis tilt assumption towards precessional all-optical switching . . . . .	76
5.3 Full scale micromagnetic modeling . . . . .	79
5.3.1 Hypothesis: can a distribution of easy-axis tilts lead to precessional AOS? . . . . .	80
5.3.2 Helicity-independent, all-optical switching after near-complete demagnetisation . . . . .	83
5.3.3 A close inspection of the observed switching dynamics . . . . .	85
5.3.4 Ring-domain pattern time evolution and instability . . . . .	88
5.4 Conclusions . . . . .	90
<b>6 Concluding remarks and perspectives</b>	<b>93</b>
6.1 English . . . . .	93
6.2 Español . . . . .	96
<b>A Supporting information for Chapter 3</b>	<b>102</b>
A.1 Instant modification of the magnetisation vector length in the chain model . . . . .	102
A.2 Field resolved contribution to the longitudinal and transverse dynamics of a single macrospin in the 1D model . . . . .	103
A.3 Domain-wall displacement for a fixed ratio between the transient and equilibrium magnetisation . . . . .	104

<b>B Supporting information for Chapter 4</b>	<b>106</b>
B.1 Obtaining the antiferromagnetic equations of motion in Mn <sub>2</sub> Au . . . . .	106
B.2 Two-temperature model of laser induced heating . . . . .	108
<b>C Supporting information for Chapter 5</b>	<b>111</b>
C.1 Analysis of longitudinal/transverse magnetisation contributions to the static hysteresis cycles in the TMspin Tb/Co model . . . . .	111
C.2 Short time-scale longitudinal fluctuations in the AOS dynamics of the Tb/Co bilayer . . . . .	112
<b>Bibliography</b>	<b>115</b>
<b>List of publications</b>	<b>137</b>



# List of Tables

3.1	Generic Co material parameters . . . . .	32
3.2	Two-temperature model parameters for a generic Co sample . . . . .	39
3.3	Final DW displacement in the stripe model with respect to increasing laser pulse duration for optimum laser fluence and transient magnetisation amplitude in the absence of DMI . . . . .	42
3.4	Revisiting the data in Table 3.3 in the presence of DMI . . . . .	43
4.1	Mn <sub>2</sub> Au material parameters used in our ASD calculations . . . . .	50
4.2	Allowed LOT symmetries in Mn <sub>2</sub> Au for an in-plane Néel vector geometry as calculated in Ref. [162] . . . . .	51
5.1	Material parameters employed in the two macrospin Tb/Co model . .	71
5.2	Two temperature model parameters for Tb/Co . . . . .	81



# List of Figures

1.1	Conceptual visualisation of the physics investigated in this thesis . . . . .	2
1.2	Representative thermal and non-thermal experimental observation of ultra-fast magnetisation dynamics . . . . .	4
1.3	Suggested spintronic devices in the literature based on manipulation of domain-walls and magnetic domains . . . . .	6
1.4	Representative state of the art experimental achievements regarding the opto-magnetic control of magnetic domain walls and domains . . . . .	10
2.1	Typical domains and domain-wall geometries encountered in this work	19
2.2	High-temperature micromagnetics in the LLB framework . . . . .	23
2.3	Understanding the two-temperature model . . . . .	26
3.1	Instantaneous longitudinal deformation of an $180^\circ$ Néel DW configuration . . . . .	33
3.2	DW motion due to the instant longitudinal deformation of the wall profile in the chain model . . . . .	35
3.3	Time variation of the Néel wall magnetisation profile along $Oy$ and $Oz$ during the dynamics induced by a transient longitudinal magnetisation	37
3.4	Final DW displacement with respect to the temperature $T$ and the amplitude $\delta m_z$ of the induced magnetisation . . . . .	38
3.5	DW dynamics in a stripe geometry under the effect of a spatially uniform, ultra-fast laser pulse heating and a transient longitudinal deformation . . . . .	41
4.1	$Mn_2Au$ unit cell and laser-excitation geometry . . . . .	52
4.2	Top view of the two sublattice picture $\vec{S}_A, \vec{S}_B$ considered in the analytical model of $Mn_2Au$ . . . . .	55
4.3	Comparison between the numerical steady-state $90^\circ$ DW dynamics and the predictions given by the SG theory . . . . .	60
4.4	LOT driving mechanism: a comparison between $90^\circ$ and $180^\circ$ DWs . .	61
4.5	Proliferation event in the supermagnonic regime . . . . .	62
4.6	Analysis of DW motion direction with respect to DW chirality . . . . .	64
4.7	Periodic ultra-fast DW contraction and expansion . . . . .	65
5.1	Comparison between HI-AOS characteristic to Gd-based systems (alloys or multilayers) and the novel, precessional-like HI-AOS observed in multilayers containing heavier rare-earths such as Tb or Dy . . . . .	69
5.2	Sketch of the Tb/Co models discussed in this Chapter . . . . .	70
5.3	Scaling of the equilibrium magnetisation in the two macrospin Tb/Co model . . . . .	72
5.4	Static hysteresis cycles for three applied field orientations $\theta_H = 2^\circ, 60^\circ$ and $89^\circ$ . . . . .	75
5.5	The local easy-axis tilting assumption . . . . .	76

5.6	Switching diagrams for an AFM coupled Tb/Co macrospins and a single Co macrospin under identical laser pulse heating conditions and tilting of the easy direction away from the Oz axis . . . . .	77
5.7	Precessional AOS example obtained in a TMspin Tb/Co model . . . . .	78
5.8	Precessional AOS example obtained in a single Co macrospin model .	79
5.9	Testing the possibility for precessional HI-AOS under a single laser-shot and distribution of local EA tilts . . . . .	82
5.10	Ring-domain pattern obtained after single-shot AOS in a Tb/Co bilayer as a function of the peak laser pulse fluence and pulse duration in regions where the condition $T_e > T_c^{\text{Co}}$ is satisfied . . . . .	84
5.11	Laser dynamics for peak fluence $F = 1.9 \text{ mJ/cm}^2$ and $t_p = 1 \text{ ps}$ in three separate regions where $T_e > T_c^{\text{Co}}$ . . . . .	86
5.12	Qualitative comparison in between experimental AOS measurements in Tb/Co multilayers and our simulation results . . . . .	87
5.13	Magnetisation snapshots as a function of time corresponding to the Co sublayer during the AOS of Tb/Co obtained for $F = 19 \text{ mJ/cm}^2$ and $t_p = 1 \text{ ps}$ . . . . .	88
5.14	Stable domain-size at 300 K as a function of layer-thickness and for different magnetocrystalline anisotropy constants (MCA) according to equation (5.16) . . . . .	89
A.1	Instant deformation of the magnetisation modulus in a 1D macrospin chain model due to the modification of the out-of-plane magnetisation component . . . . .	102
A.2	Field resolved contribution to the longitudinal and transverse dynamics of a single macrospin under the effect of a longitudinal deformation according to the LLB equation . . . . .	103
A.3	Revisiting the results in Figure 3.4 with the $\delta m_z$ values rescaled to the corresponding $m_e(T)$ value . . . . .	104
B.1	Ultrafast heating estimation during single pulse excitation . . . . .	109
C.1	Example of longitudinal contributions to the apparent non-coherent magnetisation reversal in Figure 5.4 . . . . .	111
C.2	Short-time scale longitudinal fluctuations in the AOS dynamics of the Tb/Co bilayer for three distinct regions . . . . .	113

Ție, Doamne! În memoria bunicilor mei,  
Victoria, Vasile, Verona și Constantin.



# Acknowledgements

First of all, I would like to thank dr. Oksana Chubykalo-Fesenko for the stimulating scientific discussions and her constant support in the years leading to this thesis. You answered many of my never-ending questions and pushed me forward when times were hard. Thank you equally for the tremendous help with the paperwork during my transition to Spain. Secondly, I would like to thank my co-supervisor dr. Rubén Otxoa, always a dedicated and supportive presence during my studies. I will never forget the creative discussions in San Sebastián and Cambridge. It was a pleasure working with you both, I am forever grateful for your guidance. This work would have not been possible without financial support from the EU-funded "COM-RAD" project, a Marie Skłodowska-Curie, International Training Network, under grant agreement No. 861300. In addition, the final six months of my stay in Spain were funded by the Spanish Ministry of Science, Innovation and Universities under grant agreement PID2022-137567NB-C21. Many thanks also to dr. Nicoleta Lupu, dr. Cristina Bran and my colleagues at the National Institute of Research and Development for Technical Physics in Iași, where I transitioned towards the end of my PhD and the final chapters of this thesis were written.

Dear family and close friends, thank you for your endless support and love. I would like to mention in particular my beloved fiancée Oana, I am eternally grateful for your love and care. To my parents Viorica and Constantin as well as my brother and his family, Gabriel, Ioana, Taisia, Mariam and Efrem with my sister Daria, thank you for everything. In addition I am particularly fond of the beloved Romanian and monastic community I met at the Orthodox Cathedral in Madrid "The Entrance of the Theotokos into the Temple", and in particular the fatherly love of His Grace, Teofil of Iberia, Assistant Bishop to the Diocese of Spain and Portugal. Finally, thank you Lucian, Daria-Ana, Nicolae and Raoul for your friendship. While consistent effort and determination are necessary, you were my constant emotional support, essential towards completing this PhD project.

Jackson, thank you for your friendship—it has been fantastic sharing ideas, coffee, steaks and laughs with you. I cherish in particular the time spent in York with your family, Erica, Zuko and Sokka. João, Diego and Theo, thank you for the never-ending laughs, the guitar concerts in our living-room, the trips and the meals we have shared. I will always remember the time spent with you in Madrid, abrazos. I would like to extend my thanks to the peer colleagues and researchers in the group I studied at the Materials Science Institute of Madrid: Cristina, Yogi, Elías, Jorge, Eider, Pablo, Alejandro, Agustina, Rafa, David, Unai, Miriam and Manuel. Thank you for your kindness and the friendly atmosphere.

A very important role in shaping my scientific journey so far has been played by my past mentors and colleagues at the "Alexandru Ioan Cuza" University of Iași and the University of York: the Electricity and Magnetism group led by prof. Alexandru Stancu and the Computational Magnetism group led by prof. Roy Chantrell. Thank you for your guidance and support. I would also like to mention here prof. Cristian Enăchescu, a kind person and enthusiastic researcher with whom I had the pleasure to collaborate and whose memory I cherish. In addition, thank you Mara, Sergiu and Richard for all your help during my Master and PhD studies and equally for your friendship. Many thanks to all my peer colleagues and professors involved in this project. I would like to mention here in particular the aid of Frank, Thodoris and Yuriy at Forschungszentrum Jülich, who hosted me in their research group and played an important role in understanding the ab-initio calculations in Chapter 4.

Thank you also to David, Ricardo S., Liliana and Lucian at SPINTEC for our collaboration shaping the results presented in Chapter 5. It was a pleasure to meet and discuss with the elite scientists and students in COMRAD, the acknowledgements list would require most certainly a whole page to include everyone. In addition, I would like to thank Ricardo R.-E. and Javier, two peer colleagues in San Sebastián with whom I had the pleasure to collaborate on side projects.

To everyone else I could not mention here or I might have omitted, thank you kindly.



## Chapter 1

# Introduction

### 1.1 Motivation

In the current technological era, data has emerged as one of the most valuable resources. Innovations and ongoing developments in cloud services, the internet of things (IoT) and artificial intelligence (AI) have exponentially augmented the volume and rate of data generated yearly. By 2028, it is estimated a total of 394 zettabytes of information will be globally shared across all sectors, a roughly 150% increase compared to the figures reported in 2024 [1]. This immense quantity of information and its rapid growth necessitates a robust hardware apparatus for data storage and manipulation.

Despite their essential role in supporting the backbone of the digital infrastructure, conventional logic and memory devices face several critical challenges which underscore the necessity for sustainable hardware innovations. First and foremost, data centers consume significant amounts of energy which presently sum to approximately 340 TWh or roughly 1.3% of the global electricity demands, a figure predicted to increase approximately 2.5 times just in the span of the next three years [2–4]. Concurrently, CMOS technologies are nearing their physical and practical limits, with transistor nodes being pushed towards the Angstrom scale, a threshold where quantum effects, current leakage, and heat dissipation hinder performance [5]. Furthermore, the gap between processor speeds and memory bandwidths widens continuously, leading to redundancy and inefficient information transport across the data pipeline [6].

At the fundamental research level, ultra-fast magnetism offers a potential gateway towards the next-generation of memory and logic devices. This thesis examines from a numerical and analytical point of view *the interaction between ultra-short laser pulse excitations in the fs-ps range and magnetic textures primarily in the shape of domain walls (DWs), with a combined, supplementary exploration of DWs and magnetic domains (MDs)* in the last chapter of results. From a pure conceptual perspective, a magnetic DW is the interface separating two spatial regions—namely two given MDs—which correspond to either local or global energy minima of the magnetic order parameter as seen in Figure 1.1. It is precisely this separation between two stable energy levels and their associated magnetic configurations which can potentially serve the data industry. Thus, arrays of neighbouring MDs encode information in a binary style. At the same time, DWs may be used as data carriers in between input and output terminals as is used in the concept of magnetic race-track memory [7]. Also, the DW-MD interdependence offers a platform for linking the memory and logic components on the same physical chip unlike the conventional von Neumann architecture. Additionally, these magnetic textures are universally present in all classes of magnetic materials providing a wide variety of practical advantages and/or technological opportunities discussed in detail in sections 1.3.1 and 1.3.2. At the other

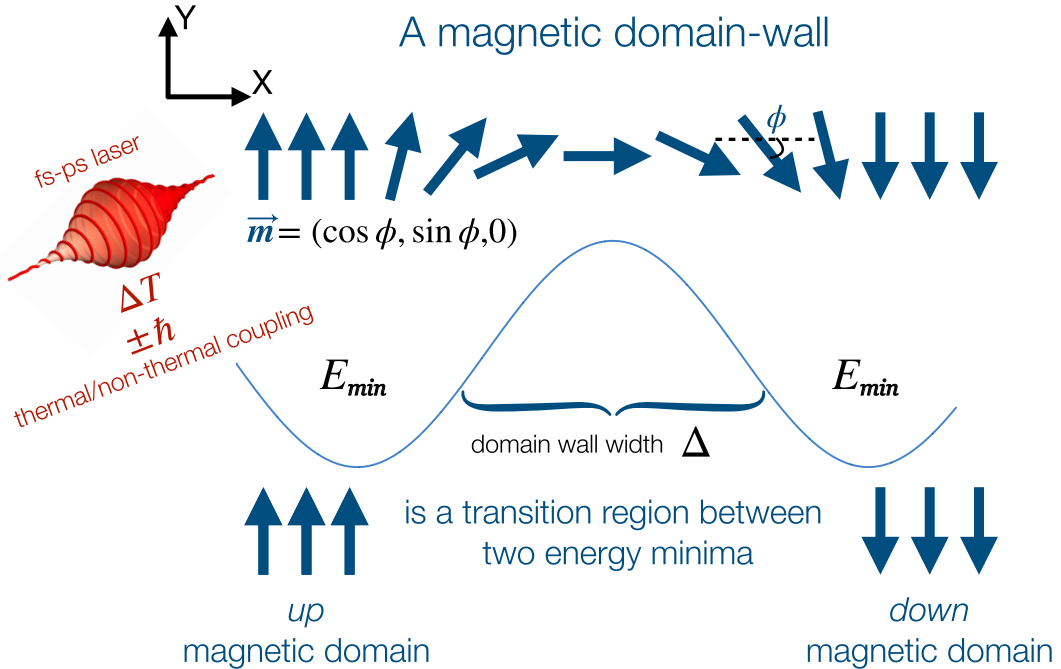


FIGURE 1.1: Conceptual visualisation of the physics investigated in this thesis: the interaction between ultra-fast laser pulse excitations in the fs-ps time-scale and magnetic textures in the shape of magnetic DWs with an additional exploration of MDs in the last chapter of results. A magnetic DW represents the spatial transition connecting two regions or MDs in which the magnetic order parameter—in this case identified with the reduced magnetisation vector  $\vec{m}(\cos \phi, \sin \phi, 0)$ —finds itself in a minimum energy state. Thus, arrays of MDs associated for example with *up/down* magnetic states can encode information in a binary style, while the DWs separating them may be viewed as data carriers which can be driven between input and output terminals to erase or write the magnetic information stored in the domains. Magnetic DW motion can be achieved in numerous ways, this thesis explores two light-matter coupling routes towards this end, namely thermal and non-thermal phenomena the distinction between them being discussed in detail in section 1.2. The DW geometry shown here for exemplification is a typical 180° Néel configuration found in magnetic systems characterised by uni-axial magnetocrystalline anisotropy. The DWs/MDs geometries investigated in this thesis is analysed in more detail in section 2.2.

end, the light-matter interaction holds the key to the fastest and least dissipative magnetisation dynamics observed so far, laying the foundation for data manipulation technologies that are both environmentally sustainable and highly performant—see sections 1.2 and 1.3.2. The major topic of investigation in this thesis is the possibility to employ ultra-fast laser pulse excitation towards driving magnetic DW dynamics in a ferromagnetic (Chapter 3) and antiferromagnetic system (Chapter 4). In a secondary topic, we evaluate the role of DW dynamics and MD nucleation in the all-optical switching of a ferrimagnetic bilayer structure (Chapter 5).

To integrate the results discussed in this work in the context of previous research we first of all examine in the next section 1.2 the distinction between the so-called thermal and non-thermal ultra-fast magnetic phenomena. In essence, these represent the two separate light-matter coupling routes employed towards the manipulation of DWs and MDs in this thesis.

## 1.2 Thermal and non-thermal light-matter coupling: a general perspective of ultra-fast phenomena

To this day, ultra-fast manipulation of the magnetic order has been explored in a wide variety of materials including metals [8–15], dielectrics [16–20] and semiconductors [21–25]. However, a complete understanding of strongly non-equilibrium magnetism is yet to be achieved, leading often to divergent opinions on the microscopic origin of the observed phenomena. While the exhaustive analysis of light-induced effects sets itself as a laborious task, the overall complexity may be reduced by isolating and classifying the distinct mechanisms based on thermodynamic considerations as discussed in the work of Kirilyuk *et al.* [26]. In this section we present this classification method in the broader context of the ultra-fast magnetism field. Although briefly mentioned here, we return to the specific optical manipulation of DWs and MDs in section 1.3.2.

### 1.2.1 Thermal mechanisms

According to Kirilyuk *et al.* [26], an ultra-fast laser excitation is seen to give rise firstly to a class of *thermal* effects in which the direct light-matter coupling is considered weak in the electric dipole approximation. The energy carried by the photon subsystem indirectly drives modifications of the magnetic order parameter by stimulating scattering events in between the sample’s microscopic degrees of freedom which can for example involve electrons, phonons, localised magnetic moments or magnons, etc. The associated scattering rates of these processes determine the time-scale of the magnetisation dynamics although external factors such as the cooling rate, absorption coefficient or the material geometry influence the total amount of laser energy transferred to the sample, and consequently, its magnetic response. The scattering events together with the energy deposited/transferred to each system is viewed as an effective temperature in a thermodynamic picture.

Irrespective of the laser polarisation, heating alone can trigger demagnetisation [8, 16, 21], precession [9, 11, 22] or complete switching of the magnetic order parameter [10, 13, 27], the latter typically referred to in the literature as helicity-independent, all-optical switching (HI-AOS). This thermal reversal has been predominantly observed for a long time in FiM alloys or layered structures based on the Gd rare-earth (RE) [13, 27–31]. Governed by the inter-sublattice exchange coupling, this mechanism allows switching for both fs and ps stimuli but requires a careful adjustment of the laser fluence in relation to the pulse duration, according to its characteristic switching diagram —see Figure 1.2(a-c). A slower, HI reversal has been identified recently in various Dy and Tb-based synthetic FiMs. Here, the laser thermal load is thought to determine an in-plane reorientation of the magnetic order under a temperature induced reduction of the perpendicular anisotropy at the interface and the presence of a local distribution of easy-axes directions which could favor the slow, in-plane precession dynamics [32–34]. In contrast with HI-AOS in FiMs containing Gd, the energy threshold to switching is independent of the pulse duration and a signature ring-domain pattern is nucleated in the excited area —see Figure 1.2(d-f). Additionally, laser thermal energy can potentially stimulate fast and long-range transport of magnetic DWs for example via established mechanisms such as entropic and magnonic torques [35–37]. Towards this end, several experimental efforts demonstrate magnetic DWs can be steered by means of fs laser-heating, although typically these studies report on observations long after the life-time of the excitation and do not examine the evolution of the DW kinematics in real time [38–42]. Evidence of

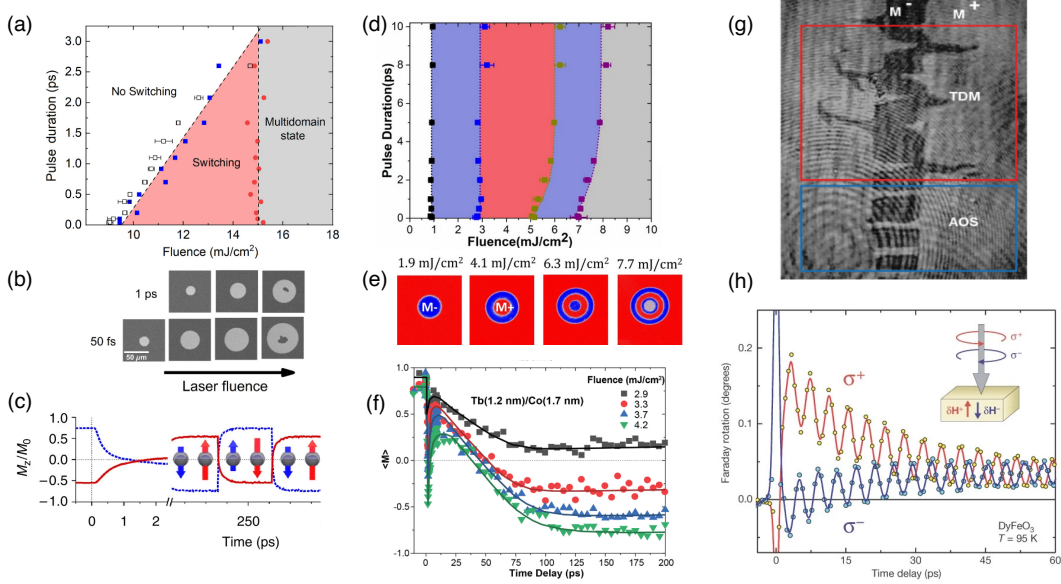


FIGURE 1.2: Representative thermal and non-thermal experimental observation of ultra-fast magnetisation dynamics. (a-c) Exchange-driven HI-AOS via transient-like ferromagnetic state (c) in Gd-based FiM alloys, with characteristic switching diagram (a) and domain pattern (b). To obtain reversal, the pulse duration must be carefully tailored for a given fluence value (a,b). Subplots (a,b) were extracted from the PhD thesis in [43] under the CC BY licence but can also be found in Ref. [30] while (c) was extracted from [27] and reproduced with permission from Springer Nature. (d) Characteristic switching diagram, (e) ring-domain pattern and (f) precessional HI-AOS dynamics in layered, synthetic FiMs based on Tb and Dy rare-earths. The laser energy threshold to switching is independent of the pulse duration. Subplots (d-f) have been extracted from the PhD thesis of [44] under the CC BY licence but can also be found in Refs. [32, 34]. (e) Thermally driven DW motion and HD-AOS in Tb-Fe alloys obtained for multiple-pulse, linear and circular polarised light respectively [41]. Reprinted with permission from John Wiley and Sons. (f) Non-thermal ultra-fast magnetic response in the canted Dy<sub>3</sub>Fe<sub>5</sub>O<sub>12</sub> AFM [45]. Reprinted with permission from Springer Nature.

DW motion under linearly polarised light —therefore under the influence of thermal effects —can for example be observed in subplot (g) of Figure 1.2 where the beam is swept across the sample.

Overall, these so-called thermal effects are inherently linked to the concept of thermodynamic quasi-equilibrium which gives meaning to the introduction of effective temperature parameters and ensures the energy (heat) transfer between distinct thermodynamic reservoirs is well defined. A standard example in this sense is the heat exchange route between the thermalised, hot electron gas and the colder phonon reservoir in metallic ferromagnets under ultra-fast laser pulse excitation [46]. However, the light-matter coupling does not necessarily require thermalization nor energy dissipation in the thermodynamic picture when angular momentum is directly transferred in between photons and the orbital or spin magnetic moments [47]. This brings us to the second category of ultra-fast magnetic phenomena according to Ref. [26], namely the broader class of *non-thermal* effects.

### 1.2.2 Non-thermal mechanisms

The geometry and/or the helicity of the laser excitation determine the strength and symmetry of non thermal mechanisms, a particular characteristic which distinguishes

them with respect to the class of thermal effects introduced earlier. With typical response times closely matching the temporal evolution of the laser excitation [26] and in the expected absence of heating, non-thermal mechanisms provide a faster and more energy efficient light-matter coupling route.

In the grand picture, these effects can induce changes in the magnetocrystalline anisotropy of garnet systems by modifying the charge distribution of magnetic ions [19, 20], as well as they allow the dynamic control of the magnetisation in ferromagnetic semiconductors for excitations above the band gap level [23, 24]. Furthermore, they can lead to oscillatory dynamics (see subplot (h) of Figure 1.2) and switching via an inverse optomagnetic route in metals and dielectrics [15, 17, 45] or give rise to spin polarisation on the basis of light-induced phonon excitation in antiferromagnetic insulators [48–50]. In addition, ultra-fast circularly polarized light was experimentally shown capable to deterministically set the DW motion direction for example via mechanisms such as the Inverse Faraday Effect (IFE), the Optical Spin Transfer Torque (OSTT) or the Magnetic Circular Dichroism (MCD) effect [24, 51–54]. Moreover, the deterministic nucleation of MDs and subsequent DW motion play an important role in helicity-dependent all-optical switching (HD-AOS) [41, 52, 55–57]. In contrast with the HI-AOS mechanism discussed in the previous section, HD-AOS requires multiple pulse excitation with the final magnetic state being determined by the helicity of the laser [12, 58, 59] (see subplot (g) of Figure 1.2).

Although in practical situations the heating of the laser-excited sample is always present to some extent, we shall further employ the non-thermal syntagma to describe only those light-induced effects which ideally do not modify, from a thermodynamic point of view, the temperature of the system. We should note here in the reference works of [26, 60], the actual class of non-thermal phenomena is split further in two distinct categories, namely photo-magnetic and opto-magnetic, depending on whether the coupling mechanism involves the annihilation/absorption of photons or can be described by direct angular momentum transfer to the magnetic system for example via stimulated Raman scattering. The particular MCD effect is *de facto* a thermal mechanism since it leads to the heating of the sample [41, 55–57, 61–63] but one may also include it in the category of photo-magnetic phenomena since it is polarisation dependent and it is mediated by photon absorption, showcasing the classification discussed here is not necessarily exhaustive and the ultra-fast magnetism topic offers an intense debate platform.

This thesis examines thermal and non-thermal light-matter coupling routes in three separate magnetic materials: a ferromagnet (FM), an antiferromagnet (AFM) and a ferrimagnetic (FiM) system. In the next section we analyse briefly the state-of-the-art and challenges in the field of spintronics with particular reference to DWs and MDs based logic and memory devices in the three aforementioned classes of magnetic systems. This discussion will help us identify current technological shortcomings with the aim of introducing ultra-fast magnetism as a potential route towards a next-generation spintronics era.

### 1.3 Magnetic domain-walls and domains: assembling the future digital world

The field of spintronics [64–66] —and its more recent sub-area of spin-orbitronics [67–73]—generally includes all the scientific and technological endeavours which aim to exploit the electron spin and orbital degrees of freedom in addition to its

charge in contrast with the current electronics industry. Magnetic DWs and domains—be it coherent or multi-domain configurations—represent elementary units of information in spintronics. Depending on the material under study, their manipulation may be achieved by distinct external stimuli such as for example magnetic fields, electrical currents, heat, strain or light. Although historically the two research fields developed separately, in a certain technological sense ultra-fast magnetism may be viewed as an adjacent or sub-branch to spintronics—sometimes referred to as opto-spintronics [74–76]—where the magnetic order control at the device level is specifically governed by fs-ps laser pulses. Let us briefly examine the advancements and challenges in the problem of DW/MD manipulation with respect to the broad field of spintronics and the three distinct classes of magnetic materials relevant to this thesis. Later on in subsection 1.3.2, we will expand upon the interaction between ultra-short laser pulse excitations at the fs-ps time-scale and DWs/MDs as a route towards the next-generation of memory and logic devices beyond conventional spintronic devices.

### 1.3.1 A discussion in the context of conventional spintronics

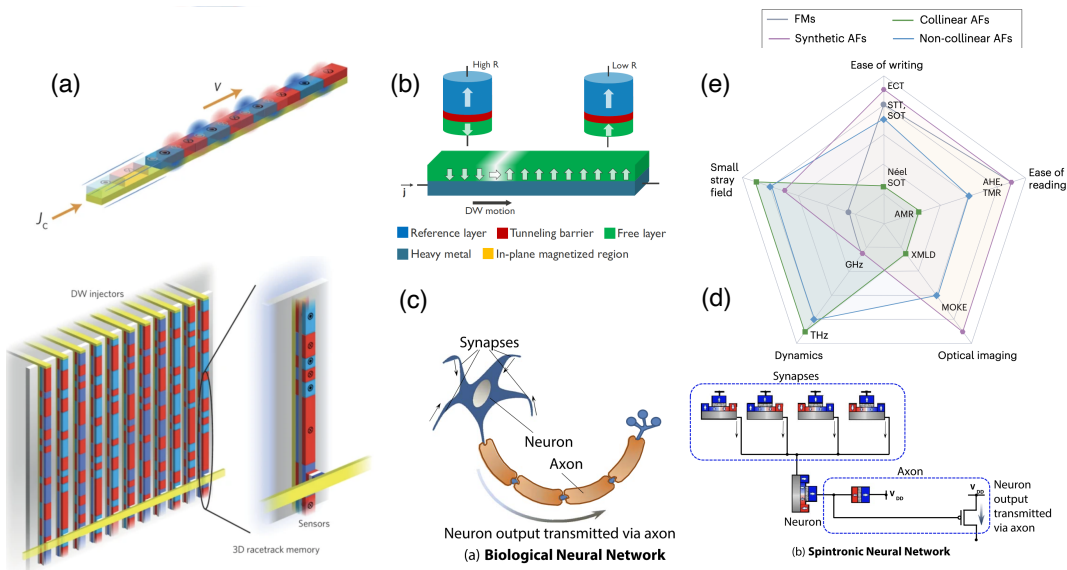


FIGURE 1.3: Suggested spintronic devices based on manipulation of DWs/MDs: (a) horizontal and vertical racetrack memories. Figure adapted and extracted from [77]. Reproduced with permission from Springer Nature. (b) RTM memory concept with MTJ-based read/write functionality—extracted from [78] under the CC BY 4.0 licence. (c-d) Spinntronic concept mimicking a biological neural network based on interconnected MTJ arrays in which synaptic weights and transfer functions are mediated by controlled DW displacement [79]. Copyright ©2016 IEEE. In (e) we display a comparative analysis of the particular advantages of FMs and distinct AFM systems for the development of future spintronic devices with respect to ease of read/write operations, scalability and time-scale of the dynamics—extracted from [80]. Although subplots (a-d) in Figure 1.3 particularly display FM-based memory and logic devices, both FiM and AFM materials may be considered in the development of analogous or improved prototypes [66, 81, 82], while of course adapting the read/write technology. Reproduced with permission from Springer Nature.

Among the three distinct classes of magnetic materials which we will discuss in this thesis, FMs are without a doubt the most extensively studied category, representing often the starting point for many innovative technologies in spintronics. The

racetrack memory (RTM) concept for example was first introduced in a FM nanowire [7, 83, 84]. The general idea of this device involves the encoding of data in sequences of MDs distributed along a magnetic track as seen in Figure 1.3(a) [77]. The whole pattern is displaced in a controlled fashion, most typically via current-induced DW motion, either through the spin-transfer torque (STT) [7] or the spin-orbit-torque (SOT) mechanisms [85]. A network of fixed data access elements in the shape of magnetic tunnel junctions (MTJ) can for example provide the read/write functionality in hybrid RTM-MTJ architectures [77, 86] as displayed in Figure 1.3(a,b) [77, 78]. One particular advantage here lies in the absence of any mechanical components compared to the operation of conventional hard-disk drive (HDD) storage devices, promising latency rates at the standard of commercial static or dynamic random-access memories [87]. Another benefit of the RTM technology is the opportunity for 3D scalability also displayed in Figure 1.3(a) [77] and its potential extension towards curved memory geometries which could be a market competitor for vertical NAND architectures available in modern solid-state drives [88].

Additionally, ferromagnetic DWs played an important role in the development of magnetic based logic devices, with some of the earliest proposals going back to the 1960s as discussed in Refs [83, 89] —factually, these works can also be considered precursors of the RTM concept. At the nanoscale, magnetic field-driven DWs in Permalloy [90] provided an initial platform for the implementation of basic logic gates such as NOT, AND/OR, in addition to fan-out and cross-over. Ever since the reference work of Allwood et al. in 2005 [90], many other DW-logic prototypes were suggested or demonstrated experimentally both in perpendicular and in-plane ferromagnetic materials [91–96], extending past the field-driven DW motion towards fully electrically controlled devices. DWs and MDs represent also an interesting candidate for brain-inspired hardware applications in this era of rapidly expanding AI technologies. For example, interconnected MTJ arrays in which synaptic weights and transfer functions are mediated by controlled DW displacement in FMs have been suggested for the implementation of artificial neural network architectures [79] as seen in subplot (c) of Figure 1.2. Such systems in addition to DW and MD patterns can emulate physical reservoir properties and perform complex neuromorphic inference tasks [97–102]. A fundamental advantage working with FM systems is represented by the non-vanishing macroscopic magnetic order parameter which enables a more straightforward detection and manipulation in comparison with AFMs as we discuss next.

Limited for a long time to a passive pinning role in the operation of magnetic read heads or random access memories [81], AFMs are envisioned now as promising active elements in the future generations of spintronic devices [80, 81, 103–105]. AFMs are characterised by a vanishing global magnetic order and negligible stray fields, making them ideal for device downscaling but posing a challenge from the perspective of read/write operations —see the comparative analysis in subplot (e) of Figure 1.3 [80]. Recent scientific milestones enabled the manipulation of the Néel order parameter via state of the art current or THz induced SOT in collinear or non-collinear AFMs [106–110]. While electrical measurements of collinear AFMs —typically via anisotropic or spin-Hall magnetoresistance [106, 107, 111–113]—exhibit small read-out signals around 0.1 – 1% [114], non-collinear AFM-based devices display a promising large tunneling magneto-resistance (TMR) signal [115, 116] up to around 100% which is comparable to FM-based tunneling junctions. In addition, depending on the presence of space and/or time symmetry breaking in the AFM sample, linear or circular dichroism may be used as an optical probe to extract the magnetic information [117, 118].

AFM DWs represent a potentially useful data carrying unit due to their greater stability compared to FM DWs [35, 119, 120]. While DW velocities in FMs are significantly hindered by internal instabilities known as the Walker breakdown [35, 119, 120] or by spin-wave (SW) emission analogous to the Cherenkov effect [121, 122] AFMs can display relativistic DW kinematics typically of the order of tens of km/s [123, 124]. Numerous theoretical investigations discussed already more than 40 years ago the exotic Lorentz-invariant dynamics of AFM DWs in weakly canted geometries under external Zeeman coupling [125–129], whereas modern studies demonstrated AFM DW kinematics induced by staggered SO fields [123, 130, 131] or even non-staggered magnetic field pulses [132]. A Walker-like breakdown effect has also been identified in the case of AFM DWs [124] in the vicinity of the magnonic limit. Experimental observations of AFM DW dynamics have so far been limited to a handful of studies and slower dynamic regimes due to the typical polycrystalline nature of the samples [133], the rather small exchange coupling in synthetic AFMs [134] or simply due to the driving mechanism [135]. Although single AFM DW transport remains very challenging at the device level, AFM magnetic textures also display an important role in the physics of Néel order switching which deserves to be carefully investigated [106–110]. It is expected synthetic and non-collinear AFMs may facilitate future progress in the experimental demonstration of controlled AFM DW dynamics [80, 103].

Lastly, FiM materials offer the possibility to combine up to some degree the advantages of both FM and AFM spintronic devices. Specifically, this translates in non-negligible stray fields which allows for easier detection and manipulation compared to AFM systems whilst offering a platform for faster magnetisation dynamics and better device scalability in comparison to FMs. This interpolation between AFM and FM-like properties results in principle from the separation in temperature between the angular momentum ( $T_A$ ) and magnetisation ( $T_M$ ) compensation points [82], both of which can be tuned in multilayered as well as in alloy FiM systems. In the context of DW dynamics, the direct consequence of this dual character takes shape in the possibility to stimulate efficient kinematics at angular momentum compensation due to the suppression of the Walker-breakdown effect and irrespective of STT [136], SOT [137] or external magnetic field driving [138]. The temperature variation of the angular momentum compensation point however represents also a disadvantage since it renders the FiM DW dynamics temperature sensitive and therefore susceptible to unwanted Joule heating effects [82, 136–140]. This becomes all more relevant in light of the recent findings which demonstrate the motion direction of a FiM DW may be flipped with a temperature variation across  $T_A$  [141]. FiM materials are an essential component to the ultra-fast magnetism field [13, 27, 32, 34, 62, 142], with ferrimagnetic DWs/MDs playing an important role in determining the speed of the helicity dependent/independent, AOS phenomena [41, 52, 55–57]. Although subplots (a-d) in Figure 1.3 particularly display FM-based memory and logic devices, both FiM and AFM materials may take their place as fundamental units of data in the development of analogous or improved prototypes [66, 81, 82], while of course adapting the read/write technology.

### 1.3.2 Opto-magnetism towards the next-generation of memory and logic devices

In contrast with the established magnetisation driving mechanisms discussed in the previous section (e.g. magnetic fields, spin-transfer and spin-orbit torques, temperature gradients etc), ultra-fast laser pulse stimuli simultaneously offer unprecedented

speed and energy efficiency advantages but constitute also a formidable theoretical and experimental challenge with many open and interesting questions left unanswered. It is instructive to compare first of all the time-scales as well as the energy requirements of these conventional driving forces with the potential of ultra-fast laser-matter coupling in driving magnetisation dynamics. Due to the limited estimations in this sense with respect to the specific laser manipulation of magnetic DWs, we can consider as sensible reference point, the figures involved in experiments of ultrafast switching of the magnetic order. As discussed in Ref. [143], conventional current induced magnetisation switching in MTJ stacks or spin valve architectures imposes increasingly large energy penalties in the attempt to go beyond the sub-100 ps threshold. Switching around this time scale in state of the art STT or SOT-based devices typically requires hundreds of fJ (femtojoules) per bit write operation [143–147]. In contrast, laser pulse excitation can routinely excite fs-ps switching dynamics for comparable fJ/bit energy consumption or even an ultra-low aJ (atto-joules)/bit regime depending on the material under study [13, 19, 27, 32, 33, 44, 143]. DW motion is a more energy demanding problem compared with single bit switching, simply if one conceptually views the wall displacement as a succession of switching events in a chain of magnetic bits going from point A to point B. Furthermore, a direct comparison between laser and electrical stimuli and their efficiency in driving DW dynamics is still difficult to achieve due to slow experimental progress in the former direction. Nonetheless, based on the magnetisation switching considerations discussed earlier, ultrafast magnetism holds great promise for efficient transport of DWs. A very interesting overview in between state of the art electrically-based DW driving and the associated energy requirements may however be found in Table 1 of Ref. [148].

Steering of DWs via ultra-fast lasers has been for a very long time studied as a secondary or integrated effect in the AOS of multilayered FM systems [42, 52, 53, 149], where typically repetitive fs-ps excitations in the kHz or MHz regime would lead to formation of stochastic multi-domain state and their subsequent growth driven by DW motion, under a debated dominant role of either thermal or non-thermal origin (see schematic representation in Figure 1.4(a) extracted from Ref. [42]). A general drawback here stems from the limited time-resolution of the optical Kerr microscopes which only allows for observation of displacement long after the excitation, so although the stimulus is ultra-fast, the DW motion in this time-scale remains difficult to probe. While the AOS of FIM alloys or multilayers is typically engineered for coherent reversal [12, 13, 27, 28], linearly polarised laser was also previously shown capable of generating transient DW dynamics [41]. Very interesting, the use of a single fs laser pulse can induce DW displacement both in FMs and FIMs [38, 39] of hundreds of nm up to 1 μm, as well as slow down the motion of propagating walls [40]. The major drawbacks of these experiments are either the challenging X-ray based imaging of the DW configurations or simply the micrometer-squared surface area of the samples which currently impedes device downscaling. Complex MDs/DWs patterns have been observed to provide routes towards accelerated ultra-fast demagnetisation and transient magnetisation enhancement [152] as well as reach extreme laser-induced velocities in the range of tens of km/s [153], making progress towards the objective of all-optical manipulation of magnetic textures at the sub-ps time-scale. It constitutes a real experimental challenge to isolate, displace and image one magnetic DW driven solely via a single-shot laser excitation. Controlled motion of a single DW structure was for example achieved in the magnetic semiconductor GaMnAsP in Refs. [24, 51] albeit multiple fs or ps ultra-fast stimuli were still required. Here, trains of circularly polarised laser excitations were able to

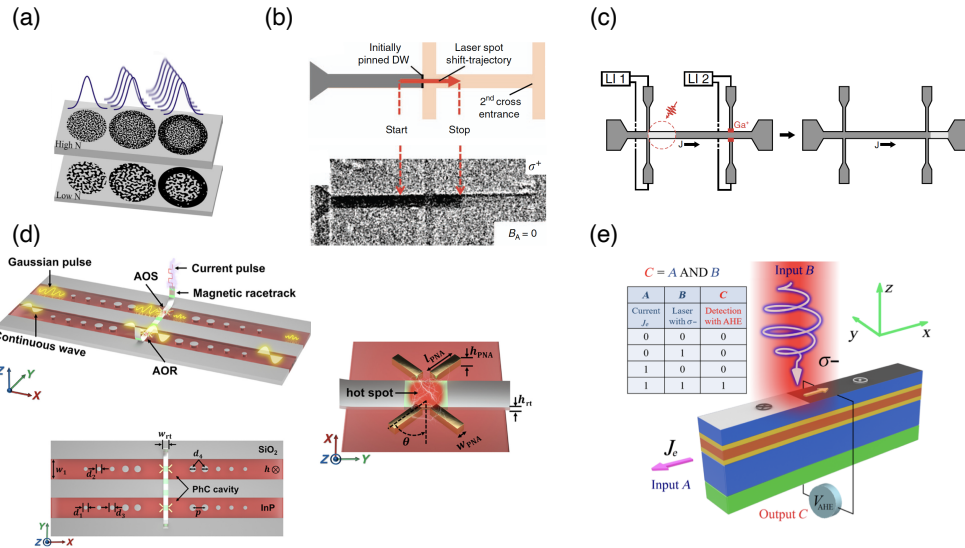


FIGURE 1.4: Representative state of the art experimental achievements regarding the opto-magnetic control of MDs/DWs configurations. (a) Typical patterns in the helicity dependent AOS of a FM system under multiple pulse excitation, where we observe stochastic nucleation of multi-domains and DW motion under combined thermal/non-thermal effects (extracted from Ref. [42]. Copyright (2018) by the American Physical Society). (b) Motion of single DW in the magnetic semiconductor GaMnAsP under a train of circularly polarised fs pulses [51] - extracted under the CC BY 4.0 licence. (c) Hybrid opto-electronic device demonstrated in the Co/Gd bilayer, where AOS is used to nucleate a single DW which is then driven across the track via the current-induced SOT mechanism [150] - extracted under the CC BY 4.0 licence. (d) Conceptual integration of nanoscale patterned optical waveguides and plasmonic antennae which could transmit and locally concentrate ultra-fast laser stimuli at the junction with a magnetic racetrack [151]. Copyright (2023) by the American Physical Society. In contrast with electrical state of the art magnetic reading, this device suggests the use of the polar Kerr magneto-optical effect, remaining to be seen whether future advances will also allow the replacement of current driven DW motion with all-optical mechanisms at the nanoscale level. (e) Hybrid opto-electronic DW/MD logic AND gate in which the input signal is encoded in the current direction and the helicity of the laser excitation. The output voltage is measured via the anomalous Hall effect and it is determined by the pinned state or the DW motion in one direction or the other [54]. Copyright (2019) by the American Physical Society.

stimulate deterministic DW dynamics via the optical spin-transfer torque (see subplot (b) in Figure 1.4). However, the size of the sample but also its very low Curie point—around three times smaller than room-temperature (300 K)—provides a real challenge for device integration. Terahertz laser pulses are known to stimulate coherent or non-coherent AFM spin dynamics [48, 110, 154–156] although controlled DW motion is yet to be achieved.

Hybrid opto-electronic schemes represent another promising route for DW/MD-based memory and logic devices. Towards this end, Co/Gd-multilayers are a good candidate material since they display both HI-AOS but can also be tuned for efficient SOT-based DW transport [28, 150, 157] as evidenced in Figure 1.4(c) [150]. Intriguingly, the work of [151] suggests an all-optical read-out scheme based on the nanoscale integration of optical waveguides and plasmonic antennae (see subplot (d) of Figure 1.4 [151]) that may facilitate the DW/MD interaction with ultra-fast light on the basis of the polar magneto-optical Kerr effect. It remains to be seen if future developments in this area will allow also for the nanoscale integration of an

equivalent DW driving scheme, based solely on optical means rather than state of the art current excitation. Hybrid opto-electronics can also provide the means for the development of logic prototypes as discussed in Refs. [54, 158]. There, input data is encoded in the current direction and the helicity of a circularly polarised pulse, the combinations of which may lead to DW pinning or bidirectional displacement. This permits the deterministic and controllable measurement of an output voltage via the anomalous Hall effect. Based on this scheme, simple logic functions such as AND, OR, NAND can be experimentally implemented [54, 158] (see example AND gate in subplot (e) of Figure 1.4 [54]). In addition, Ref. [54] demonstrates the potential "green" operation of optically assisted devices since the laser pulse excitation is shown to reduce up to 50% the threshold energy of SOT-driven DW motion.

## 1.4 The aims of this thesis and its outline

Although the goal of integrating all-optically controlled spintronic devices in a CMOS compatible technology is far from being reached [143], several interesting prototypes discussed in the last section provide an initial step in this direction. In the anticipation of further experimental progress, fundamental numerical and analytical calculations represent currently a suitable alternative tool in advancing and exploring the laser manipulation of MDs/DWs. The introductory chapter here focused on experimental state of the art achievements with the aim of providing context for the theoretical results discussed in this thesis. From a numerical point of view, the two main tools which we will use are atomistic spin dynamics (ASD) and high-temperature micromagnetic simulations based on the Landau-Lifshitz-Bloch (LLB) equation. As we discussed at the start of this chapter, two types of laser-induced effects will be studied: thermal and non-thermal. In essence, the results in this thesis are separated in three main chapters, each focusing on a distinct magnetic system: a ferromagnet, an antiferromagnet and lastly a ferrimagnetic bilayer. Additional chapters are reserved for theoretical considerations but also general conclusions and perspectives for future work. The schematic outline below provides guidelines for the thesis structure along with a brief summary of the subsequent chapters.

- **Chapter 2.** Here we review first of all the distinct microscopic magnetic interactions which determine the macroscopic magnetic ordering in a solid state-system. This discussion will facilitate the understanding and formal introduction of the ASD and micromagnetic LLB numerical models, on the basis of which we model the thermal/non-thermal phenomena. Furthermore, we touch upon a few general aspects related to DWs and MDs to aid the interpretation of the results presented subsequently.
- **Chapter 3.** The first system under investigation is a generic ferromagnetic DW. The question we answer in this chapter is whether sole longitudinal modifications of the wall structure at the fs time-scale can drive subsequent DW dynamics under a single laser excitation. As we saw in section 1.3.2, the controlled motion of single DW structures under one laser pulse constitutes a real experimental challenge and the physical mechanisms at play remain under debate. We construct our model from a generic perspective in the framework of the LLB model, considering that the transient longitudinal modification of the wall arises either due to a thermal or non-thermal coupling route [15, 55, 62, 159–161]. We present simulations of the DW dynamics in a simpler chain system as well as in a large-scale micromagnetic nanostripe. It is shown that fs

longitudinal DW deformations give rise to magnetisation modulus gradients  $\nabla|\vec{m}|$  which deterministically drive wall dynamics up to the ps-ns time-scale accompanied by an oscillatory behaviour of the magnetic texture, effectively passing angular momentum from the longitudinal to the transverse and precessional motion.

- **Chapter 4.** This chapter explores the possibility to drive AFM DW dynamics via a non-thermal laser optical torque (LOT) arising as a second-order light-induced response in the collinear antiferromagnet Mn<sub>2</sub>Au. Based on *ab-initio* LOT calculations presented in Ref. [162] and material parameters extracted from [163, 164], we construct an ASD Mn<sub>2</sub>Au model. We demonstrate that LOT can efficiently drive 90° DW dynamics but its spatial symmetry forbids the motion of 180° wall geometries. We discuss the distinction between LOT and the first-order response commonly known in the literature as the (Néel) spin orbit torque (NSOT) with respect to laser excitations in the optical and THz frequencies. The ASD simulations are compared with a theoretical, two-sublattice  $\sigma$ -model [123, 125, 126, 128, 129, 131], adapted for the present case. We demonstrate that the kinematics in a steady-state regime exhibit special relativity signatures which become observable even at low laser intensities. When the velocity surpasses the magnonic limit, part of the the AFM DW's relativistic energy is expended in generating new magnetic textures. Notably, the distinctive LOT symmetry enables precise control over the direction of the wall motion by adjusting the laser polarization direction or modifying the DW chirality.
- **Chapter 5.** Recently, a novel and rather universal HI-AOS mechanism was experimentally demonstrated in Tb and Dy-based ferrimagnetic multilayers, bilayers or trilayer systems [32, 34]. This thermal reversal process displays several interesting characteristics: (a) the energy threshold to switching is independent of the pulse duration up to several ps; (b) the laser excited area presents a concentric ring domain pattern; (c) the magnetisation exhibits a slow precessional based recovery process. In this chapter we construct a model based on the high-temperature micromagnetic framework of the LLB equation, capturing all aforementioned characteristics. While the switching kinematics along with the nucleation and evolution of the ring-domain patterns are investigated in the large-scale model, we employ a simpler two-macrospin (TM-spin) approach to study the equilibrium properties of the bilayer such as the net magnetisation variation with temperature or interlayer coupling strength. We discuss the shortcomings, achievements and potential improvements of the model in relation to available experimental evidence [32, 34].
- **Chapter 6.** This chapter is reserved for general conclusions and perspectives for future work based on the results presented along this thesis.

Lastly, for each of the results chapters, namely Chapters 3, 4 and 5, we provide supporting information in Appendix A, B and C respectively.



## Chapter 2

# Theoretical background and numerical models

In this chapter we first give a brief overview of the magnetic interactions arising at the microscopic scale which determine the magnetic ordering in a solid state-system. This discussion will serve as foundation for the understanding of the numerical models used throughout this thesis: atomistic spin dynamics, the high-temperature micromagnetic formalism of the classic Landau-Lifshitz-Bloch equation and the two-temperature model used to describe ultra-fast laser pulse heating. In addition, we touch upon a few general aspects related to magnetic DWs and domains that shall aid the interpretation of the results presented subsequently.

### 2.1 Magnetic interactions in solid-state systems

Before moving on to describe the various magnetic interactions in a solid-state system, let us first introduce two important physical quantities, namely the magnetic moment and the magnetisation vector. The description of magnetism at the atomic scale is intimately linked to the electronic angular momentum picture, involving an orbital and a separate spin contribution respectively. In a classical formulation, the net magnetic moment  $\vec{\mu}$  of an electron is linked to the total angular momentum  $\vec{j}$  via the relationship:

$$\vec{\mu} = -\gamma \vec{j}, \quad (2.1)$$

where  $\gamma$  represents the so-called gyromagnetic ratio defined as:  $\gamma = \frac{g e}{2m_e}$ . Here,  $e$  and  $m_e$  characterise the elementary charge and the electron mass, while  $g$  is the Landé splitting factor. The latter takes the distinct values of  $g = 1$  and  $g = 2$  for the orbital and spin contributions respectively. According to the laws of quantum mechanics, the allowed angular momentum values are restricted or quantized in units of the reduced Planck constant  $\hbar$ . This discrete nature reasonably extends to the magnetic moment an electron may carry such that the expectation value measured along a reference axis taken here as Oz is given by:

$$\langle \mu_z \rangle = - \underbrace{\frac{e\hbar}{2m_e} m_l}_{\text{orbital}} - \underbrace{\frac{e\hbar}{m_e} m_s}_{\text{spin}} = -g\mu_B m_j \quad (2.2)$$

where  $m_l$ ,  $m_s$  and  $m_j$  are the orbital, spin and total magnetic quantum numbers respectively, while  $\mu_B = \frac{e\hbar}{2m_e}$  is the elementary unit in electronic magnetism, known as the Bohr magneton. The calculation of the net magnetic moments and angular momenta in multi-electron atoms is simplified due to the null contribution of closed electron shells. Depending on the strength of the spin-orbit coupling, proportional to

the fourth power of the atomic number  $Z$ , two distinct vector addition schemes can be employed in the calculation of the net atomic angular momentum: the Russell-Saunders coupling [165] used for example in the case of iron and rare-earth (REs) ions [166] or the  $j-j$  coupling respectively, employed for instance in the case of actinides [167]. These semi-classical methods must obey Hund's rules [168] which determine the occupancy of the available electronic states and the configuration of the unfilled shells. Following this route, the calculated magnetic moments agree reasonably well with experimentally measured values in the case of isolated atoms or ions and even rare-earth bulk systems due to the localised nature of the  $4f$  electrons [166]. Such vector addition schemes are however inappropriate in accounting for the magnetism of transition metals due to the dual character of the  $3d$  magnetic electrons which exhibit both an itinerant and localised behaviour [169]. The band theory of magnetism gives a more appropriate picture of atomic magnetic moments in these materials. Finally, in the case of  $3d$  electrons, the orbital contribution to the total magnetic moment is "quenched" by interactions with the surrounding atomic environment (crystal field effects). For example, the magnetic moment of iron amounts to  $2.2\mu_B$  of which only 5% is of orbital origin [170]. In contrast, the  $4f$  electrons in REs ions are closer to the nucleus and screened from the crystal field by the outer electronic shells therefore displaying a strong spin-orbit coupling and weaker orbital quenching effect.

The quantum nature of the atomic magnetic moments leads to strong magnetic moment fluctuations at the sub-nanometer scale. It is therefore useful to introduce a homogeneous magnetic order parameter defined over a mesoscopic scale in a volume of a few  $\text{nm}^3$ . While in metallic systems we must take into account the delocalised electrons contributions which form bands, a macroscopic magnetisation quantity may still be introduced. Magnetism at this scale can be described by the density of atomic magnetic moments or the magnetisation vector:

$$\vec{M} = n \vec{\mu} \quad (2.3)$$

with  $n$  representing the number of atoms per unit volume which contribute a magnetic moment  $\vec{\mu}$ . Here  $\vec{M}$  is defined in units of  $\text{A/m}$ . In practical situations, this definition of the magnetisation may be substituted for a macroscopic average calculated over the entire volume of the sample.

### 2.1.1 The exchange interaction

In considering the origin of magnetic ordering at the macroscale, it is first of all sensible to examine the exchange contribution. The Coulomb interaction between two electrons is classically repulsive. In the quantum picture however, when two electrons occupy the same spatial region, their wave functions overlap, leading to a quantum mechanical correction to this classical interaction on the basis of the Pauli exclusion principle and the symmetry of wave functions. The correction results in an energy splitting between the so-called singlet (antiparallel spins) and triplet (parallel spins) states, known as the exchange energy. In the singlet state the electrons have a tendency to be close to each other favouring the atomic bonding as in the case of the hydrogen molecule [171], while the opposite is true for the triplet state where repulsive exchange forces arise. Since the symmetry analysis of the total wave function characterising a two-electron interacting system may be reduced to the spin component (with the orbital necessarily obeying the opposite wave function symmetry), the exchange energy can be naturally parametrised in terms of the relative alignment

between spins:

$$E_{\text{exchange}} = -J \vec{S}_1 \cdot \vec{S}_2, \quad (2.4)$$

where the so-called exchange integral  $J$  characterises the strength of the interaction (in Joules units) and  $\vec{S}_1, \vec{S}_2$  are two localised spin magnetic moments which can rotate freely on the unit sphere. The picture described by equation (2.4) is known as the Heisenberg model of exchange [172] and it represents the basis of modern atomistic spin dynamics (ASD) simulations [173] that will be introduced later in this chapter in section 2.3.1.

The exchange interaction can be generalised for a multi-particle system where often one might require also a tensorial formulation of the exchange integral instead of the isotropic picture given in equation (2.4). Calculating  $J$  is a complex task in general and is typically reserved for first-principle methods. In a given spin system the sign of the  $J$  constant dictates the ferromagnetic ( $J > 0$ ) or antiferromagnetic ( $J < 0$ ) ordering of the spins. Importantly, the magnitude of this interaction in transition metals is two orders of magnitude larger than the magnetostatic contribution discussed earlier [166], justifying in a first approximation the spontaneous ferromagnetic ordering up to hundreds of K of Fe, Co or Ni. However, the direct exchange mechanism described in (2.4) is often not sufficient to entirely account for the magnetic properties of the solid. For example, the highly localised  $4f$  states in REs leads to little overlapping of the orbitals rendering the Heisenberg direct exchange picture ineffective [169]. Moreover, the metallic nature of Fe, Co, Ni puts into question also the role of conduction electrons in the observed magnetic properties. Generally, indirect exchange mechanisms in conjunction with a combined itinerant/localised electron treatment are further required to fully understand the macroscopic magnetic properties. In a continuum description, the strength of the Heisenberg exchange interactions at the macroscale is expressed through the so-called *exchange stiffness* constant  $A$  measured in units of Joules/m. For a cubic atomic arrangement characterized by a lattice parameter  $a$ , the relationship between  $A$  and  $J$  is expressed via  $A \propto J/a$ , where the exact proportionality factor depends on the number of magnetic atoms in the unit cell.

### 2.1.2 The spin-orbit interaction, magnetocrystalline anisotropy and anisotropic exchange

The spin-orbit (SO) coupling although 10 – 100 times smaller in magnitude compared to the strength of the exchange interactions [169], it has great technological implications in magnetism being for example at the origin of numerous transport phenomena in spintronics [65, 174]. In the case of isolated atoms, the SO interaction can initially be understood based on a semiclassical picture or the more appropriate relativistic Dirac equation, but in solid-state systems a more complex treatment is required by means of the ligand field theory [169, 175]. In the semiclassical approach, the SO coupling is described as the interaction of the local spin magnetic moment  $\vec{\mu}_s = g\mu_B \vec{S}$  and the magnetic field  $\vec{H}_o$  arising due to the relative orbital motion of the nucleus at a distance  $\vec{r}$  with respect to an inertial frame of reference comoving with the electron [169, 176]:

$$E_{\text{spin-orbit}} = -\frac{1}{2}\mu_0 \vec{\mu}_s \cdot \vec{H}_o = \frac{1}{2} \frac{g\mu_B \hbar}{rm_e c^2} \frac{dV(\vec{r})}{dr} \vec{S} \cdot \vec{L}, \quad (2.5)$$

where  $V(\vec{r})$  is the electrostatic potential at the electron site induced by the presence of the nuclear charges and  $\hbar \vec{L} = m_e \vec{r} \times \vec{v}$  is the orbital angular momentum. Here  $\vec{v}$

denotes the orbiting velocity of the nucleus in the electron frame of reference while  $m_e$  characterises the electron mass. The relationship between  $\vec{H}_0$  and the electrostatic potential  $V(\vec{r})$  is written as:  $\mu_0 \vec{H}_0 = -\frac{\vec{r}}{r} \frac{dV(\vec{r})}{dr} \times \vec{v}/c^2$ , where  $c$  is the speed of light. In addition, the Landé factor is taken here as  $g = 2$ . One important concept related to the SO interaction is the magnetocrystalline anisotropy (MCA). As illustrated in the simple picture of equation (2.5), to minimise the  $E_{\text{spin-orbit}}$  energy penalty, the spin magnetic moment tends to align itself parallel with respect to the orbital magnetic field, whose direction is in turn determined by the crystal symmetry of the lattice. Thus, the macroscopic observation of hard and easy axes of magnetisation in a given sample is intrinsically related to the microscopic SO coupling. Based on the Heisenberg model of localised spin magnetic moments, common expressions for uni-axial and cubic MCA energy densities can be written as [173]:

$$E_{\text{uni-axial}} = k_u (\vec{S} \cdot \vec{e})^2, \quad E_{\text{cubic}} = \frac{k_c}{2} (S_x^4 + S_y^4 + S_z^4), \quad (2.6)$$

where the  $k_u$  and  $k_c$  constants expressed in units of Joules determine the strength of the MCA contribution at the atomic level. Here, the unit vector  $\vec{e}$  determines the uni-axial easy-direction and  $S_{x,y,z}$  are magnetic moment projections in the Cartesian coordinate system  $Oxyz$  whose fourth-order products determine the easy and hard cubic anisotropy directions. A more formal inspection of these parameters will be given in the context of the atomistic spin dynamics model discussed in section 2.3.1. Similar to the correspondence between the  $J$  and  $A$  parameters, the MCA can otherwise be discussed from a continuum point of view where a generic (cubic or uni-axial) anisotropy constant  $K$  expressed in units of Joules/m<sup>3</sup> is the macroscopic link of the atomic  $k$ .

Finally, the SO coupling is also at the origin of anisotropic exchange or the so-called Dzyaloshinskii-Moriya interaction (DMI) [177, 178] first introduced in bulk crystals with broken inversion symmetry. Based on the Heisenberg, localised, spin magnetic moment picture, the DMI is parametrised as:

$$E_{\text{DMI}} = \vec{D} \cdot (\vec{S}_1 \times \vec{S}_2), \quad (2.7)$$

where  $\vec{D}$  is the so-called DMI vector (assumed here in units of Joules) which depends on the crystal symmetry and the SO-coupling strength. In contrast with the isotropic exchange given in equation (2.4), the DMI energy favours a non-collinear spin alignment and in the context of this work it is relevant in the analysis of the magnetic domain walls chirality and equilibrium configuration. We will touch upon this point in the results presented in Chapter 3.

### 2.1.3 The Zeeman interaction

In addition, it is also worth mentioning the so-called Zeeman interaction between a local dipole moment  $\vec{\mu}$  and an externally applied magnetic field  $\vec{H}$ :

$$E_{\text{Zeeman}} = -\mu_0 \vec{\mu} \cdot \vec{H}. \quad (2.8)$$

In comparison to the exchange coupling described by equation (2.4) which acts directly on the spin component only, an external magnetic field acts both on the spin and orbital magnetic moments. The strength of this interaction is in principle limited by the maximum available magnetic field which can be generated in a laboratory. Practically, the Zeeman coupling in conjunction with the presence of MCA are at the

origin of magnetic hysteresis, where the magnetisation responds to an applied field and displays an irreversible behavior, central to the operation of magnetic storage devices. Lastly, in the study of opto-magnetic phenomena the influence of a laser pulse excitation on the magnetic order is often expressed in the shape of an effective Zeeman field as for example in the case of the IFE [62, 179–182], repeatedly encountered along the subsequent chapters of this thesis.

### 2.1.4 The dipolar interaction

Lastly, we examine the local magnetostatic or dipolar interaction between two dipoles  $\vec{\mu}_1$  and  $\vec{\mu}_2$  at a distance  $\vec{r}$ . The energy of this interaction is written as:

$$E_{\text{dipolar}} = \frac{\mu_0}{4\pi r^3} \left[ \vec{\mu}_1 \cdot \vec{\mu}_2 - \frac{3}{r^2} (\vec{\mu}_1 \cdot \vec{r}) (\vec{\mu}_2 \cdot \vec{r}) \right], \quad (2.9)$$

where  $\mu_0$  is the vacuum permeability. Summing over all such pair interactions within the crystal one obtains the magnetostatic contribution to the total energy which accounts for shape-induced anisotropy or the formation of magnetic domains. The summation in this discrete picture is cumbersome due to the large number of microscopic constituents, for this reason the total dipolar contribution is often expressed using the magnetisation vector  $\vec{M}$  as:

$$E_{\text{dipolar}}^{\text{total}} = \frac{1}{2} \mu_0 \int \vec{M}(\vec{r}) \cdot \vec{H}_{\text{D}}(\vec{r}) dV, \quad (2.10)$$

with  $\vec{H}_{\text{D}}$  denoting the so-called demagnetising or self-interaction field [170] measured in units of A/m. While a general analytic formula for this energy does not exist, certain homogeneously magnetised ellipsoids may be shown to allow simple expressions for  $E_{\text{dipolar}}^{\text{total}}$ . In complex geometries or large-scale systems, we generally must employ a numerical approach for this calculation as we will also discuss in section 2.3.2. Dipolar contributions cannot however account for the spontaneous magnetic ordering observed up to hundreds of Kelvin, typical for example in the case of transition metals. In equivalent temperature units, the order of magnitude of dipolar interactions revolves around  $\sim 1$  K [169, 176].

## 2.2 Magnetic domains and domain-walls

MDs and DWs are a recurrent and essential concept discussed along this thesis. Here we provide a brief overview of their origin and properties with particular reference to the configurations discussed in Chapters 3–5. In broad terms, a magnetic DW represents the spatial transition between two uniformly magnetised regions called domains in which the magnetic order parameter finds itself in a minimum energy state. Depending on the relative magnetic orientation between the domains they separate, distinct wall geometries may be encountered, most commonly in the shape of 180° or 90° configurations (see schematics in Figure 2.1 a). In FMs, the formation of magnetic domains may be understood in a first picture in terms of the magnetostatic energy contribution introduced in equation (2.10). To minimise the energy penalty associated with this term, a closure of the magnetic flux lines inside the crystal is preferred which tends to reduce the strength of the stray fields and leads to the magnetisation texture breaking into a multi-domain state, depending on the volume and crystallography of the sample as well as the energy cost associated with the DW

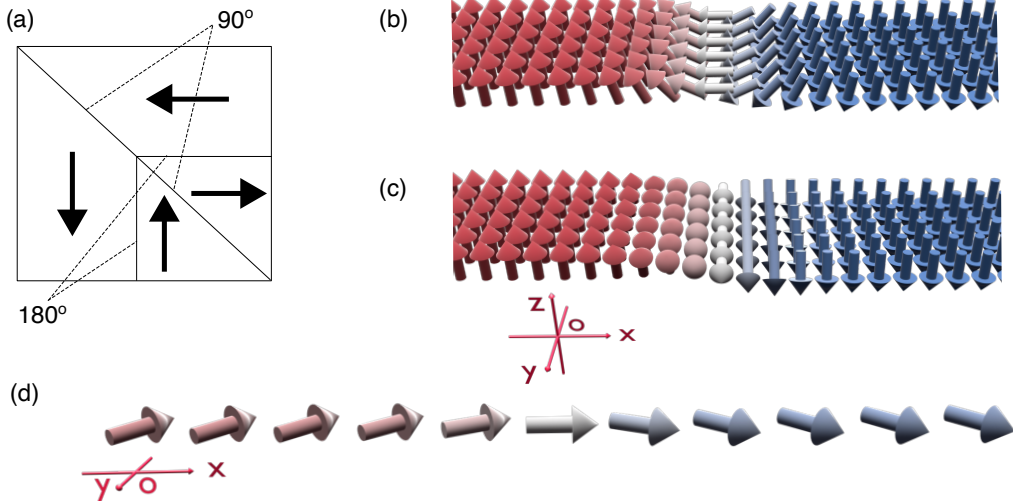


FIGURE 2.1: Typical domains and domain-wall geometries encountered in this work. (a) Schematics of 90° and 180° magnetic DWs according to the relative orientation between the MD configurations they separate. In (b) and (c) we display the magnetisation rotation in Néel and Bloch 180° DWs in perpendicularly magnetised strips. (d) 90° in-plane DW in an idealised wire. The  $Oxyz$  system of coordinates in subplot (c) corresponds also to subplot (b).

nucleation. In reality, this is a much more complex problem which often needs to be understood taking into account a rather diverse array of factors such as: magnetic sample inhomogeneities, magnetostriction effects, the presence of defects and interfaces or generally any symmetry breaking factor of the macroscopic magnetic order [176]. In fact, these ingredients become more relevant in the discussion of multi-domain structures arising in AFMs due to the minimal influence of magnetostatic effects in these materials.

In the simplest possible picture, a stable DW configuration is determined solely by the competition between exchange and MCA, which yields the characteristic DW width and energy density parameters proportional to:

$$\delta_{DW} \propto \sqrt{A/K}, \quad \sigma_{DW} \propto \sqrt{AK}, \quad (2.11)$$

where the exchange stiffness  $A$  (measured in units of Joules/m) was discussed in section (2.1.1) in relation to the exchange integral  $J$ . On the other hand,  $K$  is treated here as a generic anisotropy constant (expressed in units of Joules/m<sup>3</sup>) which characterises the volume energy density of magneto-crystalline origin associated for example with cubic or uni-axial crystal symmetry. Depending on the additional contributions,  $K$  may be adjusted to an effective anisotropy constant which for example takes into account the presence of demagnetising or magnetostrictive effects. Whereas energetically—as shown by  $\sigma_{DW}$ —an obvious balance between exchange and anisotropy must exist within the wall, the length parameter  $\delta_{DW}$  tells us wider DWs are preferred to minimise the exchange penalty, while the MCA contribution favours sharper transition regions between domains.

In perpendicularly magnetised strips (discussed in Chapters 3 and 5), we typically encounter two 180° DW configurations, shown in subplots (b) and (c) of Figure 2.1. The magnetisation plane of rotation in the wall (with respect to the geometry of

Figure 2.1) defines either a Néel ( $Oxz$ ) or Bloch DW configuration ( $Oyz$ ). The stable geometry depends on the width and thickness of the magnetic strip in relationship to the characteristic wall width parameter  $\delta_{DW}$  as shown for example in Ref [183] and can be predicted via numerical modeling by also taking into account the magneto-static effects in addition to the simplified picture in equation (2.11). The presence of interfacial DMI further complicates the DW stability analysis. Depending on the strength of the anisotropic exchange, a Bloch-Néel DW transition can occur. At the same time, the sign of the DMI biases a specific wall chirality which is of critical practical importance in race-track applications where a train of DWs with identical chirality is preferred [184]. In Chapter 4, we will focus our attention on  $90^\circ$  AFM DW geometries in an idealised magnetic wire structure (subplot (d) of Figure 2.1) where magnetostatic effects are not relevant. The  $90^\circ$  wall and generally wall angles less than  $180^\circ$  arise in materials characterised by multiaxial or higher-order MCA contributions [185]. In addition,  $180^\circ$  DWs may collapse in two separate  $90^\circ$  walls under the effect of an applied Zeeman field as predicted for example in spin-flop phase transition studies in AFMs [186] while a similar behaviour can also be achieved by magnetostrictive effects [187]. We will take a detailed look at the dynamic and static DW profiles in the particular problems discussed in Chapters 3, 4 and 5.

## 2.3 Models of magnetisation dynamics

The study of magnetisation dynamics under the action of a laser-pulse excitation is central to this work. For this, two separate but intimately linked formalisms will be employed: (1) atomistic spin dynamics (ASD) concerned with the time variation of localised atomic moments —most often associated with the spin magnetic moment  $\vec{S}$ . (2) high-temperature micromagnetics in the framework of the Landau-Lifshitz-Bloch (LLB) equation which treats the magnetisation dynamics at a mesoscopic scale with respect to a magnetic order parameter that can vary with temperature  $\vec{M}(T)$ . A very common practice in obtaining a detailed picture of a magnetic materials' behaviour at different length and time scales involves a multi-scale modeling approach. This bottom-up procedure typically starts with identifying the microscopic properties of the material (magnetic moments, strength of the exchange or SO interaction, coupling to external stimuli such as laser pulse excitation etc) via *ab-initio* calculations. While the latter do not make the central point of the thesis, we shall make extensive use of such first-principles results in parametrising the magnetic systems and laser-induced effects under study. Ab-initio methods aim to circumvent the computationally challenging problem of solving the Schrödinger equation for many-body systems. To meet this goal, the Density Functional Theory (DFT) is a widely used approach, reducing the complexity by focusing on the electron density rather than the individual microscopic degrees of freedom [188, 189]. Furthermore, extensions to this formalism as for example time-dependent DFT enable studies of dynamic phenomena, such as ultrafast spin dynamics [190]. Ab-initio methods, while highly accurate and intrinsically linked to the quantum nature of magnetism, remain still computationally intensive and generally limited to small systems of tens of atoms.

At the upper length scale limit, micromagnetic models treat the magnetisation in a continuum approximation which neglects details of the atomic structure [191, 192]. This enables the investigation of the magnetic materials' behaviour at large spatial scales (from hundreds of nm to microns) and better suits problems such as

the nucleation of magnetic domains or DW propagation. The central goal in micromagnetic models is the calculation of the spatial distribution of the mesoscopic vector  $\vec{M}$  which yields the minimum free energy of the system. At the dynamic level, equations such as the stochastic LLG or the LLB model well describe magnetisation dynamics at low and elevated temperatures respectively [193–198]. It is specifically the LLB equation which we will use later in Chapters 3 and 5. The main advantage represented by the continuum approximation introduces also a limitation: the absence of atomic level details makes it often challenging to correctly describe phenomena at magnetic interfaces, account for finite-size effects in granular systems and model the intrinsic antiferromagnetic or ferrimagnetic coupling.

### 2.3.1 Atomistic spin dynamics

The ASD framework employed in Chapter 4 is part of a general class of numerical models which bridge the gap between ab-initio and micromagnetism by simulating systems on a scale of several Å to hundreds of nm. ASD takes into account the atomic details of the crystal structure thus resolving the micromagnetic limitation. The time evolution of the local magnetic moments is governed by an atomistic LLG equation, often extended with stochastic thermal fields to simulate temperature effects. This makes ASD particularly useful in investigating ultrafast demagnetization or switching processes triggered by femtosecond laser pulses [13, 27, 62, 199–201]. Moreover, ASD typically incorporate first-principles parameters and serve in turn as an useful tool for obtaining the correct temperature scaling of anisotropy, exchange stiffness or saturation magnetisation parameters used in micromagnetic calculations [202–204]. The localised Heisenberg description of exchange discussed in section 2.1.1 serves as basis for the ASD model presented here. The degree to which this formalism correctly describes magnetism in both 3d and 4f species is an ongoing debate due to the itinerant electron behaviour which most often is neglected in 3d metals, the little wave function overlap in the case of 4f orbitals, or generally the competition between orbital and spin magnetic moments. Nonetheless, in many practical situations, ASD remains an useful tool in modeling experimental results. The main assumption in this model is the existence of a locally collinear magnetisation density  $\vec{\mu}_{\text{at}}^i$ , defined over a spatial region  $\Omega_i$  surrounding an atomic site  $i$ , which is proportional to  $\propto \int_{\Omega_i} \vec{\mu}(\vec{r}) d\vec{r}$  [205]. Although technically both orbital and spin magnetic moments contribute to  $\vec{\mu}_{\text{at}}^i$ , ASD models refer to the local magnetisation density attached to an atomic site via *spin vectors*  $\vec{S}_i$  freely rotating on the unit sphere, reminiscent of the often quenched orbital contribution in 3d metals [173]. We shall maintain hereon this *spin vector*—or simply *spin*—terminology keeping in mind this is not necessarily appropriate particularly in the case of the 4f series. Explicitly, the  $\vec{S}_i$  vector is written as  $\vec{S}_i = \vec{\mu}_{\text{at}} / |\vec{\mu}_{\text{at}}|$ . Here,  $\mu_{\text{at}}$  is expressed in Bohr magneton units.

Starting from equation (2.4) and depending on the magnetic system under study, one typically arrives at an extended Heisenberg Hamiltonian in the simplest case written as:

$$\mathcal{H} = -J \sum_{\langle i,j \rangle}^N \vec{S}_i \cdot \vec{S}_j - k_u \sum_i^N \left( \vec{S}_i \cdot \vec{e} \right)^2 - \mu_0 \mu_{\text{at}} \sum_i^N \vec{S}_i \cdot \vec{H}. \quad (2.12)$$

The first term in equation (2.12) denotes the isotropic exchange interaction of strength  $J$  (measured in units of Joules/atomic link) between the normalised magnetic moments  $\vec{S}_i, \vec{S}_j$ , with the summation  $\langle i, j \rangle$  considering only nearest-neighbours interactions in a system of  $N$  total atomic sites. In more complex structures, the  $J$  constant must be written in a tensorial form to account both for symmetric and antisymmetric exchange contributions. We also assume here the spin vectors  $\vec{S}_{i,j}$  are attached to atomic sites of the same species. The second energy term represents the MCA contribution arising from the SO-coupling being written here in the simplest uniaxial form which tends to align the  $\vec{S}_i$  vectors along a direction defined by the unit vector  $\vec{e}$  (taken for example along  $Oz$ ). The strength of the MCA is set here by the  $k_u$  constant expressed in units of Joules/atomic site. The last term in equation (2.12) characterises the Zeeman interaction between the local moment  $\vec{S}_i$  and an externally applied field  $\vec{H}$ . As discussed in the introductory part of section 2.3, the parameters  $k_u, \mu_{\text{at}}, J$  are most typically extracted from ab-initio calculations.

To describe the dynamics of a magnetic system described by a model Hamiltonian given in (2.12), we employ an atomistic-like LLG equation:

$$\frac{d\vec{S}_i}{dt} = -\frac{\gamma}{1+\lambda^2} \vec{S}_i \times \left[ \vec{H}_{\text{eff}}^i + \lambda \left( \vec{S}_i \times \vec{H}_{\text{eff}}^i \right) \right], \quad (2.13)$$

where the effective field  $\vec{H}_{\text{eff}}^i$  is given by  $\vec{H}_{\text{eff}}^i = -\frac{1}{\mu_0 \mu_{\text{at}}} \frac{\delta \mathcal{H}}{\delta \vec{S}_i}$ . The single and double cross products in equation (2.13) characterise the precession and transverse dynamics respectively of the spin vector  $\vec{S}_i$  under the action of  $\vec{H}_{\text{eff}}^i$ . Finally,  $\lambda$  represents a phenomenological damping parameter which typically takes values  $\leq 1$ , with 1 denoting a critical threshold beyond which the motion is overdamped. Often, the effective field  $\vec{H}_{\text{eff}}^i$  is augmented with a stochastic white noise contribution  $\vec{\xi}_i$  to describe thermally induced magnetic disorder. This noise term as introduced by Brown [193] is characterised by the following statistical properties:

$$\langle \xi_i^l(t) \rangle = 0 \quad (2.14)$$

$$\langle \xi_i^l(t) \xi_j^l(t+t') \rangle = \underbrace{\frac{2\lambda k_B T}{\gamma \mu_{\text{at}}}}_{\text{noise strength}} \delta_{ij} \delta(t'), \quad (2.15)$$

where  $\langle \dots \rangle$  is a time average,  $l = x, y, z$  denotes the Cartesian component of  $\vec{\xi}_i$ , the  $i, j$  indices denote the atomic sites,  $\delta_{ij}$  is the Kronecker delta and  $\delta(t')$  is the Dirac delta function. Equations (2.14) and (2.15) ensure the thermal noise is stationary and isotropic, the  $\xi_i^l$  components are normally distributed around a mean value of zero and are uncorrelated for  $t$  greater than  $t'$  (an upper bound around  $t' = 1$  fs is considered in the context of ultra-fast spin dynamics simulations [173]). The strength of this stochastic noise is directly proportional to the damping  $\lambda$  and the thermal energy  $k_B T$  where  $k_B$  is the Boltzmann constant and  $T$  is the temperature of the thermostat. In Chapter 4 however, where we will employ the ASD model in the study of LOT-driven  $\text{Mn}_2\text{Au}$  DW dynamics, we will consider the  $T \rightarrow 0$  K limit only. We conduct the ASD simulations using the open-source software package VAMPIRE developed at the University of York [173]. The time-integration of the LLG equation in (2.13) is based on a simple Heun scheme.

### 2.3.2 High temperature micromagnetics: the classical Landau-Lifshitz-Bloch equation

Another important numerical model in the context of this thesis is the Landau-Lifshitz-Bloch (LLB) equation. This formalism resolves the limitations of standard micromagnetics allowing the study of magnetisation dynamics at elevated temperatures. In the initial micromagnetic picture introduced by Brown [191, 192], the main disadvantage is the conservation of the magnetisation vector  $|\vec{M}| = \text{const.}$  during all dynamic processes, which naturally precludes any thermal quenching or disorder in the system. A typical approach in attempting to circumvent this problem relies on a

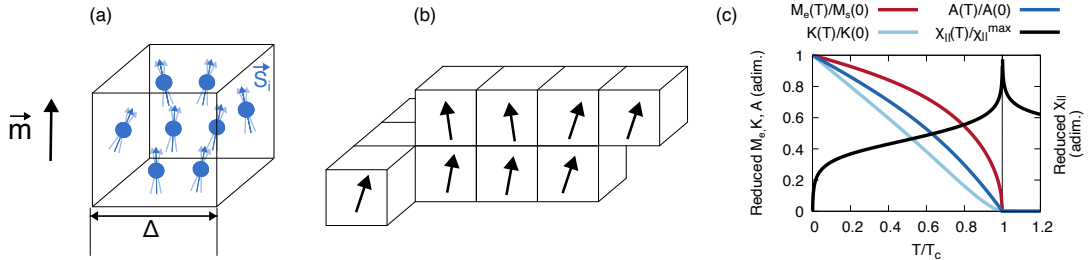


FIGURE 2.2: High-temperature micromagnetics in the LLB framework. (a) The reduced magnetisation vector (macrospin)  $\vec{m}$  calculated as the thermal average over an ensemble of atomic spins  $\vec{S}_i$  in a given cubic volume of lateral spacing  $\Delta$ . (b) Finite-difference discretisation scheme employed in this work. (c) Typical temperature scaling of the equilibrium magnetisation  $M_e(T)$ , exchange stiffness  $A(T)$ , anisotropy constant  $K(T)$  and parallel susceptibility  $\chi_{||}(T)$  for a generic Co system ( $T_c = 1480$  K). The latter is represented separately along the right hand side ordinate axis in logarithmic scale. To plot the diagram we consider  $A(T) \propto m_e^2$  as obtained in the MFA [198] and  $K(T) \propto m_e^3$ —the so-called Callen-Callen scaling [206]—while  $\chi_{||}(T)$  is given in expression (2.19) and  $M_e(T)$  is obtained solving the self-consistent Curie-Weiss equation.

Langevin dynamic picture which considers the effect of a fluctuating thermal contribution in the total field acting upon  $\vec{M}$ , an idea also first introduced by Brown [193]. It has been shown however that this method strongly underestimates the Curie temperature  $T_c$  of the material. Particularly, near  $T_c$ , the critical slowing down effects introduce a competition between transverse and longitudinal relaxation mechanisms [197]. This issue is also strongly connected to the spatial discretisation employed in the typical finite-difference scheme of micromagnetics, which cuts off high frequency spin waves and contributes to the inaccurate representation of magnetisation dynamics at elevated temperatures [207].

We shall here discuss the essential concepts of the alternative high-temperature micromagnetic formalism based on the classic LLB equation. Introduced by Garanin in Ref. [208]—much later than the quantum version [209]—the classical LLB derivation starts off from an ensemble of atomic spins  $\vec{S}_i$  in which the spin-spin interactions are described within the mean-field approximation (MFA) in addition to coupling the system to a thermal bath via stochastic Langevin fields. Based on a Fokker-Planck equation describing the time dynamics of the probability density of the ensemble, Garanin arrives at a macroscopic equation for the thermally averaged spin polarisation or reduced magnetisation vector  $\vec{m} = \langle \vec{S}_i \rangle$  (Figure 2.2 a) where  $\langle \dots \rangle$  denotes thermal averaging over the ensemble of fluctuating atomistic moments. This macrospin model later was adapted for large-scale micromagnetic problems based on the finite-difference scheme [198] which we employ also in this work (Figure 2.2 b). In a generic ferromagnetic system discretised in  $i = 1, N$  cubic cells with lateral

spacing  $\Delta$ , the classical LLB equation per individual cell reads:

$$\frac{d\vec{m}_i}{dt} = -\gamma\vec{m}_i \times \vec{H}_{\text{eff}}^i - \gamma\alpha_{\perp} \frac{\vec{m}_i \times (\vec{m}_i \times \vec{H}_{\text{eff}}^i)}{m_i^2} + \gamma\alpha_{||} \frac{(\vec{m}_i \cdot \vec{H}_{\text{eff}}^i)\vec{m}_i}{m_i^2}. \quad (2.16)$$

The unit vector  $\vec{m}_i$  is defined as  $\vec{m}_i = \vec{M}_i(t, T)/M_s(0)$  with  $M_s(0)$  being the saturation magnetisation at 0 K while  $\vec{M}_i(t, T)$  is the time and temperature dependent magnetisation vector. Compared to standard micromagnetics, equation (2.16) naturally incorporates both the precession and transverse magnetic relaxation as well as allows the longitudinal deformation of  $\vec{m}_i$  as a function of temperature. Further, the constant  $\gamma$  denotes the electron gyromagnetic ratio, while  $\alpha_{||}$  and  $\alpha_{\perp}$  are the dimensionless longitudinal and transverse damping parameters defined as:

$$\alpha_{||} = \lambda \frac{2T}{3T_c}, \quad \alpha_{\perp} = \lambda \begin{cases} (1 - \frac{T}{3T_c}) & T \lesssim T_c, \\ \frac{2T}{3T_c} & T \gtrsim T_c. \end{cases} \quad (2.17)$$

The proportionality factor  $\lambda$ —equivalent to the damping factor in the ASD model in section 2.3.1—is a measure of the intrinsic spin-flip scattering events which defines the coupling strength between the spin degrees of freedom and the thermal bath. The damping parameters  $\alpha_{||}$  and  $\alpha_{\perp}$  are directly proportional to the  $T/T_c$  ratio where  $T$  is the bath temperature and  $T_c$  is the Curie point of the ferromagnetic sample. The dynamics of each macrospin  $i$  are governed by the total effective field  $\vec{H}_{\text{eff}}^i$ , defined most typically as:

$$\vec{H}_{\text{eff}}^i = \vec{H}_{\text{ex}}^i + \vec{H}_{\text{ani}}^i + \vec{H}_{\text{dem}}^i + \begin{cases} \frac{1}{2\chi_{||}} \left(1 - \frac{m_e^2}{m_c^2}\right) \vec{m}_i & T \lesssim T_c, \\ -\frac{1}{\chi_{||}} \left(1 - \frac{3T_c}{5(T-T_c)} m_e^2\right) \vec{m}_i & T \gtrsim T_c. \end{cases} \quad (2.18)$$

The temperature dependent  $m_e = M_e(T)/M_s(0)$  value is the macrospin vector length at thermal equilibrium which can be measured experimentally or obtained via ASD simulations. Here it is obtained within the MFA by solving the self-consistent Curie-Weiss equation. Assuming a classical spin system this evaluates to:  $m_e = L(\beta J_0 m_e)$ , where  $L$  is the Langevin function,  $J_0 = 3k_B T_c$  expresses the strength of the Heisenberg exchange coupling and  $\beta = 1/(k_B T)$  is a measure of the thermal field with  $k_B$  the Boltzmann constant. The  $\chi_{||}$  term denotes the longitudinal susceptibility which in the MFA evaluates to:

$$\chi_{||}(T) = \begin{cases} \frac{\mu_{\text{at}} \beta L'}{1 - \beta J_0 L'} & T \lesssim T_c, \\ \frac{\mu_{\text{at}} T_c}{J_0(T-T_c)} & T \gtrsim T_c, \end{cases} \quad (2.19)$$

where  $L'$  represents the derivative of the Langevin function with respect to the argument  $x = \beta J_0 m_e$  and the  $\mu_{\text{at}}$  constant denotes the atomic magnetic moment.

The exchange field  $\vec{H}_{\text{ex}}^i$  field term accounts for the micromagnetic exchange interaction between macrospins, being fundamentally defined and numerically approximated in the following manner [198]:

$$\vec{H}_{\text{ex}}^i = \frac{2A(T)}{M_s(0)m_e^2} \nabla^2 \vec{m}_i \simeq \frac{2A(T)}{M_s(0)m_e^2 \Delta^2} \sum_{j=1}^{n_i} (\vec{m}_j - \vec{m}_i), \quad (2.20)$$

with the summation taking into account all the  $n_i$  neighbours of each individual macrospin vector  $\vec{m}_i$  and the  $A(T)$  parameter indicating the temperature-dependent exchange stiffness.

Given a Cartesian  $Oxyz$  frame of reference, we consider an uni-axial MCA with the easy-axis (EA) taken along the  $Oz$  direction. This MCA contribution will be employed both in Chapters 3 and 5. The anisotropy field  $\vec{H}_{\text{ani}}^i$  is thus defined as:

$$\vec{H}_{\text{ani}}^i = -\frac{(m_x^i \vec{e}_x + m_y^i \vec{e}_y)}{\chi_{\perp}(T)}. \quad (2.21)$$

For practical reasons, the transverse susceptibility  $\chi_{\perp}(T)$  is linked to a temperature dependent, anisotropy constant  $K(T)$  via the relationship:

$$\chi_{\perp}(T) = \frac{M_s(T)}{2K(T)}. \quad (2.22)$$

The demagnetising field  $\vec{H}_{\text{dem}}^i$  is expressed as a discrete convolution sum of the demagnetising tensor  $\vec{N}(\vec{r}_i - \vec{r}_j)$  and the reduced magnetisation vector  $\vec{m}_j$ , taking into account the contribution of all macro-cells in the system:

$$\vec{H}_{\text{dem}}^i = -\mu_0 M_s(0) \sum_j N(\vec{r}_i - \vec{r}_j) \cdot \vec{m}_j. \quad (2.23)$$

Since the demagnetising tensor depends only on the relative positions  $\vec{r}_{i,j}$  of the cells, its calculation is done only once at the start of each simulation employing the method of Newell *et al.* [210]. The overall calculation of the  $\vec{H}_{\text{dem}}^i$  field is carried out using the traditional approach based on the use of the Fast Fourier Transform (FFT) algorithm.

The last term in Eq. (2.18) constitutes the so-called longitudinal field  $\vec{H}_{\text{lon}}^i$ , a measure of the competition between the atomic spin ordering and the disorder induced by the thermal bath, which ultimately dictates the length of the macroscopic vector  $\vec{m}_i$ . Importantly, we need to distinguish this contribution from  $\vec{H}_{\text{ex}}$ .  $\vec{H}_{\text{lon}}$  acts internally at the level of each macrospin and characterises the magnetisation dynamics at the ultra-fast time-scale (from fs to ps) determined by high-frequency spin wave excitations inside each macrocell. In contrast,  $\vec{H}_{\text{ex}}$  is a much weaker field (10 – 100 times smaller) which defines the coupling between distinct macrospins, being relevant for the magnetisation dynamics beyond the ps time-scale and is determined by low-frequency spin-waves. Lastly, the LLB model takes as input several temperature-dependent material parameters:  $M_e(T)$ ,  $A(T)$ ,  $K(T)$  and  $\chi_{||}(T)$  which can be extracted experimentally or within a multi-scale modeling approach via ASD simulations. In Figure 2.2(c) we represent a typical temperature scaling for a generic Co system ( $T_c = 1480$  K) with  $A(T) \propto m_e^2$  as obtained in the MFA [198] and  $K(T) \propto m_e^3$  —the so-called Callen-Callen scaling [206]—while  $\chi_{||}(T)$  is given in expression (2.19) and  $M_e(T)$  is obtained solving the self-consistent Curie-Weiss equation as explained in the text. While the majority of the assumptions discussed here are valid for the results presented in Chapter 3, this model will be adapted for a ferrimagnetic system in Chapter 5.

### 2.3.3 The two-temperature model

The two-temperature model (TTM) is a widely used approach in the description of ultrafast phenomena in solids [211–217]. This model characterises the temperature dynamics to equilibrium of electron and phonon subsystems under an external excitation in the picture of two coupled thermal reservoirs [46, 218, 219]. In this work we will often require the description of ultrafast heating effects on the magnetisation dynamics excited by fs-ps laser excitations. Here we discuss the assumptions of the TTM and explain the connection with the magnetisation dynamics implemented in the ASD or LLB models.

In metallic systems, a typical ultra-fast laser pulse excitation with photon en-

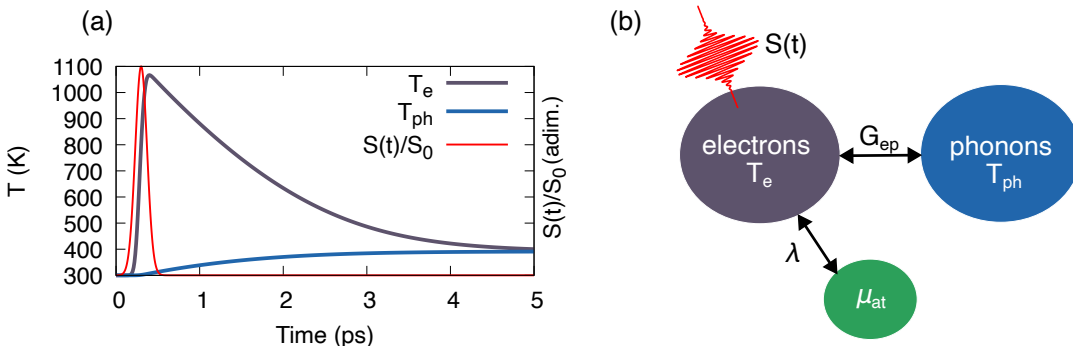


FIGURE 2.3: Understanding the TTM. (a) Heat dynamics example of the electron ( $T_e$ ) and phonon subsystems ( $T_{ph}$ ) in a metallic system excited by a fs laser pulse. The laser pulse power  $S(t)$  is normalised to the peak intensity  $S_0$ . (b) Schematics of the distinct coupled systems in the TTM. The laser pulse heats the electron reservoir and the excess energy is transferred to the lattice at a rate determined by  $G_{ep}$ . The atomic magnetic moments are directly coupled to the electron bath via the microscopic damping parameter  $\lambda$ . Hence,  $T_e$  determines the temperature of the magnetisation dynamics.

ergies in the visible spectrum leads to the formation of electron-hole pairs with a characteristic time of approximately 1 fs [169]. The highly non-equilibrium electron gas thermalises subsequently on a time-scale of tens to hundreds of fs reaching a thermodynamic quasi-equilibrium characterised by a temperature  $T_e$ . Due to its smaller heat capacity the electron subsystem experiences a large temperature increase whilst the temperature of the lattice subsystem  $T_{ph}$  remains very little affected as seen in Figure 2.3(a). On a longer ps time-scale, the electron-phonon coupling allows the transfer of excess thermal energy from the hot electron subsystem to the lattice. The main justification for the TTM resides in the faster characteristic timescales associated with the electron-electron and phonon-phonon interactions respectively, in comparison to the slower, electron-phonon processes [211]. Historically, the electron-phonon relaxation problem in metals was analytically addressed for an arbitrary  $T$  value in Ref. [218], although a solution in a high-temperature limit was encountered earlier [220]. The theory was later extended to ultrafast laser excitation scenarios, establishing TTM as a core model for studying electron relaxation dynamics in metals [46].

In a general form, the TTM equations employed in this work read:

$$C_e \frac{dT_e}{dt} = -G_{ep}(T_e - T_{ph}) + S(t, x), \quad (2.24)$$

$$C_{ph} \frac{dT_{ph}}{dt} = G_{ep}(T_e - T_{ph}), \quad (2.25)$$

where  $C_e$  and  $C_{ph}$  are the electron and phonon volumetric heat capacities and  $G_{ep}$  is a measure of the coupling between the two baths—see schematics in Figure 2.3(b). Working within the free electron approximation, the specific heat  $C_e$  is taken as  $C_e = \gamma_e T_e$ , where  $\gamma_e$  is a material dependent proportionality factor. Assuming  $T_{ph}$  to be larger than the Debye temperature,  $C_{ph}$  will be considered constant. A laser power term  $S(x, t)$  is assumed to transfer energy directly into the electron subsystem. The (Gaussian) spatial or temporal laser power profile will be adapted and detailed in reference to the problem at hand in Chapters 3, 4 and 5. In many works the spin system is included as the third temperature reservoir characterized by the spin temperature [8, 199, 221–224]. Here and in accordance with previous works [13, 15, 27, 198, 199, 225], we consider the spin system fluctuations explicitly by coupling directly the local atomic magnetic moments to the electron bath through the microscopic damping parameter  $\lambda$ , both in the ASD and the LLB model. In the ASD simulations presented in Chapter 4 we will discuss the non-thermal IFE which can drive AFM DW dynamics in Mn<sub>2</sub>Au via the so-called LOT assuming the  $T \rightarrow 0$  limit. Since heating effects cannot be completely disregarded, we will separately analyse the expected heat dynamics as a function of pulse duration or cooling in an isolated TTM. In Chapters 3 and 5 however, the magnetisation dynamics described by the LLB model are directly coupled to the TTM equations, wherein  $T_e$  sets the temperature-scaling of the micromagnetic parameters  $M_e(T)$ ,  $A(T)$ ,  $K(T)$  and  $\chi_{||}(T)$  [198].

## 2.4 Summary

In this chapter we gave a brief overview of several important concepts, relevant towards the understanding of the results presented onwards. First of all, in section 2.1 we discussed the microscopic interactions at play which are responsible for the macroscopic magnetic ordering of a solid-state system. Secondly, in 2.2 we introduced the magnetic DW notion along with the characteristic length and associated energy in a simple picture. In addition, we presented the typical 180° and 90° DW geometries encountered in the following chapters. Finally, in section 2.3 we analysed the numerical models we employ in the study of thermal/non-thermal optomagnetic phenomena and their effect on magnetic DWs: atomistic spin dynamics and the high-temperature micromagnetic framework of the Landau-Lifshitz-Bloch equation. To account for the ultra-fast heating dynamics of the studied metallic systems we reviewed the basic concepts of the two-temperature model.



## Chapter 3

# Domain wall dynamics via a laser-induced transient magnetisation

One of the fundamental effects of the laser-matter interaction is the appearance of an induced *transient magnetisation*. While the underlying phenomena differ in their microscopic origin and cover a diverse array of materials, here we address a fundamental question about the possibility to drive domain-wall (DW) dynamics on the femtosecond timescale of the exchange interactions solely by longitudinal changes of the magnetic moments.

We verify the viability of this hypothesis in the case of a generic ferromagnetic system described in the framework of the high-temperature micromagnetic model based on the Landau-Lifshitz-Bloch (LLB) equation. The effect is investigated in a 1D system at constant temperature as well as in a full micromagnetic model considering realistic laser-induced heating. Our results demonstrate that DW deformation in a femtosecond timeframe leads to the displacement of the wall on a larger timescale up to nanoseconds accompanied by a release of excess energy in the form of spin waves (SWs). The DW deformation leads to the appearance of a magnetisation gradient across the wall which promotes the motion towards the region consisting of spins with decreased magnetisation length. The total displacement is enhanced at larger temperatures and smaller damping due to an increase of the longitudinal relaxation time which ensures the longer presence of the induced magnetisation gradient. We also report a small enhancement of the DW displacement with the addition of an interfacial DMI energy contribution. A parallel is drawn between the numerical results and the IFE, well studied and parametrised at the ab-initio level in the ultrafast magnetism community. Our results are important towards the understanding of laser-induced, highly non equilibrium, magnetisation dynamics on the sub-picosecond timescale.

### 3.1 Introduction

The *transient magnetisation* terminology has been previously used in the literature to define the after-effect of a given laser-matter interaction, which can include the individual or combined effect of thermal or non-thermal phenomena. This umbrella term is generally expressed mathematically as a time-dependent, vector quantity  $\delta\vec{m}(t)$  which is used to describe laser-induced changes of the (reduced) magnetisation vector  $\vec{m}$  that may or may not outlive the timescale of the excitation. In the work of John *et al.* [15], the origin of the transient  $\delta\vec{m}(t)$  magnetisation is assumed to be the non-thermal mechanism of the inverse Faraday effect (IFE), a phenomenon widely

investigated in many classes of materials as for example metals [159–161, 226–228], plasmonic systems [229, 230] as well as non-traditional materials such as molecular magnets [231] and magnetic ionic liquids [232]. In the recent *ab-initio* study of Ref. [233], it was shown that the absorption of circularly polarised light can further induce a cumulative, helicity-dependent, magnetisation component in FMs. Unlike the IFE, the latter mechanism is of dissipative nature and scales linearly both with the laser pulse intensity and with time, being also argued it becomes dominant in the little explored ultra violet regime [234]. In a different fashion, THz driven phonon excitation has been shown capable of inducing an ultra-fast, first-order phase transition in the magnetic insulator DyFeO<sub>3</sub> [49]. Additionally, the use of a sub-ps, mid-infrared electric field pulse in resonance with an optical phonon mode leads to the appearance of a macroscopic transient magnetisation in the system which accompanies the internal coherent spin reorientation from an antiferromagnetic to an weakly ferromagnetic state. Similarly, THz excitation of optical phonons in the antiferromagnetic difluoride CoF<sub>2</sub>, followed by subsequent lattice dynamics in conjunction with transverse or longitudinal piezomagnetism gives rise to a transient net magnetisation [48, 50]. Ultimately, the study of magneto-optical phenomena might benefit from the advancements in the quantum optics field as the ultra-strong, light-matter coupling regime is being explored [235]. For example, the adjacent topic of cavity magnonics offers the promise of enhanced magneto-optical fields with tailored chirality at desired wavelengths [236–238], which might augment the degree of control as well as the amplitude of an optically induced transient magnetisation component.

It is well-known that both longitudinal and transverse relaxation mechanisms influence ultrafast and fast magnetisation dynamics, see for example Refs. [198, 209, 239–244]. Here we focus on an excitation protocol at the ultra-fast time scale based solely on a non-thermal longitudinal modification of magnetisation which will spark first longitudinal and then transverse dynamics up to the ps-ns timescale. Typical numerical models of laser-induced magnetisation dynamics describe non-thermal phenomena more often via transverse and precession dynamics or relaxation mechanisms [17, 18, 23, 245, 246], with any optically induced longitudinal magnetisation changes being usually neglected due to their smaller amplitudes or much faster equilibration times. Modifications of the magnetisation vector length are ultimately introduced as a result of the thermal effect of the laser pulse excitation in stochastic atomistic modelling [27, 62, 247], employing the LLB equation [15, 24, 181] or using variations of the Landau-Lifshitz-Bar'yakhtar model [200, 240–244]. Furthermore, the IFE is often taken into account as a local field of very large amplitude of the order of 10 T and even above [62, 179–182]. In previous micromagnetic works concerning the investigation of laser-induced DW dynamics, the light-matter interaction primarily leads to the appearance of temperature gradients or SW excitations which ultimately drive DWs via entropic and magnonic torques [35–37]. Generally in such situations, thermally induced transverse and precessional relaxation processes dominate the dynamics on the ps-ns timescale, where spatial non-uniformities in the anisotropy or exchange stiffness parameters become relevant.

Concerning *ab-initio* models, it has been argued that the IFE produces both magnetisation torque [161] as well as the modification of spin and orbital magnetic moment [159, 160]. In an attempt to reflect the results of the *ab-initio* theory, in relation to electrically induced Rashba Edelstein effect in Mn<sub>2</sub>Au, recent atomistic spin-resolved models include explicitly the presence of the orbital magnetic moment, and its interaction with the spin moment [248].

In this chapter, we investigate the possibility to convert a transient, non-thermal,

magnetisation contribution into a transverse DW motion in a ferromagnetic system. As pointed out by Zhang *et al.* [54], a femtosecond laser pulse excitation can help reduce the energy cost of current induced DW dynamics in perpendicularly magnetised wires. In their work, it is shown that the presence of a helicity-dependent, optical effect can reduce by 50% the threshold density current of a spin-orbit torque driving mechanism in ultra thin Co/Ni/Co films, motivating from a technological point of view the potential importance of our study.

The influence of pure, non-thermal excitation of ultra-fast magnetisation dynamics via longitudinal magnetisation changes remains little or completely unexplored. Owing to the diversity of light-induced phenomena which can lead to the appearance of a transient magnetisation contribution, we approach the problem of DW dynamics without reference to a particular effect. The key idea of our study relies on the assumption that a non-thermal  $\delta\vec{m}(t)$  contribution manifests as a longitudinal distortion in the magnetic texture. The fundamental question which we try to answer here is the following: *could pure longitudinal relaxation processes pass angular momentum to the transverse dynamics and lead to translational DW motion?* In order to model this mechanism we make use of the micromagnetic LLB equation which naturally allows for the description of longitudinal relaxation processes.

In the immediate section following this introductory part, we briefly comment on the numerical model of our ferromagnetic sample, the material parameters used throughout the chapter and their temperature scaling. The subsequent *Results* section is divided in two parts. Firstly, in 3.3.1 we approach the problem of DW dynamics in a 1D model. It is assumed the induced transient magnetisation acts instantaneously on the magnetic texture, all while disregarding any heating effects which might arise during a laser pulse excitation. The aim of this model is to present in a clear picture the mechanism of converting a longitudinal deformation of the magnetic texture into a DW motion based on the appearance of a non-thermal magnetisation gradient. A more realistic full micromagnetic analysis of DW dynamics is employed in 3.3.2. Based on the conclusions obtained in the chain model, the stripe DW dynamics are investigated for an optimal laser fluence and transient magnetisation amplitude in order to maximise the final DW displacement. Two distinct longitudinal deformation methods are formulated in the LLB equation based on the assumption that the opto-magnetic effect under study is either cumulative as a function of time and can outlive the laser pulse excitation or immediately vanishes in the absence of the latter. The two distinct methods are qualitatively compared and their physics analysed with respect to the chain model. A quantitative analysis of final DW displacement as a function of laser pulse duration supplements the discussion. The final section is reserved for conclusions, perspectives of the developed model and a discussion within the context of available ab-initio results in the literature.

## 3.2 Numerical model and material parameters of a generic ferromagnet

We consider a micromagnetic model describing a ferromagnetic sample discretised in a lattice of  $N$  identical cubic elements (finite-differences) with lateral spacing  $\Delta$ . To each cubic cell  $i = 1, N$  we assign an individual macrospin vector  $\vec{m}_i$  whose dynamics are governed by the classical LLB equation [197, 198, 208, 209] given in (2.16). The total effective field  $\vec{H}_{\text{eff}}^i$  acting locally on  $\vec{m}_i$  is defined in this chapter according to Eqs. (2.18), (2.19), (2.20), (2.21), (2.22), (2.23). Importantly, this formalism is valid at high temperatures and does not conserve the magnetisation length, thus, allowing

the modelling of longitudinal dynamics. The magnetostatic contribution to the total effective field given in Eq. (2.18) is neglected in the case of the 1D model in Section 3.3.1 and later taken into account in the stripe model discussed in 3.3.2.

The material parameters characterising the sample correspond to a generic Co system with perpendicular anisotropy and can be consulted in Table 3.1. Their temperature scaling is obtained making use of the equilibrium magnetisation  $m_e$  discussed in the previous chapter in the context of the MFA (see section 2.3.2). Thus, the uni-axial anisotropy constant is assumed to follow the Callen-Callen scaling law  $K(T) \propto m_e^3$  [206], while for the exchange stiffness parameter we initially consider the MFA result  $A(T) \propto m_e^2$  [198]. The latter will be revised in the case of the more realistic micromagnetic model used to describe DW dynamics in a stripe geometry. If otherwise not specified, the microscopic damping parameter is set to  $\lambda = 0.1$ , according to the order of magnitude given in Ref. [249], which gives good agreement between the LLB model and experimental results of laser-induced demagnetisation [250] and precession relaxation rates in Co [251, 252].

Parameter	Value
$M_s(0)$	1400 kA/m [253]
$A(0)$	10 pJ/m
$K(0)$	0.45 MJ/m <sup>3</sup> [253]
$T_c$	1480 K [204]

TABLE 3.1: Generic Co material parameters. The exchange stiffness parameter has been chosen smaller than the typical values found in literature [204, 253] in order to decrease the 0 K DW width.

### 3.3 Results

In this section we apply the micromagnetic model described previously to the problem of DW dynamics in a FM, assuming the presence of a transient, non-thermal magnetisation contribution  $\delta\vec{m}(t)$  which longitudinally deforms the magnetic texture. Throughout this study, the  $\delta\vec{m}(t)$  term will only be assumed to act along the Oz direction (parallel to the laser propagation direction). The transient magnetisation in the 1D model discussed in 3.3.1 is considered instantaneous, i.e. assumed faster than the magnetisation relaxation time. Later in the case of the thin film geometry presented in 3.3.2,  $\delta\vec{m}(t)$  follows the time-variation of the laser excitation. For these reasons, in the following pages we will be using either the  $\delta m_z$  or  $\delta m_z(t)$  notations when referring to the induced magnetisation component.

#### 3.3.1 Domain-wall dynamics in a 1D model following an instant magnetisation change of non-thermal origin

Let us consider first a macrospin chain of 500 nm in length which contains at a constant temperature close to the Curie point  $T = 0.91T_c$  an 180° Néel wall in the  $Oxz$  plane as seen in Figure 3.1(a). To verify that we obtain a correct static Néel DW configuration within our model, we compare the numerically extracted wall width against the temperature-dependent expression given by [254]:

$$\delta(T) = \sqrt{\frac{2\chi_\perp(T)A(T)}{M_s(0)m_e^2}} = \sqrt{\frac{A(T)}{K(T)m_e}}, \quad (3.1)$$

Numerically we obtain the DW width fitting the  $m_z$  magnetisation profile along the

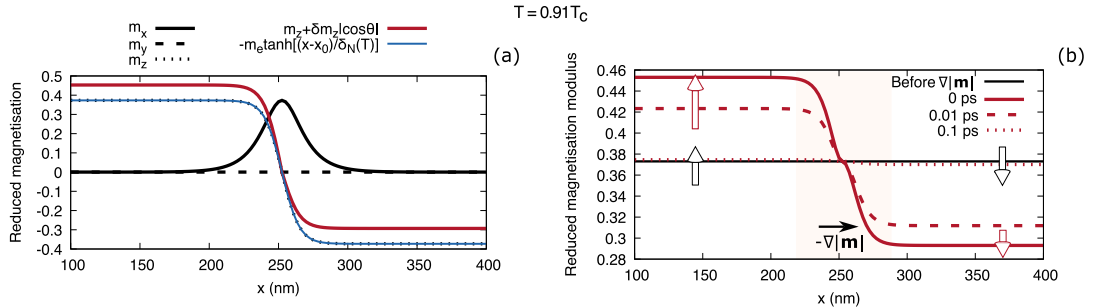


FIGURE 3.1: (a) The DW profile in a 500 nm chain at  $T = 0.91T_c$ . By fitting the  $m_z$  magnetisation profile we extract a wall width of  $\delta_N(T) = 12.62$  nm which compares well with the analytical value  $\delta(T) = 12.64$  nm given by Eq. (3.1). (b) The effect of the longitudinal magnetisation change introduced via Eq. (3.3) on the modulus of each macro-spin vector in the chain. The black straight line denotes the situation before the deformation is introduced, wherein all spins are characterised by the same modulus  $|\vec{m}|$ . Depending on their orientation with respect to the  $Oz$  axis, the spins will either elongate or contract their length—graphically exemplified for two edge spins—leading to a magnetisation gradient  $\nabla|\vec{m}|$  across the DW as it can be seen in the highlighted region, obtaining the initial configuration at  $t = 0$  ps. Subsequently,  $\nabla|\vec{m}|$  will rapidly vanish on a fs time-scale as suggested by the snapshots at  $t = 0.01$  ps and  $t = 0.1$  ps.

chain using the following equation:

$$m_z = -m_e \tanh[(x - x_0)/\delta_N(T)], \quad (3.2)$$

where  $x$  denotes the individual position of the spins and  $x_0$  is the center of the wall. In our case,  $\delta_N(T)$  evaluates to 12.62 nm at  $T = 0.91T_c$ , in good agreement with the analytically obtained value of  $\delta(T) = 12.64$  nm.

Starting from the equilibrium DW configuration displayed in Figure 3.1(a), we introduce a magnetisation contribution which alters the macrospins' vector component along the easy-axis (EA) direction in the following manner:

$$m_z^{*i} = m_z^i + \delta m_z |\cos \theta|, \quad (3.3)$$

where  $m_z^i$  and  $m_z^{*i}$  are the  $Oz$  magnetisation components of each macro-spin before and after the system is deformed. Following,  $\delta m_z$  is the amplitude of the longitudinal magnetisation change, modulated by the angle  $\theta$  in turn defined by the relative orientation of the macro-spin vector with respect to the EA. Equation (3.3) reflects the fact that our assumed non-thermal phenomenon as in the case of the IFE, depends on the angle between the laser polarisation and the magnetisation direction [161]. Thus, we consider there is no modification of the  $m_z$  component, i.e.  $\delta m_z |\cos \theta| = 0$ , when the laser polarisation vector  $\vec{k} \parallel Oz$  is perpendicular to the local magnetisation direction. In Appendix A.1 we discuss in more detail the length modification of the macrospin vectors in the presence or absence of the  $|\cos \theta|$  term.

The LLB model allows one to go beyond the rigid macrospin approximation of standard micromagnetism ( $|\vec{m}| = 1$ ). The longitudinal magnetisation change introduced in Eq. (3.3) will distinctly modify the length of each spin vector, which in thermodynamic equilibrium conditions should be uniform across the chain and readily available solving the self-consistent Curie-Weiss equation as discussed previously in Section 2.3.2. In Figure 3.1(b) we represent the change in the local magnetisation modulus  $|\vec{m}|$  across our spin chain due to the magnetisation contribution

introduced along Oz. As it can be seen in the initial configuration displayed at  $t = 0$  ps, depending on their relative orientation with respect to the Oz axis, the spin vectors will either elongate or contract their magnetisation length leading to a  $\nabla|\vec{m}|$  gradient across the DW.

Note that a similar magnetisation gradient might occur during an ultrafast laser pulse excitation of a magnetic system leading to a non-uniform temperature profile in the sample. This can arise either due to the spatial profile of the laser pulse itself or due to a differential absorption of circularly polarized light for the spin-up and spin-down expectation values on account of the magnetic circular dichroism (MCD) effect [55, 61, 62]. Ultimately, all these effects translate into the appearance of the *hot/cold* regions, where locally the magnetic parameters  $M_s(T)$ ,  $K(T)$ ,  $A(T)$ ,  $\alpha(T)$  are uneven through their temperature dependence.

A pure optical route to induce a magnetisation gradient might be based on the IFE [159–161]. In this case, the temperature across the sample may remain uniform during excitation as presented in our model. However, since the strength of the magneto-optical response in the presence of the IFE depends on the relative orientation between the light propagation axis and the local magnetic vector, magnetisation gradients are expected to arise in non-coherent spin systems as for example in a DW configuration. Thus, although we study this effect at constant temperature, we shall use in the next paragraphs the *hot/cold* terminology to describe the regions of *small/large* magnetisation. Moreover, in similar fashion to the spin-Seebeck driven motion [35], we report the displacement of our Néel DW towards the *hot* region of the system, that is the region where the macro-spin vectors have reduced their magnetisation length. In Figure 3.2(a), we track the DW motion in time for three different magnetisation deformation strengths. The position of the wall is calculated by identifying its center of mass from the  $m_x$  magnetisation profile [255]:

$$X_{\text{DW}} = \frac{\sum_i m_x^i x^i}{\sum_i m_x^i}, \quad (3.4)$$

where  $x^i$  represents the position along the chain of macrospin  $i$ .

In all situations investigated, the dynamic response can be separated in three distinct regions:

(I) Firstly, a rapid displacement is obtained on the fs timescale. Governed by longitudinal relaxation effects, the induced change in magnetisation is converted into a transverse motion of the DW in the direction of a smaller magnetisation length. During this process, the longitudinal field will revert the spin vectors' length back to the initial value before the transient magnetisation is introduced, thus neutralising the observed  $\nabla|\vec{m}|$  gradient. In Figure 3.1(b) one can see how does  $|\vec{m}|$  vary across the chain at different moments in time for the smallest deformation considered. Interestingly, already at the 0.1 ps mark the magnetisation gradient nearly vanishes and the spin vectors regain their original lengths.

(II) No more longitudinal relaxation processes take place in the absence of  $\nabla|\vec{m}|$ . Furthermore, since the dynamics timescale is yet too short for any relevant transverse or precessional torques to act, the DW practically preserves its acquired position for several ps.

(III) Beyond 10 ps the remaining excess energy induced by the presence of the transient magnetisation is invested in much slower transverse and precessional relaxation processes which promote an oscillating behaviour of the DW on the ns timescale until its final equilibrium position is reached.

As we mention above, the direction of motion is towards the so-called *hot* region,

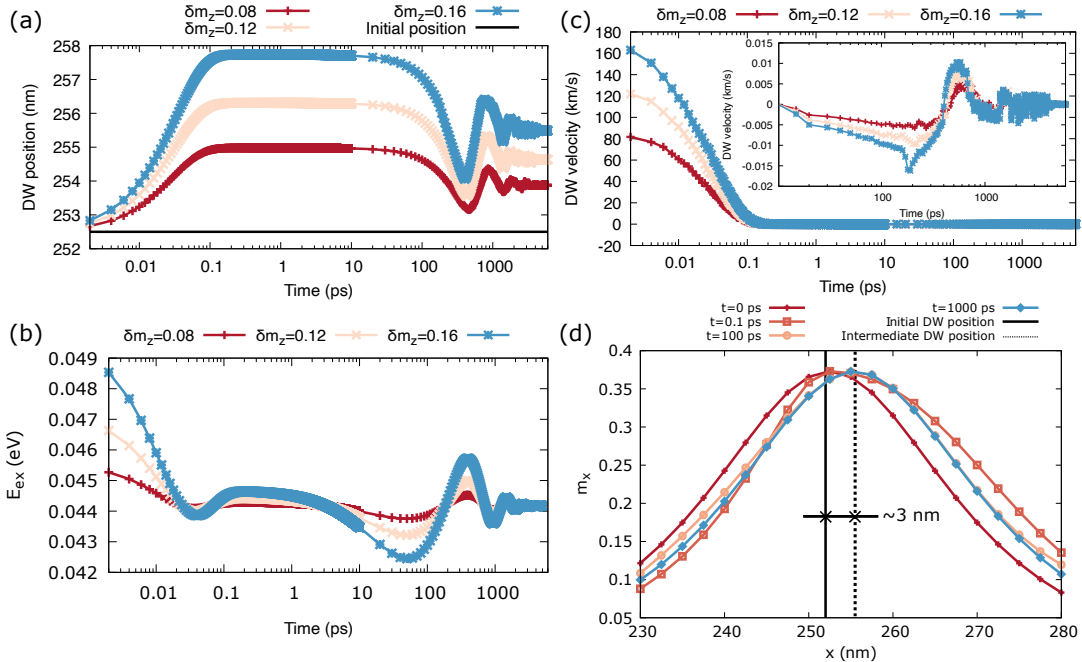


FIGURE 3.2: 1D DW motion due to the instant longitudinal deformation of the wall profile. (a) DW displacement in time for different non-thermal, transient magnetisation contributions along  $Oz$ . The black solid line indicates the initial position of the wall. The DW position ( $X_{\text{DW}}$ ) is tracked based on the relationship given in Eq. (3.4). (b) The time variation of the micromagnetic exchange energy stored in the chain for all three different scenarios. (c) Instantaneous DW velocity extracted as the time derivative of the data presented in subfigure (a). The inset is adjusted to fit the points beyond the 10 ps time mark. (d) Time dependence of the Néel wall magnetisation profile along  $Ox$  during the dynamics induced by a transient magnetisation of amplitude  $\delta m_z = 0.16$ . The solid vertical line defines the initial DW position while the dotted line marks an intermediate state at which the wall finds itself approximately 3 nm away from the starting point according to Eq. (3.4). The horizontal axes in subplots (a) (b) and (c) are logarithmic.

as it also takes place in the DW motion driven by temperature gradients. Previously, Schlickeiser *et al.* [36] have explained the motion of DWs in the presence of temperature gradients based on the existence of the so-called entropic torque which induces dynamics in a direction given by the  $-\nabla A(T)$  gradient. Interestingly, in their analytical treatment of the DW dynamics developed in the framework of the LLB equation, they include also a driving mechanism due to the magnetisation gradient  $-\nabla|\vec{m}|$  term —see Eqs. 8 and 9 found in the Supplementary Material of Ref. [36]—but conclude its effect is small in comparison to the former  $-\nabla A$  contribution. In their situation, the dynamics were investigated on a longer time-scale where any longitudinal relaxation processes had already taken place.

In order to understand the driving mechanism, we evaluate the time evolution of the exchange energy, using its discretised form:

$$E_{\text{ex}} = A(T)V \sum_i \sum_j \left( \frac{\vec{n}_j - \vec{n}_i}{\Delta^2} \right)^2, \quad (3.5)$$

where the counters  $i, j$  loop over all the macro-spins in the system and their individual neighbours respectively and  $V = \Delta^3$  is the volume of the cubic macro-cell. In standard micromagnetics the macrospin's vector length is always conserved ( $|\vec{m}| = 1$ ). To recover a similar definition, we normalise the  $\vec{m}$  vector to the equilibrium

magnetisation value  $m_e$  and define  $E_{\text{ex}}$  making use of the variable  $\vec{n} = \vec{m}/m_e = \vec{M}(t)/M_s(T)$ , where  $|\vec{n}| \neq 1$ . In Figure 3.2(b) we represent the time variation of the micromagnetic exchange energy  $E_{\text{ex}}$  stored in the chain in all three situations. Comparing the initial and final states, one can appreciate qualitatively the amount of exchange energy introduced in the system due to the elongation/contraction of the spins. Thus, the DW distortion produces a large torque on neighboring spins through their elongation/contraction. Beyond the 10 ps time threshold, the oscillating behaviour described earlier is also clearly observed in the exchange energy. In this timescale, however,  $|\vec{n}| = 1$ .

A further mention here refers to the timescale and huge instantaneous velocity acquired by the DW during its initial displacement seen in Figure 3.2(c). Indeed, at this timescale the change of  $\vec{m}(t)$  is governed by the longitudinal field  $\vec{H}_{\text{lon}}$ —consequence of the relaxation process determined by the internal Heisenberg interactions within an ensemble of atomic spins. On average the disorder present at the atomic level will be translated at the macroscopic scale as a change in the instantaneous magnetisation  $\vec{m}(t)$ , a representation of the competition between internal exchange fields and thermal fluctuations. The Heisenberg exchange coupling is the strongest interaction in a ferromagnet such as Co, opening the possibility for ultra-fast dynamics on the fs timescale. For our chosen system this internal exchange field  $J_0/\mu_{\text{at}}$  evaluates to approximately  $1.68 \times 10^4$  T. As evidenced in subplot (b) of Figure 3.1, the induced magnetisation gradient vanishes around the 0.1 ps time threshold. Up to this point dominant longitudinal relaxation processes will take place under large  $\vec{H}_{\text{lon}}$  fields giving rise to the enormous instantaneous velocities seen in Figure 3.2(c). These large velocity values arise due to the ultra-fast timescale imposed by the longitudinal field. Any displacement of just a few nm on the fs timescale will lead to transient DW velocities in the km/s domain. The analysis of the magnetisation profile ( $m_x$  component) in Figure 3.2(d) shows that the displacement of the DW center of mass results from the accommodation of the DW profile to the equilibrium one on the timescale of longitudinal relaxation. The snapshot at  $t = 0.1$  ps presents the largest shape deviation from the initial configuration corresponding to the maximum DW displacement of approximately 5 nm recorded in Figure 3.2(a).

As discussed earlier, the excess energy introduced in the system will be invested on the ps-ns timescale in transverse and precession-like torques which will lead finally to smaller velocities since the dynamics are governed then by the much smaller anisotropy  $\vec{H}_{\text{ani}}$  and the micromagnetic exchange  $\vec{H}_{\text{ex}}$  fields with  $|\vec{n}| = 1$ . A detailed comparison between the contributions of  $\vec{H}_{\text{ani}}$ ,  $\vec{H}_{\text{ex}}$  and  $\vec{H}_{\text{lon}}$  at different timescales can be seen in Appendix A.2. An oscillating behaviour of the DW position is observed in the subsequent time snapshots taken at  $t = 100$  ps and  $t = 1000$  ps. At this latter time threshold, a clear shift in the  $m_x$  curve peak—seen in Figure 3.2(d)—with respect to the initial state can be easily identified as direct evidence of the wall motion we have claimed. The DW will display onwards a back and forth motion until final equilibration is reached. The oscillations mentioned so far become more obvious turning our attention to the time-dependent  $m_y$  and  $m_z$  magnetisation profiles discussed in Figure 3.3, under the influence of a transient magnetisation of amplitude  $\delta m_z = 0.16$ . Although the initial DW structure is characterised by  $m_y = 0$  along its length as seen in subplot (a) of Figure 3.3, the macro-spins will deviate away from the  $Oxz$  plane due to the instability introduced in the system by the transient magnetisation. Thus, a non-zero  $m_y$  component will appear along the chain displaying an oscillatory behaviour which will continuously decrease in amplitude as a function of time. Though not directly shown, a similar behaviour is seen also in the  $m_x$

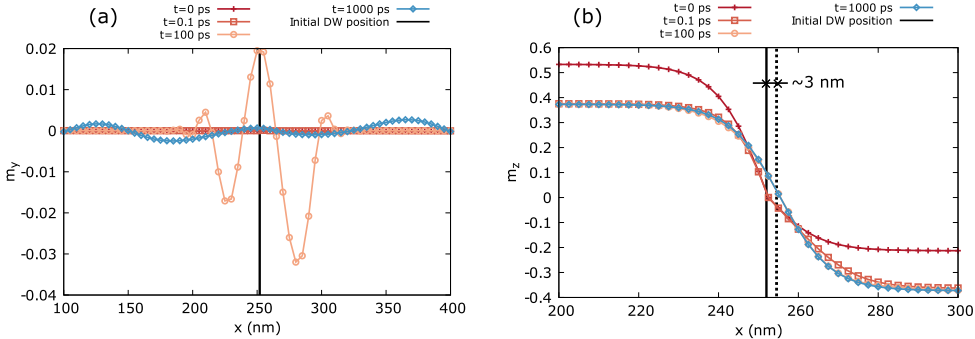


FIGURE 3.3: Time variation of the Néel wall magnetisation profile along  $Oy$  and  $Oz$  during the dynamics induced by a transient magnetisation of amplitude  $\delta m_z = 0.16$ . The range of the horizontal axes as well as the frequency of the point representation is adapted for each subplot for better visualisation. The continuous vertical line in subplots (a), (b) defines the initial DW position while the dotted vertical line in (b) marks an intermediate state ( $t = 1000$  ps) at which the wall finds itself approximately 3 nm away from its starting point according to Eq. (3.4).

and  $m_z$  magnetisation profiles. The oscillations along  $Ox$  will directly influence the DW position, giving rise to the sinusoidal behaviour seen in Figure 3.2(a) beyond the 100 ps time threshold. While slightly more difficult to identify visually, evidence of DW motion due to the induced transient magnetisation can also be extracted from the  $m_z$  magnetisation profile in subplot (b) of Figure 3.3. The symmetry point splitting the characteristic hyperbolic tangent profile in half clearly displaces in time as indicated by the vertical lines marking the initial state and the configuration we obtain at  $t = 1000$  ps. One should note that the range of the horizontal axes in the subplots of Figure 3.3 as well as the frequency of the point representation have been individually adapted for better visualisation.

To inquire the possibility for augmented DW dynamics, we investigate the displacement of the Néel wall as a function the applied temperature  $T$  and the amplitude  $\delta m_z$  of the induced transient magnetisation for two different values of the microscopic damping  $\lambda$ . For any given set of parameters, we run the LLB dynamics for several ns extracting the final DW displacement after complete equilibration is reached. The result of this parameter sweep can be seen in Figure 3.4. For any transient magnetisation amplitude  $\delta m_z$  and irrespective of  $\lambda$ , the final displacement will be increased as we get closer to the Curie point. In the Appendix section A.3 we present this displacement with respect to the  $\delta m_z / m_e(T)$  ratio, showing the parabolic-like dependence for all temperatures. Interestingly, a smaller microscopic damping of  $\lambda = 0.01$  affects the end result to a very small extent, leading to a slightly larger final displacement at  $T = 0.98T_c$  and  $\delta m_z = 0.16$ . The enhancement in displacement achieved when the temperature is increased can be explained referring ourselves solely to the longitudinal relaxation processes. The LLB equation allows to define a longitudinal relaxation time as [198, 256]:

$$\tau_{||} = \frac{\chi_{||}}{\gamma\alpha_{||}} = \frac{3\chi_{||}}{2\gamma} \frac{T_c}{\lambda T}. \quad (3.6)$$

A general effect characteristic of second order phase transitions [197, 257], the longitudinal relaxation time experiences a critical slowing down approaching the Curie

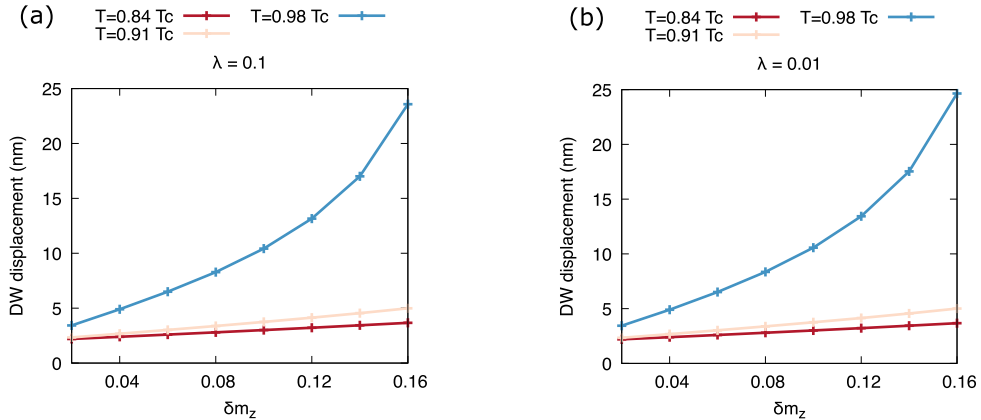


FIGURE 3.4: Final DW displacement with respect to the temperature  $T$  and the amplitude  $\delta m_z$  of the induced magnetisation. The data is presented for two distinct microscopic damping parameter values: (a)  $\lambda = 0.1$  and (b)  $\lambda = 0.01$ .

temperature  $T_c$ . The main factor responsible for the overall increase of the  $\tau_{||}$  relaxation time is the divergence of the parallel susceptibility  $\chi_{||}$  near the phase transition point, which dominates the  $1/\lambda T$  dependence resulting from the longitudinal damping parameter  $\alpha_{||}$ . In our case we can turn the "slow" longitudinal dynamics at elevated temperatures to our advantage: the key driving mechanism in this study is the magnetisation gradient  $\nabla|\vec{m}|$  we induce across the DW through a longitudinal deformation of the system. As seen in Figure 3.1(b) and 3.2(a), as long as  $\nabla|\vec{m}|$  is preserved, the wall will continue in its displacement until temporarily reaching a halt when  $\nabla|\vec{m}| = 0$ . Thus, increasing the life-time of  $\nabla|\vec{m}|$  will lead to larger DW displacements overall. The behavior of  $\tau_{||}$  also explains a slight increase of the DW displacement for a smaller damping value.

To summarise, in this subsection we demonstrate the possibility to convert a non-thermal, transient magnetisation contribution followed by longitudinal relaxation processes into a subsequent transverse DW motion in a ferromagnetic system. The fundamental mechanism at the origin of the effect is the appearance of a magnetisation gradient  $\nabla|\vec{m}|$  along the DW which allows for a displacement towards the *hot* region, that is the area of small magnetisation. The total distance covered by the DW depends on the life-time of the induced gradient as well the amplitude of the magnetisation increment. Increasing the temperature of the bath  $T$ , one can delay the relaxation of the macro-spin vectors towards their equilibrium lengths allowing for a prolonged displacement of the wall.

### 3.3.2 Domain-wall displacement in a stripe system with heat and transient magnetisation

Moving away from the simple chain system discussed in the previous subsection, we further inquire the possibility for DW dynamics in a more complex situation by taking into account also the heating produced by the laser. We consider a stripe geometry, introducing also the magnetostatic contribution to the total effective field. Given the current perpendicular magnetic recording paradigm, an OOP anisotropy is preferred. For the material parameters presented in Table 3.1, the competition between the OOP anisotropy and the magnetostatic interactions produces a spin-reorientation transition below room temperature. To circumvent this, we augment the magnetocrystalline anisotropy of the system by increasing the  $K(0)$  constant to  $2.25 \text{ MJ/m}^3$ .

Parameter	Value
$\gamma_e$	$5.53 \times 10^3 \text{ Jm}^{-3}\text{K}^{-2}$
$C_{\text{ph}}$	$2.07 \times 10^6 \text{ Jm}^{-3}\text{K}^{-1}$
$G_{\text{ep}}$	$4.05 \times 10^{18} \text{ Js}^{-1}\text{m}^{-3}\text{K}^{-1}$
$\tau_{\text{th}}$	50 ps

TABLE 3.2: TTM parameters for a generic Co sample as extracted from [250, 258].

We consider a  $1500 \text{ nm} \times 50 \text{ nm} \times 1 \text{ nm}$  stripe system discretised in cubic cells of lateral size of  $\Delta = 1 \text{ nm}$ . While in the chain model the exchange length parameter  $l_{\text{ex}} = \sqrt{\frac{2A(T)}{\mu_0 M_s^2(T)}}$  was temperature independent due to the assumed MFA  $A(T) \sim m_e^2$  scaling law, here we use a more realistic scaling  $A(T) \sim m_e^{1.8}$  [204] which leads to an increasing  $l_{\text{ex}}$  as a function of temperature starting from the 0 K value of 2.85 nm, assuring ourselves the discretisation size  $\Delta$  is properly chosen. Although not directly shown here, at room temperature ( $T = 300 \text{ K}$ ), the DW configuration is of Bloch type. Starting from this initial state, we consider a spatially uniform ( $\nabla T = 0$ ) laser-pulse heating of the thin film sample on the fs time-scale. This rapid heating of the system is described by the following TTM equations:

$$C_e \frac{dT_e}{dt} = -G_{\text{ep}}(T_e - T_{\text{ph}}) + S(t) - C_e \frac{T_e - T_{\text{room}}}{\tau_{\text{th}}}, \quad (3.7)$$

$$C_{\text{ph}} \frac{dT_{\text{ph}}}{dt} = G_{\text{ep}}(T_e - T_{\text{ph}}). \quad (3.8)$$

In addition to the TTM equations discussed in section 2.3.3 of the previous chapter, here we introduce also a simple Newton cooling law to model the heat transfer with the external medium ( $T_{\text{room}}$ ) at a rate given by  $\tau_{\text{th}}$ . The time dependent laser pulse power is given by:

$$S(t) = \frac{A_{\text{ab}}F}{1.0645t_p 2\sqrt{\ln 2}\delta_{\text{opt}}} \exp \left[ -\left( \frac{t - t_0}{t_p} \right)^2 \right], \quad (3.9)$$

where  $A_{\text{ab}}$  is an absorption coefficient,  $F$  is the laser fluence at full width half maximum (FWHM),  $\delta_{\text{opt}}$  is the optical penetration depth,  $t_p$  is the pulse duration and  $t_0$  denotes the moment of time when the laser pulse power reaches its peak amplitude. The numerical constants arise due to the FWHM relationship between the laser fluence  $F$  and intensity  $I$ :  $F = (\tau/2)\sqrt{\pi/\ln 2}I \approx 1.0645\tau I$ , where  $\tau = 2t_p\sqrt{\ln 2}$ . Here,  $t_p$  is set at 200 fs. The TTM parameters we are employing are listed in Table 3.2. The  $\gamma_e$ ,  $C_{\text{ph}}$  and  $G_{\text{ep}}$  values correspond to a generic Co sample and have been extracted from [250, 258] while the  $\tau_{\text{th}}$  parameter has been set to a standard value of 50 ps. The absorption coefficient is set to 25% similar to the work reported in [15] and  $\delta_{\text{opt}}$  is considered equal to the thin film thickness of 1 nm.

In this full micromagnetic approach we introduce the magnetisation length modification due to the laser-matter interaction in two ways. First, to mimic the instantaneous modification of the previous section but giving it a finite duration (given by the laser pulse), in what we call below Method I, we augment the right-hand side

part of the LLB Eq. in (2.16) —denoted by  $f(\vec{m}_i, t)$ —with an additional term:

$$\begin{aligned}\frac{d\vec{m}_i}{dt} &= f(\vec{m}_i, t) + \delta m_z^I(t), \\ &= f(\vec{m}_i, t) + A \exp \left[ -\left( \frac{t - t_0}{t_p} \right)^2 \right] \hat{z},\end{aligned}\quad (3.10)$$

where the parameter  $A$  plays the role of a rate constant expressed in units of  $s^{-1}$  whilst carrying also the information regarding the total laser induced magnetisation. Integrating Eq.(3.10) with no LLB part —that is, without the term  $f(\vec{m}_i, t)$ —until infinite time, it allows us to relate the parameter  $A$  with the total magnetisation modification, assumed in the previous section:

$$A = \frac{\delta m_z^0 |\cos \theta_i|}{t_p \sqrt{\pi}} \quad (3.11)$$

Thus, in comparison to the instantaneous description in the chain model, Eq. (3.10) assumes that the transient magnetisation follows the same Gaussian time profile as the laser pulse power given in Eq. (3.9). The longitudinal mechanism introduced in Method I is intrinsically cumulative, that is for every time-step  $\Delta t$ , we add along the  $Oz$  magnetisation direction the quantity  $\delta m_z^I(t)\Delta t$  which similarly to a Zeeman-like interaction, modifies the total energy of the system with a certain quantity  $\Delta E$  that can persist even in the absence of the laser pulse excitation, its subsequent expenditure and recovery of the ground state energy being governed by the intrinsic relaxation mechanisms in the LLB equation. The total induced magnetisation in this case is given by the total area spanned in time by the Gaussian profile of  $\delta m_z^I(t)$ .

A transient, non-cumulative modification of the macrospin vectors' length labeled hereon as Method II assumes the following:

$$\begin{aligned}\frac{d\vec{m}_i}{dt} &= f(\vec{m}_i, t) + \delta m_z^{II}(t), \\ &= f(\vec{m}_i, t) - \frac{2\delta m_z^i(t - t_0)}{t_p^2} \exp \left[ -\left( \frac{t - t_0}{t_p} \right)^2 \right] \hat{z},\end{aligned}\quad (3.12)$$

where  $\delta m_z^{II}(t)$  is the time-derivative of  $\delta m_z^i \exp \left[ -\left( \frac{t - t_0}{t_p} \right)^2 \right] \hat{z}$ , underlying the immediate disappearance of the effect in the absence of the laser pulse excitation, in stark contrast with Method I. We define here the pre-factor  $\delta m_z^i$  in the same manner as before:  $\delta m_z^i = \delta m_z^0 |\cos \theta_i|$ .

In the following we provide examples of simulations of ultrafast magnetisation dynamics designed to inquire the qualitative differences of the two distinct longitudinal mechanisms in Eqs. (3.10) and (3.12). Given the results discussed in Fig. 3.4, it is expected the DW displacement is maximised for laser pulse heating near the Curie point and evidently for increasingly large values of the optically induced magnetisation. Therefore, we tailor the fluence of the laser excitation ( $F = 3 \text{ mJ/cm}^2$ ) such that for our chosen pulse duration of  $t_p = 200 \text{ fs}$ , the electron temperature increment is maximum without irreversibly modifying the shape of the DW due to the temperature induced loss of the OOP anisotropy. Moreover, we assume the presence of a sufficiently large transient magnetisation with amplitude of  $\delta m_z^0 = 20\% M_s(0 \text{ K})$

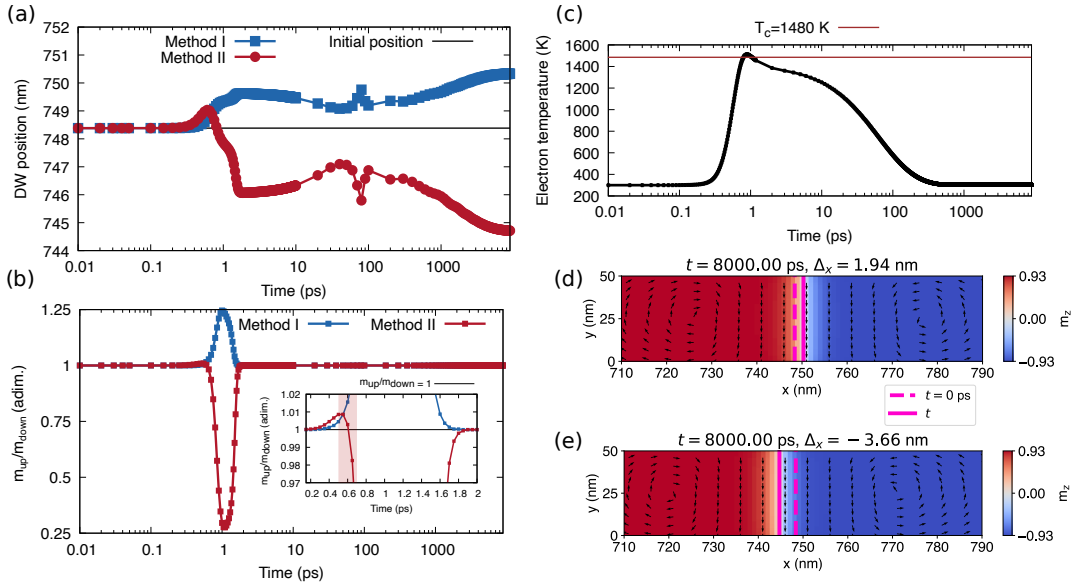


FIGURE 3.5: DW dynamics in a stripe geometry under the effect of a spatially uniform, ultra-fast laser pulse heating ( $F = 3 \text{ mJ/cm}^2$ ,  $t_p = 200 \text{ fs}$ ,  $t_0 = 3t_p = 600 \text{ fs}$ ) and a transient magnetisation component of amplitude  $\delta m_z^0 = 20\% M_s(0 \text{ K})$  induced along the  $Oz$  direction. (a) Comparative DW displacement as a function of time for Methods I and II obtained via the longitudinal deformations described in Eqs. (3.10) and (3.12). The DW position is extracted via the center of mass method presented in Eq. (3.4) along the bottom region of the track corresponding to the  $y = 0$  coordinate. (b) Time variation of the magnetisation modulus ratio  $\frac{m_{\text{up}}}{m_{\text{down}}}$  of reference up and down spins at the edges of track with the inset graphic capturing the short time scale behaviour between 0.1 and 2 ps. The red highlighted region presents the Method II behaviour crossing into a sub-unitary  $\frac{m_{\text{up}}}{m_{\text{down}}}$  regime. (c) Temporal evolution of the electron temperature shown to briefly cross the Curie point of the sample (the  $T_c$  threshold is denoted by the horizontal red line). Finally, subplots (d) and (e) present the final DW configuration and associated displacement ( $\Delta_x$ ) 8000 ps after the laser excitation for Method I and II respectively. While the color plot gives the  $Oz$  magnetisation component, the black vector plot displays the  $Oxy$  macrospin alignment. In (a), (b) and (c) the time axis is logarithmic.

in comparison to the zero-Kelvin saturation magnetisation of the sample. In Figure 3.5(a), we display the comparative DW displacement as a function of time obtained via Methods I and II. Irrespective of the method employed here we observe a dynamic profile which can be separated in distinct regimes similarly to the chain model. First of all, at the fs-ps time-scale we identify a rapid DW displacement of several nm governed by longitudinal relaxation processes followed by an apparent halt in the motion of the wall up to the 10 ps time mark. Subsequently, we notice once again the presence of oscillations in the DW position on the 100 ps time scale, evidence of angular momentum transfer from the longitudinal to the precessional and transverse reservoirs followed by complete expenditure of the excess energy and DW relaxation to a final position in a ns time-frame.

The most striking feature in between the two cases however is the opposite DW direction of motion. This comes as a consequence of the flipped magnetisation gradient sign obtained at the ultra-fast time scale due to the distinct longitudinal deformation encoded in the  $\delta m_z^I(t)$  and  $\delta m_z^{II}(t)$  functions respectively. To visualise their effect on the wall configuration, we graphically represent in Figure 3.5(b) the magnetisation modulus ratio of reference up and down spins near the edges of the track where the longitudinal elongation and contraction are maximal. In Method I, the  $\frac{m_{\text{up}}}{m_{\text{down}}}$  ratio is greater or equal to 1 leading to a transient increment/decrement of

Pulse duration $t_p$	Final DW displacement (I)	Final DW displacement (II)
200 fs	1.94 nm	-3.66 nm
1 ps	1.57 nm	-2.14 nm
10 ps	2.31 nm	-3.77 nm
100 ps	0.53 nm	-0.04 nm
1000 ps	0.39 nm	0 nm

TABLE 3.3: Final DW displacement in the stripe model with respect to increasing laser pulse duration for a maximum allowed laser fluence  $F = 3 \text{ mJ/cm}^2$  and a large transient magnetisation amplitude of  $\delta m_z^0 = 20\% M_s(0 \text{ K})$ . The second and third column correspond to the transient magnetisation models implemented via Methods I and II respectively —See Eqs. (3.10) and (3.12).

the up/down spins' magnetisation, in qualitative agreement with the picture presented in the chain model. On the other hand, this ratio is overall sub-unitary in the case of Method 2 leading to an opposite behaviour in which a positive induced  $\delta m_z^0$  magnetisation leads to the contraction/elongation of the up/down spins. The  $\delta m_z^{\text{II}}(t)$  longitudinal deformation is built inherently as the time derivative of the  $\delta m_z^{\text{I}}(t)$  function (but for a multiplying constant). Since the latter is characterised by a Gaussian profile in time, naturally the  $\delta m_z^{\text{II}}(t)$  expression will display evidence of a sign change associated with the slope of the Gaussian curve. As seen in the inset of subplot (b) of Figure 3.5, this leads to an initial yet brief increase of the up spins' magnetisation in Method II followed by a subsequent and enhanced contraction, with the down spins displaying the opposite behaviour. The asymmetric magnetisation increment/decrement with respect to time comes as a result of the complex heat dynamics which enhance the longitudinal effect the closer one gets to the Curie point. In subplot (c) of the same Figure 3.5 it is clear the electron temperature reaches its peak value several hundreds of fs later compared to the moment in time when the  $\frac{m_{\text{up}}}{m_{\text{down}}}$  ratio in Method II crosses to a sub-unitary regime at around the 0.6 ps time mark. Finally, in subplots (d) and (e) we display the equilibrium DW configuration and the associated displacement obtained 8000 ps after the laser pulse excitation for the two separate scenarios.

While our aim here is not a quantitative comparison between the two implementations, we appreciate in this particular instance a larger displacement is obtained in the case of Method II. Although the physics under study concern a generic and non-thermal opto-magnetic effect, the thermal quenching of the magnetisation up to the Curie point plays a crucial role in determining the strength and relevance of the transient longitudinal magnetisation similarly to the conclusion inferred by Figure 3.4 in the chain analysis. This is supported further by the results presented in Table 3.3 where we display the complex behaviour of the final DW displacement with increasing the  $t_p$  parameter. The laser pulse duration  $t_p$  directly influences the electron temperature dynamics and therefore the degree and duration of the magnetisation quenching. Incrementing  $t_p$  beyond the  $\geq 10 \text{ ps}$  time limit overall leads to a decrease of the final DW displacement due to the radical flattening of the peak electron temperature. In this time-scale thermal effects become less and less relevant and consequently the magnetisation quenching is not sufficient in order to bring the equilibrium magnetisation value  $m_e(T)$  in the limit defined by the optically induced component of amplitude  $\delta m_z^0$  which ultimately defines the final DW displacement according to the chain model. For shorter laser pulse excitations, the behaviour is

Pulse duration $t_p$	Final DW displacement (I)	Final DW displacement (II)
200 fs	2.30 nm	-4.15 nm
1 ps	1.86 nm	-2.35 nm
10 ps	2.59 nm	-4.08 nm
100 ps	0.61 nm	-0.04 nm
1000 ps	0.48 nm	0 nm

TABLE 3.4: Revisiting the data in Table 3.3 considering the presence of an interfacial DMI contribution  $D(0) = 2 \text{ mJ/m}^2$ .

more complex and difficult to predict due to the distinct phenomena at play, the transient magnetisation and the heat dynamics interfering both with the longitudinal as well as the transverse magnetisation relaxation processes. A possible explanation for the increment in the final DW displacement observed going from  $t_p = 1 \text{ ps}$  to  $t_p = 10 \text{ ps}$  may rely in the transition between heat-dominated and non-thermal longitudinal effects although their explicit separation is impossible in this model.

From a fundamental point of view, it is interesting to inquire whether the presence of an interfacial DMI contribution in the total effective field acting upon the macrospin vectors can aid increment the observed DW displacement. While this antisymmetric exchange contribution has been shown detrimental to the field driven DW dynamics of in-plane magnetised ferromagnet/heavy-metal nano-wires [259], in perpendicularly magnetised systems the DMI is seen capable of suppressing the Walker breakdown field thus enhancing the DW velocities [184, 260]. On the other hand, a magnon-driven DW motion in systems with DMI and in the presence of an easy-plane anisotropy is shown to be more efficient in driving DWs by inducing linear angular momentum transfer compared to the angular momentum transfer mechanism [261]. Thus, depending on the geometry of the system and the driving force, an interfacial DMI can have different effects on the dynamics of DWs. In what follows, we revisit the results presented in Table 3.3, only now we include an interfacial DMI contribution which can arise for example due to the coupling to a heavy-metal layer such as Pt. Thus, we add an additional term in the total effective field acting on each macro-spin (2.18) in the following manner [262, 263]:

$$\vec{H}_{\text{DMI}} = -\frac{2D(T)}{M_s(0)m_e} [\nabla m_z - (\nabla \cdot \vec{m})\hat{z}]. \quad (3.13)$$

The temperature scaling of the DMI constant is set to:  $D(T) = D(0)m_e^2$  (MFA), where  $D(0) = 2 \text{ mJ/m}^2$  is taken at 0 K. It should be noted, the equilibrium DW configuration at room temperature transitions from the previously Bloch to a Néel type due to the antisymmetric exchange.

Interestingly, for all pulse durations considered, the DW displacement trend is preserved in the presence of the interfacial DMI and a slight increment is achieved—in agreement with previous reports in perpendicularly magnetised samples [184, 260]—as seen in Table 3.4 in comparison with Table 3.3.

### 3.4 Conclusions

Making use of the inherent longitudinal dynamics described by the LLB equation, we have demonstrated the possibility to convert a transient, non-thermal induced magnetisation followed by a subsequent longitudinal relaxation of the macro-spins

into a transverse DW motion.

First of all, we approached the problem in a simpler, chain macro-spin model where no heating effects have been considered nor the presence of the magnetostatic interaction has been taken into account. Nonetheless, we showed that by virtue of a longitudinal deformation of the magnetic texture induced by a transient, magnetisation it is possible to displace a ferromagnetic DW. The mechanism is based on the appearance of a non-thermal magnetisation gradient  $\nabla|\vec{m}|$  which enables the motion of the DW towards the "hot" region corresponding to an area of smaller magnetisation. It has been shown that the displacement primarily takes places on a very fast fs timescale where longitudinal relaxation processes are dominant. In our analysis, we have seen that the distance covered by the DW is proportional to the life-time of the induced gradient as well as the amplitude of the transient magnetisation. The role of the precession and transverse relaxation mechanisms in the acquired displacement is reduced to some DW oscillations on the ns timescale in this chain model as the DW loses its main drive on the longer ps-ns timescale where the  $\nabla|\vec{m}|$  has already vanished. It is fundamentally interesting that an instantaneous DW deformation of opto-magnetic origin generates in the 1D model such interesting and rich dynamics on much longer ps-ns time scales.

Secondly, we verified the viability of the suggested driving mechanism in a more realistic micromagnetic study of a stripe system. In this case, we expand the complexity of the model by taking into account the presence of magnetostatic interactions as well as consider a spatially uniform, time-dependent heating of the sample area ( $\nabla T = 0$ ) using an ultra-fast laser pulse excitation described by the TTM. It is remarkable that although the general features of the results of the chain model remain the same, depending on the nature of the magnetisation modification, we obtained the DW motion to either "hot" or "cold" region, although we should stress that strictly speaking "hot" and "cold" spins were flipped due to complexity of the dynamics.

A laser-induced transient magnetisation equivalent to our  $\delta m_z^0$  parameter was calculated for example in the case of L1<sub>0</sub> FePt in the work of John *et al.* [15] on account of the quantum theory of the IFE [159]. The  $\delta m_z^0$  contribution at a photon energy of 1.55 eV and laser intensity of 68 GW/cm<sup>2</sup> was found to be  $-7.1\%M_s(0\text{ K})$  or  $-3.45\%M_s(0\text{ K})$  for a left ( $\sigma-$ ) and right ( $\sigma+$ ) circularly polarised laser pulse. In a Co sample, Berritta *et al.* [160] calculated in the same approach the IFE induced magnetisation for an identical photon energy but smaller laser intensity of 10 GW/cm<sup>2</sup>, obtaining contributions of  $-4.8 \times 10^{-3} \mu_B/(\text{at. vol.})$  and  $-13 \times 10^{-3} \mu_B/(\text{at. vol.})$  for a  $\sigma+$  and  $\sigma-$  polarisation respectively. Assuming a cubic atomic volume of lateral size 0.25 nm [173] and considering the saturation magnetisation of our Co sample  $M_s(0\text{ K}) = 1400 \text{ kA/m}$ , the latter *ab-initio* result evaluates to approximately  $-0.2\%M_s(0\text{ K})$  and  $-0.55\%M_s(0\text{ K})$ . In our full micromagnetic model these small transient magnetisation contributions would lead to insignificant displacements since our chosen  $\delta m_z^0$  amplitude is set to a very large value of 20%  $M_s(0\text{ K})$  of the zero-Kelvin  $M_s$  and the final displacement in this case is between 2-4 nm. Since the IFE scales linearly with the laser pulse intensity  $I$ , it is expected an (unphysical) intensity of 200 GW/cm<sup>2</sup> would induce the required 20% of  $M_s(0\text{ K})$ . Based on this, the DW motion by the non-thermal mechanism of the IFE in Co with only one laser pulse is unlikely. At the same time, one could envision the use of multiple laser pulse excitations or the investigation of large Verdet constants materials which display a better suitability for the magneto-optical coupling based on the IFE [264, 265], although a transient magnetisation can be attributed to a broad range of light-induced phenomena [15, 48–50, 233, 234] and not solely the IFE. Overall, the small DW displacement presented

in Tables 3.3, 3.4 indicates that a measurable effect experimentally would require multiple pulses. Additionally, it remains to be seen how taking into account an absorption based contribution to the induced magnetisation as discussed by Scheid *et al.* [233, 234] can further enhance the dynamics. Finally, noncollinear spiral systems have been reported to contribute significantly to the magnitude of optically induced effects [266].



## Chapter 4

# Efficient 90° domain wall motion in Mn<sub>2</sub>Au via pure optical torques

A non-thermal, opto-magnetic phenomenon—such as the inverse Faraday effect—we saw may produce longitudinal modifications of the magnetic order parameter. An ultra-fast deformation of this kind can open complex angular momentum transfer pathways with the transverse and precession dynamic reservoirs which can survive on much longer timescales compared to the life-time of the laser excitation. In the results presented in Chapter 3, the transient modification of the magnetisation vector length across a ferromagnetic DW at the fs time-scale was shown to give rise to a translational motion of the wall up to the ps-ns regime. Here in Chapter 4 we shall explore another perspective or interpretation of non-thermal, opto-magnetic phenomena with direct reference to the IFE in the collinear antiferromagnet Mn<sub>2</sub>Au. Instead of the magnetisation vector length modification and depending on the system geometry, the IFE can also introduce an opto-magnetic torque acting on the local spin magnetic moments in an atomistic picture. For reasons which will become clear in the introductory part of this chapter, we hereon refer to the opto-magnetic torque associated with the IFE via the laser-optical torque (LOT) terminology. For now, it is sufficient to keep in mind this will help us distinguish the LOT mechanism from the so-called (Néel) Spin Orbit Torque (NSOT) effect frequently discussed in PT-symmetric AFMs such as Mn<sub>2</sub>Au or CuMnAs. Therefore in this chapter we show via atomistic spin dynamics simulations—parametrised with *ab-initio* calculations from collaborators—that the LOT mechanism can efficiently drive 90° DWs in Mn<sub>2</sub>Au but its spatial symmetry forbids the motion of 180° walls. In the steady-state regime, the kinematics display special relativity signatures accessed for low laser intensities. At velocities higher than the magnonic limit, the AFM DW enters a proliferation regime in which part of its relativistic energy is invested into the nucleation of novel magnetic textures. The unique LOT symmetry allows the precise control of the DW motion direction by rotating the laser polarisation or selecting the wall chirality. Our investigation contributes towards the fundamental understanding of opto-magnetic effects, supporting also the development of next generation, all-optically controlled antiferromagnetic spintronics.

### 4.1 Introduction

Antiferromagnets (AFMs) are currently being envisioned as promising active elements for the next-generation of spintronic devices [81, 267, 268]. To this end, a rapid and efficient manipulation of magnetic domain walls (DWs) is desired, aiming towards the realisation of race-track memories [7, 269], logic architectures [90, 135, 270]

or unconventional computing protocols [99, 271, 272]. In ferromagnets, DW velocities are significantly hindered by internal instabilities known as the Walker breakdown [35, 119, 120] or by spin-wave (SW) emission analogous to the Cherenkov effect [121, 122]. AFMs however, can display relativistic DW kinematics limited only by the maximum group velocity of the medium, typically of the order of tens of km/s [123, 124].

The state of the art mechanism employed to manipulate the AFM order relies on the relativistic, current-induced Néel Spin Orbit Torque (NSOT) effect [273]. In specific crystal structures where neighbouring magnetic atoms in distinct sublattices form non-centrosymmetric local inversion partners, a current excitation gives rise to a non-equilibrium spin polarisation of alternating sign with respect to the AFM bipartite subsystem, manifesting ultimately through staggered spin-orbit fields capable of inducing switching [107, 111, 274–276] or DW motion [123, 124, 133, 277]. At the same time, laser pulse excitation displays the fastest and least dissipative control of the magnetic order observed so far [143]. Several previous experimental and theoretical works addressed the question of light-matter interaction in AFM materials [48, 135, 154–156, 187, 278, 279], with THz laser pulse excitation shown recently capable of driving non-linear dynamics in Mn<sub>2</sub>Au via NSOT acting on the ultra-fast timescale [110]. However, the experimental demonstration of all-optical AFM DW dynamics is yet to be achieved.

A recent *ab-initio* investigation concerning the symmetry and magnitude of the laser-induced magnetic response in the layered AFM Mn<sub>2</sub>Au [162, 280] revealed the appearance of a substantial torque on the Néel order parameter  $\vec{l}$  of tens of mT, as a result of visible light excitation, thus far above the THz regime typically employed experimentally. Based on the non-equilibrium Keldysh formalism [161, 162], a linearly or circularly polarised laser pulse excitation at optical frequencies was shown to excite such a torque through the appearance of a staggered opto-magnetic field which couples to the Mn spins in the distinct AFM sublattices. To distinguish this effect from the previously studied NSOT, we will hereon employ the laser optical torque (LOT) terminology. The physical origin of the calculated effect is being attributed to the Inverse Faraday Effect (IFE) [45, 53]. The NSOT scales linearly with the laser electric field  $\vec{E}$  and is dominant at THz frequencies. Since this first-order response oscillates with the frequency  $\omega$  of the laser field, in the visible frequency spectrum the NSOT cannot excite the Mn<sub>2</sub>Au AFM due to the large mismatch between  $\omega$  and the AFM resonant frequencies. In contrast, the LOT is a second-order response which scales quadratically with  $\vec{E}$ . The dc contribution of this second-order response makes LOT dominant at optical frequencies [161, 162]. Recently, this LOT mechanism was predicted capable of inducing coherent 90° and 180° switching of the AFM order parameter on the ultra-fast time-scale [281]. Importantly, the symmetry of the LOT effect is radically distinct from NSOT which in Ref. [281] is shown to give rise to toggle switching by means of the same laser polarisation, in contrast with conventional NSOT where the polarity of the  $\vec{E}$ -field must be flipped (be it with current or THz excitation) [107, 110, 275]. It is thus fundamentally interesting to apply the little explored LOT mechanism also in the problem of DW dynamics.

In the following sections we combine the *ab-initio* results in Ref. [162] with atomistic spin dynamics (ASD) simulations implemented in the open-source, software package VAMPIRE [173], in an investigation of optically-driven DW kinematics in a Mn<sub>2</sub>Au track. Depending on the relative orientation between the Néel vector  $\vec{l}$  and the electrical field component  $\vec{E}$  of the applied laser pulse, the symmetry and magnitude of the LOT can be established. We demonstrate that the LOT mechanism

predicted in [162] may drive 90° DW dynamics. Interestingly, its symmetry does not allow the motion of 180° DWs, in contrast with NSOT [123, 124, 133, 277]. Our numerical study is complemented by a theoretical, two-sublattice  $\sigma$ -model [123, 125, 126, 128, 129, 131], adapted for the present case. Therefore, in sections 4.2 and 4.3 we describe in detail the extended Mn<sub>2</sub>Au Heisenberg Hamiltonian we use and the relationship between the ab-initio calculations in [162] and the implementation of the LOT in our ASD model respectively. Subsequently in section 4.4 we introduce the adapted  $\sigma$  model for the description of LOT-driven 90° DW dynamics. Equipped with these tools, we analyse first in section 4.5 the special relativity signatures of the AFM DW dynamics in Mn<sub>2</sub>Au, comparing the steady-state kinematics for constant laser-pulse excitation in the ASD simulations and the  $\sigma$  model. Next, we present a detailed look at the LOT DW driving mechanism and the physical reason which allows the motion of 90° walls but impedes the kinematics of 180° geometries (section 4.6). Finally, we describe the activation of highly non-linear AFM DW dynamics in the supermagnetic regime accompanied by spontaneous DWs proliferation events in section 4.7 as well as analyse the DW direction of motion in terms of the wall chirality and the sign of the LOT 4.8. The last section of this chapter is devoted to discussion and perspectives of the developed ASD model.

## 4.2 Extended Heisenberg Hamiltonian of Mn<sub>2</sub>Au

Mn<sub>2</sub>Au is a layered, collinear AFM with four magnetic sublattices in the unit cell (see sketch in Figure 4.1 and characterised by the so-called PT-symmetry [273]. Inside each layer, Mn atoms are ferromagnetically coupled. This material possesses a complex set of anisotropies with cubic and uniaxial in-plane as well as uniaxial out-of-plane components. Thus, in principle, both 180° and 90° in-plane DWs are possible in Mn<sub>2</sub>Au, although experimentally, when grown in a thin film form, mostly 90° domains have been reported [110, 187, 282]. The special PT-symmetry ensures the existence of intrinsic NSOT which can efficiently move 180° DWs in Mn<sub>2</sub>Au by applying electric current [123, 124, 277].

The extended Heisenberg Hamiltonian describing the energy contributions in our Mn<sub>2</sub>Au system [124, 131, 275] is:

$$\begin{aligned}
 \mathcal{H} = & - \sum_{\langle i,j \rangle} J_{ij} \vec{S}_i \cdot \vec{S}_j - K_{2\perp} \sum_i (\vec{S}_i \cdot \vec{z})^2 - \frac{K_{4\perp}}{2} \sum_i (\vec{S}_i \cdot \vec{z})^4 - \\
 & - \frac{K_{4||}}{2} \sum_i \left[ (\vec{S}_i \cdot \vec{u}_1)^4 + (\vec{S}_i \cdot \vec{u}_2)^4 \right] - \mu_0 \mu_{\text{at}} \sum_i \vec{S}_i \cdot \vec{H}_{\text{opt}}^i,
 \end{aligned} \quad (4.1)$$

where the adimensional  $\vec{S}_{i,j}$  unit vectors denote the orientation of the local spin magnetic moments at sites  $i$  and  $j$ . The first energy term characterises the nearest-neighbours exchange interactions between magnetic moments  $\vec{S}_i$  and  $\vec{S}_j$ . The exchange integral  $J_{ij} = (J_1, J_2, J_3)$  collectively denotes three types of interactions present within the tetragonal unit cell (seen in subplot (a) of Fig. 4.1), two of AFM kind ( $J_1, J_2$ ) and a third FM-like exchange ( $J_3$ ).

The Hamiltonian also contains three magnetocrystalline anisotropy terms which stabilise an in-plane 90° DW configuration: one easy-plane contribution  $K_{2\perp}$  and two tetragonal terms  $K_{4\perp}$  and  $K_{4||}$ . The unit vectors  $\vec{u}_1, \vec{u}_2$  denote the in-plane, diagonal directions [110] and [1̄10], respectively. Finally, the last energy term describes the Zeeman interaction between the local spin moment  $\vec{S}_i$  and the staggered optical

Parameter	Value			Unit
$J_1$	$-5.467$	$-7.345$	$1.588$	$\text{J/link} (\times 10^{-21})$
$K_{2\perp}$		$-1.303 \times 10^{-22}$		$\text{J/atom}$
$K_{4\parallel}$		$1.855 \times 10^{-25}$		$\text{J/atom}$
$K_{4\perp}$		$3.71 \times 10^{-25}$		$\text{J/atom}$
$\mu_{\text{at}}$		$3.73$		$\mu_{\text{B}}$
$a_0$	$3.328$	$8.539$		$\text{\AA}$

TABLE 4.1: Mn<sub>2</sub>Au material parameters used in our ASD calculations. The exchange and lattice constants are extracted from Ref. [163] while the anisotropy terms were previously calculated in Ref. [164]. The atomic magnetic moment of the Mn atoms was set equal to the value found in Ref. [162]. Finally, two distinct damping parameters are considered:  $\lambda = 10^{-2}$  and  $\lambda = 10^{-3}$  [124, 248, 277, 283].

field  $\vec{H}_{\text{opt}}^i$  originating from the IFE, where the  $\mu_{\text{at}}$  constant stands for the Mn atomic magnetic moment and  $\mu_0$  represents the vacuum permeability. In the next section we will carefully analyse the strength and symmetry of the  $\vec{H}_{\text{opt}}$  term. The values of the material parameters employed here can be consulted in Table 4.1. Importantly, Mn<sub>2</sub>Au with its material parameters such as anisotropy and exchange in addition to the LOT magnitude have been obtained previously via *ab-initio* calculations [162–164]. The unit-cell geometry as well as the extended Heisenberg Hamiltonian in Eq. (4.1) correspond to previous Mn<sub>2</sub>Au studies in Refs. [124, 131, 275]. Here by means of large-scale ASD modelling we investigate DW dynamics driven by LOT. For this purpose we numerically integrate the set of coupled LLG equations for localised atomic magnetic moments in a 7 μm long Mn<sub>2</sub>Au track.

### 4.3 Antiferromagnetic order control via non-thermal laser-induced torques

We consider the Mn<sub>2</sub>Au AFM as a two-sublattice system for which we define the Néel order parameter  $\vec{l} = (\vec{S}_B - \vec{S}_A)/2$  and the magnetisation vector  $\vec{n} = (\vec{S}_A + \vec{S}_B)/2$  with respect to the vector fields  $\vec{S}_A, \vec{S}_B$ . In the next section we link the  $\vec{S}_A, \vec{S}_B$  terms with the embedded magnetisation planes in the four-layered Mn<sub>2</sub>Au crystal displayed in Fig. 4.1(a). For now, the definition of  $\vec{l}$  and  $\vec{n}$  is postulated.

The question of light-matter interaction in Mn<sub>2</sub>Au was first raised theoretically in Ref. [162] as a comparative study of opto-magnetic torques acting on the Néel vector  $\vec{l}$ , in the visible and THz frequency regimes. In this *ab-initio* study, the AFM crystal—effectively an interacting, many-electron system—is described in the Kohn Sham density functional theory by a single-particle Hamiltonian, to which the interaction with the laser pulse is added as a perturbation. This picture leads to the appearance of a non-equilibrium, laser-induced spin polarisation which couples with the local magnetic moments and gives rise to an opto-magnetic torque [161] called here LOT. The LOT which is a second-order contribution with respect to the electric field polarisation vector  $\vec{E}$ , is attributed to the IFE. Compared to the first-order response in  $\vec{E}$  which is more relevant in the THz regime—and otherwise identified with the NSOT torque—the LOT is dominant in the visible frequency spectrum. In a general, tensor form, the LOT can be expressed in terms of the  $\vec{l}$  and  $\vec{E}$  vector components

as [161, 162, 280]:

$$T_i = \frac{r_0^3 I}{c} \left( \frac{\mathcal{E}_H}{\hbar \omega} \right)^2 \text{Im} \sum_{j k p q} \chi_{ijkpq} \varepsilon_j \varepsilon_k^* l_p l_q. \quad (4.2)$$

In Eq. (4.2),  $\omega$  is the light frequency,  $r_0 = 4\pi\epsilon_0\hbar^2/(me^2)$  is the Bohr radius,  $I = \epsilon_0 c E_0^2 / 2$  is the intensity of the light with  $E_0^2$  defining the amplitude of the laser electric field and  $\mathcal{E}_H = e^2/(4\pi\epsilon_0 r_0)$  is the Hartree energy. The remaining constants are the speed of light  $c$ , the vacuum permittivity  $\epsilon_0$ , the elementary charge  $e$ , the electron rest mass  $m$  and finally the reduced Planck constant  $\hbar$ . Further,  $\varepsilon_j, \varepsilon_k^*$  denote the  $j, k$  Cartesian components of the light polarization vector and their complex conjugates respectively, while  $l_p, l_q$  indicate the Cartesian components of the Néel vector. The tensor components  $\chi_{ijkpq}$  describe the allowed LOT symmetries in Mn<sub>2</sub>Au given its crystallographic point group and the positions of the up/down spins in the unit cell. Table I in Ref. [162] presents thirty possible torque symmetries for Mn<sub>2</sub>Au which according to equation (4.2) depend both on the orientation of the Néel vector  $\vec{l}$  as well as the direction of the  $\vec{E}$  polarisation vector. In spherical coordinates these vectors can be written as:

$$\vec{l} \equiv (\sin \theta_l \cos \varphi, \sin \theta_l \sin \varphi, \cos \theta_l), \quad (4.3)$$

$$\vec{E} \equiv (\sin \theta_e \cos \psi, \sin \theta_e \sin \psi, \cos \theta_e), \quad (4.4)$$

where  $\theta_l, \theta_e$  are the polar and  $\varphi, \psi$  the azimuthal angles respectively. The large number of allowed  $\chi_{ijkpq}$  tensors reduces greatly for an in-plane orientation of the Néel vector ( $\theta_l = \pi/2$ ), typical for Mn<sub>2</sub>Au experimental samples. In Ref. [162] these are labelled as tensors 3, 4, 9 and 24. Below we discuss the symmetries of these torques and link the notation employed in Ref. [162] with expressions useful for our ASD. To simplify the discussion we assume the laser polarisation is fixed in the  $Oxy$  plane ( $\theta_e = \pi/2$ ). Equations (4.3),(4.4) thus can be recast as:

$$\vec{l} \equiv (\cos \varphi, \sin \varphi, 0), \quad (4.5)$$

$$\vec{E} \equiv (\cos \psi, \sin \psi, 0). \quad (4.6)$$

The relationship between the opto-magnetic torques in tensorial notation found in [162] and the trigonometric representation based on the  $\varphi, \psi$  angles is detailed in Table 4.2. First of all, it is easy to see that given the  $\theta_e = \pi/2$  condition, tensors 3

ID in Ref. [162]	$\chi_{ijkpq}$ given in Ref. [162]	$T_i \propto \chi_{ijkpq}$	$T_i \propto \varphi, \psi$
3	$\langle 23212 \rangle - \langle 13121 \rangle$	$T_{yx} \propto \varepsilon_z \varepsilon_y^* l_x l_y - \varepsilon_z \varepsilon_y^* l_y l_x$	$T_{yx} = 0 (\varepsilon_z = 0)$
4	$\langle 32221 \rangle - \langle 31112 \rangle$	$T_z \propto \varepsilon_y \varepsilon_y^* l_y l_x - \varepsilon_x \varepsilon_x^* l_x l_y$	$T_z \propto -\sin(2\varphi) \cos(2\psi)$
9	$\langle 21311 \rangle - \langle 12322 \rangle$	$T_{yx} \propto \varepsilon_x \varepsilon_z^* l_x l_x - \varepsilon_y \varepsilon_z^* l_y l_y$	$T_{yx} = 0 (\varepsilon_{z,z^*} = 0)$
24	$\langle 31211 \rangle - \langle 32122 \rangle$	$T_z \propto \varepsilon_x \varepsilon_y^* l_x l_x - \varepsilon_y \varepsilon_x^* l_y l_y$	$T_z \propto \cos(2\varphi) \sin(2\psi)$

TABLE 4.2: Allowed LOT symmetries in Mn<sub>2</sub>Au for an in-plane Néel vector geometry as calculated in Ref. [162]. The table discusses the link between the angular-dependent expressions of the LOT used throughout this work and the original tensorial notation.

and 9 become null in our geometry since  $\varepsilon_{z,z^*}$  are zero. Secondly, it is worth pointing out tensors 4 and 24 are linked via  $\pm\pi/4$  rotations with respect to  $\varphi$  and  $\psi$ . As such, if we set  $\psi = 45^\circ$  to maximise the magnitude of tensor 24, tensor 4 becomes zero.

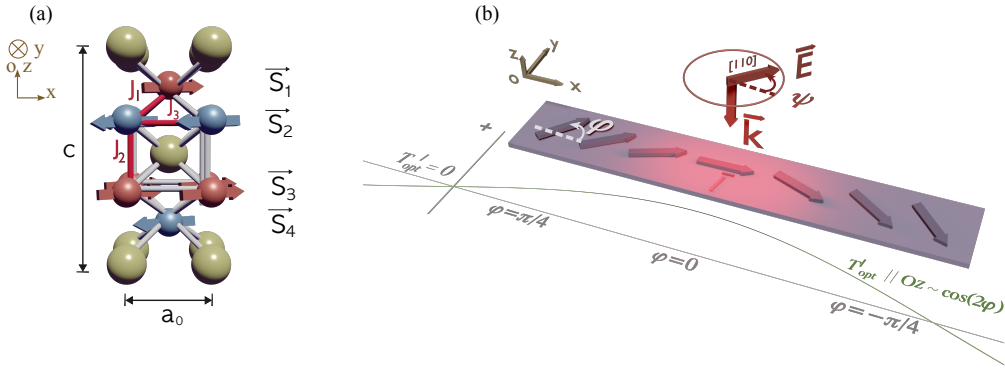


FIGURE 4.1: (a) Mn<sub>2</sub>Au tetragonal unit cell and the four staggered Mn magnetisation layers. With yellow we represent the Au atoms. (b) All-optical excitation of in-plane 90° AFM DW. A laser pulse in the optical frequency range propagating with  $\vec{k} \parallel O_z$  and with its electric field component  $\vec{E}$  polarised along the [110] diagonal ( $\psi = 45^\circ$ ), will lead to an OOP torque determined by the local spin orientation and proportional to the laser intensity [162]. In our geometry, the spins at the DW boundaries will experience no torque while the spins corresponding to  $\varphi = 0$  will experience a maximum torque. The green curved line displays the magnitude and sign of the OOP optical torque as a function of the  $\varphi$  angle. Both angles  $\varphi$  and  $\psi$  are defined with respect to the  $O_x$  axis.

Finally, the spatial variation of tensor 24 can be written in a compact, vector form as:

$$\vec{T}_{\text{opt}}^l = A \cos(2\varphi) \sin(2\psi) \hat{z}, \quad (4.7)$$

where we insert the proportionality factor  $A$  in units of Tesla and use the notation  $\vec{T}_{\text{opt}}^l$  to enforce this torque acts on the Néel vector  $\vec{l}$ . In subplot (b) of Figure 4.1 we display the magnitude variation of this LOT symmetry as a function of the local Néel order in a 90° wall geometry. The amplitude  $A$ , depends on the laser pulse parameters as well as the quasi-particle broadening, the latter being a measure of the disorder and the lifetime of the electronic states within the Keldysh formalism [161]. As presented in Fig. 2 of Ref. [162], for a typical laser intensity of  $I = 10 \text{ GW/cm}^2$ , photon energy of 1.55 eV and  $\Gamma = 25 \text{ meV}$ ,  $A$  evaluates to 12 yJ (yoctoJoules)/μ<sub>at</sub> or approximately 0.346 T. The  $A(I)$  variation follows a linear scaling law as inferred from Eq. (4.2).

The main result of this chapter is the demonstration of laser-induced 90° DW displacement in Mn<sub>2</sub>Au via the LOT symmetry given in equation (4.7). In an experimental setup, this may be achieved for example —according to Ref. [162]—for a linearly polarised pulse at visible frequency, propagating with  $\vec{k} \parallel O_z$  (perpendicular to the Mn planes) and with the electric field  $\vec{E}$  set parallel to the [110] direction with respect to the Mn<sub>2</sub>Au unit cell (see Figure 4.1). This leads to the appearance of the LOT given in equation (4.7) which depends on the local orientation of  $\vec{l}$  and the polarisation of the  $\vec{E}$ -field vector via the azimuthal angles  $\varphi$  and  $\psi$  measured with respect to the  $O_x$  axis which coincides with the [100] crystallographic direction (see subplot (b) of Figure 4.1). Crucially, the NSOT has the symmetry of Zeeman torque (i.e. proportional to  $\cos(\varphi)$  when the current is applied parallel to the [100] direction) [123, 124] and thus radically distinct compared to the LOT mechanism described here. The LOT symmetry in (4.7) leads to canting of the Néel vector  $\vec{l}$  in the  $O_z$  direction. This torque corresponds to a staggered opto-magnetic field  $\vec{H}_{\text{opt}}^l$ ,

which in our ASD model we couple to the local spin  $\vec{S}_i$  via the relationship:

$$\vec{H}_{\text{opt}}^i = \frac{1}{\mu_0} \vec{T}_{\text{opt}}^i \times \vec{S}_i. \quad (4.8)$$

To study the possibility for optically driven DW dynamics in our Mn<sub>2</sub>Au system, we numerically integrate the set of coupled LLG equations given in (2.13). The effective field  $\vec{H}_{\text{eff}}^i$  acting at each atomic site  $i$  is calculated via the relationship:  $\vec{H}_{\text{eff}}^i = -\frac{1}{\mu_0 \mu_{\text{at}}} \frac{\delta \mathcal{H}}{\delta \vec{S}_i}$ , where  $\mathcal{H}$  is given by Eq. (4.1). The simulated system is 7 μm in length with open boundary conditions along the  $Ox$  and  $Oz$  directions. To ensure full, symmetric exchange for at least two sublayers, the track is four Mn wide and four Mn tall, with periodic boundary conditions along the  $Oy$  axis.

#### 4.4 Analytic description of laser-driven antiferromagnetic domain wall dynamics

The ASD simulations will be compared with an adapted non-linear  $\sigma$ -model, which takes its name from a scalar field theory originally introduced by Gell-Mann and Lévy in the context of pion decay studies in nuclear physics [284]. Historically,  $\sigma$ -models found applications in other branches of physics as they were shown to be closely related with non-linear evolution equations such as the sine-Gordon (SG), Korteweg-de-Vries, or the non-linear Schrödinger equation [285]. These form a special category of integrable partial differential equations that admit a large number of solutions and exhibit special symmetries from which emerge constants of motion and conservation laws [286]. In magnetism, some of the most famous  $\sigma$ -like models represent in fact continuum approximations of low-dimensional Heisenberg spin lattices, either ferro- or antiferro-magnetically ordered [130, 287–293]. Special cases of AFM spin systems with or without inclusion of anisotropy contributions are well studied in the literature and appeal due to their intrinsic relativistic properties [126, 128, 129, 288–290, 294, 295]. The corresponding  $\sigma$ -models are associated with Lorentz-invariant, dynamic equations of the SG type that can be derived for example from the Landau-Lifshitz-Gilbert (LLG) equations of motion, or phenomenologically via symmetry arguments [127, 128, 295–298]. Their usefulness resides in the reduction of rather complex problems to readily integrable analytic equations without loss of physical depth.

In what follows, we will lay the ground for the analytic description of AFM dynamics in our Mn<sub>2</sub>Au system. The first aim in the  $\sigma$ -like model will be to pass Eq. (4.1) in the continuum limit and define an energy density  $\mathcal{E}$  with respect to a two sublattice magnetisation system. Reducing the analysis of Mn<sub>2</sub>Au to a two-variable problem will allow us to introduce an unique Néel order parameter whose dynamics will eventually be described by an equation of the SG type. To this end, we make the following observations. The tetragonal unit cell presented in subplot (a) of Fig. 4.1 displays four staggered magnetisation layers along the c-axis (parallel to the  $Oz$  direction) denoted by  $(\vec{S}_1, \vec{S}_2, \vec{S}_3, \vec{S}_4)$ , where  $\vec{S}_i = \vec{S}_i(\vec{r}_i)$  is localised in the Cartesian coordinate system via the positional vector  $\vec{r}_i$ . The reduction to a system of two-variables can be achieved since the magnetisation vectors in layers 1 and 3, respectively 2 and 4, are parallel with respect to each other and thus can be assumed magnetically indistinguishable ( $\vec{S}_1 = \vec{S}_3$  and  $\vec{S}_2 = \vec{S}_4$ ). However, it is obvious the number of exchange interactions is distinct in the embedded planes compared to the outer layers due to the  $J_2$  AFM exchange. In a previous work concerned with the

NSOT-driven, DW dynamics in a Mn<sub>2</sub>Au thin film [131], this exchange contribution was shown to have a negligible role in the dynamic as well as the static properties of an in-plane 180° wall as long as it is not small and maintains the (almost) collinear AFM coupling. We will maintain this assumption in our study of optically driven 90° DW dynamics in the same in-plane geometry and thus neglect  $J_2$ . Therefore, we characterise the Mn<sub>2</sub>Au system solely on the basis of an effective Néel order parameter  $\vec{l} = (\vec{S}_B - \vec{S}_A)/2$  and a magnetisation vector  $\vec{n} = (\vec{S}_A + \vec{S}_B)/2$ , which form an orthogonal basis  $\vec{n} \cdot \vec{l} = 0$  and where  $\vec{S}_A, \vec{S}_B$  can be identified with the embedded magnetic planes  $\vec{S}_2$  and  $\vec{S}_3$  respectively. Since we neglect the  $J_2$  exchange penalty (in the limit of strong AFM coupling of distinct Mn planes), these definitions could also be given in terms of  $\vec{S}_1$  and  $\vec{S}_4$ .

In the following subsections, we will pass the discrete Heisenberg Hamiltonian of Eq. (4.1) to the continuum limit and define an energy density in terms of the  $(\vec{l}, \vec{n})$  basis. The final aim of this procedure is to construct a set of AFM LLG equations of motion which can be mapped onto a Lorentz-invariant, SG equation, following the pioneering work in Refs [125–129] and in similar fashion with more recent studies in [123, 130, 131].

#### 4.4.1 Two-sublattice based energy density of the Mn<sub>2</sub>Au crystal

In the limit of a considerably large number of spins and within the continuum approximation, Eq. (4.1) can be written as [128–130, 288]:

$$\mathcal{H} \approx \frac{1}{D} \int \mathcal{E} d\vec{r}, \quad (4.9)$$

where the constant  $D$  ensures  $\mathcal{H}$  and  $\mathcal{E}$  are expressed in units of energy and can be in principle adapted to the spatial dimension of the problem. Here we are interested in finding the functional form of the energy density  $\mathcal{E} = \mathcal{E}(\vec{l}, \vec{n})$ . Once obtained, the AFM equations of motion for the  $(\vec{l}, \vec{n})$  vectors can be constructed either following a variational approach as in classical field theory or via linearly combined LLG equations corresponding to the sublattice magnetisation vectors  $\vec{S}_{A,B}$  [130]. In the next subsection we will discuss the latter approach. To construct  $\mathcal{E}$  let us turn our attention first to the exchange interactions in our Mn<sub>2</sub>Au system. A given Mn atom at a position  $\vec{r}_i$  (see Figure 4.2) is characterised by four inter-layer exchange interactions of type  $J_1$ , with (first) nearest neighbours found at a distance of  $a_0/2$  along diagonal  $Oxy$  directions. To this we should in principle add four intra-layer exchange interactions of type  $J_3$  (two along  $Ox$  and other two along  $Oy$ ) with (first) nearest neighbours found at a distance  $a_0$ . However, we can make room for another simplification assuming a coherent in-plane rotation of the spins along  $Oy$ , biasing the extension of the DW along  $Ox$  and neglecting the  $J_3$  penalty along  $Oy$ . Thus, the total exchange energy for our two-sublattice magnetisation system is:

$$E_{\text{exc}} = E_{\text{exc}}(J_1) + E_{\text{exc}}(J_3), \quad (4.10)$$

where the exchange contribution  $E_{\text{exc}}(J_1)$  is given by:

$$E_{\text{exc}}(J_1) = 2|J_1| \sum_i^N \vec{S}_A(\vec{r}_i) \cdot \left[ \vec{S}_B\left(\vec{r}_i - \frac{a_0}{2}\hat{x}\right) + \vec{S}_B\left(\vec{r}_i + \frac{a_0}{2}\hat{x}\right) \right]. \quad (4.11)$$

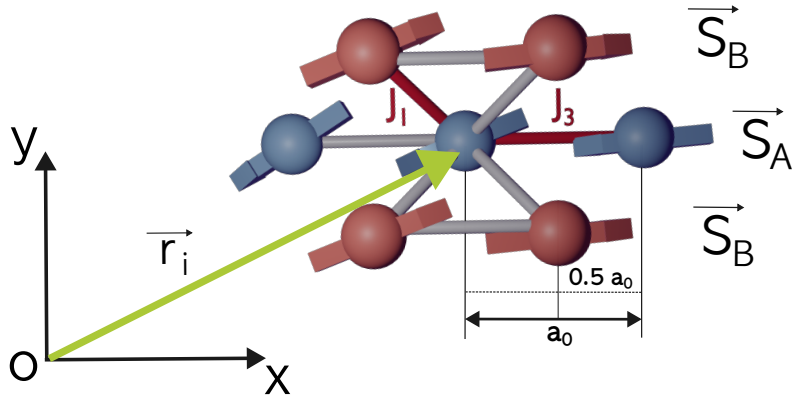


FIGURE 4.2: Top view of the two sublattice picture  $\vec{S}_A, \vec{S}_B$  considered in the analytical model of Mn<sub>2</sub>Au. To grasp the relevant exchange contributions we analyse for reference a Mn atom found at a distance  $\vec{r}_i$  in sublattice A. We thus count two FM interactions ( $J_3$ ) along  $Ox$  and four AFM interactions ( $J_1$ ) along the diagonal directions [110], [1̄10]. The Figure is adapted from Ref. [131].

Making use of a second-order Taylor series expansion of the  $\vec{S}_B(\vec{r}_i - \frac{a_0}{2}\hat{x})$  and  $\vec{S}_B(\vec{r}_i + \frac{a_0}{2}\hat{x})$  variables around the  $\vec{r}_i$  point (in the  $Ox$  direction) we can obtain from Eq. (4.11) an exchange penalty density in the continuum limit as:

$$\mathcal{E}_{\text{exc}}(J_1) = 4|J_1| \vec{S}_A \cdot \left[ \vec{S}_B + \frac{1}{2} \left( \frac{a_0}{2} \right)^2 \partial_x^2 \vec{S}_B \right]. \quad (4.12)$$

In principle, the relationship between  $E_{\text{exc}}$  and  $\mathcal{E}_{\text{exc}}$  can be written in a similar manner to Eq. (4.9) by integrating the exchange contributions across the whole system in the limit of a large number of spins  $N$ . We neglect now the discrete spatial indices  $\vec{r}_i$  and assume two continuous sublattices  $\vec{S}_{A,B}$ . This is allowed in the approximation  $|\vec{S}_\beta(\vec{r}_i) - \vec{S}_\beta(\vec{r}_j)| \approx \vec{r}_{ij} \cdot \nabla \vec{S}_\beta$ , where  $\beta = A, B$ . Given the relationships:  $|\vec{n}|^2 \ll |\vec{l}|^2$  (exchange limit),  $|\vec{n}|^2 + |\vec{l}|^2 = 1$ ,  $\vec{l} \cdot \partial_x \vec{l} = 0$  (homogeneous material) and  $\vec{S}_A \cdot \partial_x^2 \vec{S}_B \approx -\vec{l} \cdot \partial_x^2 \vec{l} = (\partial_x \vec{l})^2$ , Eq. (4.12) can be redefined in terms of the  $\vec{n}$  and  $\vec{l}$  variables:

$$\mathcal{E}_{\text{exc}}(J_1) = 8|J_1| \left[ |\vec{n}|^2 + \frac{a_0}{16} (\partial_x \vec{l})^2 \right]. \quad (4.13)$$

At the same time, the total exchange term  $E_{\text{exc}}(J_3)$  for our system is given by:

$$E_{\text{exc}}(J_3) = -J_3 \sum_i^N \vec{S}_A(\vec{r}_i) \cdot \left[ \vec{S}_A(\vec{r}_i - a_0 \hat{x}) + \vec{S}_A(\vec{r}_i + a_0 \hat{x}) \right]. \quad (4.14)$$

Once more we neglect the exchange penalty along  $Oy$  assuming a coherent motion of the spins in this direction. Following a similar procedure as in the case of  $E_{\text{exc}}(J_1)$

we can define from Eq. (4.14) a second exchange density penalty of  $J_3$  type:

$$\mathcal{E}_{\text{exc}}(J_3) = -2J_3 \vec{S}_A \cdot \left[ \vec{S}_A + \frac{a_0^2}{2} \partial_x^2 \vec{S}_A \right]. \quad (4.15)$$

Since the dot product  $\vec{S}_A \cdot \vec{S}_A$  evaluates to a constant it can be absorbed in  $\mathcal{E}_{\text{exc}}(J_3)$ . Given that  $\vec{S}_A \cdot \partial_x^2 \vec{S}_A \approx \vec{l} \cdot \partial_x^2 \vec{l} = -(\partial_x \vec{l})^2$ , we can write the final shape of  $\mathcal{E}_{\text{exc}}(J_3)$  as:

$$\mathcal{E}_{\text{exc}}(J_3) = J_3 a_0^2 (\partial_x \vec{l})^2. \quad (4.16)$$

As we pass from discrete to infinitesimal spatial variations, we neglect the  $\vec{r}_i$  indices. Finally, summing its distinct contributions and after grouping the terms with respect to the  $\vec{n}$  and  $\vec{l}$  vectors, the total exchange density can be cast in the form [130, 131]:

$$\mathcal{E}_{\text{exc}} = \frac{1}{2} A |\vec{n}|^2 + \frac{1}{8} a (\partial_x \vec{l})^2, \quad (4.17)$$

where we made use of the notation  $A = 16|J_1|$  and  $a = 8a_0^2(J_3 + |J_1|/2)$ , thus separating the equation into homogeneous and inhomogeneous exchange contributions.

Before moving on to discuss the anisotropy energy in our Mn<sub>2</sub>Au crystal, an important point needs to be underlined here. The functional form of  $\mathcal{E} = \mathcal{E}(\vec{l}, \vec{n})$  and the associated AFM equations of motion described later are intrinsically built assuming a two-sublattice magnetic system. However, the actual DW dynamics can be spatially reduced to a single magnetisation sheet without loss of model accuracy. This implies simply that the anisotropy energy contribution considered onwards will be half the total value for an actual two-sublattice system since the displacement of the wall is equivalent in either of the embedded magnetisation planes we are working with. Also, by not counting twice the anisotropy contribution to the energy density we avoid an artificial and unwanted doubling of the DW width. Thus, the total anisotropy energy in a single magnetic plane is given by three distinct terms:

$$E_{\text{ani}} = E(K_{2\perp}) + E(K_{4\perp}) + E(K_{4\parallel}). \quad (4.18)$$

While the first two contributions bias the magnetic configuration in the plane of the thin film, the latter stabilises a 90° DW geometry as seen in Fig. 4.1(b). To simplify the analytic calculations we will realign the easy-axes (EAs) corresponding to the  $E(K_{4\parallel})$  energy along the  $Ox$  and  $Oy$  directions. Taking as reference the spins in sublattice A we can write Eq. (4.18) in its expanded form:

$$E_{\text{ani}} = \sum_i^N \left\{ |K_{2\perp}| \left( \vec{S}_A^i \cdot \hat{z} \right)^2 - \frac{K_{4\perp}}{2} \left( \vec{S}_A^i \cdot \hat{z} \right)^4 - \frac{K_{4\parallel}}{2} \left[ \left( \vec{S}_A^i \cdot \hat{x} \right)^4 + \left( \vec{S}_A^i \cdot \hat{y} \right)^4 \right] \right\}, \quad (4.19)$$

where we replaced the  $\vec{S}_A(\vec{r}_i)$  notation with  $\vec{S}_A^i$  for reasons of typographic alignment. Given that  $\vec{S}_A = (\vec{n} - \vec{l})$  in a continuous vector form, we can obtain from Eq. (4.19) a corresponding anisotropy energy density in the shape of:

$$\mathcal{E}_{\text{ani}} = |K_{2\perp}| \left( \vec{l} \cdot \hat{z} \right)^2 - \frac{K_{4\perp}}{2} \left( \vec{l} \cdot \hat{z} \right)^4 - \frac{K_{4\parallel}}{2} \left[ \left( \vec{l} \cdot \hat{x} \right)^4 + \left( \vec{l} \cdot \hat{y} \right)^4 \right]. \quad (4.20)$$

In writing the expression of  $\mathcal{E}_{\text{ani}}$  we neglected the terms proportional to  $|\vec{n}|^2$  and  $|\vec{n}|^4$  since in the exchange limit  $|\vec{n}|^2 \ll |\vec{l}|^2$  they closely evaluate to zero in comparison

with the high-order terms in  $\vec{l}$ .

The last contribution to  $\mathcal{E}(\vec{l}, \vec{n})$  which needs to be discussed comes from the Zeeman interaction between the Mn magnetic moments and the external field, arising in our case via the IFE. The spatial symmetry and magnitude of this field was discussed in section 4.3 of this Chapter. Taking as reference a single magnetisation sheet just like in the anisotropy case earlier, we write the total energy of Zeeman origin for the spins in sublattice A as:

$$E_{\text{zee}} = -\mu_0 \mu_{\text{at}} \sum_i^N \vec{S}_A^i \cdot \vec{H}_{\text{opt}}^i. \quad (4.21)$$

In an energy density form this contribution boils down to:

$$\mathcal{E}_{\text{zee}} = 2\gamma\hbar \vec{l} \cdot \vec{H}_{\text{opt}}, \quad (4.22)$$

where we made use of the relationships  $\mu_0 \mu_{\text{at}} \approx 2\gamma\hbar$  and  $\vec{S}_A = \vec{n} - \vec{l}$ . Here,  $\gamma$  is the electron gyromagnetic ratio expressed in units of A/m and conventionally it is taken as a positive value, while  $\hbar$  is the reduced Planck constant. Due to the large  $K_{2\perp}$  anisotropy, the dynamics of the  $\vec{l}$  vector will be constrained to the Oxy plane. In the presence of the opto-magnetic coupling described in Eqs. (4.7), (4.8) a small magnetisation component  $\vec{n} \equiv n_z \hat{z}$  will arise due to a non staggered, out-of-plane canting of the sublattices. Since during the dynamics,  $\vec{H}_{\text{opt}}$  remains perpendicular to  $\vec{n}$  we can cancel the  $\vec{n} \cdot \vec{H}_{\text{opt}}$  contribution. Finally, summing all terms in Eqs. (4.17), (4.20) and (4.22) we can write within a  $\sigma$ -like model the energy density of our Mn<sub>2</sub>Au system [128–131]:

$$\mathcal{E} = \frac{1}{2} A |\vec{n}|^2 + \frac{1}{8} a \left( \partial_x \vec{l} \right)^2 + \mathcal{E}_{\text{ani}} (\vec{l}) + 2\gamma\hbar \vec{l} \cdot \vec{H}_{\text{opt}}. \quad (4.23)$$

In the following subsection we will discuss how we can make use of Eq. (4.23) to write down the AFM equations of motion for the  $\vec{l}, \vec{n}$  vector pair.

#### 4.4.2 The antiferromagnetic Landau-Lifshitz-Gilbert equations of motion

Let us now introduce the LLG equations of motion for our two sublattice magnetisation system ( $\vec{S}_A, \vec{S}_B$ ) which in the limit  $\lambda \ll 1$  can be written in a Landau-Lifshitz (LL) form [127, 128]:

$$\dot{\vec{S}}_A = -\gamma \vec{S}_A \times \vec{H}_{\text{eff}}^A - \gamma \lambda \vec{S}_A \times (\vec{S}_A \times \vec{H}_{\text{eff}}^A), \quad (4.24)$$

$$\dot{\vec{S}}_B = -\gamma \vec{S}_B \times \vec{H}_{\text{eff}}^B - \gamma \lambda \vec{S}_B \times (\vec{S}_B \times \vec{H}_{\text{eff}}^B). \quad (4.25)$$

Introducing the effective magnetic fields  $\vec{H}_{\text{eff}}^{n,l} = -\frac{1}{\mu_0 \mu_{\text{at}}} \frac{\delta \mathcal{E}(\vec{n}, \vec{l})}{\delta(\vec{n}, \vec{l})}$  corresponding to the  $\vec{n}$  and  $\vec{l}$  vectors and defined with respect to the energy density given in (4.23), it can be shown  $\vec{H}_{\text{eff}}^{A,B}$  in Eqs. (4.24), (4.25) satisfy the following relationships:

$$\vec{H}_{\text{eff}}^A = \vec{H}_{\text{eff}}^n - \vec{H}_{\text{eff}}^l, \quad (4.26)$$

$$\vec{H}_{\text{eff}}^B = \vec{H}_{\text{eff}}^n + \vec{H}_{\text{eff}}^l. \quad (4.27)$$

These identities hold given that  $\vec{H}_{\text{eff}}^{\text{A},\text{B}}$  are constructed as  $\vec{H}_{\text{eff}}^{\text{A},\text{B}} = -\frac{2}{\mu_0\mu_{\text{at}}} \frac{\delta\mathcal{E}(\vec{n}, \vec{l})}{\delta(\vec{n}, \vec{l})}$ . Based on equations (4.24), (4.25), (4.26) and (4.27) it is possible to reduce the dynamics of our two sublattice magnetisation system in the exchange limit  $|\vec{n}| \ll |\vec{l}|$  to the form below [128, 130, 131]:

$$\dot{\vec{l}} = \gamma \vec{H}_{\text{eff}}^n \times \vec{l}, \quad (4.28)$$

$$\dot{\vec{n}} = \left( \gamma \vec{H}_{\text{eff}}^l - \lambda \dot{\vec{l}} \right) \times \vec{l}. \quad (4.29)$$

In Appendix B.1, we detail the calculations needed to arrive at Eqs. (4.28), (4.29). Writing the explicit form  $\vec{H}_{\text{eff}}^n = A \vec{n}$  in equation (4.28), it can be seen the effective magnetisation vector  $\vec{n}$  plays only a *slave variable* role which we can ultimately express as a function of  $\vec{l}$  in (4.29). Hence, the system of equations (4.28), (4.29) can be rewritten solely in terms of the Néel order parameter  $\vec{l}$  [126, 128, 129]:

$$\vec{l} \times \left[ \partial_x^2 \vec{l} - \frac{1}{v_m^2} \ddot{\vec{l}} - \frac{4}{a} \frac{\partial \mathcal{E}_{\text{ani}}}{\partial \vec{l}} - \vec{h}_{\text{opt}} - \eta \dot{\vec{l}} \right] = 0. \quad (4.30)$$

The constant  $v_m$  denotes the effective *speed of light* of the medium defined as  $v_m = \sqrt{aA}/(4\hbar) = 43.39$  km/s, the term  $\vec{h}_{\text{opt}} = \frac{8\gamma\hbar}{a} \vec{H}_{\text{opt}}$  represents the reduced opto-magnetic field arising due to the IFE, while the constant  $\eta = \frac{8\lambda\hbar}{a}$  encodes the strength of the dissipations.

To simplify the description of the in-plane, Néel vector dynamics, we consider the spherical coordinates:

$$\vec{l} \equiv \vec{u}_r = \cos \varphi \vec{u}_x + \sin \varphi \vec{u}_y, \quad (4.31)$$

$$\vec{u}_\varphi = -\sin \varphi \vec{u}_x + \cos \varphi \vec{u}_y, \quad (4.32)$$

$$\vec{u}_\theta = -\vec{u}_z. \quad (4.33)$$

This way equation (4.30) can be reduced to the familiar SG-like equation below:

$$\partial_x^2 \varphi - \frac{1}{v_m^2} \ddot{\varphi} - \frac{1}{4\Delta_0^2} \sin 4\varphi - h_{\text{opt}} \sin(2\varphi) - \eta \dot{\varphi} = 0. \quad (4.34)$$

Here, the parameter  $\Delta_0$  represents the domain wall width at rest which evaluates to:  $\Delta_0 = \sqrt{a/(8K_{4||})} = 50.8$  nm. The anisotropy contributions represented by the  $K_{2\perp}$  and  $K_{4\perp}$  cancel because the Néel vector  $\vec{l}$  does not project along the Oz direction in our in-plane dynamics approximation. We underline the  $K_{4||}$  anisotropy term in (4.1) is defined with respect to the diagonal directions [110] and [1̄10]. For ease of calculation in the analytical model presented here, we perform a 45° in-plane rotation such that the easy-axes point along the Ox and Oy cartesian directions instead. For this reason, the angular variation of the optical torque acting on the Néel vector  $\vec{l}$  also needs to be adjusted here to  $\propto \sin(2\varphi)$  compared to the expression given in (4.7). In a more clear picture,  $\vec{h}_{\text{opt}}$  is thus described by:

$$\vec{h}_{\text{opt}} = \frac{8\gamma\hbar}{a} \vec{H}_{\text{opt}} = \frac{8\gamma\hbar}{a} \vec{T}_{\text{opt}}^l \times \vec{l} = -\frac{8\gamma\hbar A \sin(2\varphi)}{a} \vec{u}_\theta \times \vec{u}_r = -h_{\text{opt}} \vec{u}_\phi l, \quad (4.35)$$

where the magnitude  $H_{\text{opt}}$  is obtained from equation (4.8).

In the next section we will discuss the solution to the SG-like equation in (4.34)

and the associated special relativity signatures —characteristic of AFM DW dynamics —revealed in a comparison between theoretical predictions and ASD simulations.

## 4.5 Special relativity signatures in antiferromagnetic domain-wall kinematics

In broad terms, DW textures belong to a class of non-linear objects called *solitons*, which represent spatially localised solutions in classical field theories with non-trivial vacuum topology, with or without inclusion of relativistic effects [299]. Solitons are typically characterised by a non-vanishing energy density in the long time limit, steady-state dynamics and stability under perturbation which protects their morphology, in some cases also in the eventuality of soliton-soliton collisions [300]. In practice however, the soliton terminology may be extended to numerous other solutions of non-linear differential equations which may not necessarily satisfy all the properties discussed above [291]. Depending on the spatial dimensions and topology of the problem, magnetic soliton-like textures may be identified as kinks (equivalent to one-dimensional DWs), vortices, skyrmions, magnon droplets and so forth [301].

AFM DWs are an extensively studied category of relativistic solitons, which were discussed both in 90° and 180° wall geometries for different anisotropy contributions or external field configurations [126, 128, 129, 288–290, 294, 295]. In the recent years marked by a migration towards AFM-based spintronics, analytical models of two-sublattice magnetisation systems resurfaced particularly in relationship to AFM DW dynamics driven by electrically-induced NSOT [123, 124]. Here, we show the laser-induced dynamics of our 90° wall also display the typical special relativity signatures in AFMs, manifesting through wall-width contraction as the propagation velocity approaches the magnonic barrier as seen in Figure 4.3. This is revealed in the ASD simulations by applying a LOT of increasing strengths which allows us to access a steady-state DW motion regime. To compare the numerical results we will introduce here the analytical predictions which arise from the two-sublattice,  $\sigma$ -like model described in the previous section. In a steady-state motion regime, when the optical excitation counterbalances the dissipation, expression (4.34) takes the shape of a double SG equation which admits the following solution corresponding to a 90° DW profile:

$$\varphi(x, t) = \arctan \left[ e^{(x-vt)/\Delta(v)} \right]. \quad (4.36)$$

The equilibrium between the damping and the field-like term induced by the optical excitation ensures the Lorentz invariance of the dynamical equation (4.34) and yields the velocity-dependent wall width:

$$\Delta(v) = \Delta_0 \beta(v) = \Delta_0 \sqrt{1 - \frac{v^2}{v_m^2}} \quad (4.37)$$

Here  $\beta(v)$  stands for the reciprocal Lorentz factor and  $v$  is the steady-state velocity of the wall. Equating the last two terms in (4.34), we can obtain the following analytical expression for  $v$ :

$$v = \frac{v_m}{\sqrt{1 + (v_m/v_0)^2}}, \quad (4.38)$$

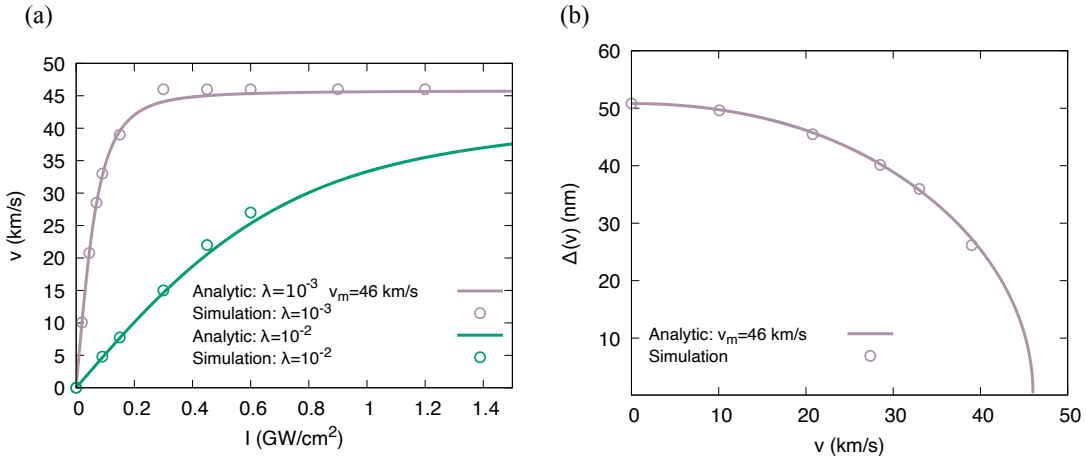


FIGURE 4.3: Comparison between the numerical steady-state 90° DW dynamics and the predictions given by the SG theory: (a) Velocity saturation as a function of the laser intensity for two distinct damping parameters:  $\lambda = 10^{-3}$  and  $\lambda = 10^{-2}$ . (b) Contraction of the DW width as a function of the propagation velocity. The comparison matches well below the magnonic barrier. In particular, theory and calculations yield the same wall width at rest (up to two decimals):  $\Delta_0 = 50.82$  nm. The numerical results overestimate the maximum propagating velocity to a value of 46 km/s compared to the analytical prediction of 43.39 km/s. Thus, the  $v_m$  constant is adjusted to the former value in subplots (a) and (b) such that the analytical curves fit the numerical results.

where  $v_0 = 2h_{\text{opt}}\Delta_0/\eta$  characterises the low-intensity, linear regime  $v(I)$  which resembles the well-known result of the FM DW theory below the Walker breakdown threshold [119, 302]. Interestingly, the relationship obtained for  $v_0$  contains an extra factor of 2 compared to the expression one would arrive at in the analytical treatment of 180° AFM DWs as in the study of Ref. [131]. This underlines in conjunction with the larger wall width at rest  $\Delta_0$  a higher mobility of 90° DWs in Mn<sub>2</sub>Au compared to their 180° counterpart. Unfortunately, as we will see in the upcoming section, a direct comparison of laser-induced dynamics of the two distinct wall geometries is impossible due to the spatial symmetry of the LOT given in Eq. (4.7).

As seen in Fig. 4.3 the results of ASD simulations compare well with the theoretically predicted behaviour described by the analytic expressions (4.37) and (4.38), in particular below the magnonic barrier. In the case of AFM DW dynamics, a single SW mode with group velocity  $v_g < v$  may be observed lagging behind during the motion of the wall [303, 304]—seen also in our simulations as for example in Fig. 4.5(a). This kinematic particularity is however not captured within the non-linear  $\sigma$  model. As previously discussed by Yang *et al.* [303], this lagging SW excitation may be responsible for a broadening of the DW width and a corresponding increase of its propagation velocity beyond the expected theoretical result of the SG theory [303]. Although not visually described here, we also have to take into account the effect of the optical torque symmetry given in Eq. (4.7). Nearing the supermagnonic limit the  $\vec{T}_{\text{opt}}^l$  term exhibits a stronger coupling to the lagging SW excitation and thus can introduce an additional factor in the small discrepancy between theory and simulations. Thus, to better fit the numerical results in subplot (a) of Figure 4.3 making use of equation (4.38), we need to adjust the  $v_m$  parameter to 46 km/s. In turn, the DW width at rest matches the theoretically predicted value up to two decimals.

## 4.6 Optical torque driving mechanism: a comparison between 90° and 180° domain-walls

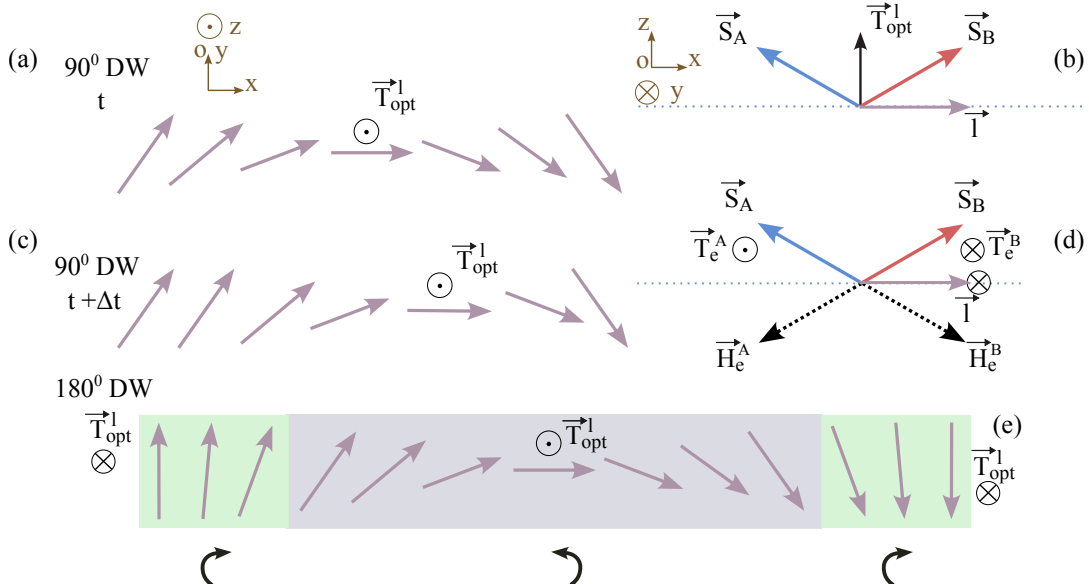


FIGURE 4.4: At a given time  $t$ , the LOT acting along  $Oz$  will give rise to an OOP canting of the magnetic sublattices  $\vec{S}_A, \vec{S}_B$  as suggested by subplots (a-b). Under the strong AFM coupling, large exchange fields  $\vec{H}_e^A, \vec{H}_e^B$  will torque the bipartite system such that the Néel vector will rotate counter clockwise in the  $Oxy$  plane, promoting the displacement of the 90° DW in the subsequent time step  $t + \Delta t$  (c-d). The displacement of an 180° DW under the same optical torque symmetry is not allowed. In such a geometry (see subplot e),  $\vec{T}_{\text{opt}}^l$  changes sign twice, such that the boundaries (green shaded) and wall region (purple shaded) will tend to rotate in opposite directions, leading to expansion/contraction of the DW, but no overall displacement. In the 90° configuration, the optical torque preserves the same sign within the boundaries of the wall such that a preferential direction of motion can be set.

To understand how the LOT introduced in equation (4.7) leads to the displacement of a 90° DW, let us turn our attention to Figure 4.4. In subplot (a) we schematically represent the top view of the Néel configuration across our track at a given moment of time  $t$  during the laser pulse excitation. Focusing on the atomic site at which  $\vec{l}$  lies parallel to the  $Ox$  direction ( $\varphi = 0$ ), we can appreciate the appearance of a LOT canting the magnetic sublattices  $\vec{S}_A, \vec{S}_B$  towards  $Oz$ , as graphically detailed in (b). Under the strong AFM coupling, local exchange fields  $\vec{H}_e^A, \vec{H}_e^B$  will torque the bipartite system such that the Néel vector will rotate counter clockwise in the  $Oxy$  plane, driving the motion of the 90° DW in the subsequent time step  $t + \Delta t$ , as seen in (c) and (d).

The  $\cos(2\varphi)$  spatial variation of the  $\vec{T}_{\text{opt}}^l$  term hinders the possibility to drive dynamics in an 180° DW configuration. The key factor which enables the 90° displacement with LOT is that it acts along the same direction (parallel or antiparallel to  $Oz$ ) at all the atomic sites within the boundaries of the wall such that a preferential DW sense of motion can be established. This resembles the NSOT-driven dynamics in the 180° DW geometry [123, 124]: the NSOT symmetry—with the torque proportional to  $\cos(\varphi)$ —leads to zero torque at the boundaries of the 180° configuration and preserves the same sign torque across the transition region between domains. Contrarily, LOT changes sign twice in an 180° geometry such that the boundaries (green shaded) and the wall region (purple shaded) tend to rotate

in opposite directions (clockwise and counter-clockwise, respectively) leading to an expansion/contraction of the DW texture but no overall displacement, as suggested graphically in subplot (e) of Figure 4.4. Direct ASD simulations have confirmed that  $90^\circ$  DWs are efficiently moved by LOT and that  $180^\circ$  DWs under its action only contract or expand. A second out-of-plane (OOP) optical torque labeled tensor 4 in Ref. [162] and in Table 4.2 is predicted to arise for light polarised either along  $Ox$  or  $Oy$ , given an in-plane Néel vector. This term is proportional to  $-\sin(2\varphi)\cos(2\psi)$ , which changes sign across the  $90^\circ$  wall due to the  $\sin(2\varphi)$  angular variation and thus cannot move it. Additionally, for  $\psi = 45^\circ$  which corresponds to the laser geometry in Figure 4.1, this contribution is zero. At the same time, the combined effect of tensors 4 and 24 can efficiently switch the AFM domains [281]. The two other in-plane torques, labeled 3 and 9 arise for  $\vec{E}$  polarised in the  $Oxz$  or  $Oyz$  planes. However, these torque components cannot take advantage of the exchange enhanced dynamics discussed in Figure 4.4. This comes as a result of the large  $K_{2\perp}$  anisotropy which competes against any OOP AFM torques arising due to the optical canting of the individual sublattices in the  $Oxy$  plane.

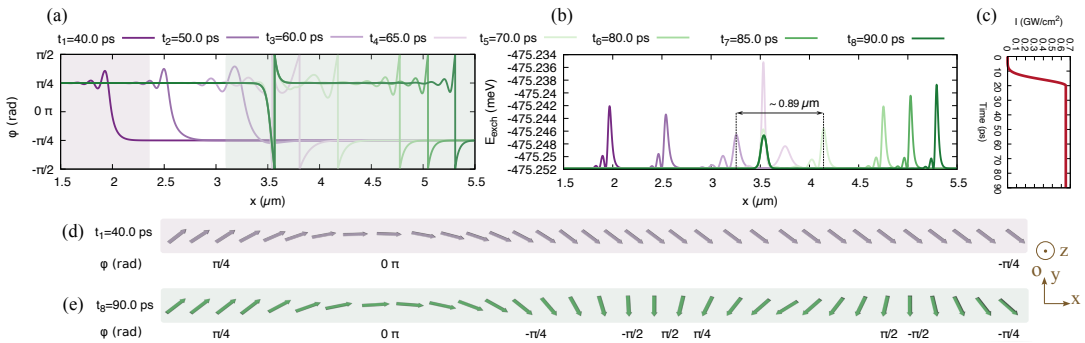


FIGURE 4.5: Proliferation event in the supermagnonic regime. (a) Time-dependent azimuthal angle  $\varphi$  along the track during the  $90^\circ$  DW displacement. Time snapshots  $t_1$ ,  $t_2$  and  $t_3$  showcase a gradual wall width broadening and a corresponding decrease in the exchange energy penalty  $E_{\text{exc}}$  (b) under the influence of the lagging SW mode. A subsequent rebound contraction process (and substantial increase of  $E_{\text{exc}}$ ) takes place due to the competition between the exchange and anisotropy energies, leading to additional oscillatory patterns at the front of the propagating wall, which will result into the nucleation of an additional magnetic texture as evidenced by  $t_4$  and  $t_5$ . The initially moving DW morphs into a static magnetic pattern pinned around the  $x = 3.5 \mu\text{m}$  mark, while the surplus relativistic energy is invested towards pushing ahead the novel spin structure. The energy transfer from the parent to the child magnetic texture takes place with an average velocity approximately equal to  $89 \text{ km/s}$ , extracted by comparing snapshots  $t_3$  and  $t_5$ . Subplots (a) and (b) share the time legend. (c) Optical excitation protocol with peak laser intensity of  $I = 0.65 \text{ GW/cm}^2$ . (d-e) In-plane rotation of the Néel vector corresponding to the purple and green shaded regions in (a), at  $t_1 = 40 \text{ ps}$  and  $t_8 = 90 \text{ ps}$  respectively. The latter schematics are scaled in width to fit identical plot regions.

## 4.7 Magnetic texture proliferation nearing the supermagnonic limit

An AFM DW driven by NSOT near the magnonic barrier can enter a highly non-linear regime, leading to the proliferation of additional magnetic textures, breaking

of the Lorentz invariance, and allowing a supermagnonic motion [124]. As presented in Figure 4.5, a similar effect can occur in our optical excitation protocol for a sufficiently large pulse intensity. From an energetic point of view, the LOT "Zeeman-like" energy ( $\vec{S}_i \cdot \vec{H}_{\text{opt}}^i$ ) always remains zero in our case, as the geometry presented in equation (4.8) maintains  $\vec{H}_{\text{opt}}^i$  always perpendicular to the local spin direction  $\vec{S}_i$  (note that the torque is not zero). The question is, therefore, *where does the energy required for the nucleation of additional magnetisation textures arise from?* In subplot (a) of Figure 4.5, we represent the azimuthal angle  $\varphi$  along the track during a 90° wall displacement excited via a half-Gaussian, laser pulse of peak intensity  $I = 0.65 \text{ GW/cm}^2$  (see laser profile in subplot c). Time-steps  $t_1, t_2, t_3$  show the characteristic low-frequency SW, lagging behind and broadening the width of the 90° DW as it is pushed beyond the magnonic barrier. A gradual, corresponding decrease in the exchange energy is evidenced by subplot (b) of the same Figure. Due to the competition between the anisotropy and exchange energies, this broadening cannot indefinitely take place, forcing a rebound process characterised by a contraction of the wall. Under the strong inertial effects intrinsic to AFM dynamics, a drastic reduction of the DW width parameter can be observed in between time-steps  $t_3$  and  $t_4$  in parallel with a large increase in the exchange energy. This continuous deformation leads to the appearance of oscillatory patterns at the front of the propagating wall, which on a ps time-scale invest part of the relativistic energy carried by the DW towards the nucleation of an additional magnetisation texture, as evidenced at  $t_4$  and  $t_5$ . Unlike the 180° NSOT-driven DW case [124], the newly formed pattern does not follow the geometry of the parent texture as further evidenced by subplots (d) and (e). At  $t_6, t_7$  and  $t_8$  it can be seen how the initial spin structure has morphed into a static magnetisation texture pinned around the  $x = 3.5 \text{ } \mu\text{m}$  mark, while its surplus, relativistic energy is invested towards pushing ahead a novel spin structure. Just like the motion of the 90° DW before the nucleation event, a low frequency SW can be observed lagging behind the newly nucleated texture. The physical origin of the effect relies on the rapid conversion of relativistic energy from a propagating DW near the magnonic barrier into new stable magnetisation textures. Comparing snapshots  $t_3$  and  $t_5$ , we estimate the energy transfer across the track from the parent to the child magnetic texture takes place with an average velocity of 89 km/s (0.89  $\mu\text{m}$  travelled in 10 ps), largely exceeding the speed limit of a steady state soliton, also called the "effective speed of light". This breakdown of the Lorentz invariance and soliton-like behavior occurs due to dynamical changes of the DW shape which result in the creation of new textures with repulsive interaction leading to acceleration. Interestingly, these results can find similarities with dislocation dynamics. As shown in [305, 306], dislocations may enter a super-sonic regime surpassing the sonic barrier, the underlying reason for this being the generation of secondary kinks (topological defects) via the so-called "mother-daughter" kink nucleation.

## 4.8 Spin texture chirality analysis in optically driven 90° wall geometries

Owing to the spatial symmetry imposed by the  $K_{4||}$  tetragonal anisotropy, the 90° DW profile associated with the ground-state energy in the model Hamiltonian of Eq. (4.1) presents an eight-fold degeneracy. The corresponding spin arrangements can be obtained mapping the local Néel vector orientation in the track along the unit circle given in Figure 4.6(a). Since the DW boundary spins must be separated by an angle of  $\pm\pi/2$ , tracing the unit circle reveals four distinct 90° wall arrangements

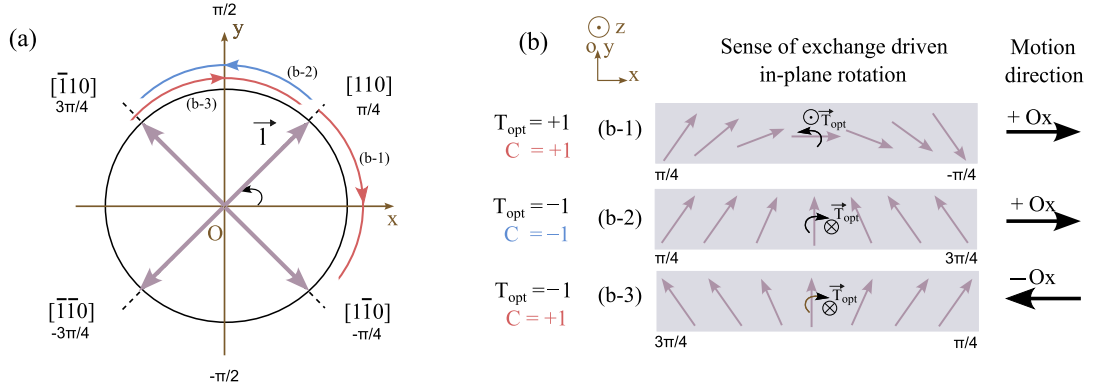


FIGURE 4.6: Analysis of DW motion direction with respect to DW chirality. (a) Mapping the in-plane Néel vector orientation in the magnetic track along the unit circle. We display the four possible 90° DW boundaries corresponding to the  $K_{4||}$  easy directions. Taking as reference the Néel vector parallel to the [110] diagonal, we can obtain two DW geometries with right and left hand side chirality (the sense of rotation and the colors of the red/blue arrows in (a) represent the right/left hand-side chirality) labeled (b-1) and (b-2) respectively. The corresponding spin configurations are displayed in subplot (b). ASD simulations reveal these two DWs displace in the same direction  $+Ox$  because the hardness of the in-plane Néel vector rotation opposes the chirality of the wall in both cases. Distinctly, the (b-3) wall geometry is driven towards  $-Ox$  because the in plane spin reorientation matches the chirality of the wall.

in both the clock-wise (CW) and counter clock-wise (CCW) directions. ASD simulations reveal four of these configurations will displace along  $+Ox$  while the other four in the opposite  $-Ox$  direction. The direction of motion depends on the sign of the optical torque relative to the chirality of the wall. We assign  $C = +1$  for right-hand side DW chirality (clock-wise spin rotation) and  $C = -1$  for left-hand side DW chirality (counter clock-wise spin rotation). Since the optical torque maintains its sign across the DW configuration, we can distinguish two situations, positive and negative optical torque  $T_{\text{opt}} = \pm 1$ . If the product  $T_{\text{opt}}C$  is positive, the DW will displace towards  $+Ox$ , otherwise the motion will take place in the opposite direction.

In Figure 4.6 we exemplify this behaviour for three distinct DW configurations. Taking as a reference the Néel vector parallel to the [110] direction in subplot (a), we construct two 90° DW configurations following a right or left-hand side rotation along the unit circle. The corresponding spin arrangements labeled (b-1) and (b-2) can be observed in subplot (b) of Figure 4.6. Both  $T_{\text{opt}}$  and  $C$  change their sign in between the two geometries, hence the product  $T_{\text{opt}}C$  remains positive and the DW displacement direction is preserved. This can be understood in light of the strong in-plane AFM torque excited in the two-step driving mechanism discussed in Figure 4.4. Depending on the sign of  $T_{\text{opt}}$ , the resulting in-plane rotation of the Néel vector will take place in opposite directions.  $T_{\text{opt}} = +1$  gives rise to counter clock-wise rotation, while  $T_{\text{opt}} = -1$  promotes clock-wise rotation. To maintain the DW direction of motion, the hardness of this in-plane rotation must oppose the chirality of the wall. Therefore the  $T_{\text{opt}}$  change of sign in between configurations (b-1) and (b-2) matches this requirement and thus preserves the direction of motion towards  $+Ox$ . The situation changes if we compare the (b-2) and (b-3) 90° DW profiles. Here the  $T_{\text{opt}}C$  product changes sign which promotes displacement in opposite directions as confirmed by our ASD simulations. Taking as reference any other 90° DW configuration along the unit circle in Figure 4.6(a), we observe the same behaviour.

It is also worth pointing out here that a 90° rotation of the  $\vec{E}$ -vector to the [1̄10]

( $\psi = -45^\circ$ ) direction changes the sign of the LOT according to equation 4.7 and consequently the direction of motion. In turn, a 180° rotation to [1̄10] ( $\psi = -135^\circ$ ) preserves the positive sign of the torque and the motion direction towards +Ox given  $C = +1$ .

## 4.9 Driving periodic ultra-fast domain-wall contraction and expansion

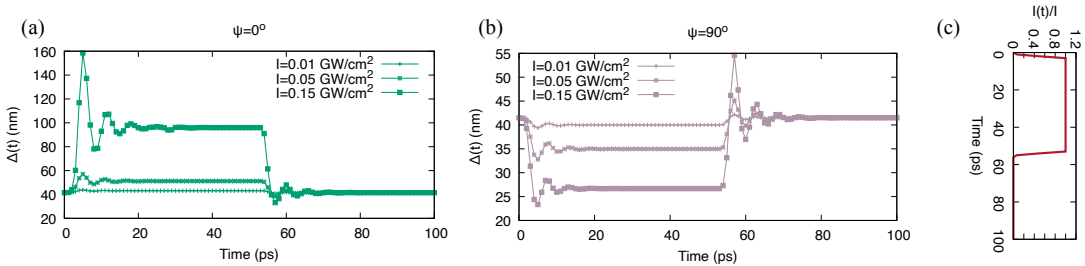


FIGURE 4.7: Periodic ultra-fast DW contraction and expansion. Subplots (a) and (b) display the time variation of the DW width for increasing laser pulse intensity with the  $\vec{E}$ -field vector polarised along [100] ( $\psi = 0^\circ$ ) and [010] ( $\psi = 90^\circ$ ) respectively. It is however important to underline that in this geometry, tensor 24 in Table 4.2 becomes zero but tensor 4 is maximal with respect to  $\vec{E}$  and the LOT symmetry is determined by the  $\sin(2\varphi)$  function here. The DW in these situations is pinned and no overall displacement along the track is observed. Subplot (c) displays the laser intensity as a function of time normalised to the peak intensity. The LOT magnitude is proportional to the laser intensity as discussed in section 4.3.

Finally, we would like to point out another interesting effect obtained under a rotation of the  $\vec{E}$ -field laser polarisation vector. So far, the LOT was calculated with the assumption that the  $\psi$  azimuthal angle is 45°, or in other words the electric field  $\vec{E}$  was aligned parallel to the [110] direction. Interestingly, rotating the  $\psi$  angle to 0° or 90° which corresponds to  $\vec{E} \parallel [100]$  and  $\vec{E} \parallel [010]$  respectively, leads to periodic DW contraction and expansion on the ultra-fast time-scale. It is however important to underline that in this geometry, tensor 24 in Table 4.2 becomes zero but tensor 4 is maximal with respect to  $\vec{E}$  and the LOT symmetry is determined by the  $\sin(2\varphi)$  function here. In Figure 4.7 we display the time variation of the DW width as a function of increasing laser pulse intensity for the two distinct  $\vec{E}$ -field geometries, demonstrating periodic contraction and expansion of the wall on the ultra-fast time scale. Notably, the amplitude of the oscillations is proportional to the laser pulse intensity and the time-dependent signal is dephased in between the two laser polarisations leading first to expansion followed by contraction in the  $\psi = 0^\circ$  case whilst the situation is reversed at  $\psi = 90^\circ$ . Since the exchange contributions to the total energy of the DW are prevalent over their anisotropic counterparts, naturally the expansion processes of the wall are enhanced in amplitude compared to the observed contraction. It would be interesting to explore whether this periodic contraction-expansion can be used for a potential application in AFM domain wall-based nano-oscillators [307, 308].

## 4.10 Conclusions and discussions

In conclusion, ASD simulations revealed the possibility to drive a 90° AFM DW under the so-called LOT mechanism arising due to the non-thermal IFE. Interestingly, unlike the NSOT mechanism, this excitation protocol does not allow the motion of 180° DWs. Typical experiments of laser-induced DW dynamics in FMs make use of fluences in the range of a few mJ/cm<sup>2</sup> which amount to intensities normally in the 1 and 10 GW/cm<sup>2</sup> interval [42, 53]. In comparison, we predict 90° DW kinematics up to the supermagnonic limit ( $v = 46$  km/s) by single pulse excitation below 0.3 GW/cm<sup>2</sup>. Although heating effects are expected due to the metallic nature of Mn<sub>2</sub>Au, we estimate via the TTM the ultrafast picosecond phonon heating timescale with temperature going back to the room one at a timescale below 1 ns (see Appendix B.2). A particularly important advantage of LOT compared to the NSOT mechanism is its reliance on laser excitations in the visible spectrum routinely excited in ultra-fast experiments in contrast with the much more challenging THz setups.

In the vicinity of the magnonic limit, the kinematics reveal the appearance of proliferation events in which part of the propagating DW's energy is invested into the nucleation of novel magnetic textures. Manipulating highly non-linear dynamics in magnetic systems may play an important role in the development of future neuromorphic reservoir computing archetypes [102, 111, 272, 309]. We envision thus a combined, opto-electronic experimental scheme, towards the realisation of a multiple-node reservoir. Driven by an optical input, fast and periodic nucleation events could be manipulated in an AFM DW fabric [97], whereas based on the anisotropic magnetoresistive effect [107], an output electrical signal may be correlated to changes in the magnetic texture, thus posing an interest for pattern recognition and prediction applications.

Evidently, in experiments the DW dynamics may be influenced by the presence of defects, magnetostriction effects, multi-domain states etc and all pose interesting fundamental questions which deserve to be analysed. A particularly interesting question is the influence of acoustic waves and the spin-phonon coupling on the DW velocity. Previously, in orthoferrites crystals certain velocity anomalies with respect to the strength of the excitation were attributed to magnetoelastic contributions [310]. Lastly, the diversity and natural abundance of antiferromagnetically ordered materials calls for an exploration of similar optical torque symmetries in other crystal structures, as well the natural extension towards the emergent landscape of altermagnets [311].



## Chapter 5

# Domain nucleation and domain-wall kinematics in the all-optical switching of a Tb/Co bilayer

Chapters 3 and 4 addressed distinct non-thermal opto-magnetic coupling routes towards the manipulation of specific FM and AFM DW configurations at the ultra-fast time-scale. However, as we saw in Chapter 1, laser thermal energy alone can also trigger demagnetisation, precession or even switching of the magnetic order parameter, the latter typically referred to in the literature as helicity-independent, all-optical switching (HI-AOS). In relation to this final point, DWs and MDs have long been investigated from a secondary perspective in the context of AOS experiments, where laser-driven nucleation of a single or multi-domain states as well as domain-wall kinematics have been recorded.

A novel HI-AOS mechanism has recently been experimentally demonstrated in several Tb or Dy-based FIM multilayers, bilayers or trilayer systems but proper theoretical attempts to discuss the origin and characteristics of the observed dynamics have been lacking. This chapter aims to circumvent this problem and provide an initial corresponding model in a test Tb/Co bilayer. The following main features observed experimentally need to be recovered (see also subplots b, d and f in Figure 5.1): (a) the energy threshold to switching is independent of the pulse duration up to several ps; (b) the laser excited area presents a concentric ring domain pattern; (c) the magnetisation exhibits a slow precessional based recovery process. The results presented onwards represent a collaboration with peer colleagues at SPINTEC within the COMRAD ITN Marie-Curie consortium, in particular we would like to mention David Salomoni, Liliana Buda-Prejbeanu and Lucian Prejbeanu as well as Ricardo Sousa with whom we had several private discussions related to their experimental work.

### 5.1 Introduction

Ultrashort laser pulses can manipulate the magnetic order at unprecedented speeds and for small energy consumption levels, supporting the migration towards the next generation of magnetic memory and logic devices. The laser thermal energy alone was shown capable of inducing HI-AOS for single pulse excitation, predominantly in Gd-based ferrimagnetic alloys and multi-layers [27–29]. In these cases, switching is of thermal origin, it is driven by the inter-sublattice exchange coupling and

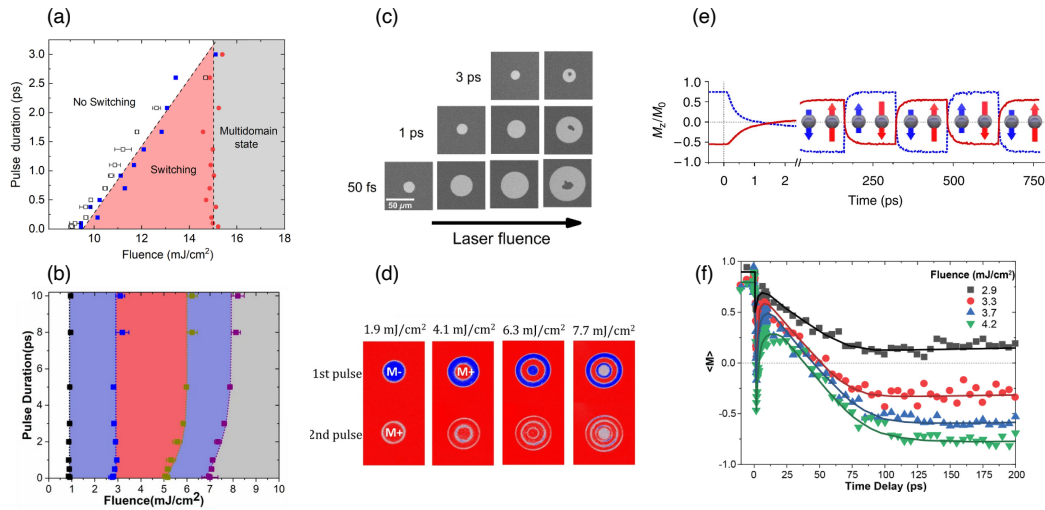


FIGURE 5.1: Comparison between (top) HI-AOS characteristic to Gd-based systems (alloys or multilayers) and (bottom) the novel, precessional-like HI-AOS observed in multilayers containing heavier rare-earths such as Tb or Dy: (a-b) laser fluence and pulse duration requirements for AOS, (c-d) examples of domain-patterns nucleated in the laser-excited regions and (e-f) characteristic out-of-plane magnetisation dynamics during AOS. Subplots (a and c) were extracted from the PhD thesis in [43] under the CC BY licence but can also be found in Ref. [30] while (e) was extracted from [27] and reproduced with permission from Springer Nature. Subplots (b,d and f) have been extracted from the PhD thesis of [44] under the CC BY licence but can also be found in Refs. [32, 34].

it can occur both for fs and ps laser pulse excitation —see example of (experimental) switching diagram, switched domain patterns and (calculated) AOS dynamics of GdFeCo alloy shown in Figure 5.1(a, c and e). However, the reversal requires a careful adjustment of the laser energy input in relation to the duration of the pulse —seen in Figure 5.1(a)—which undermines its technological potential. In contrast, the novel HI-AOS mechanism discussed in Refs. [32–34] is practically independent of the pulse duration at a constant fluence and in a wide fs-ps range (compare subplots (a) and (b) in Figure 5.1) but is characterised by slower reversal dynamics driven by incoherent magnetisation processes —see comparison of Figures 5.1(c and d) and 5.1(e and f) respectively. The switching has been explained to occur due to an in-plane reorientation of the magnetisation under a temperature induced reduction of the perpendicular anisotropy at the interface and the presence of a local distribution of easy-axes directions which could favor a slow, in-plane precession [32]. Here, we provide an initial high-temperature micromagnetic model to test this hypothesis which seems to explain up to some level the experimental observations, choosing as reference system a Tb/Co bilayer structure. So far, an explanation for this AOS mechanism was attempted only in a simpler macrospin approach in Ref. [33] which obviously cannot capture incoherent magnetisation processes such as domain nucleation and DW displacement as well as it also completely disregards the two-sublattice dynamics and the role of the interlayer AFM coupling. We construct our model based on the high-temperature micromagnetic framework of the LLB equation [198, 208, 209]. While the switching kinematics along with the nucleation and evolution of the ring-domain patterns are investigated in a large-scale system, we employ a simpler two-macrospin (TMspin) approach to evaluate the equilibrium properties of the bilayer such as the net magnetisation variation with temperature or interlayer coupling strength. The main role of the TMspin model is to parametrise

the large-scale simulations. In the following pages, we discuss the shortcomings, achievements, and potential improvements of the model in relation to available experimental evidence [32, 34].

## 5.2 Studying a Tb/Co bilayer in a two macrospin picture

The TMspin model described here was initially developed to account in a simple picture for several equilibrium properties of the Tb/Co films experimentally studied by our SPINTEC collaborators. Although non-coherent magnetisation processes cannot be captured, the results presented in this section calibrate the material parameters and support the implementation of the large-scale micromagnetic model described in section 5.3. One of the main advantages of the TMspin approach is the small run-time required per simulation, useful for large parameter sweeps such as for example in the calculation of hysteresis cycles or switching diagrams. The next subsections cover first the LLB formalism supporting the backbone of our model. We then discuss the equilibrium magnetisation as a function of temperature and strength of the interlayer coupling, as well as identify the magnetisation compensation point in relation to the experimental results discussed in Refs. [32, 34, 312, 313]. In addition, we analyse static hysteresis cycles for out-of plane and tilted field geometries as a function of the interlayer coupling with the aim of matching the experimentally measured coercivity. Finally, we make an attempt to obtain laser-induced switching in this simplified TMspin model.

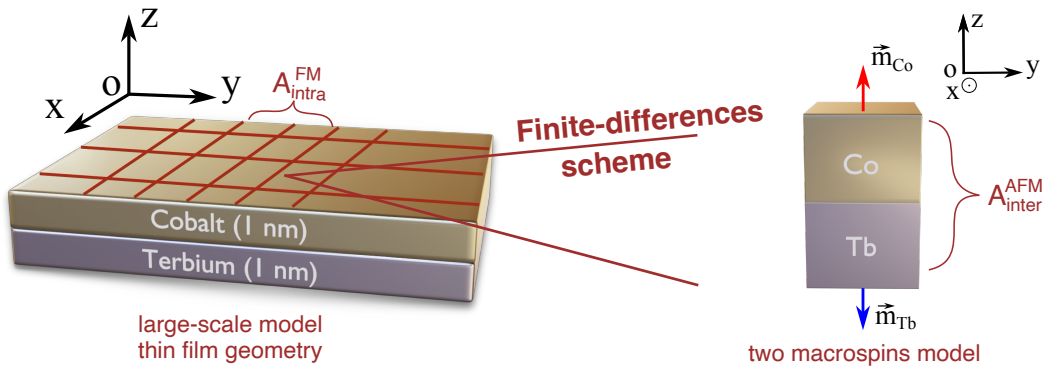


FIGURE 5.2: Sketch of the Tb/Co models discussed in this Chapter. In the two macrospin approach (right-hand side) we employ a system of pair ferromagnetic LLB equations to describe the dynamics of the reduced magnetisation vectors  $\vec{m}_{\text{Co}}$  and  $\vec{m}_{\text{Tb}}$  within each layer (5.1). The AFM coupling between the two macrospins is achieved via a phenomenological exchange field proportional to the free parameter  $A_{\text{inter}}^{\text{AFM}}$  as shown in equation (5.4). The primary role of this simple model is to approximate unknown physical parameters such as the strength of the exchange coupling at the interface or the zero Kelvin anisotropy constant based on several experimental guidelines. These parameters will serve as input in the large-scale micromagnetic model of the Tb/Co thin films (left-hand side). In addition to considering  $A_{\text{inter}}^{\text{AFM}}$  between macrospins of opposite sublattices, in between cells corresponding to the same layer we take into account a micromagnetic exchange coupling of ferromagnetic origin and proportional to  $A_{\text{intra}}^{\text{FM}}$  for both Co and Tb. In the large scale model we include also the presence of the demagnetising field whereas in the simple two macrospin picture we assume a shape factor correction in the MCA contribution only.

### 5.2.1 Basis of the TMspin model

We consider a system of two macrospin vectors associated with a Tb and a Co layer respectively (right hand side plot in Figure 5.2), whose individual magnetisation dynamics are described by classic, ferromagnetic LLB equations [198, 208] in which an AFM coupling is introduced in the effective field acting upon each macrospin:

$$\frac{d\vec{m}_v}{dt} = -\gamma\vec{m}_v \times \vec{H}_{\text{eff}}^v + \gamma\alpha_{||}^v \frac{(\vec{m}_v \cdot \vec{H}_{\text{eff}}^v)\vec{m}_v}{m_v^2} - \gamma\alpha_{\perp}^v \frac{\vec{m}_v \times (\vec{m}_v \times \vec{H}_{\text{eff}}^v)}{m_v^2}. \quad (5.1)$$

In expression (5.1), the  $v$  label identifies either the Tb or the Co macrospin respectively. Thus, the unit vector  $\vec{m}_v$  is defined as  $\vec{m}_v = \vec{M}_v(t, T) / M_s^v(0 \text{ K})$  with  $M_s^v(0 \text{ K})$  being the saturation magnetisation at 0 K while  $\vec{M}_v(t, T)$  is the time and temperature dependent magnetisation vector. The constant  $\gamma$  denotes the electron gyromagnetic ratio, while  $\alpha_{||}^v$  and  $\alpha_{\perp}^v$  are the dimensionless longitudinal and transverse damping parameters defined as:

$$\alpha_{||}^v = \lambda_v \frac{2T}{3T_c^v}, \quad \alpha_{\perp}^v = \lambda_v \begin{cases} \left(1 - \frac{T}{3T_c^v}\right) & T \lesssim T_c^v, \\ \frac{2T}{3T_c^v} & T \gtrsim T_c^v. \end{cases} \quad (5.2)$$

For simplicity, the microscopic damping  $\lambda_v$  is assumed identical in both layers (and set to 0.1). However,  $\alpha_{||}^v$  and  $\alpha_{\perp}^v$  are scaled in (5.2) by the individual  $T_c^v$  Curie temperatures of each sublattice. For Co we adjust the critical temperature to  $T_c^{\text{Co}} = 1228$  K [314] whilst for Tb we set  $T_c^{\text{Tb}} = 237$  K [315]. The effective field  $\vec{H}_{\text{eff}}^v$  in equation

Parameter	Terbium	Cobalt
$M_s^v(0 \text{ K})$ (kA/m)	2150 [316, 317]	1400 [253]
$K_v(0 \text{ K})$ (MJ/m <sup>3</sup> )	2.3	2.3
$T_c^v$ (K)	237 [315]	1228 [314]
$\mu_{\text{at}}^v$ ( $\mu_B$ )	9.3 [44, 315]	1.7 [44]
$A_{\text{inter}}^{\text{AFM}}$ (pJ/m)	-0.83	-0.83
$\lambda_v$ (adim.)	0.1	0.1

TABLE 5.1: Parameters employed in the two macrospin Tb/Co model. In the case of the 0 K anisotropy constants  $K_v(0 \text{ K})$  and the interlayer coupling  $A_{\text{inter}}^{\text{AFM}}$ , we tailored their values in order to match a series of experimental observations in Refs. [32, 34, 312, 313] as detailed in subsections 5.2.2 and 5.2.3. Although we choose a generic and identical microscopic damping value  $\lambda_v$  in both layers, it should be noted the macroscopic longitudinal and transverse damping terms in equation (5.2) are scaled by the individual Curie temperatures  $T_c^v$ .

(5.1) is defined as:

$$\vec{H}_{\text{eff}}^v = \vec{H}_{\text{ex}}^v + \vec{H}_{\text{ani}}^v + \begin{cases} \frac{1}{2\chi_{||}^v} \left[1 - \left(\frac{m_v}{m_e^v}\right)^2\right] \vec{m}_v & T \lesssim T_c^v, \\ -\frac{1}{\chi_{||}^v} \left[1 - \frac{3T_c^v}{5(T-T_c^v)} m_v^2\right] \vec{m}_v & T \gtrsim T_c^v, \end{cases} \quad (5.3)$$

with the first term  $\vec{H}_{\text{ex}}^v$  characterising the AFM exchange between Tb and Co,  $\vec{H}_{\text{ani}}^v$  stands for an out-of-plane MCA, while the last term encapsulates the longitudinal field  $\vec{H}_{\text{lon}}^v$ . In the next two subsections we analyse the implementation of these field terms in connection with the experimental results in Refs. [32, 34, 312, 313]. Finally,

all the parameters employed in the TMspin model can be consulted in Table 5.1, with the rationale behind their values and our assumptions being provided subsequently.

### 5.2.2 Temperature scaling of the Tb/Co magnetisation. The effect of the interlayer coupling

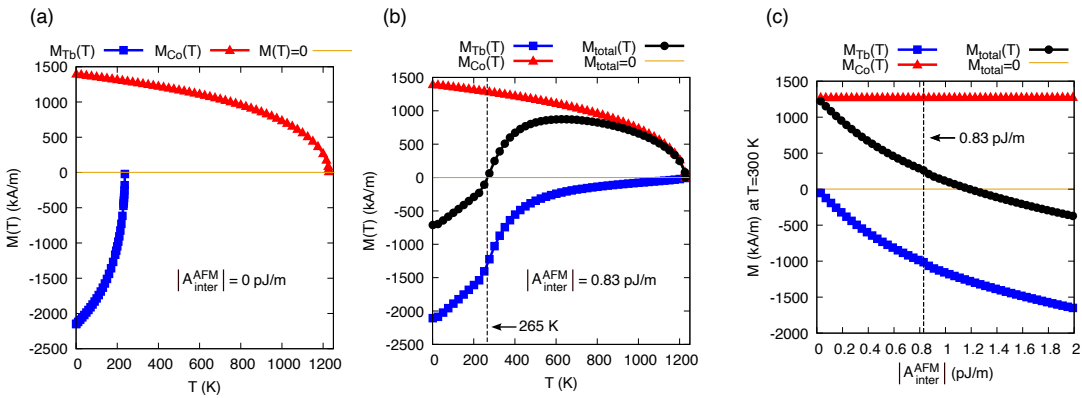


FIGURE 5.3: Scaling of the equilibrium magnetisation in the two macrospin Tb/Co model: (a)  $M(T)$  variation in the absence of any AFM coupling between the layers. (b)  $M(T)$  variation for  $|A_{\text{inter}}^{\text{AFM}}| = 0.83 \text{ pJ/m}$ . Note the magnetisation compensation point appearing at  $T_M = 265 \text{ K}$  (black dashed line) and the strong polarisation of the Tb subsystem by Co. (c) Variation of the room-temperature magnetisation  $M(300 \text{ K})$  with respect to the interlayer coupling  $A_{\text{inter}}^{\text{AFM}}$ . At  $|A_{\text{inter}}^{\text{AFM}}| = 0.83 \text{ pJ/m}$  (black dashed line) the system finds itself in a Co-dominated region ( $M_{\text{Co}} > M_{\text{Tb}}$ ), but relatively close to the magnetisation compensation point as indicated by the horizontal gold line. The Co and Tb magnetisation is displayed in red and blue respectively while the total magnetisation is given in black.

In equation (5.3),  $m_e^\nu = M_e^\nu(T)/M_s^\nu(0 \text{ K})$  represents the macrospin vector length at thermal equilibrium, obtained as solution in the MFA to the Curie-Weiss equation in the absence of the interlayer AFM coupling:  $m_e^\nu = L(\beta J_0^\nu m_e^\nu)$ , where  $L$  is the Langevin function, the parameter  $J_0^\nu = 3k_B T_c^\nu$  expresses the strength of the (FM) Heisenberg exchange coupling within each macrospin  $\nu$ , while  $\beta = 1/(k_B T)$  is a measure of the thermal bath fluctuations. In Figure 5.3(a) we display the temperature scaling of the equilibrium magnetisation  $M_\nu(T) \equiv M_e^\nu(T) = M_s^\nu(0 \text{ K})m_e^\nu$  of the layers in the absence of any AFM coupling. The 0 K saturation magnetisation of Co is kept identical to the value employed in Chapter 3:  $M_{\text{Co}}^{\text{Co}}(0 \text{ K}) = 1400 \text{ kA/m}$  [253]. In the RE case, we refer to the results presented in Ref. [316] in regards to sputtered thin film Tb structures. Depending on the amorphous or epitaxial nature of the sample, two saturation magnetisation values are reported at a temperature of 150 K: 68 emu/g and 183 emu/g respectively. Taking into account the Tb density  $\rho_{\text{Tb}} = 8.23 \text{ g/cm}^3$  (also mentioned in Ref. [316] and extracted from [318]), we obtain  $M_s^{\text{Tb}}(150 \text{ K}) = 560 \text{ kA/m}$  and  $M_s^{\text{Tb}}(150 \text{ K}) = 1506 \text{ kA/m}$  respectively. To maintain a larger saturation magnetisation at 0 K for the RE system in comparison with the TM (thus ensuring the existence of a compensation magnetisation point given the  $T_c^\nu$  of each layer) we choose the epitaxial  $M_s^{\text{Tb}}(150 \text{ K}) = 1506 \text{ kA/m}$  value. By extrapolation we obtain at 0 K an (approximate value) of  $M_s^{\text{Tb}}(0 \text{ K}) = 2150 \text{ kA/m}$ . For comparison, in bulk, single crystal Tb we have  $M_s^{\text{Tb}}(0 \text{ K}) = 2700 \text{ kA/m}$  [317]. In the presence of an interlayer coupling, Co polarizes Tb as seen in Figure 5.3(c) and modifies the temperature scaling of the magnetisation as shown in Figure 5.3(b). All the results presented in Figure 5.3 have been obtained by integration of the TMspin LLB equations in the presence or absence of this polarising effect. The  $\vec{H}_{\text{ex}}^\nu$  field in

(5.3) describes an AFM coupling between the two sublattices governed by a phenomenological coupling strength  $A_{\text{inter}}^{\text{AFM}}$  similar to the work in Refs. [319–321]:

$$\vec{H}_{\text{ex}}^\nu = \frac{A_{\text{inter}}^{\text{AFM}}}{M_s^\nu(0)l^2} \vec{m}_{\nu*}, \quad (5.4)$$

where the label  $\nu*$  identifies the opposing magnetic sublattice acting on the  $\nu$  macrospin and  $l = 2.5 \text{ \AA}$  is an ad-hoc atomic length characterising the interfacial thickness.

The strength of the exchange stiffness constant  $A_{\text{inter}}^{\text{AFM}}$  (expressed in units of J/m) was adjusted by a trial and error procedure to reproduce several experimental observations. First of all, in Ref. [34] (in Figures 1 and 7 respectively) it is shown the AOS in Tb/Co takes place for samples which at room-temperature (RT) find themselves in a so-called Cobalt-dominant magnetisation region ( $M_{\text{Co}} > M_{\text{Tb}}$ ) and relatively close to the magnetisation compensation point ( $T_M$ ), experimentally shown to be slightly below 300 K. In subplot (c) of Figure 5.3 we can see the RT variation of the Co, Tb and total magnetisation of the system as a function of the interlayer coupling  $A_{\text{inter}}^{\text{AFM}}$ . For the majority of the results presented in this Chapter and if not specified otherwise, we consider  $A_{\text{inter}}^{\text{AFM}} = -0.83 \text{ pJ/m}$  which places the Tb/Co system in a Cobalt-dominated magnetisation region at RT. Since the Curie point of isolated Tb is set at 237 K,  $M_{\text{Tb}}$  at room temperature exhibits a substantial polarisation effect due to the AFM coupling. In contrast,  $M_{\text{Co}}$  is very little affected by  $A_{\text{inter}}^{\text{AFM}}$  at this temperature, since the dominant contribution to the Co magnetisation comes from the intrinsic ferromagnetic exchange inside the macrocell. In Figure 5.3(b) we display the temperature variation of the magnetisation (Co, Tb and total) for  $A_{\text{inter}}^{\text{AFM}} = -0.83 \text{ pJ/m}$ . The dashed black line marks the magnetisation compensation point, approximately equal to  $T_M = 265 \text{ K}$ . We once again observe the large polarisation effect on the Tb sublattice: in the presence of the interlayer coupling, its ferromagnetic-paramagnetic phase transition takes place in the vicinity of the Co Curie point of 1228 K. It is also important to note the increasing trend of the net Tb/Co magnetisation above RT, in qualitative agreement with the experimental samples in Ref. [34] which display HI-AOS. For comparison we also graphically represent the temperature variation of the Tb and Co magnetisation in the absence of any AFM coupling in Figure 5.3(a). Finally, we must underline that  $A_{\text{inter}}^{\text{AFM}}$  is assumed temperature independent, a rather crude approximation but necessary in the absence of supporting literature for the investigated system. Lastly, we define here the longitudinal susceptibility in each sublattice  $\chi_{||}^\nu$  as:

$$\chi_{||}^\nu(T) = \begin{cases} \frac{\mu_{\text{at}}^\nu \beta L'}{1 - \beta J_0^\nu L'} & T \lesssim T_c^\nu, \\ \frac{\mu_{\text{at}}^\nu I_\nu'}{J_0^\nu (T - T_c^\nu)} & T \gtrsim T_c^\nu, \end{cases} \quad (5.5)$$

where  $L'$  represents the derivative of the Langevin function with respect to the argument  $x = \beta J_0^\nu m_e^\nu$  and the  $\mu_{\text{at}}^\nu$  constant denotes the sublattice atomic magnetic moment which evaluates to  $\mu_{\text{at}}^{\text{Tb}} = 9.3 \mu_B$  [315] and  $\mu_{\text{at}}^{\text{Co}} = 1.7 \mu_B$  respectively [44].

### 5.2.3 Static hysteresis cycles for in-plane and tilted external field

In the reference experimental results of [32, 34, 312, 313], the Tb/Co films under study which exhibit the HI-AOS behaviour are characterised by perpendicular magnetic ordering near RT. Thus, the anisotropy field in equation (5.3) is tailored to describe an uni-axial MCA contribution with the easy-axis set parallel to  $Oz$ :

$$\vec{H}_{\text{ani}}^{\nu} = \frac{2K_{\text{eff}}^{\nu}(T)}{M_s^{\nu}(T)} (\vec{m}_{\nu} \cdot \vec{e}). \quad (5.6)$$

For practical purposes we choose to define  $\vec{H}_{\text{ani}}^{\nu}$  in terms of the explicit easy-axis direction  $\vec{e}$  contrary to the definition based on the orthogonal plane given in (2.21). The effective anisotropy  $K_{\text{eff}}^{\nu}(T)$  takes into account a thin film shape anisotropy correction to the MCA constant  $K_{\nu}(T)$ :

$$K_{\text{eff}}^{\nu}(T) = K_{\nu}(T) - \frac{1}{2}\mu_0[M_s^{\nu}(T)]^2. \quad (5.7)$$

In the absence of the coupling term  $\vec{H}_{\text{ex}}^{\nu}$  given in (5.4), the two macrospins behave as two isolated systems and the temperature scaling of their magnetisation  $M_s^{\nu}(T)$  is determined solely by atomic exchange contributions of ferromagnetic origin (consult subplot (a) of Figure 5.3). The angular momentum transfer between the two subsystems is enabled via  $\vec{H}_{\text{ex}}^{\nu}$  and implicitly the instantaneous magnetisation vector  $\vec{m}_{\nu}$  of one sublattice can be polarised by the presence of the other (thus,  $|\vec{m}_{\nu}|$  may be larger than  $m_e^{\nu}$ ). We take this spin polarisation effect into account in the temperature scaling of the anisotropy via the relationship  $K_{\nu}(T) = K_{\nu}(0)|\vec{m}_{\nu}|^3$ , where the temperature variation of  $K_{\nu}(T)$  is set by the modulus of  $\vec{m}_{\nu}$  and not by  $m_e^{\nu}$ . The same Callen-Callen power scaling law is considered for both layers [206]. We also assume the perpendicular magnetic ordering is mostly influenced by the presence of the interface and thus  $K_{\nu}(0) = 2.3 \text{ MJ/m}^3$  is set equal in both subsystems. In the absence of a direct experimental verification, this value was chosen such that in combination with the interlayer coupling strength, we can reproduce the range of coercivity fields and qualitatively match the RT hysteresis cycles reported in Refs. [34, 312].

In Figure 5.4, we display static hysteresis loops obtained by integration of the TMspin LLB equations at RT for three applied field orientations:  $\theta_H = 2^\circ, 60^\circ$  and  $89^\circ$  (where  $\theta_H$  denotes the deviation with respect to the EA, i.e. normal to the thin film plane) in addition to varying the interlayer coupling  $A_{\text{inter}}^{\text{AFM}}$  within the Co-rich region ( $M_{\text{Co}}$  is kept larger than  $M_{\text{Tb}}$ ). First, in the perpendicular field geometry in subplots (a), (b) and (c) we can appreciate the reduction in the hysteresis loop area with an increasing strength of the  $A_{\text{inter}}^{\text{AFM}}$  constant. One reason behind this is attributed to the decrease of the net magnetisation parameter  $M_{\text{total}}$  on the basis of the increasing RE magnetisation (taken in modulus) as we saw earlier in Figure 5.3(c). The more relevant contribution to this behaviour stems however from the reduction of the coercive field  $H_c$  as  $A_{\text{inter}}^{\text{AFM}}$  is raised, an effect previously observed for example in Ref. [322] also for an applied field parallel to an easy direction. Increasing the field tilting to  $\theta_H = 60^\circ$  (subplots d, e and f) this trend is preserved. Interestingly, going towards larger AFM coupling we observe apparent evidence of non-coherent magnetisation reversal which is otherwise typical in two-component magnetic systems. It is important to underline however that for the displayed field range of  $\pm 400 \text{ mT}$  in either subplots of Figure 5.4, the macrospin vectors are perfectly antiparallel and the hysteresis loops are determined by coherent rotations or small longitudinal modifications of the macrospin vectors due to the competition between the applied field

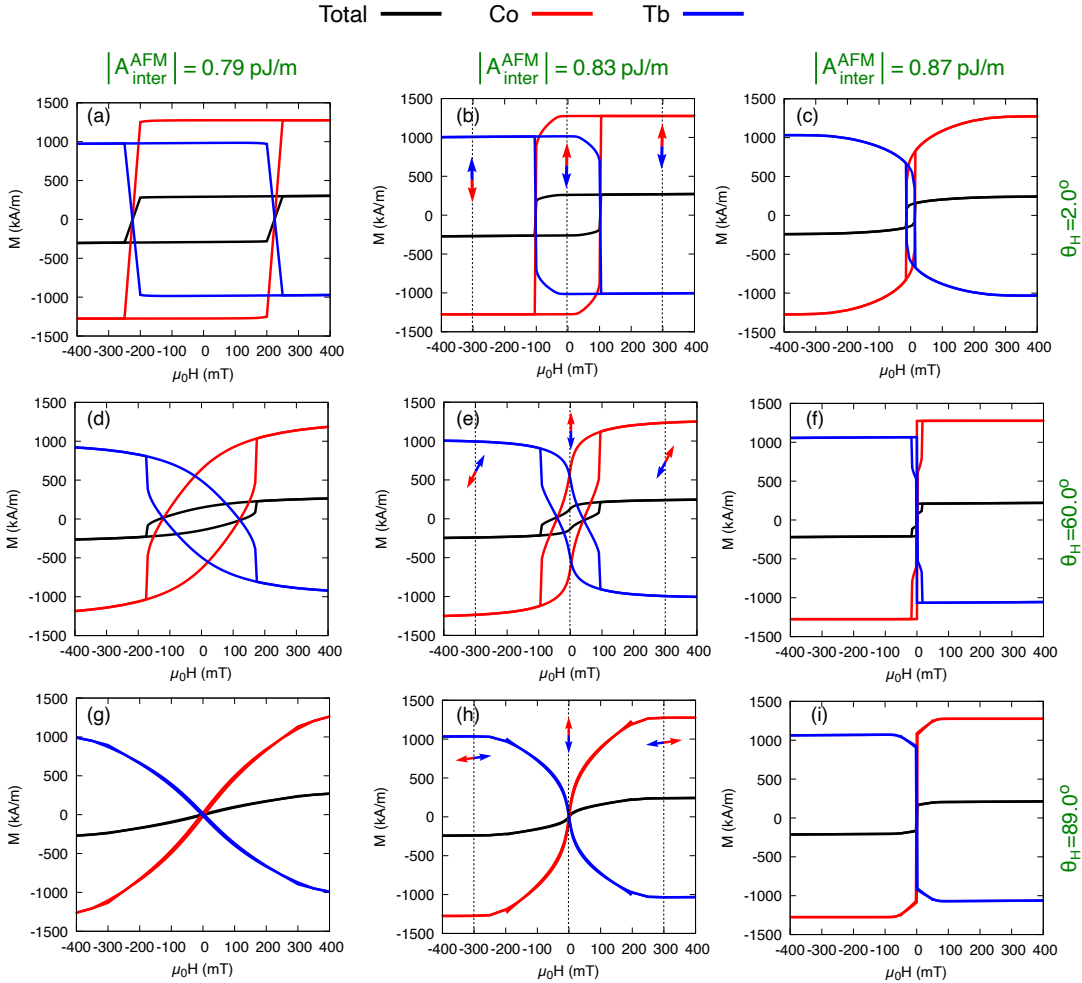


FIGURE 5.4: Static hysteresis cycles for three applied field orientations  $\theta_H = 2^\circ$ ,  $60^\circ$  and  $89^\circ$  (where  $\theta_H$  is measured with respect to the easy direction identified with  $Oz$ ). The y-axis magnetisation represents the component parallel to the direction of the field. For each geometry we display also the effect of varying the interlayer coupling  $A_{\text{inter}}^{\text{AFM}}$ . For  $|A_{\text{inter}}^{\text{AFM}}| = 0.83 \text{ pJ/m}$  we represent schematically the orientation of the Tb/Co macrospins at remanence and at the edges of the hysteresis loops for  $\pm 300 \text{ mT}$ . The apparent non-coherent shape of the hysteresis loops as for example in the case of subplots (e) and (f) stems exclusively from longitudinal modifications of the macrospin vector lengths due to the competition between the externally applied field and the AFM coupling as discussed in the main text. For clarity we preferred a continuous line representation instead of discrete points.

and the AFM coupling (see Appendix C.1). Lastly, the hard-axis hysteresis loops in subplots (g), (h) and (i) display mostly a typical continuous magnetisation rotation but for certain magnetisation jumps which may be identified visually for example in (h) around  $\pm 200 \text{ mT}$ . Although this TMspin model cannot capture non-coherent magnetisation reversal via domain nucleation, propagation or pinning of DWs, we underline the coercive field strength and the overall shape of the hysteresis loops obtained for  $|A_{\text{inter}}^{\text{AFM}}| = 0.83 \text{ pJ/m}$  matches with the experimental results reported in Refs. [34, 312]. In these works, depending on the thickness and the repetition of the Tb/Co multilayer stacks, it is reported at RT a coercivity typically in the range of 100 to 250 mT in the out-of-plane field geometry. Finally, the specific  $|A_{\text{inter}}^{\text{AFM}}| = 0.83$  interlayer coupling is chosen as a reference parameter for the upcoming discussion in the full-scale micromagnetic model also for the step-like behaviour shown for

example in subplot (e) of Figure 5.4 which resembles exactly a series of experimental results discussed in our private communications with the SPINTEC collaborators that are not published at the moment. In Refs. [34, 312] only out-of-plane or in-plane hysteresis cycles are discussed but not intermediary applied field geometries.

### 5.2.4 Easy-axis tilt assumption towards precessional all-optical switching

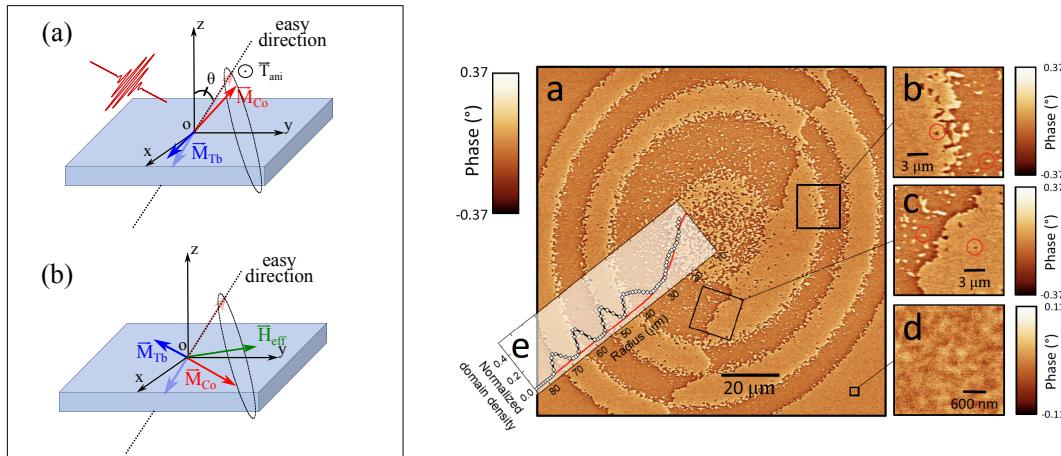


FIGURE 5.5: Left-hand side: (a,b) a local tilting  $\theta$  of the easy axis  $\vec{e}$  away from  $Oz$  is thought to promote a precessional AOS behaviour around an effective field  $\vec{H}_{eff}$  in Refs. [32–34] triggered by a laser-induced loss of the perpendicular order. Depending on the period of precession and the trajectory of the dynamics, the system can recover its initial configuration or switch to  $-Oz$  during the cooling process. Right-hand side: MFM analysis of a typical TM/RE multilayer stack extracted from Ref. [32] which presents the granular texture on the surface of a sample, long after exposure to an ultra-fast laser pulse excitation. The size of the small switched/not switched "domains" or "grains" ranges from 100 to 300 nm. Reprinted with permission from Springer Nature.

The assumption of the local EA tilt in the description of HI-AOS dynamics of Tb/Co was previously conjectured in Refs. [32, 34] and later implemented in a simple macrospin model in Refs. [33, 44]. The main hypothesis which motivated the tilted easy-axes scenario concerns itself with the "granular" texture of the multilayer Tb/Co stacks. Their magnetic force microscopy (MFM) analysis (see right-hand side plot in Figure 5.5) [32] revealed the presence of small domains or grains of a few hundred nanometers in size on the surface of the stack, with an increasing density towards the center of the laser excited area and in the transition regions between the ring domain patterns. Interestingly, neighbouring grains as for example in the center of the illuminated region may be found in opposite "up" and "down" magnetic states hinting at a rather localised switching mechanism as well as a certain distribution of the magnetic properties across the sample. The latter was further motivated in Refs. [32, 33] on account of the polycrystalline nature of the multilayer stacks. It is generally sensible to assume a certain degree of non-uniformity across the sample which naturally arises during the fabrication process unless the material under study is a single crystal. The local EA tilt is thought to be the ingredient determining the precessional-like AOS behaviour [32–34] and therefore the appearance of the ring-domain pattern shown in Figure 5.5. In our TMspin model this assumption can be pictured as: first, the local EA tilt creates a necessary torque on the macrospins which are pushed out of equilibrium during the laser pulse heating due to a temperature-induced loss of the perpendicular order. This triggers a precession

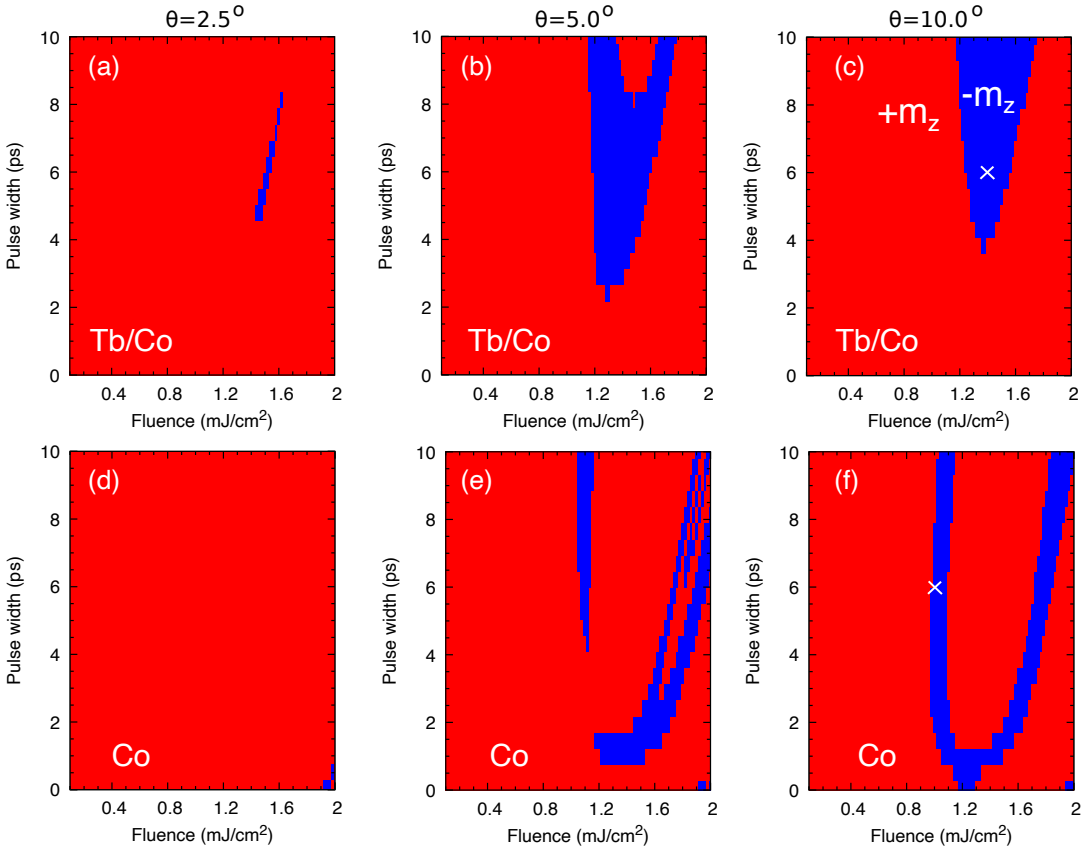


FIGURE 5.6: Switching diagrams for an AFM coupled Tb/Co bilayer (a-c) and a single Co macrospin (d-f) under identical laser pulse heating conditions and tilting of the easy direction  $\vec{e}$  at  $2.5^\circ$ ,  $5^\circ$  and  $10^\circ$  away from the Oz axis. In either scenario, the starting configuration at 300 K finds Co in a perpendicular orientation. The red/blue colors correspond to positive/negative Co  $m_z$  orientation obtained integrating the LLB equation in (5.1) for several ns after the laser-pulse excitation. The cross marks in (c) and (f) identify the AOS examples presented in Figures 5.8 and 5.7.

around an effective field  $\vec{H}_{\text{eff}}$  which continues during the cooling process. Secondly, supposing the initial net magnetisation is along  $+Oz$  and depending on the period of precession, the system can recover its initial configuration or switch to  $-Oz$ . In a large-scale system, the Gaussian laser leads to a spatial temperature distribution across the sample which determines a variation of this period of precession. Due to the radial symmetry of the laser excitation and consequently of the temperature distribution, ring-domain patterns form which correspond to  $\pm Oz$  final magnetic states. This precessional-like switching in conjunction with the ring-domain pattern have been previously discussed experimentally albeit typically in the presence of an external magnetic field which biases the precession [323, 324]. In the case of Tb/Co, the local EA tilt is thought to determine this precession.

Here we model the AOS of the Tb/Co bilayer in the TMspin model under the assumption of an easy-axis tilting with respect to the Oz direction (see subplots (a,b) in Figure 5.5). Thus, differently to Ref. [33] we take into account the presence of two AFM-coupled sublattices, with temperature-dependent parameters in addition to longitudinal magnetic relaxation. In Figure 5.6 we display precessional switching diagrams (red/blue colors correspond to positive/negative  $m_z$  orientation of Cobalt sublattice long after laser excitation) obtained under distinct laser pulse heating conditions.

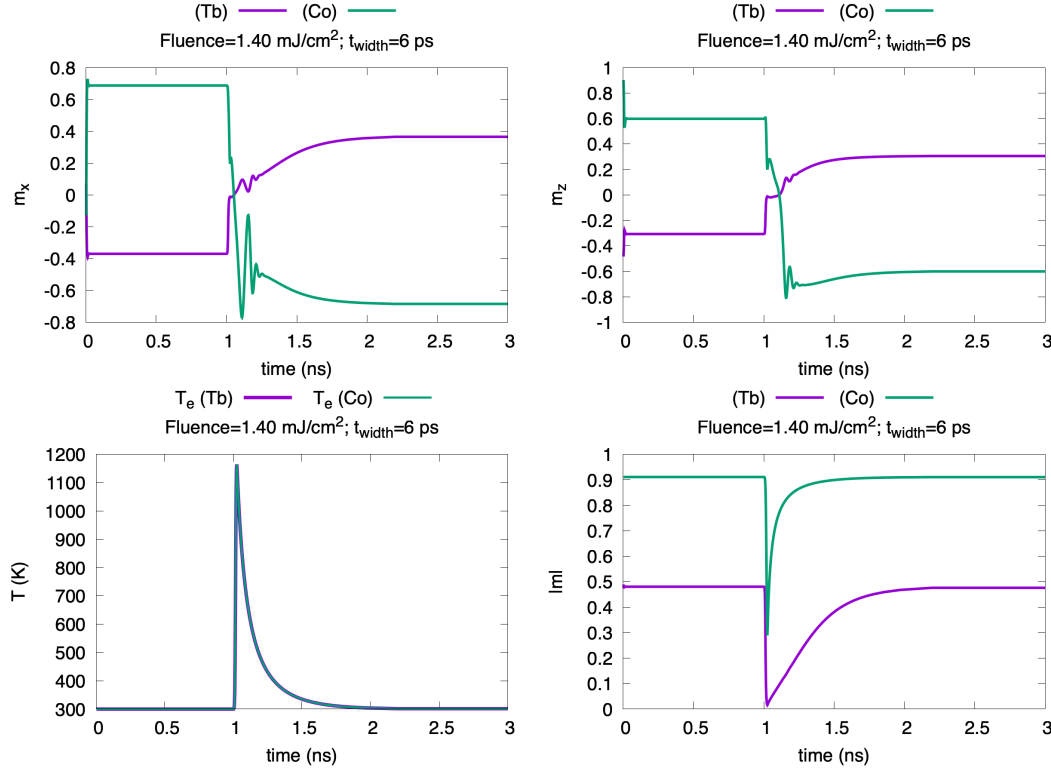


FIGURE 5.7: Precessional AOS example obtained in a TMspin Tb/Co model for laser pulse heating at a fluence of  $F = 1.4 \text{ mJ/cm}^2$  and pulse duration of 6 ps. We provide the time-variation of  $m_x$ ,  $m_z$ , the instantaneous modulus  $|\vec{m}|$  and the electron temperature  $T_e$ . Initially Co(Tb) lies along  $+Oz(-Oz)$ . The system is equilibrated for 1 ns at 300 K and the laser-induced dynamics for 2 ns. This simulation corresponds to the marked point in Figure 5.6(c).

We omit here the details of the TTM used to describe the heat dynamics since the same parameters and equations will be employed in the large-scale Tb/Co model discussed in the next section and they can be consulted in Eqs. (5.13), (5.14) and Table 5.2. Subplots (a-c) of Fig. 5.6 display the obtained AOS diagrams for EA tilting at  $2.5^\circ$ ,  $5^\circ$  and  $10^\circ$  away from the  $Oz$  direction. In the starting configuration at 300 K, Co points along  $+Oz$ . It is instructive to compare this approach with a single macrospin model. The latter was used previously in Ref. [33] to explain the Tb/Co precessional-like AOS. Therefore, subplots (d-f) correspond to a single Co macrospin subject to identical laser heating conditions and easy-axis tilting as in the TMspin picture. Qualitatively, both scenarios accommodate for AOS in the presence of increasingly large EA deviations, although interestingly in the Tb/Co coupled system a larger tilt of  $10^\circ$  leads to a narrowing of the switching window in comparison with  $5^\circ$ . It is important to underline the results in the two models are qualitatively distinct at least for the material parameters we employ. A series of heat and magnetisation dynamics are provided in Figures 5.8 and 5.7 which correspond to the marked regions in diagrams (c) and (f) of Figure 5.6. In both situations, a clear precession of the macrospin vectors in the  $Oxz$  plane triggered by the rapid laser heating can be identified. The simple macrospin model seems to reflect better the experimental results in Refs. [32, 33] by capturing AOS for both fs and ps excitation. The dynamics in the TMspin are inherently more complex due to the interplay between the AFM exchange coupling, magnetocrystalline anisotropy and laser pulse heating. On the other hand, a single macrospin may not be considered suitable to model this AOS behaviour since it fundamentally neglects the AFM coupling at the Tb/Co interface

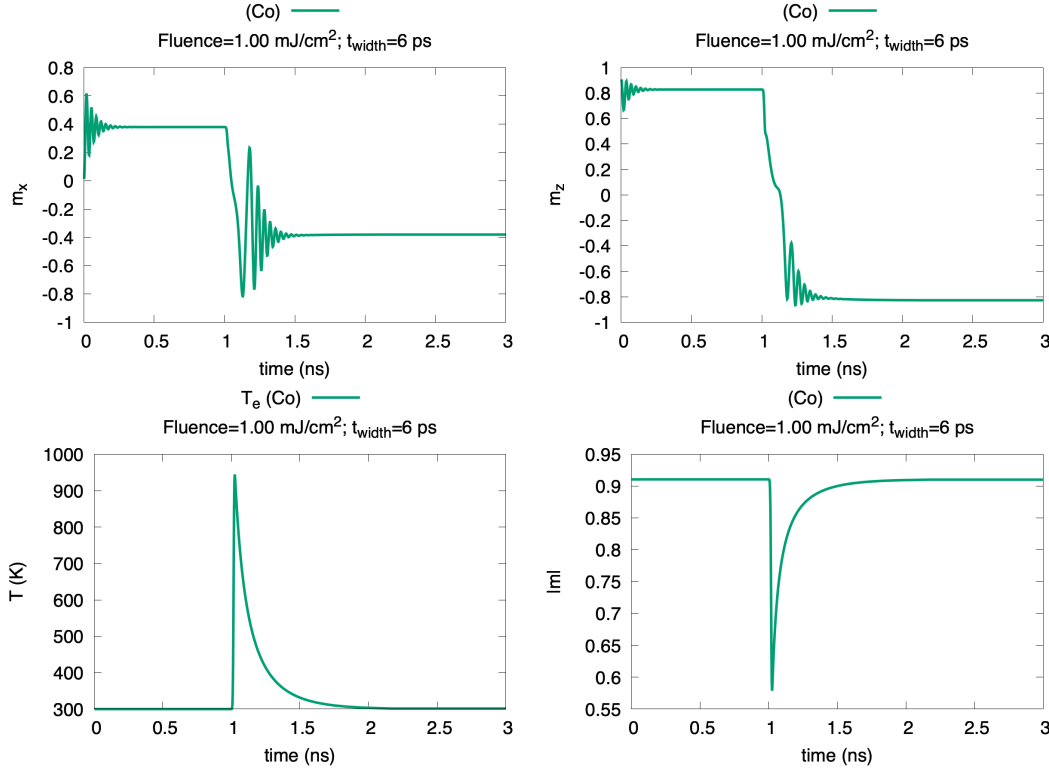


FIGURE 5.8: Precessional AOS example obtained in a single Co macrospin model for laser pulse heating at a fluence of  $F = 1.0 \text{ mJ/cm}^2$  and pulse duration of 6 ps. We display  $m_x$ ,  $m_z$ , the instantaneous modulus  $|\vec{m}|$  and the electron temperature  $T_e$ . Co magnetisation points initially along  $+Oz$ . The system is first equilibrated for 1 ns at 300 K laser-induced dynamics for 2 ns. The easy-axis is tilted 10° away from the perpendicular  $Oz$  direction. This simulation corresponds to the marked point in Figure 5.6(f).

and cannot distinguish the roles of the TM and RE in the magnetisation dynamics. As we will see, the complex magnetisation dynamics in the large-scale Tb/Co model presented next do not necessarily reflect the results of Figure 5.6.

### 5.3 Full scale micromagnetic modeling

Moving away from the TMspin picture, here we analyse the Tb/Co system in a full micromagnetic model consisting of two coupled thin films of 1 nm thickness each and a  $1.536 \mu\text{m} \times 1.536 \mu\text{m}$  surface area. The layers are individually discretised using a finite-differences scheme —as seen in the left-hand side illustration of Figure 5.2—in identical elements of  $3 \text{ nm} \times 3 \text{ nm} \times 1 \text{ nm}$  in size. The magnetisation dynamics in each macrocell are described in a similar manner as in the TMspin model, where the LLB equation in (5.1) now sums over all the distinct  $i$  elements of each sublayer  $\nu$ :

$$\frac{d\vec{m}_\nu^i}{dt} = -\gamma \vec{m}_\nu^i \times \vec{H}_{\text{eff}}^{i(\nu)} + \gamma \alpha_{||}^\nu \frac{\left( \vec{m}_\nu^i \cdot \vec{H}_{\text{eff}}^{i(\nu)} \right) \vec{m}_\nu^i}{(m_\nu^i)^2} - \gamma \alpha_\perp^\nu \frac{\vec{m}_\nu^i \times \left( \vec{m}_\nu^i \times \vec{H}_{\text{eff}}^{i(\nu)} \right)}{(m_\nu^i)^2}. \quad (5.8)$$

The transverse and longitudinal damping parameters  $\alpha_\perp^\nu, \alpha_{||}^\nu$  preserve the definition given in Eq. (5.2). The effective field  $\vec{H}_{\text{eff}}^{i(\nu)}$  is constructed based on Eqs. (5.1), (5.4),

(5.6) with the inclusion of an additional demagnetising term:

$$\vec{H}_{\text{eff}}^{i(\nu)} = \vec{H}_{\text{ex}}^{i(\nu)} + \vec{H}_{\text{ani}}^{i(\nu)} + \vec{H}_{\text{lon}}^{i(\nu)} + \vec{H}_{\text{dem}}^{i(\nu)}. \quad (5.9)$$

In this large-scale micromagnetic model, the exchange field  $\vec{H}_{\text{ex}}^{i(\nu)}$  contains both AFM and FM contributions:

$$\vec{H}_{\text{ex}}^{i(\nu)} = \frac{A_{\text{inter}}^{\text{AFM}}}{M_s^{i(\nu)}(0)l^2} \vec{m}_{\nu*}^i + \frac{2A_{\text{intra}}^{i(\nu)\text{FM}}(T)}{M_s^{i(\nu)}(0)|\vec{m}_\nu^i|^2\Delta^2} \sum_{j=1}^{n_i} (\vec{m}_\nu^j - \vec{m}_\nu^i). \quad (5.10)$$

Thus, for a given macrospin  $\vec{m}_\nu^i$  we consider the AFM interaction of strength  $A_{\text{inter}}^{\text{AFM}}$  with the macrocell  $\vec{m}_{\nu*}^i$  in the opposite layer  $\nu*$  at the same lattice point. In addition we add the FM exchange contribution of strength  $A_{\text{intra}}^{i(\nu)\text{FM}}$  counting over all first-nearest neighbours  $\vec{m}_\nu^j$  in the same layer up to a total  $n_i$  sites (see Figure 5.2). The temperature independent  $A_{\text{inter}}^{\text{AFM}}$  parameter is set to the same value employed in the TMspin model (see Table 5.1). The FM exchange stiffness  $A_{\text{intra}}^{i(\nu)\text{FM}}(T)$  is defined as:  $A_{\text{intra}}^{i(\nu)\text{FM}}(T) = A^{i(\nu)}(0)|\vec{m}_\nu^i|^{k_1}$ , where  $A^{i(\nu)}(0)$  is the 0 K constant and the temperature variation is given by the scaling exponent  $k_1$  and the instantaneous magnetisation magnitude  $|\vec{m}_\nu^i|$ . In the case of Co,  $k_1 = 1.8$  and  $A_\nu^i(0) = 30 \text{ pJ/m}$  are well suited values as previously discussed in Ref. [204]. For simplicity and for lack of relevant literature, we consider the same parametrisation also for the Tb sublattice. Given the generic exchange length  $l_{\text{ex}} = \sqrt{2A(T)/[\mu_0 M_s^2(T)]}$  and substituting for each layer, we obtain an increasing  $l_{\text{ex}}$  as a function of temperature starting from the 0 K values of 4.94 nm (Co) and 3.21 nm (Tb), which ensures the 3 nm discretisation length in the plane of the films is properly tailored.

Following, due to the direct inclusion of a full magnetostatic field term in Eq. (5.9), the definition of the anisotropy field in this large-scale model—in comparison to the TMspin approach—does not contain the thin-film shape anisotropy correction of the  $K_\nu^i(T)$  constant:

$$\vec{H}_{\text{ani}}^{i(\nu)} = \frac{2K_\nu^i(T)}{M_s^{i(\nu)}(T)} (\vec{m}_\nu^i \cdot \vec{e}_i). \quad (5.11)$$

Otherwise, the temperature scaling law  $K_\nu^i(T) = K_\nu^i(0)|\vec{m}_\nu^i|^{k_2}$  (with  $k_2 = 3$ ) employed in section 5.2, as well as the zero-Kelvin anisotropy constant  $K_\nu^i(0)$  given in Table 5.1 are maintained identical in here. Finally, the longitudinal  $\vec{H}_{\text{lon}}^{i(\nu)}$  and demagnetising field terms  $\vec{H}_{\text{dem}}^{i(\nu)}$  preserve the definitions introduced in equations (5.3) and (2.23) respectively, with an obvious notation distinction which must be adapted to a two-sublattice, multiple-macrospin system.

### 5.3.1 Hypothesis: can a distribution of easy-axis tilts lead to precessional AOS?

Here we extend the assumption of the local easy axis tilt used in section 5.2.4 to the multi-spin Tb/Co system. Therefore, at the level of each macro-cell  $i$  we consider a  $\theta_i$  deviation of the EA. In a spherical coordinates system we can express the orientation of the  $\vec{e}_i$  versor as:

$$\vec{e}_i \equiv (\sin \theta_i \cos \varphi_i, \sin \theta_i \sin \varphi_i, \cos \theta_i). \quad (5.12)$$

In this particular case we attempt to optimise the tilt in accordance with the results presented in Figure 5.6(b) where a larger AOS window is obtained at  $\theta_i = 5^\circ$ . To avoid an average in-plane anisotropy at RT —in accordance with Refs. [32, 34]—we uniformly distribute the azimuthal angles  $\varphi_i$  in the  $[0^\circ, 360^\circ]$  interval around the Oz direction (Figure 5.9f) as well as normally distribute  $\theta_i$  around a  $0^\circ$  mean value with a standard deviation  $\sigma_{\text{std}} = 5.0^\circ$  (Figure 5.9e). The easy-directions  $\vec{e}_i$  attached to the macrocells in the entire simulated system are thus radially symmetric with respect to the azimuthal plane perpendicular to the Oz axis as shown in the inset of Figure 5.9(e).

Next, we consider the single-shot, ultra-fast heating of the Tb/Co bilayer with a laser pulse characterised by a Gaussian spatio-temporal profile as seen in Figure 5.9(g). The heat dynamics are described by the following TTM equations:

$$\gamma_e T_e \frac{dT_e}{dt} = -G_{\text{ep}}(T_e - T_{\text{ph}}) + S(x, y, t) - \gamma_e T_e \frac{T_e - T_{\text{room}}}{\tau_{\text{th}}}, \quad (5.13)$$

$$C_{\text{ph}} \frac{dT_{\text{ph}}}{dt} = G_{\text{ep}}(T_e - T_{\text{ph}}). \quad (5.14)$$

The  $\gamma_e$ ,  $C_{\text{ph}}$  and  $G_{\text{ep}}$  values (see Table 5.2) correspond to previous numerical studies of ultrafast magnetisation dynamics in amorphous GdFeCo, TbCo and (Gd,Tb)Co alloys respectively [27, 31, 325] and the  $\tau_{\text{th}}$  cooling rate is set to a generic value of 15 ps. The profile of the laser pulse power  $S(x, y, t)$  is written here in the form:

$$S(x, y, t) = \frac{A_{\text{ab}} F}{\alpha_c t_p \delta_{\text{opt}}} \exp \left[ - \left( \frac{t - t_0}{t_p} \right)^2 - \left( \frac{x - x_0}{\sigma_x} \right)^2 - \left( \frac{y - y_0}{\sigma_y} \right)^2 \right]. \quad (5.15)$$

While the temporal width is set by the  $t_p$  constant, the laser spatial extension across the Oxy plane —or equivalently along the surface of the Tb/Co bilayer—is determined by the  $\sigma_x$  and  $\sigma_y$  variables respectively. For all the simulations discussed in this chapter these parameters are adjusted to  $\sigma_x = \sigma_y = 700$  nm. The pair  $(x_0, y_0)$

Parameter	Value
$\gamma_e$ ( $\text{Jm}^{-3}\text{K}^{-2}$ )	700
$C_{\text{ph}}$ ( $\text{Jm}^{-3}\text{K}^{-1}$ )	$3 \times 10^6$
$G_{\text{ep}}$ ( $\text{Js}^{-1}\text{m}^{-3}\text{K}^{-1}$ )	$1.7 \times 10^{18}$
$\tau_{\text{th}}$ (ps)	15

TABLE 5.2: TTM parameters for the Tb/Co bilayer system extracted from previous ultrafast magnetisation dynamics studies of amorphous GdFeCo, TbCo and (Gd,Tb)Co alloys respectively [27, 31, 325]. The constants are assumed identical in the two sublayers.

coordinates determine the center of the laser spot and correspond exactly to the central region of the thin film —see purple cross mark in Figure 5.9(g). Finally,  $t_0$  sets the moment of time when the laser pulse heating reaches its peak amplitude and it is set here here as:  $t_0 = 3t_p$ . Although a more realistic description should distinguish the heat dynamics of the phonon-electron reservoirs in the individual Tb and Co layers, we choose to reduce the complexity of our model and the large number of variables by assigning the same TTM constants in both subsystems —see Table 5.2. For a detailed explanation behind the meaning of each parameter included in Eqs. (5.13), (5.14), we refer to sections 2.3.3 and 3.3.2. The absorption coefficient  $A_{\text{ab}}$  is set to 25% identical to the results discussed in Chapter 3 and  $\delta_{\text{opt}}$  is considered equal to the thickness of the bilayer stack of 2 nm. Finally, the  $\alpha_c$  parameter is an

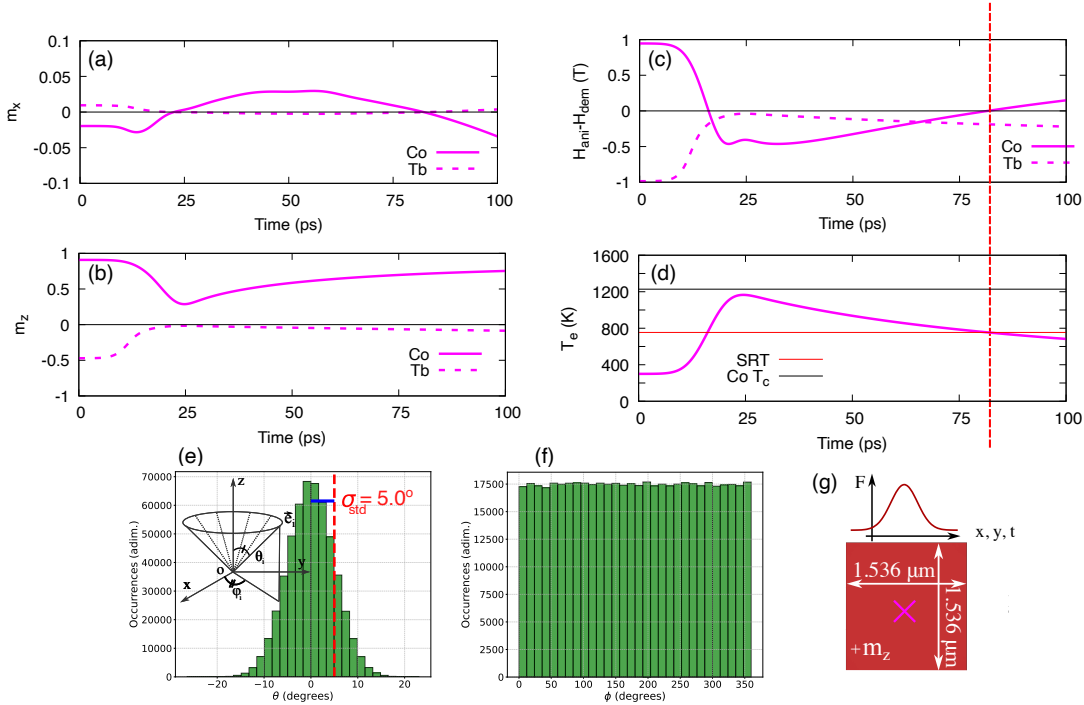


FIGURE 5.9: Testing the possibility for precessional HI-AOS under a single laser-shot and distribution of local EA tilts. (a,b) Isolated  $m_x$  and  $m_z$  time dynamics in the center of laser excited area with corresponding evolution of the  $|\vec{H}_{\text{ani}}| - |\vec{H}_{\text{dem}}|$  field difference (c) and electron temperature  $T_e$  (d). In the vicinity of the spin-reorientation temperature (SRT) the condition  $|\vec{H}_{\text{ani}}| - |\vec{H}_{\text{dem}}| \approx 0$  is satisfied for the Co phase. (e,f) Normal and uniform distribution of the  $\theta_i$  and  $\phi_i$  angles characterising the orientation of the EA directions  $\vec{e}_i$  according to equation (5.12). (g) Gaussian laser pulse profile in time and space. The time dynamics in (a-d) correspond to the marked purple region. In red we display the net Co magnetic ordering along  $+Oz$ .

umbrella term for the numerical constants which arise due to the FWHM relationship between the laser fluence  $F$  and intensity  $I$ :  $F = (\tau/2)\sqrt{\pi/\ln 2}I \approx 1.0645\tau I$ , where  $\tau = 2t_p\sqrt{\ln 2}$ . Thus,  $F \approx \alpha_c t_p I$ , with  $\alpha_c = 1.0645\sqrt{4\ln 2}$ .

In the experimental results of Refs. [32–34, 44] we encounter the precessional AOS hypothesis, thought to arise due to the in-plane reorientation of the net magnetisation vector. The heat-induced loss of the perpendicular order is seen to induce precessional dynamics under an effective magnetic field which may include demagnetising and magnetocrystalline anisotropy contributions [33, 44] but does not require any Zeeman coupling. The AOS dynamics presented for example in Refs. [32, 34] seem to follow a three step procedure including: (1) ultrafast demagnetisation where  $T_e$  is not expected to overcome the TM's Curie point, (2) an initially fast recovery and (3) slower precessional dynamics to equilibrium (an example of these magnetization dynamics is shown in Figure 5.1(f)). Here we attempt to test this hypothesis by tailoring the laser pulse parameters such that the peak  $T_e$  value remains below the  $T_c$  of Co while optimising the local EA tilt as discussed above to trigger the expected in-plane precession. In subplots (a), (b), (c) and (d) of Figure 5.9 we display the single-shot results obtained for  $F = 1.4 \text{ mJ/cm}^2$  and  $t_p = 6 \text{ ps}$  according to the calibration in Figure 5.6(b). For simplicity we focus our attention solely on the center of the laser spot marked with purple in Figure 5.9(g). The initial configuration at 300 K finds Co (Tb) in a net  $+Oz(-Oz)$  perpendicular orientation. The isolated dynamics in Figure 5.9(a-b) reveal the laser pulse heating gives rise to a

rapid demagnetisation of the sample but only a very small in-plane tilting as the loss of the perpendicular order takes place via longitudinal rather than transverse magnetic relaxation processes. In colder regions surrounding this central point, a small in-plane tilting is still observed but in none of the areas we obtain local reversal of the magnetisation for  $T_e < T_c^{\text{Co}}$ .

In comparison with the TMspin model, it is also possible that the FM exchange contribution within the layers leads to a somewhat increased perpendicular rigidity, making it more difficult to obtain a sufficiently large deviation from the easy-axis under identical laser pulse conditions. Obviously, one should also take into account the laser heating profile follows a spatial Gaussian distribution here. The heat dynamics in Figure 5.9(d) demonstrate  $T_e$  does not overcome the TM Curie point while it crosses the spin-reorientation temperature (SRT) promoting a transition from OOP to IP magnetic ordering. The SRT point is obtained observing the time evolution of the anisotropy and demagnetising field amplitudes  $|\vec{H}_{\text{ani}}| - |\vec{H}_{\text{dem}}|$  for Co in relation with the temperature dynamics as seen in Figure 5.9(c,d). Although the result in this section does not support the precessional AOS hypothesis, it is most likely this constitutes an optimisation problem of both the material and laser pulse parameters. Possible exploration routes in this sense can involve for example varying the microscopic damping parameter  $\lambda$  or the interlayer coupling strength  $A_{\text{inter}}^{\text{AFM}}$  as well as skewing the EA tilt distribution. The latter however may need to be achieved dynamically since RT experiments do not reveal a substantial in-plane magnetisation component of the samples [34]. The simulation in Figure 5.9 was repeated for a large number of pair parameters ( $F, t_p$ ) without crossing the Co critical temperature but obtaining similarly small amplitudes of in-plane dynamics.

### 5.3.2 Helicity-independent, all-optical switching after near-complete demagnetisation

Now we consider the situation when  $T_e$  overcomes the Curie point of the TM and near-complete demagnetisation is reached. Figure 5.10 presents the effect of a single-shot laser excitation for distinct peak laser fluences  $F$  and pulse durations which satisfy the aforementioned condition. Each individual subplot displays the  $m_z$  component of the Co sublayer approximately 500 ps after exposure to the laser pulse. It is also important to mention the standard deviation  $\sigma_{\text{std}}$  characterising the  $\theta_i$  distribution is lowered to  $2.5^\circ$  in this new series of results. We note first of all the appearance of a well defined concentric ring-domain pattern at  $t_p = 50$  fs, with an increasing number of rings with respect to an increase in  $F$ , similarly to the results reported in Refs. [32, 34]. Due to the finite-size of the laser spot we nucleate bubble-type domains. It is important to underline the laser spot size we can simulate is much smaller than in reality (see for example Figure 5.5). The experimental laser spot is of the order of the stable bubble domain size. Although not entirely preserved at the  $t_p = 2.5$  ps threshold and above, this trend of the magnetisation pattern with respect to the fluence of the laser is clearly displayed also at  $t_p = 500$  fs and  $t_p = 1$  ps. On one hand, an increase in the laser pulse duration  $t_p$  —or similarly a decrease in the fluence  $F$ —naturally flattens and narrows the Gaussian profile of the excitation. From another point of view, due to the small size of the simulated system—but already computationally expensive—the spatial extension of the laser is concentrated in a narrow area. Therefore in our simulations, even slight modifications in the pulse duration as for example going from 500 fs to 1 ps reflect greatly in the temperature distribution across the  $Oxy$  plane and consequently in the shape of the

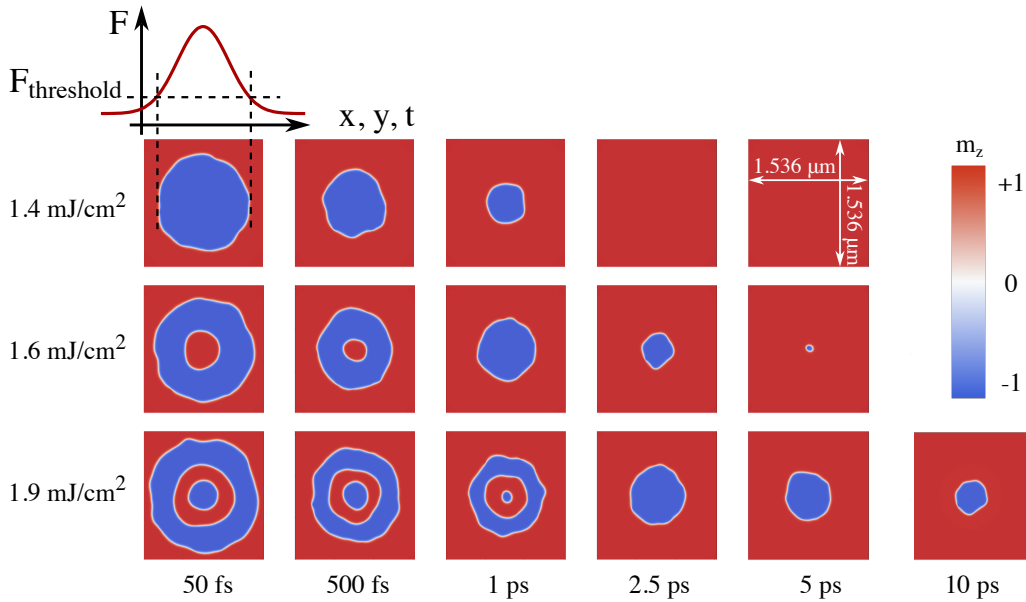


FIGURE 5.10: Ring domain-pattern obtained after single-shot AOS in a Tb/Co bilayer as a function of the peak laser pulse fluence (columns) and pulse duration (rows) in regions where the condition  $T_e > T_c^{Co}$  is satisfied. The colours display the magnetisation configuration along  $Oz$  solely for the Co layer. Each individual plot is a snapshot taken approximately 500 ps after the laser pulse excitation. We remind the reader the Co macrospins are initially oriented along the  $+Oz$  direction on average—considering also the small EA tilt at the level of each discretisation cell. Therefore, the blue regions correspond to switching of the Co magnetisation. The laser pulse distribution follows a Gaussian distribution in time and spatially along  $Ox$  and  $Oy$  according to the top-left sketch.

ring-domain pattern. According to the discussion in Figure 5.6 as well as previous works in Refs. [32, 34, 323, 324], the appearance of the rings comes as a result of the Gaussian profile of the laser which leads to a radial temperature distribution across the sample. Ultimately this dictates the precession period of the magnetic moments under an effective field  $\vec{H}_{\text{eff}}$  and the  $\pm m_z$  final magnetic states.

Another important detail captured in Figure 5.10 and experimentally shown for numerous Tb or Dy-based heterostructures in Ref. [32], it is the observation of AOS at constant fluence for a wide laser pulse duration window, including both the ultra-short fs time-scale as well as for longer excitations reaching up to 10 ps. For all the fluences considered ( $1.4 \text{ mJ/cm}^2$ ,  $1.6 \text{ mJ/cm}^2$  and  $1.9 \text{ mJ/cm}^2$ ) we obtain switching for  $t_p$  ranging from 50 fs up to at least 1 ps. Remarkably, this threshold increases up to the  $t_p = 5 \text{ ps}$  and  $t_p = 10 \text{ ps}$  limits for the intermediate and largest  $F$  respectively. In establishing this approximate maximum  $t_p$  value at a given fluence, there are two obvious drawbacks: (i) Our switched magnetisation domains are not indefinitely stable in time but they gradually shrink in size and ultimately disappear for reasons directly linked to the ratio between the stable domain and the system size we simulate which will be discussed later in section 5.3.4. Therefore, choosing when to evaluate the AOS criterion in universal fashion is detrimental in some situations. We remind that the magnetic configurations shown in Figure 5.10 are obtained approximately 500 ps after excitation. On longer time-scales with respect to this threshold and depending on the  $t_p$  value, the ring-domains might not survive and consequently the AOS criterion would be negatively evaluated. (ii) The pair parameters  $F$  and  $t_p$  influence the spatial distribution of the laser pulse heating and in consequence the extension of the reversed domains. Given the limitation in the

system dimensions we can simulate, it is expected the  $t_p$  limit for switching in our model is in fact closer to the experimentally reported threshold of 10 ps also at lower fluences. This limit could be attained for all peak  $F$  values by increasing the size of the system and spatially widen the heat distribution (by augmenting the  $\sigma_x$  and  $\sigma_y$  variables). In this way at a longer time-scale the fluence threshold  $F_{\text{threshold}}$  required for switching is satisfied and the reversed domains would still be visible.

### 5.3.3 A close inspection of the observed switching dynamics

Here we analyse the AOS results presented earlier for the specific pair parameters: peak fluence  $F = 1.9 \text{ mJ/cm}^2$  and pulse duration of  $t_p = 1 \text{ ps}$ . To this end, we choose three separate point regions extending from the center of the laser excitation and within the ring-domain pattern as shown in the top right snapshot of Figure 5.11 (we display this as a whole-page figure for better visibility). Based on this snapshot, we hereon name the regions according to the cross-marking colour: magenta, green and orange. In a top-down display, for each distinct point we present the time variation of the  $m_x, m_z$  magnetisation components, the field amplitude difference  $|\vec{H}_{\text{ani}}| - |\vec{H}_{\text{dem}}|$  and the electron temperature  $T_e$  for both the Co and Tb layers.

First of all, in all three situations we can appreciate the  $T_e$  parameter exceeds the Curie point of the Co phase as evidenced in subplots (d),(h) and (l) of Figure 5.11. Following this large heating, the magnetisation dynamics along  $Ox$  and  $Oz$  display an apparent complete reduction in amplitude for several tens of ps. In reality, Figure C.2 in Appendix C.2 showcases very small fluctuations of the  $m_z$  component under the influence of the interlayer exchange which we underline it is determined by a temperature independent constant  $A_{\text{inter}}^{\text{AFM}}$  according to equation (5.10). The final switched/non-switched state of the distinct investigated regions seems to be determined also by the precession of this residual magnetisation for the duration  $T_e > T_c^{\text{Co}}$  remains satisfied. While it can be argued the introduction of thermal fluctuations can prove detrimental to our observations here, it is also interesting to question whether they would facilitate the angular momentum transfer between Tb and Co as for example in the situation presented in Figure 5.9(b) where Tb could randomly cross the  $m_z = 0$  threshold and therefore allow switching of the TM. This however, remains a problem for future investigations due to present time constraints.

Following a subsequent cooling at a characteristic time of  $\tau_{\text{th}} = 15 \text{ ps}$ , the electron temperature  $T_e$  eventually drops below the  $T_c^{\text{Co}}$  value triggering a secondary oscillatory regime with a large magnetisation amplitude in the  $Oxy$  plane as observed in subplots (a,b), (e,f) and (i,j) of Figure 5.11. In comparison with the longitudinal fluctuations observed for  $T_e > T_c^{\text{Co}}$ , at this longer time-scale and for  $T_e < T_c^{\text{Co}}$ , we observe relevant transverse and precessional dynamics determined by a competition between the anisotropy and demagnetising fields —see subplots (c),(g) and (k) in the same Figure 5.11. An intriguing question that still needs to be answered concerns the gap between the two oscillatory regimes in our model and how these large amplitude transverse and precessional dynamics can be driven in the low-ps time scale, typically dominated by longitudinal processes, in order to observe the hypothesized AOS mechanism discussed in the previous section. Depending on the moment of time when the SRT point is crossed in relation to the  $Oxy$  precession and the anisotropy starts dominating over the demagnetising field contribution, the system may revert to the starting configuration after having switched initially as for example in the circled areas in the green region dynamics presented in subplots (f)

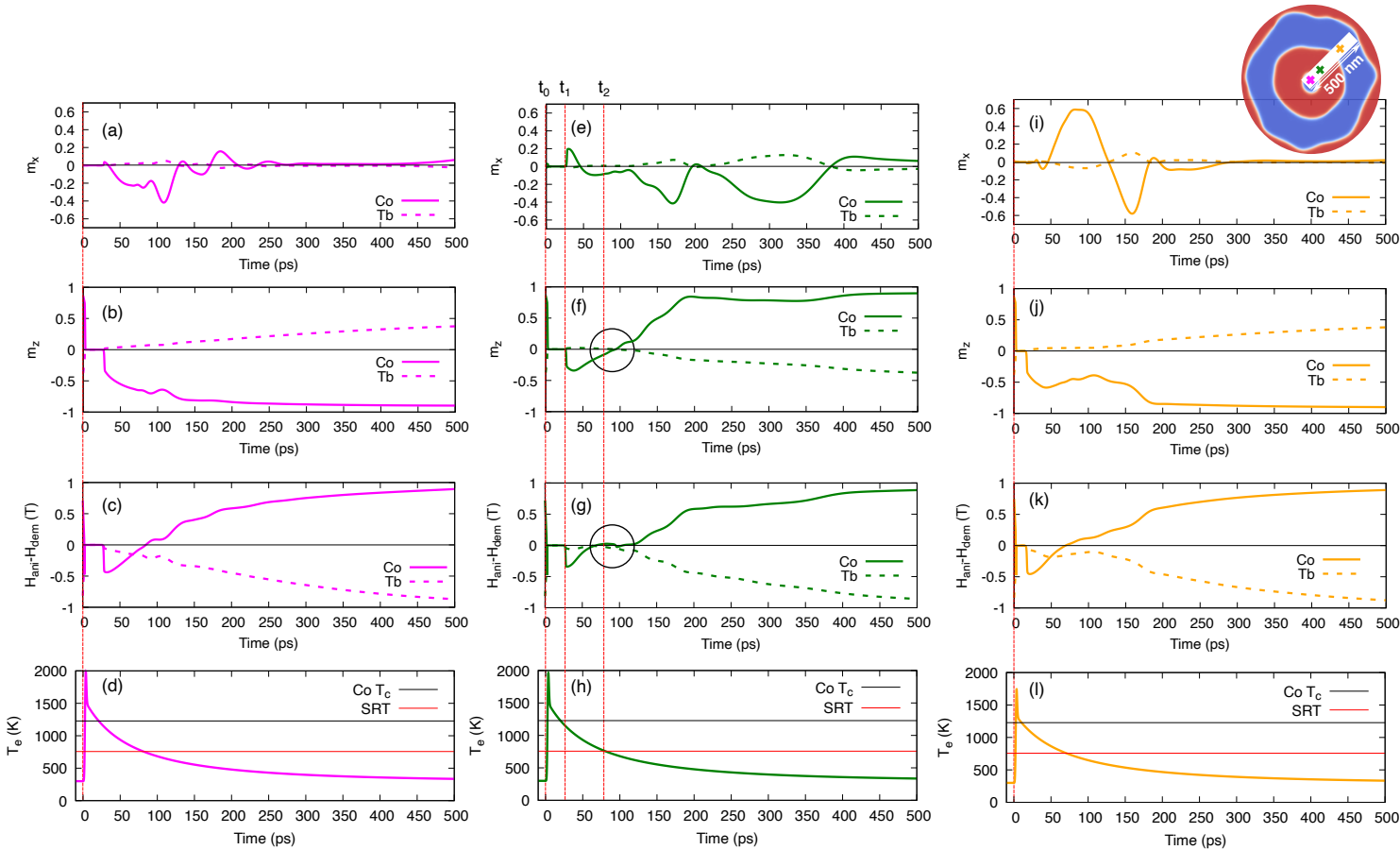


FIGURE 5.11: Laser dynamics for peak fluence  $F = 1.9 \text{ mJ/cm}^2$  and  $t_p = 1 \text{ ps}$  in three separate regions (see color marks in top-right snapshot). From top to bottom we display the  $m_x$ ,  $m_z$ ,  $|\vec{H}_{\text{ani}}| - |\vec{H}_{\text{dem}}|$  and  $T_e$  dynamics for the purple (a-d), green (e-h) and orange (i-l) regions. The horizontal red and black lines in (d,h,l) mark the Co Curie point and the spin-reorientation temperature while the vertical red lines are a visual aid between  $t_0 = 0 \text{ ps}$  and the moment when  $T_e$  drops below  $T_c^{\text{Co}}$  ( $t_1$ ) or SRT is reached ( $t_2$ ). Circled areas in (g) and (h) present a backswitching event.

and (g). The near-complete demagnetisation in our simulations represents an obvious discrepancy in comparison with the dynamics observed in the experiments of Refs [32, 34]. From another point of view it may even be argued this residual magnetisation state in conjunction with the observed longitudinal fluctuations represent the starting point of a zero-field cooling procedure above  $T_c$  rather than a constituent step of a switching experiment. However, it remains very interesting several AOS characteristics observed in Refs. [32, 34] are captured by our model as for example the ring-domain pattern in Figure 5.10 and in particular its nucleation for both fs and ps laser excitation.

Another interesting point of view may be obtained comparing side by side our simulation results with AOS measurements in the Tb/Co multilayer from Ref. [34]. In Figure 5.12(a) we provide a snapshot of these experiments extracted with permis-

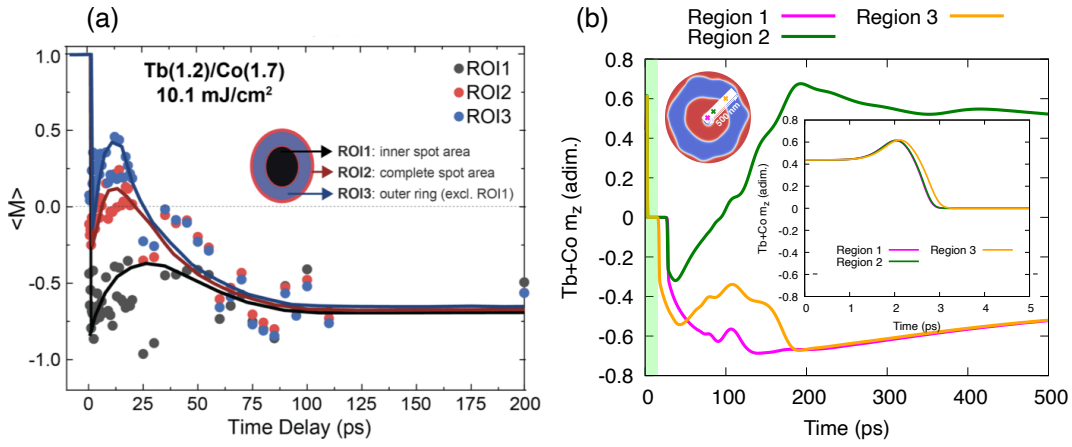


FIGURE 5.12: Qualitative comparison in between experimental AOS measurements in Tb/Co multilayers from Ref. [34] (Copyright (2023) American Physical Society) and our simulation results. In (a) time-resolved magneto-optics display the perpendicular magnetisation in distinct ROIs centered around the laser peak energy spot. In (b) we contrast the net  $m_z$  component (summing the Tb and Co contributions) for the magenta, orange and green regions discussed also in Figure 5.11.

sion from the American Physical Society and one of the lead authors. The data was obtained for single-shot AOS under a fs laser excitation (the precise temporal width of the pulse is not given). Time-resolved magneto-optics reveal the perpendicular magnetisation component of the multilayer —although it is not clear to what degree Co and Tb contribute to this signal —in three regions of interest (ROI) centered around the peak laser heating spot. Alongside in Figure 5.12(b) we qualitatively compare the net  $m_z$  component (summing the Co and Tb contributions) in the magenta, green and orange regions discussed previously in Figure 5.11. Although the experimental AOS dynamics are several tens of ps faster compared to our simulations and disregarding the near-complete demagnetisation phase (highlighted in green in subplot (b) of Figure 5.12), the switched magenta and in particular the orange regions seem to qualitatively match the oscillatory behaviour observed experimentally after the initial rapid demagnetisation process. In the inset presented in Figure 5.12(b) we also display an initial ultrafast magnetisation increase due to the rapid loss of the Tb magnetic moment, otherwise also observed experimentally.

### 5.3.4 Ring-domain pattern time evolution and instability

In Figure 5.13 we display several magnetisation snapshots in time obtained during the AOS process of the Tb/Co bilayer corresponding to  $F = 19 \text{ mJ/cm}^2$  and  $t_p = 50 \text{ fs}$  (this simulation result was also inspected in Figures 5.11 and 5.12). For simplicity, we display only the Co magnetisation, where the first two rows correspond to the time-variation of the perpendicular  $Oz$  component while the last two rows exhibit the in-plane  $Ox$  magnetisation. The initial moment of time  $t = 0$  is set such that the peak laser fluence is reached  $3t_p$  seconds later. The  $Oy$  magnetisation component is omitted here due to its similar behaviour in comparison to  $Ox$ . Despite some

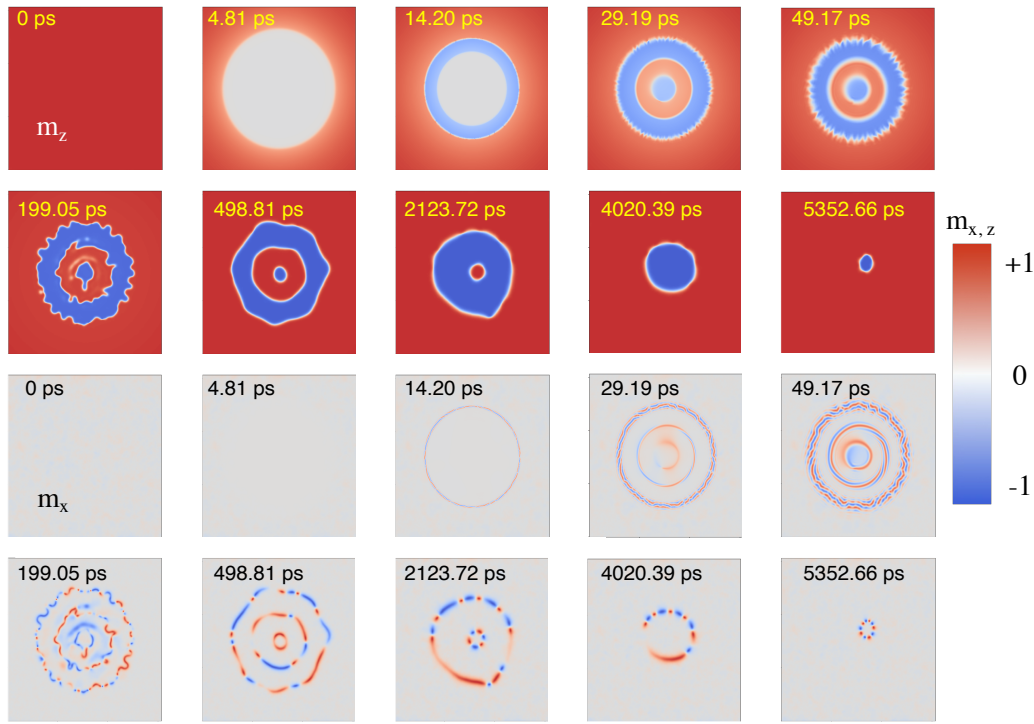


FIGURE 5.13: Magnetisation snapshots as a function of time corresponding to the Co sub-layer during the AOS of Tb/Co, obtained for  $F = 19 \text{ mJ/cm}^2$  and  $t_p = 1 \text{ ps}$ . The first two rows display the perpendicular  $Oz$  component while the last two exhibit the in-plane  $Oy$  magnetisation. The colorbar corresponds to all given subplots. The initial moment of time  $t = 0$  is chosen such that the laser fluence peaks exactly  $3t_p$  seconds later, where  $t_p$  is the duration of the pulse. The magnetisation component along  $Oy$  is left out since its behaviour resembles in good proportion the time variation of the  $Oy$  magnetisation.

discrepancies in between simulations and experiment discussed in the previous section, it is remarkable our model yields a "dynamic" ring-domain pattern similar to the results presented in Ref. [34]. Several interesting features can be underlined in this incoherent switching process. First of all, the nucleation of the rings is promoted from the edges towards the center of the Gaussian laser distribution, which according to the analysis provided in Figure 5.11 relates to the peak  $T_e$  temperature in each region and how fast this parameter drops below the Curie point of the TM. Once this threshold is crossed, transverse and precessional relaxation process arise (see snapshots at 14.20 and 29.19 ps) which contribute to the switching of the bilayer in addition to the longitudinal fluctuations discussed in detail in Figure C.2 in Appendix C.2. As we saw in Figure 5.11, the competition between the anisotropy

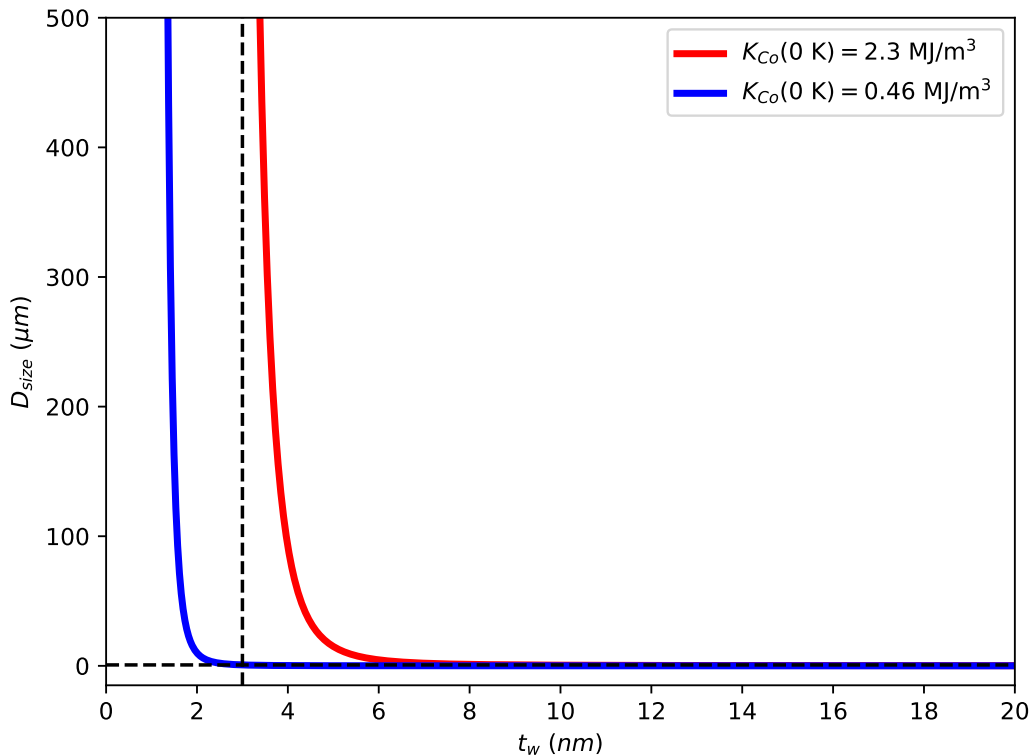


FIGURE 5.14: Stable domain-size at 300 K as a function of layer-thickness and for different magnetocrystalline anisotropy constants (MCA) according to equation (5.16). Calculations are employed using Co parameters. Compared to the red curve, the blue line corresponds to a five-fold decrease in the MCA at 0 K. To obtain the MCA at 300 K, we use the relationship:  $K_{Co}(T) = K_{Co}(0)m_e^3$ . The intersection of the dashed lines corresponds to  $t_w = 3 \text{ nm}$  layer thickness and domain-size  $D_{size} = 0.71 \mu\text{m}$ .

and the demagnetising fields leads to an oscillatory behaviour, evidenced in the snapshots taken 49.17 ps and 199.05 ps. Very interesting and complex vortex-like magnetic textures are clearly observed in the  $m_x$  component precisely defining the boundaries of the up/down ring domain-pattern. On longer time-scales this precessional behaviour stalls although the nucleated magnetic textures start shrinking in size until their eventual disappearance occurs. This is expected to take place on one hand due to the thermal gradients generated by the spatial Gaussian profile of the laser, which promotes a DW motion towards the hotter central region of the film [36].

From another point of view, we must underline here another important distinction in between experiment and our model. Going back to the MFM representation in Figure 5.5, the surface area of the investigated samples is exceedingly large in comparison to our numerical capabilities. To obtain a better picture, the lateral size of our films is 1.536  $\mu\text{m}$  only, which does even capture the width of a single ring pattern in Figure 5.5. This can lead firstly to increased temperature gradients in our simulations simply because the spatial extension of the laser is concentrated in a smaller area. The instability of the nucleated magnetic domains may also be understood from a magnetostatics point of view. The domain size which minimises the total energy of the system in equilibrium can be approximately calculated via the

formula [326, 327] (tailored for cgs units):

$$D_{\text{size}} = t_w \exp \left[ \frac{\pi D_0}{2t_w} + \ln \pi - 1 + \mu \left( \frac{1}{2} - \ln 2 \right) \right], \quad (5.16)$$

where  $t_w$  is the layer thickness,  $D_0 = \frac{\sigma_{\text{DW}}}{E_d}$  characterises the range of the dipole-dipole interactions and  $\mu = 1 + \frac{E_d}{K}$  is the magnetic susceptibility. Finally,  $\sigma_{\text{DW}} = 4\sqrt{AK}$  represents the well known expression of the DW energy per unit surface and  $E_d = 2\pi M_s^2$  is the demagnetising energy per unit volume. Substituting in equation (5.16) the material parameters corresponding for Co or Tb at RT —another possibility is to make this calculation employing a net Tb/Co magnetisation —, the  $D_{\text{size}}$  parameter diverges towards unphysically large values (see red curve in Figure 5.14 calculated for Co), a situation encountered also in Ref. [327] for example in very thin magnetic layers. We estimate an increase of the thickness to 3 nm as well as a five-fold decrease of the anisotropy constant  $K$  in our case would lead to domain sizes small enough to fit in the simulated area (see blue curve in Figure 5.14). Nonetheless, these material parameter changes must be carefully tailored such that the perpendicular magnetic order at RT is not lost, the interlayer AFM coupling is preserved and in-plane tilting is allowed.

## 5.4 Conclusions

The investigation in this chapter attempted to provide a better suited model to explain the HI-AOS experiments in Refs. [32–34] taking as reference system a Tb/Co FiM bilayer. Towards this end, we first discussed in a bottom-up approach the structure’s equilibrium magnetic properties using a TMspin model that allowed us to match RT experimental observations such as the range of coercivities or the equilibrium magnetic state at remanence. Building upon the work of Ref. [33, 44] we extended and tested the EA tilt assumption to this TMspin picture comparing the field-free AOS diagram with results obtained in a simple macrospin method under identical laser heating conditions. While the switching behaviour in the two models is distinct and the one macrospin displays both fs and ps AOS in comparison with the TMspin picture (ps), it is very well possible this constitutes an optimisation problem that requires further screening of multiple material and laser parameters. Next, we extended our analysis to a large-scale Tb/Co model including the effect of the magnetostatic interaction, exploring the possibility for non-coherent magnetisation reversal otherwise inaccessible in the macrospin approximation. The precessional, HI-AOS hypothesis [32, 34] was tested taking into account a distribution of EA tilts and heating the electron bath at temperatures below the critical point of the TM layer. Unfortunately, this hypothesis could not be confirmed due to the small amplitude of the in-plane magnetisation dynamics, a possible mitigating solution we believe may be the introduction of a skewed EA distribution of tilts as well as a reduction of the uniaxial anisotropy constant to reduce the perpendicular rigidity of the system. This is however not an easy task since these adjustments need to preserve the RT equilibrium configuration observed experimentally, determined by the careful balance between the interlayer AFM coupling and the magnetocrystalline anisotropy as discussed in the TMspin approach. An important numerical scenario was encountered for laser pulse heating above the Co Curie point. In this case, several features of the AOS dynamics were reproduced, in particular the nucleation of the ring-domain pattern and the reversal of the FiM structure for laser pulse durations in the wide

fs-ps range at constant fluence.

The results presented in this chapter as well as the previous conjectures provided in Refs. [32–34] can be considered a work-in-progress at the theoretical level, the complex HI-AOS problem in Tb and Dy-based FIM systems deserving further attention in our opinion. Regardless of whether the HI-AOS hypothesis is confirmed or not, this ultimately does not explain why substituting Gd for Tb in multilayered FIM systems alters fundamentally the switching properties. The local EA tilt distribution may very well be assumed in the realistic modeling of any magnetic system since structural inhomogeneities are always bound to arise at the level of experimental samples. Therefore an interesting question which still needs to be answered here is whether simply the inhomogeneity in the local magnetic properties is stronger in Tb-based systems compared to Gd-samples for example due to a presumed spherimagnetic nature of the former [33, 44]? Another interesting unanswered question is why the HI-AOS in Tb/Co is observed for samples displaying a near magnetisation compensation at RT as discussed the work of [34] and whether the angular momentum compensation point is relevant or not.



## Chapter 6

# Concluding remarks and perspectives

### 6.1 English

In general lines, this thesis explored theoretically distinct thermal and non-thermal light matter coupling routes towards the manipulation of magnetic DWs, in addition with a combined, supplementary investigation of DWs and MDs in the last chapter of results. Our calculations were based on the established ASD methodology and the high-temperature micro-magnetic framework of the LLB equation. Below we give a brief summary of all previous five chapters, emphasizing the motivation behind this thesis, the methodology and the results, as well as discuss potential future work or unanswered questions.

#### Chapter 1

Here we formulated our motivation for this study in the context of current challenges faced by the data industry and the potential mitigating solutions offered by a migration towards all-optical memory and logic devices. Although CMOS integration remains a fundamental and technological challenge even for conventional spintronics —where the magnetic information is typically manipulated electrically—ultra-fast laser stimuli we saw, promise significant speed and energy efficiency gains [143]. Distinct MD/DW-based memory and logic device concepts were discussed in relation to the three classes of magnetic materials studied in this work: ferromagnets, ferrimagnets and antiferromagnets. From a fundamental point of view, we reviewed and adapted the distinction between thermal and non-thermal light-matter interaction according to the classification discussed in Ref. [26] and in the context of MD/DW textures. We avoided a formal discussion here around standard theoretical methods in the study of DW dynamics but reserved in this sense an extensive and specific literature review at the introduction of each chapter of results.

#### Chapter 2

The role of this chapter was to introduce the main theoretical concepts necessary to understand the competing microscopic interactions which dictate the preferred magnetic order in a solid-state system, as well as the formation of DWs and multi-domain textures at the macro-scale. Here we also touched upon elementary DW concepts such as width and energy definitions in relation to the competition between exchange and magnetocrystalline anisotropy in addition to exemplifying several wall structures studied along the subsequent results chapters. Next, we formally introduced the basic ideas behind the atomistic spin dynamics model [173] and the

high-temperature framework of the ferromagnetic LLB equation [198, 208, 209] giving also an overview of the TTM [46, 218, 219]. These constitute the numerical tools we employed to study thermal/non-thermal ultra-fast phenomena and their role in manipulating DWs/MDs in this thesis.

## Chapter 3

The investigation in this chapter led to the demonstration of a novel DW driving mechanism in a generic perpendicular ferromagnet. Making use of the inherent longitudinal dynamics described by the LLB equation, we demonstrated the possibility to convert a fs longitudinal magnetisation deformation into a transverse DW motion up to the ps-ns time-scale, effectively passing angular momentum from the longitudinal to the transverse and precessional reservoirs. In principle, a longitudinal deformation  $\delta\vec{m}(t)$  may arise due to the action of both non-thermal and thermal light-matter coupling [15, 35–37, 48–50, 55, 61, 62, 233, 234].

In a first step, we consider a simpler 1D model at constant temperature, where  $\delta\vec{m}(t)$  instantaneously modifies the length of the macrospin vectors across a Néel wall configuration. Since we neglect heat dynamics here, this can be considered a pure non-thermal effect which as shown, can lead to DW propagation. The mechanism is based on the appearance of a magnetisation gradient  $\nabla|\vec{m}|$  which enables the motion of the DW towards the "hot" region corresponding to an area of smaller magnetisation. The displacement primarily takes places on a very fast fs timescale where longitudinal relaxation processes are dominant. In contrast, the role of precession and transverse relaxation mechanisms is diminished, only giving rise to some DW oscillations on the ns timescale as the driving force  $\nabla|\vec{m}|$  has already vanished at this time-scale. The total distance covered by the wall is proportional to the lifetime of the induced gradient as well as the amplitude of the transient magnetisation in relation to the equilibrium  $m_e$ .

Secondly, we investigated the longitudinal DW driving mechanism in a full-scale micromagnetic model, accounting both for magnetostatic as well as heating effects. One can consider the transient magnetisation  $\delta\vec{m}(t)$  in this picture appears for example as a result of the non-thermal IFE [15, 159, 160], which in the Co metallic system we simulate, is expected to be accompanied by a transient heating of the sample under the same fs laser excitation. The general features of the wall displacement in this stripe model are preserved in relation to the chain system, although interestingly the motion direction may be steered towards the "hot" or "cold" region under the complex competition between thermal and non-thermal mechanisms. A quantitative analysis was made relating the amplitude of the simulated transient magnetisation with *ab-initio* calculations of the IFE in Co and FePt [15, 160], reaching the conclusion a multiple-pulse excitation may be required to observe a sensible wall displacement under this effect or engineering materials with larger Verdet constants.

The model employed in this chapter as well as the generality of the  $\delta\vec{m}(t)$  parameter offer several subsequent directions of research. A straightforward extension of our work is the investigation of DW dynamics under transient laser-induced magnetisation in FMs and AFM systems, potentially reaching towards faster as well as larger wall displacements. Another interesting possibility is the exploration of fs longitudinal effects in other non-collinear magnetic textures such as skyrmions, which similar to magnetic DWs represent a platform for enhanced opto-magnetic effects in contrast with coherent systems as discussed in Ref. [266]. Beyond the IFE, the  $\delta\vec{m}(t)$  parameter can also be discussed in relation to other opto-magnetic phenomena such as the MCD effect or the novel absorption contribution introduced by

Scheid et al. in Refs. [233, 234]. On the experimental side, the recent results in Ref. [152] display complex magnetic patterns consisting of DWs and bubble domains can lead to a transient magnetisation enhancement in the sample under fs laser excitation, when typically ultra-fast demagnetisation is expected. In another work, similar domain patterns are shown to give rise to extreme wall velocities up to 66 km/s and displacements proportional to the DW curvature [153]. It would be interesting to apply the high-temperature micromagnetic formalism of the LLB equation and test whether transient longitudinal deformations  $\delta\vec{m}(t)$  of multi-domain configurations can reproduce these experimental results.

## Chapter 4

This chapter discussed the LOT, non-thermal mechanism arising as a second order response to an ultra-fast laser excitation in the visible spectrum and its potential use towards the dynamic control of the AFM order in  $Mn_2Au$ . The investigation here was primarily supported by ASD calculations parametrised with material constants and LOT amplitude estimations previously obtained in Refs. [162–164]. While the investigation in Ref. [162] revealed a linear or circularly polarised light can generate a substantial LOT on the Néel order parameter due the IFE, we precisely characterised the conditions in which this torque can trigger AFM DW dynamics in  $Mn_2Au$ .

Taking into account that the torque symmetry depends on the local Néel vector orientation  $\vec{I}$  in relation to the laser polarisation direction  $\vec{E}$ , we arrived at the remarkable conclusion: the LOT can drive 90° wall kinematics but it forbids the motion of 180° DWs in contrast with the established first-order, NSOT mechanism [123, 124, 133, 277]. Experimental studies on laser-induced DW dynamics in FMs typically make use of fluences in the range of a few mJ/cm<sup>2</sup> with equivalent intensities in the 1 and 10 GW/cm<sup>2</sup> interval [42, 53]. Our simulations predict single pulse excitation below 0.3 GW/cm<sup>2</sup> can drive 90° DW kinematics up to the supermagnonic limit ( $v = 46$  km/s). Via TTM estimations, we expect the ultrafast heat load deposited in the phonon subsystem dissipates and cools the sample to room temperature below 1 ns. The numerical results have been compared with an analytical and adapted  $\sigma$ -model [123, 125, 126, 128, 129, 131] yielding a good fit of the steady-state velocity and corresponding DW width as a function of the external perturbation in the picture of Lorentz invariant kinematics. Interesting DW proliferation events were demonstrated in the limit of supermagnonic propagation, an effect also previously discussed for example in Ref. [124].

A curious point here which could be tackled in a future work in more detail stems from the apparent lack of Zeeman like energy contribution of the LOT term in the  $Mn_2Au$  Hamiltonian. We generally believe the energy requirements for a parent-child nucleation event are met due to the relativistic DW motion itself, where the LOT acts as a perturbation of the AFM coupled system and the complex set of energy contributions in the unit cell fuels the efficient DW transport. The idea then is to check whether a direct link can be established between the energy of a propagating parent DW and the resulting velocity of the child magnetic texture in the steady state as well as whether optimum and controlled nucleation conditions can analytically be formulated. Additionally, an obvious extension of the numerical model's complexity requires the simultaneous calculation of the magnetisation and temperature dynamics with the description of a three-dimensional numerical object instead of the 1D system we model. The introduction of thermal fluctuations may provide a way to unpin or break the LOT symmetry in the case 180° DW configurations but

also put to test the efficiency of the 90° kinematics in a numerical picture closer to experimental conditions.

## Chapter 5

In this final chapter of results we investigated a thermal laser-driven route towards the manipulation of MDs and DWs in a Tb/Co FiM system. The main objectives of this work were to understand the universal HI-AOS results obtained in Refs. [32, 34] and test the in-plane precession hypothesis thought to be at the origin of this reversal mechanism. Towards this end, we followed a two step investigation procedure using first a TMspin description and a large-scale micromagnetic model subsequently both built around AFM coupled ferromagnetic LLB equations.

The principal role of the simpler TMspin picture was to determine the equilibrium magnetic properties of the Tb/Co bilayer such as the net magnetisation variation with respect to temperature and interlayer coupling as well as to match the experimental hysteresis cycles presented in [34, 312] or privately discussed with our SPINTEC collaborators. Interestingly, although this TMspin framework cannot capture incoherent magnetisation dynamics such as domain nucleation or DW motion, we obtained quantitative agreement with the experimental coercivity range at RT in the Co-dominant magnetisation region. As an extension to the work presented in Refs. [33, 44] we tested the EA tilt assumption in a field-free AOS experiment constructed in the TMspin model and compared with a single macrospin approach under identical laser heating conditions. It remains to be seen in a future work whether the material parameters can be optimised for both fs and ps switching in the TMspins picture, in contrast with the sole ps reversal observed presently.

In a second phase, we built a large-scale micromagnetic model of Tb/Co based on the TMspin parametrisation and including demagnetising field calculations as well as a distribution of local EA tilts around the perpendicular Oz direction. We tested the precessional, HI-AOS hypothesis conjectured in Refs. [32, 34] for optimum laser pulse parameters according to the TMspin results but could not confirm it due to the small amplitude of the in-plane magnetisation dynamics. To circumvent this issue, we believe skewing the EA distribution away from the 0° mean value can be a first step towards stimulating stronger in-plane dynamics. An interesting numerical result emerged in the case of laser pulse heating above the Co Curie point which although differs from the experimentally observed AOS kinematics, it reproduces the ring-domain pattern for both fs and ps excitation and displays qualitatively similar precessional-like dynamics. Although the hypotheses launched by Refs. [32, 34] need further confirmation in our opinion, the work here represents an important step in this direction. Fundamentally, the role of Tb or Dy in contrast with Gd remains an interesting and open question in the ultrafast magnetism community. If the EA tilt distribution is validated for Tb/Co, an important question arises: what precludes a similar hypothesis from being formulated in the case of Gd/Co or even a traditional Co/Pt sample as well as equally engineering irregularities at the granular level to promote a similar switching mechanism?

## 6.2 Español

En líneas generales, esta tesis exploró teóricamente distintas rutas de acoplamiento luz-magnetismo, de tipo térmicas y no-térmicas, hacia la manipulación de DWs,

además de una investigación combinada y suplementaria de MDs y DWs en el último capítulo de resultados. Nuestros cálculos se basaron en la metodología ASD y en el marco micromagnético de alta temperatura de la ecuación LLB. A continuación ofrecemos un breve resumen de los cinco capítulos anteriores, subrayando la motivación de esta tesis, la metodología y los resultados, así como analizando posibles trabajos futuros o preguntas sin respuesta.

## **Capítulo 1**

Aquí formulamos nuestra motivación en el contexto de la industria de datos y las posibles ventajas que ofrece una migración hacia dispositivos lógicos y de almacenamiento ópto-magnéticos. Si bien la integración de CMOS sigue siendo un desafío fundamental y tecnológico incluso para la espintrónica convencional —donde la información magnética se manipula eléctricamente—los estímulos láser ultrarrápidos prometen ganancias significativas en velocidad y eficiencia energética [143]. Se discuten distintos conceptos de dispositivos lógicos y de almacenamiento basados en MD/DW en relación con las tres clases de materiales magnéticos estudiados en este trabajo: ferro-, ferri- y antiferro-magnéticos. Desde un punto de vista fundamental, revisamos y adaptamos la distinción entre la interacción luz-magnetismo de tipo térmica y no-térmica según la clasificación en [26] y en el contexto de las texturas MD/DW. Evitamos aquí una discusión formal sobre los métodos teóricos estándar en el estudio de la dinámica de DWs/MDs, pero reservamos en este sentido una revisión extensa y específica de la literatura en la introducción de cada capítulo de resultados.

## **Capítulo 2**

Aquí intentamos introducir los principales conceptos teóricos necesarios para comprender las interacciones microscópicas que determinan el orden magnético preferente en un material de estado sólido, así como la formación de DWs y texturas multidominio a escala macro. También abordamos conceptos teóricos básicos como las definiciones de anchura y energía de una pared magnética, en relación con la competición entre la energía de intercambio y la energía de anisotropía magnetocrystalina, además de ejemplificar diversas estructuras de paredes estudiadas en los capítulos de resultados. A continuación, presentamos formalmente las ideas básicas del modelo de dinámica de espín atomístico (ASD) [173] y el marco de alta temperatura de la ecuación ferromagnética LLB [198, 208, 209], ofreciendo también una visión general del modelo de dos temperaturas (TTM) [46, 218, 219]. Estas constituyen las herramientas numéricas que empleamos para estudiar los fenómenos ultrarrápidos térmicos/no térmicos y su potencial en la manipulación de DWs/MDs en esta tesis.

## **Capítulo 3**

La investigación de este capítulo condujo a la demostración de un mecanismo novedoso de desplazamiento de DWs en un FM perpendicular genérico. Utilizando la dinámica descrita por la ecuación LLB, demostramos la posibilidad de convertir una deformación de imanación longitudinal a fs en un movimiento de DW hasta ps-ns, transfiriendo eficientemente el momento angular entre la contribución longitudinal, transversal y precesional. En principio, una deformación longitudinal  $\delta\vec{m}(t)$  puede

surgir debido a la acción del acoplamiento luz-materia, tanto térmico como no térmico [15, 35–37, 48–50, 55, 61, 62, 233, 234].

En primer lugar, consideramos un modelo unidimensional a temperatura constante, donde  $\delta\vec{m}(t)$  modifica instantáneamente la longitud de los vectores de macroespín a lo largo de una configuración de pared Néel. Dado que aquí se descuida la dinámica térmica, esto puede considerarse un efecto puramente no térmico que, como se muestra, puede conducir a la propagación de DWs. El mecanismo se basa en la aparición de un gradiente de imanación  $\nabla|\vec{m}|$  que permite el movimiento de la pared hacia la región "caliente" correspondiente a un área de baja imanación. El desplazamiento ocurre principalmente en una escala de tiempo fs muy rápida, donde predominan los procesos de relajación longitudinal. Por el contrario, el papel de los mecanismos de precesión y relajación transversal se ve disminuido, dando lugar únicamente a algunas oscilaciones de la DW en la escala de tiempo ns, ya que la fuerza impulsora  $\nabla|\vec{m}|$  desaparece antes de esta escala de tiempo. La distancia total recorrida por la pared es proporcional a la vida media del gradiente inducido, así como a la amplitud de la imanación transitoria en relación con el valor de equilibrio  $m_e$ .

En segundo lugar, analizamos el mecanismo de deformación longitudinal en un modelo micromagnético a escala real, considerando tanto los efectos magnetostáticos como los de calentamiento. Se puede considerar que la imanación transitoria  $\delta\vec{m}(t)$  en esta imagen aparece, por ejemplo, como resultado del efecto no térmico IFE [15, 159, 160], que en el sistema metálico de Co se espera que esté acompañada de un calentamiento transitorio de la muestra bajo la misma excitación láser de fs. Las características generales del desplazamiento de la pared en este modelo se mantienen en relación con los resultados obtenidos en la aproximación de cadena, aunque curiosamente la dirección del movimiento puede orientarse hacia la región "caliente" o "fría" bajo la compleja competencia entre mecanismos térmicos y no térmicos. Se realizó un análisis cuantitativo relacionando la amplitud de la imanación transitoria simulada con cálculos ab-initio del IFE en Co y FePt [15, 160] llegando a la conclusión de que, para observar un desplazamiento de pared sensible bajo este efecto, se requiere una excitación con múltiples pulsos o identificar materiales caracterizados por constantes de Verdet mayores.

El modelo empleado en este capítulo, así como la generalidad del parámetro  $\delta\vec{m}(t)$ , ofrecen varias líneas de investigación posteriores. Una extensión directa de nuestro trabajo es la investigación de la dinámica de paredes bajo el mismo efecto longitudinal en sistemas FiMs y AFMs, lo que podría conducir a desplazamientos de pared más rápidos y mayores. Otra posibilidad interesante es la exploración de los efectos longitudinales fs en otras texturas magnéticas no colineales, como los skyrmions, que, igual que las DWs, representan una plataforma para aumentar la amplitud de los efectos optomagnéticos, en contraste con los sistemas coherentes, como se describe en la referencia [266]. Más allá del IFE, el parámetro  $\delta\vec{m}(t)$  también puede analizarse en relación con otros fenómenos optomagnéticos, como el efecto MCD o la novedosa contribución a la absorción introducida por Scheid et al. en las referencias [233, 234]. En el ámbito experimental, los resultados recientes de la referencia [152] muestran que bajo excitación láser fs, la presencia de patrones magnéticos complejos, compuestos por DWs y dominios de burbujas, puede aumentar de manera transitoria la imanación en la muestra, en vez de mostrar una típica desimanación ultrarrápida. En otro trabajo, se demuestra que patrones de dominio similares dan lugar a velocidades de pared extremas de hasta 66 km/s y desplazamientos proporcionales a la curvatura de DWs [153]. Sería interesante aplicar el formalismo

micromagnético de la ecuación LLB y comprobar si las deformaciones longitudinales transitorias  $\delta\vec{m}(t)$  de configuraciones multidominio pueden reproducir estos resultados experimentales.

## Capítulo 4

Este capítulo discutió el LOT, un mecanismo no térmico que surge como una respuesta de segundo orden a una excitación láser ultrarrápida en el espectro visible, y su posible uso para el control dinámico del orden AFM en Mn<sub>2</sub>Au. La investigación presentada aquí se basó principalmente en cálculos ASD parametrizados con constantes materiales y estimaciones de la amplitud del LOT obtenidas previamente en las referencias [162–164]. Mientras que la investigación en la Ref. [162] reveló que la luz polarizada lineal o circularmente, puede generar un LOT sustancial sobre el parámetro de orden de Néel debido al IFE, nosotros caracterizamos con precisión las condiciones en las que este torque puede inducir la dinámica de las paredes de dominio (DW) AFM en Mn<sub>2</sub>Au.

Teniendo en cuenta que la simetría del torque depende de la orientación local del vector de Néel  $\vec{l}$  en relación con la dirección de polarización del láser  $\vec{E}$ , llegamos a la notable conclusión de que el LOT puede impulsar la cinemática de paredes de 90°, pero impide el movimiento de paredes de 180°, en contraste con el mecanismo establecido de primer orden, el NSOT [123, 124, 133, 277]. Estudios experimentales sobre la dinámica de DW inducida por láser en materiales ferromagnéticos (FMs) suelen emplear fluencias en el rango de unos pocos mJ/cm<sup>2</sup> con intensidades equivalentes en el intervalo de 1 a 10 GW/cm<sup>2</sup> [42, 53]. Nuestras simulaciones predicen que una excitación de un solo pulso de una intensidad inferior a 0.3 GW/cm<sup>2</sup> puede impulsar la cinemática de DW de 90° hasta el límite supermagnónico ( $v = 46$  km/s). A través de estimaciones basadas en el modelo de dos temperaturas (TTM), esperamos que el calor transferido de forma ultrarrápida en el subsistema de fonones se disipe y enfríe la muestra a temperatura ambiente en menos de 1 ns. Los resultados numéricos han sido comparados con un modelo  $\sigma$  adaptado [123, 125, 126, 128, 129, 131], obteniendo un buen ajuste de la velocidad en estado estacionario y del ancho de la DW en función de la perturbación externa dentro del marco de la cinemática invariante de Lorentz. Se demostraron eventos interesantes de proliferación de DWs en el régimen de propagación supermagnónica, un efecto discutido previamente, por ejemplo, en la Ref. [124].

Un punto curioso que podría abordarse en un trabajo futuro con mayor detalle, surge de la aparente ausencia de una contribución de energía tipo Zeeman del término LOT en el Hamiltoniano de Mn<sub>2</sub>Au. Creemos, en términos generales, que los requisitos energéticos para un evento de nucleación padre-hijo se cumplen debido al propio movimiento relativista de la DW, donde el LOT actúa como una perturbación del sistema AFM acoplado, y el complejo conjunto de contribuciones energéticas en la celda unitaria impulsa un transporte eficiente de DW. La idea, entonces, es comprobar si se puede establecer un vínculo directo entre la energía de una DW padre en propagación y la velocidad resultante de la textura magnética hija en estado estacionario, así como si pueden formularse analíticamente condiciones óptimas y controladas de nucleación. Además, una extensión obvia de la complejidad del modelo numérico requiere el cálculo simultáneo de la dinámica de la imanación y la temperatura con la descripción de un objeto numérico tridimensional en lugar del sistema en cadena que modelamos. La introducción de fluctuaciones térmicas podría proporcionar una forma de desacoplar o romper la simetría del LOT en configuraciones

de DW de  $180^\circ$ , pero también permitiría poner a prueba la eficiencia de la cinemática de  $90^\circ$  en una imagen numérica más cercana a las condiciones experimentales.

## Capítulo 5

En este capítulo final de resultados, abordamos una ruta de manipulación térmica ultrarrápida de MDs y DWs en un sistema de prueba FiM Tb/Co. Los principales objetivos de este trabajo fueron replicar los resultados de HI-AOS obtenidos en las Refs. [32, 34] y probar la hipótesis de precesión en el plano, que se cree que está responsable por este mecanismo de inversión. Para ello, seguimos un procedimiento de investigación en dos pasos, utilizando primero una descripción TMspin y posteriormente un modelo micromagnético a gran escala, ambos construidos en torno a ecuaciones LLB ferromagnéticas acopladas por un intercambio AFM.

El papel principal del modelo TMspin, fue determinar las propiedades magnéticas de equilibrio de la bicapa Tb/Co, como la variación de la imanación neta con la temperatura y el acoplamiento entre capas, así como reproducir los ciclos de histéresis experimentales presentados en [34, 312] o discutidos de forma privada con nuestros colaboradores de SPINTEC. Curiosamente, aunque este marco TMspin no puede capturar dinámicas de imanación incoherentes como la nucleación de dominios o el movimiento de DWs, obtuvimos un acuerdo cuantitativo con el rango de coercitividad experimental, a temperatura ambiente y en la región de imanación dominante de Co. Como una extensión del trabajo presentado en las Refs. [33, 44], probamos la hipótesis de inclinación de la EA en una simulación de AOS sin campo dentro del modelo TMspin, comparando el resultado con un modelo de macroespín bajo condiciones idénticas de calentamiento láser. Queda por verse en un trabajo futuro si los parámetros del material pueden optimizarse para obtener AOS tanto en fs como en ps dentro del marco TMspin, en contraste con la inversión observada recientemente sólo con excitación en el rango del ps.

En una segunda fase, construimos un modelo micromagnético a gran escala de Tb/Co basado en la parametrización TMspin, incluyendo cálculos del campo desimánador, así como una distribución de inclinaciones locales de la EA alrededor de la dirección perpendicular Oz. Probamos la hipótesis precesional de HI-AOS propuesta en las Refs. [32, 34] para parámetros de pulso láser óptimos según los resultados TMspin, pero no pudimos confirmarla debido a la pequeña amplitud de la dinámica de imanación en el plano. Para solucionar este problema, creemos que sesgar la distribución de la EA alejándola del valor medio de  $0^\circ$  podría ser un primer paso para estimular dinámicas más intensas en el plano. Un resultado numérico interesante surgió en el caso del calentamiento laser por encima del punto Curie del Co, que, aunque difiere de la cinemática de AOS observada experimentalmente, reproduce el patrón de dominio de tipo anillos tanto para excitación en fs como en ps y muestra dinámicas cualitativamente similares a las de tipo precesional en experimentos. Aunque, en nuestra opinión, las hipótesis planteadas en las Refs. [32, 34] requieren una confirmación adicional, el trabajo aquí presentado representa un paso importante en esta dirección.

Finalmente, el papel del Tb o Dy en contraste con el Gd en relación al HI-AOS, sigue siendo una cuestión abierta e interesante dentro de la comunidad de magnetismo ultrarrápido. Si la distribución de inclinaciones de la EA es validada para Tb/Co, surge una pregunta importante: ¿qué impediría que se formule una hipótesis similar en el caso de Gd/Co o incluso en una muestra Co/Pt tradicional, así como el diseño de manera artificial de irregularidades a nivel granular para promover un mecanismo de inversión similar?



## Appendix A

# Supporting information for Chapter 3

The additional information presented here corresponds to the results discussed in Chapter 3.

### A.1 Instant modification of the magnetisation vector length in the chain model

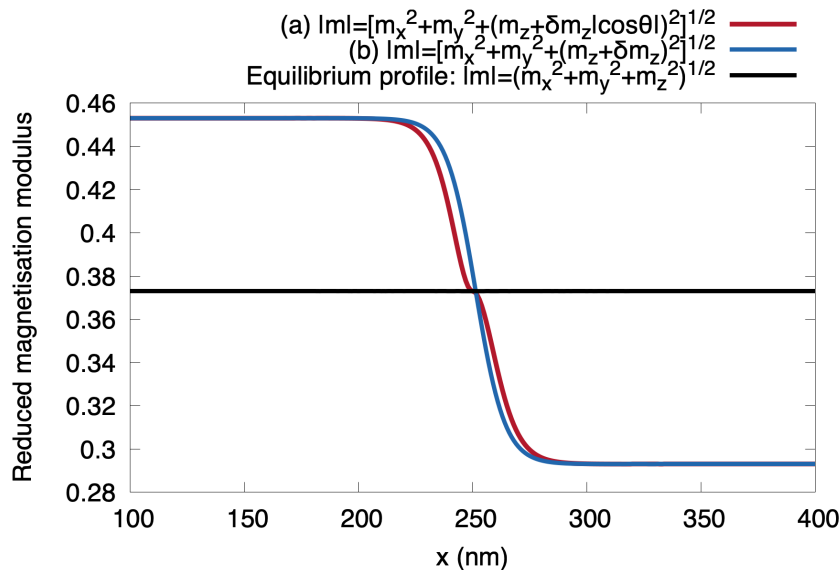


FIGURE A.1: Instant deformation of the magnetisation modulus in a 1D macrospin chain model due to the modification of the out-of-plane magnetisation component. (a) Spatially non-uniform deformation of  $m_z$  via the  $\delta m_z |\cos \theta|$  contribution. (b) Spatially uniform deformation of  $m_z$  via the  $\delta m_z$  contribution. The black line denotes the magnetisation modulus across the macrospin chain before the deformation is introduced.

The longitudinal deformation of the magnetisation profile —red curve in Figure 3.1 (a)—is obtained adding the contribution  $\delta m_z |\cos \theta|$  to the equilibrium magnetisation along  $Oz$  analytically described by Eq. (3.2). Due to this procedure, the modulus  $|\vec{m}|$  of the macrospin vectors along the chain will deform as a result of the relationship  $|\vec{m}| = \sqrt{(m_x)^2 + (m_y)^2 + (m_z^*)^2}$ , where  $m_z^*$  for a given macrospin is defined by Eq. (3.3) giving rise to the modulus profile depicted with a continuous red line in Figure 3.1 (b) of Chapter 3 as well as here in Figure A.1. The origin of the kink in this profile is the  $|\cos \theta|$  term which comes into effect far away from the domains,

nearing the center of the wall. This can be better understood if we visually compare the following situations: (a) We add to the equilibrium magnetisation profile along  $Oz$  (3.2) the contribution  $\delta m_z |\cos \theta|$ . (b) We add solely the  $\delta m_z$  term. In Fig. A.1 one can see the effect scenarios (a), (b) have on the magnetisation modulus across the macrospin chain compared to the equilibrium case. Although not shown here we qualitatively observe the same tendency of the wall to displace towards the “hot” region irrespective of scenario (a) or (b). The presence of the  $|\cos \theta|$  term closely follows the case of the inverse Faraday Effect [161] where the modification of the  $m_z$  component is maximum along the propagation direction (in our case  $\vec{k} \parallel Oz$ ) of the incident beam and largely reduced for an orthogonal direction. The exact magnetisation gradient profile should be adapted to the opto-magnetic effect under study. However, a comparison between different magnetisation gradient profiles is beyond the scope of Chapter 3 which we underline aims to show a non-thermal, longitudinal deformation at the fs time-scale can lead to domain-wall displacement.

## A.2 Field resolved contribution to the longitudinal and transverse dynamics of a single macrospin in the 1D model

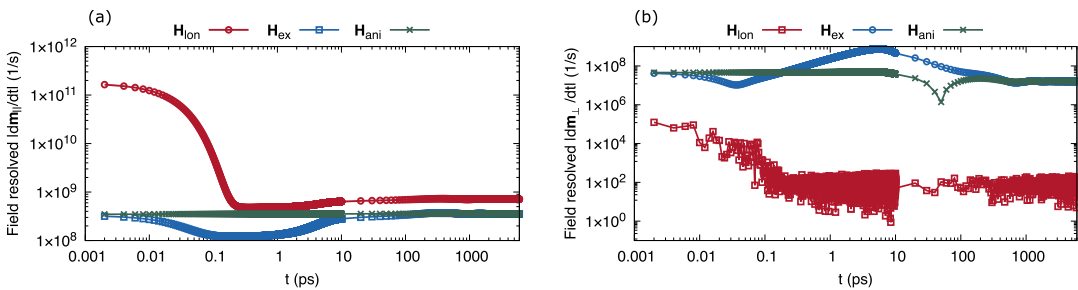


FIGURE A.2: Field resolved contribution to the longitudinal (a) and transverse (b) dynamics according to the LLB equation, for  $\delta m_z = 0.16$  at  $T = 0.91T_c$  and corresponding to the macrospin found at  $x = 252.5$  nm along the chain. This region is of relevance since the DW center of mass displaces in its vicinity as discussed in Figure 3.3. To obtain the plots, we calculate the modulus of the second and third terms given in (2.16) as a function of time. The time axis is represented in logarithmic scale.

The micromagnetic exchange and anisotropy fields  $\vec{H}_{\text{ex}}, \vec{H}_{\text{ani}}$  play an important role in the DW dynamics on the ps-ns timescale compared to the longitudinal field  $\vec{H}_{\text{ion}}$  which is more relevant at the fs timescale in the presence of the magnetisation modulus gradient. In Figure A.2, we present the time varying contribution of these three fields to the longitudinal (a) and transverse (b) dynamics of a single macrospin found at  $x = 252.5$  nm (approximately the center of the 1D chain) for the maximum longitudinal deformation discussed in Figure 3.2. This point in space is relevant since the DW center of mass displaces in the vicinity of this region. As it can be seen in subplot (a), the longitudinal dynamics are dominated by the  $\vec{H}_{\text{ion}}$  field whose contribution is several orders of magnitude larger than  $\vec{H}_{\text{ex}}$  and  $\vec{H}_{\text{ani}}$  up to 0.1 ps, in accordance with the life-time of the magnetisation gradient discussed in Figure 3.1(b). On the contrary,  $\vec{H}_{\text{ion}}$  does not directly contribute to the transverse dynamics (only by angular momentum transfer between  $|\frac{d\vec{m}}{dt}|_{\parallel}$  and  $|\frac{d\vec{m}}{dt}|_{\perp}$ ) since it always acts parallel to the direction of  $\vec{m}$ , hence the dominant  $\vec{H}_{\text{ex}}$  and  $\vec{H}_{\text{ani}}$  contributions in subplot (b). These latter fields manifest stronger between 0.1 to 100 ps matching the time-scale of the  $m_x$  peak displacement presented in Figure 3.2(d).

### A.3 Domain-wall displacement for a fixed ratio between the transient and equilibrium magnetisation

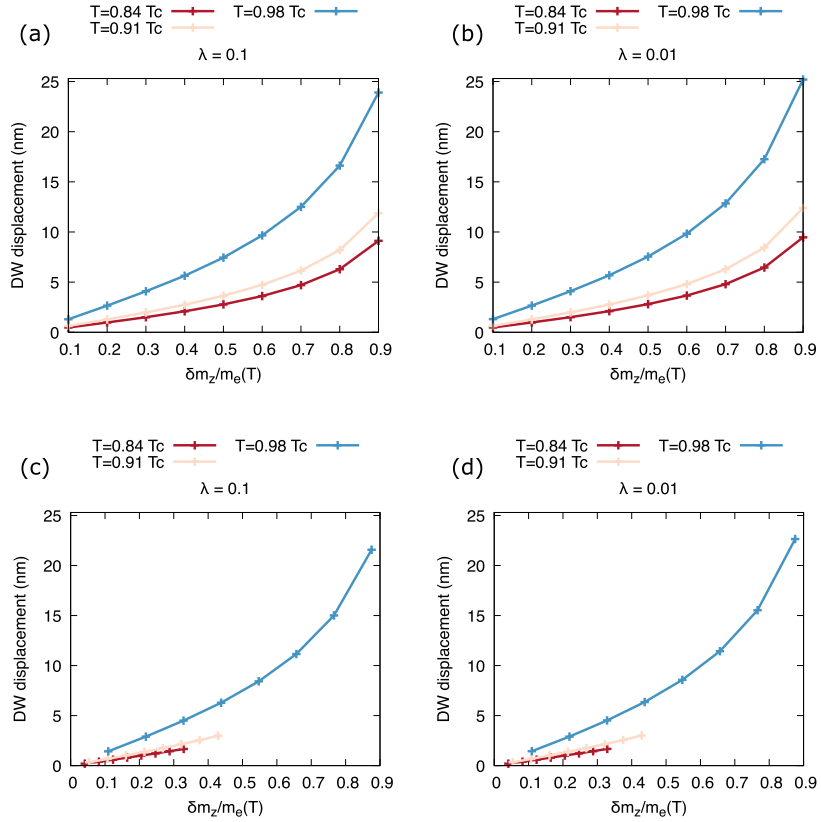


FIGURE A.3: Final DW displacement as a function of  $\delta m_z/m_e(T)$  and  $T$  for two different damping values:  $\lambda = 0.1$  and  $\lambda = 0.01$ . In subplots (a), (b) we plot the results of novel calculations for  $T = 0.84T_c$ ,  $0.91T_c$  and  $0.98T_c$  varying the  $\delta m_z/m_e(T)$  ratio from 0.1 to 0.9. In subplots (c) and (d) we represent the data in Figure 3.4 with the  $\delta m_z$  values rescaled to the corresponding  $m_e(T)$  value.

Here we recalculate the final DW displacement in the 1D model, keeping the  $\delta m_z/m_e(T)$  ratio constant in the range of 0.1 to 0.9, for all temperature values previously discussed in section 3.3.1:  $T = 0.84T_c$ ,  $0.91T_c$ , and  $0.98T_c$ . For comparison, we rescale the horizontal axis in Figure 3.4 to the corresponding  $m_e(T)$  value. The results are presented here in Fig. A.3, for two damping values:  $\lambda = 0.1$  and  $\lambda = 0.01$ . As seen in subplots (a) and (b), the final DW displacement is proportional to the  $\delta m_z/m_e(T)$  ratio, a result which helps to recover the parabolic-like behaviour at all three distinct temperatures compared to subplots (c) and (d) which denote the original but rescaled data in Figure 3.4. Nonetheless, for a fixed  $\delta m_z/m_e(T)$  ratio, the DW displacement increases as a function of the working temperature  $T$ , a sign the relaxation rate to equilibrium as discussed in Section 3.3.1 is relevant in controlling the life-time of the magnetisation gradient and consequently the motion of the wall. Consistent with this assumption and equation (3.6), a smaller damping increases the final displacement slightly, an effect more visible in the case of  $T = 0.98T_c$ .



## Appendix B

# Supporting information for Chapter 4

The additional information presented here corresponds to the results discussed in Chapter 4.

### B.1 Obtaining the antiferromagnetic equations of motion in Mn<sub>2</sub>Au

Let us start from the LLG equations of motion for the two sublattice vectors  $\vec{S}_{A,B}$  which in the limit  $\lambda \ll 1$  can be written in the LL form [127, 128]:

$$\dot{\vec{S}}_A = -\gamma \vec{S}_A \times \vec{H}_{\text{eff}}^A - \gamma \lambda \vec{S}_A \times (\vec{S}_A \times \vec{H}_{\text{eff}}^A), \quad (\text{B.1})$$

$$\dot{\vec{S}}_B = -\gamma \vec{S}_B \times \vec{H}_{\text{eff}}^B - \gamma \lambda \vec{S}_B \times (\vec{S}_B \times \vec{H}_{\text{eff}}^B). \quad (\text{B.2})$$

Defining the effective fields  $\vec{H}_{\text{eff}}^{n,l} = -\frac{1}{\gamma \hbar} \frac{\delta \mathcal{E}(\vec{n}, \vec{l})}{\delta(\vec{n}, \vec{l})}$  and  $\vec{H}_{\text{eff}}^{A,B} = -\frac{2}{\gamma \hbar} \frac{\delta \mathcal{E}(\vec{n}, \vec{l})}{\delta(\vec{S}_A, \vec{S}_B)}$  with respect to the energy density given in (4.23), we can write down the following relationships:

$$\vec{H}_{\text{eff}}^A = \vec{H}_{\text{eff}}^n - \vec{H}_{\text{eff}}^l, \quad (\text{B.3})$$

$$\vec{H}_{\text{eff}}^B = \vec{H}_{\text{eff}}^n + \vec{H}_{\text{eff}}^l. \quad (\text{B.4})$$

To recover Eqs. (4.28),(4.29) in the main text, we will consider a set of linear combinations employing the expressions given in (B.1), (B.2) and making use of the  $\vec{H}_{\text{eff}}^{A,B}$  definitions in (B.3), (B.4). Let us first subtract the vector precession terms in (B.1), (B.2) and equate the result with a new variable  $\vec{P}_-$  to obtain:

$$\vec{P}_- = -\gamma \left[ \vec{S}_B \times (\vec{H}_{\text{eff}}^n + \vec{H}_{\text{eff}}^l) - \vec{S}_A \times (\vec{H}_{\text{eff}}^n - \vec{H}_{\text{eff}}^l) \right] \quad (\text{B.5})$$

$$= -\gamma \left[ \vec{S}_B \times \vec{H}_{\text{eff}}^n + \vec{S}_B \times \vec{H}_{\text{eff}}^l - \vec{S}_A \times \vec{H}_{\text{eff}}^n + \vec{S}_A \times \vec{H}_{\text{eff}}^l \right] \quad (\text{B.6})$$

$$= -\gamma \left[ (\vec{S}_B - \vec{S}_A) \times \vec{H}_{\text{eff}}^n \right]. \quad (\text{B.7})$$

Making use of the relationship  $\vec{l} = (\vec{S}_B - \vec{S}_A)/2$  we arrive at the expression:

$$\frac{1}{2} \vec{P}_- = -\gamma \vec{l} \times \vec{H}_{\text{eff}}^n. \quad (\text{B.8})$$

This term evidently describes a precession of the Néel vector due to the presence of the net magnetisation vector  $\vec{n}$ . We can follow a similar procedure for the transverse components in the right hand side part of the LLG equations (B.1), (B.2). Taking their difference and defining the vector  $\vec{T}_-$  we obtain:

$$\vec{T}_- = -\gamma\lambda \left\{ \vec{S}_B \times \left[ \vec{S}_B \times \left( \vec{H}_{\text{eff}}^n + \vec{H}_{\text{eff}}^l \right) \right] - \vec{S}_A \times \left[ \vec{S}_A \times \left( \vec{H}_{\text{eff}}^n - \vec{H}_{\text{eff}}^l \right) \right] \right\} \quad (\text{B.9})$$

$$= -\gamma\lambda \left[ \vec{S}_B \times \left( \vec{S}_B \times \vec{H}_{\text{eff}}^l \right) + \vec{S}_A \times \left( \vec{S}_A \times \vec{H}_{\text{eff}}^l \right) \right] \approx 0. \quad (\text{B.10})$$

In expression (B.10) we assume the transverse dynamics of the sublattice magnetisation vectors  $\vec{S}_{A,B}$  due to the  $\vec{H}_{\text{eff}}^l$  field are negligible since the three vectors  $\vec{S}_A$ ,  $\vec{S}_B$  and  $\vec{H}_{\text{eff}}^l$  are nearly collinear under the strong AFM exchange coupling.

In turn, adding the precession terms in Eqs. (B.1), (B.2) and equating the result with the vector  $\vec{P}_+$ , we have:

$$\vec{P}_+ = -\gamma \left[ \vec{S}_B \times \left( \vec{H}_{\text{eff}}^n + \vec{H}_{\text{eff}}^l \right) + \vec{S}_A \times \left( \vec{H}_{\text{eff}}^n - \vec{H}_{\text{eff}}^l \right) \right] \quad (\text{B.11})$$

$$= -\gamma \left[ \vec{S}_B \times \vec{H}_{\text{eff}}^n + \vec{S}_B \times \vec{H}_{\text{eff}}^l + \vec{S}_A \times \vec{H}_{\text{eff}}^n - \vec{S}_A \times \vec{H}_{\text{eff}}^l \right] \quad (\text{B.12})$$

$$= -\gamma \left[ \left( \vec{S}_B - \vec{S}_A \right) \times \vec{H}_{\text{eff}}^l \right]. \quad (\text{B.13})$$

Writing  $\vec{P}_+$  in terms of the Néel vector  $\vec{l}$  we finally arrive at:

$$\frac{1}{2} \vec{P}_+ = -\gamma \vec{l} \times \vec{H}_{\text{eff}}^l. \quad (\text{B.14})$$

This precession term is crucial to the fast reorientation of the two-sublattice magnetisation system under the optical torque excitation and the subsequent DW dynamics as shown in Fig. 4.4 of Chapter 4.

Lastly, we add the transverse components in the AFM LLG equations to obtain:

$$\vec{T}_+ = -\gamma\lambda \left\{ \vec{S}_B \times \left[ \vec{S}_B \times \left( \vec{H}_{\text{eff}}^n + \vec{H}_{\text{eff}}^l \right) \right] + \vec{S}_A \times \left[ \vec{S}_A \times \left( \vec{H}_{\text{eff}}^n - \vec{H}_{\text{eff}}^l \right) \right] \right\} \quad (\text{B.15})$$

$$= -\gamma\lambda \left[ \vec{S}_B \times \left( \vec{S}_B \times \vec{H}_{\text{eff}}^n \right) + \vec{S}_A \times \left( \vec{S}_A \times \vec{H}_{\text{eff}}^n \right) \right] \quad (\text{B.16})$$

$$= -\gamma\lambda \left[ \vec{S}_B \times \left( \vec{S}_B \times \vec{H}_{\text{eff}}^n \right) - \vec{S}_A \times \left( \vec{S}_B \times \vec{H}_{\text{eff}}^n \right) \right] \quad (\text{B.17})$$

$$= -\gamma\lambda \left[ \left( \vec{S}_B - \vec{S}_A \right) \times \left( \vec{S}_B \times \vec{H}_{\text{eff}}^n \right) \right]. \quad (\text{B.18})$$

Since  $\vec{l} = (\vec{S}_B - \vec{S}_A)/2$  and  $\vec{S}_B = \vec{n} + \vec{l}$  we obtain in the end:

$$\frac{1}{2} \vec{T}_+ = -\gamma\lambda \left[ \vec{l} \times \left( \vec{l} \times \vec{H}_{\text{eff}}^n \right) + \vec{l} \times \left( \vec{n} \times \vec{H}_{\text{eff}}^n \right) \right] \quad (\text{B.19})$$

$$= -\gamma\lambda \vec{l} \times \left( \vec{l} \times \vec{H}_{\text{eff}}^n \right). \quad (\text{B.20})$$

In obtaining expression (B.20) we cancel the term proportional to  $\vec{n}$  since  $\vec{n} \parallel \vec{H}_{\text{eff}}^n$ . Moreover, since  $\vec{l} \cdot \vec{n} = 0$  we can no longer neglect the contribution in (B.20) to the transverse dynamics of the Néel vector compared to the expression given in (B.10).

Finally, we can rewrite the LLG equations in (B.1) and (B.2) using the vectors  $\vec{n}$  and  $\vec{l}$  as:

$$\dot{\vec{l}} = \frac{\vec{P}_-}{2} + \frac{\vec{T}_-}{2} = -\gamma \vec{l} \times \vec{H}_{\text{eff}}^n, \quad (\text{B.21})$$

$$\dot{\vec{n}} = \frac{\vec{P}_+}{2} + \frac{\vec{T}_+}{2} = -\gamma \vec{l} \times \vec{H}_{\text{eff}}^l - \gamma \lambda \vec{l} \times (\vec{l} \times \vec{H}_{\text{eff}}^n). \quad (\text{B.22})$$

At this point it is clear we can introduce the  $\dot{\vec{l}}$  term in Eq. (B.22). After rearrangement we finally recover the AFM equations given in (4.28), (4.29):

$$\dot{\vec{l}} = \gamma \vec{H}_{\text{eff}}^n \times \vec{l}, \quad (\text{B.23})$$

$$\dot{\vec{n}} = \left( \gamma \vec{H}_{\text{eff}}^l - \lambda \vec{l} \right) \times \vec{l}. \quad (\text{B.24})$$

This result can otherwise be obtained employing a variational approach based on constructing an appropriate Lagrangian density  $\mathcal{L}$  and making use of the Euler-Lagrange equations.

## B.2 Two-temperature model of laser induced heating

We consider the physical effects from heating caused by the pulse durations and laser intensities used in our simulations on the Mn<sub>2</sub>Au sample and substrate using the TTM described by Eqs. (B.25), (B.26). Laser energy is added using the source term  $S(t)$ . Constants are from [277] and are consistent with experimental results in [110, 187].  $C_e = 1 \times 10^3 \text{ J/(Km}^3)$  is the electron heat capacity,  $C_{\text{ph}} = 6.934 \times 10^6 \text{ J/(Km}^3)$  is the phonon heat capacity,  $G = 2.5 \times 10^{17} \text{ J/(Ksm}^3)$  the electron-phonon coupling constant, and  $\tau_e$  the substrate cooling factor. For electron temperature  $T_e$ , phonon temperature  $T_{\text{ph}}$ , and substrate temperature  $T_s$ , the differential equation without diffusion is:

$$C_e \frac{dT_e}{dt} = G_{\text{ep}}(T_{\text{ph}} - T_e) + S(t), \quad (\text{B.25})$$

$$C_{\text{ph}} \frac{dT_{\text{ph}}}{dt} = G_{\text{ep}}(T_e - T_{\text{ph}}) + C_{\text{ph}} \frac{(T_e - T_{\text{ph}})}{\tau_e}. \quad (\text{B.26})$$

The relationship between laser intensity and laser power is described in detail in [215]. For simplicity we approximate a depth-independent absorption.

$$S(t) = \frac{2\sqrt{\ln 2}}{\delta \tau_p \sqrt{\pi}} F \exp \left[ -4\ln 2 \left( \frac{t}{\tau_p} \right)^2 \right], \quad (\text{B.27})$$

where,  $F$  is the fluence and  $\delta$  the film thickness for which we assume 50 nm as in [110]. Since according to Figure 4.5, fast DW kinematics in the range of tens of km/s can be achieved in a wide laser intensity range, we make our estimations considering a Gaussian laser pulse with peak intensity 0.15 GW/cm<sup>2</sup> and full width at half maximum of 40 ps. The cooling rate which influences the peak electron and phonon temperatures depends largely on the substrate, for which here we consider two reasonably distinct values of 20 and 100 ps. According to the calculations presented in Fig. B.1, the maximum electron/phonon heating can be contained only to a couple of hundreds of K above room temperature which is one order of magnitude lower

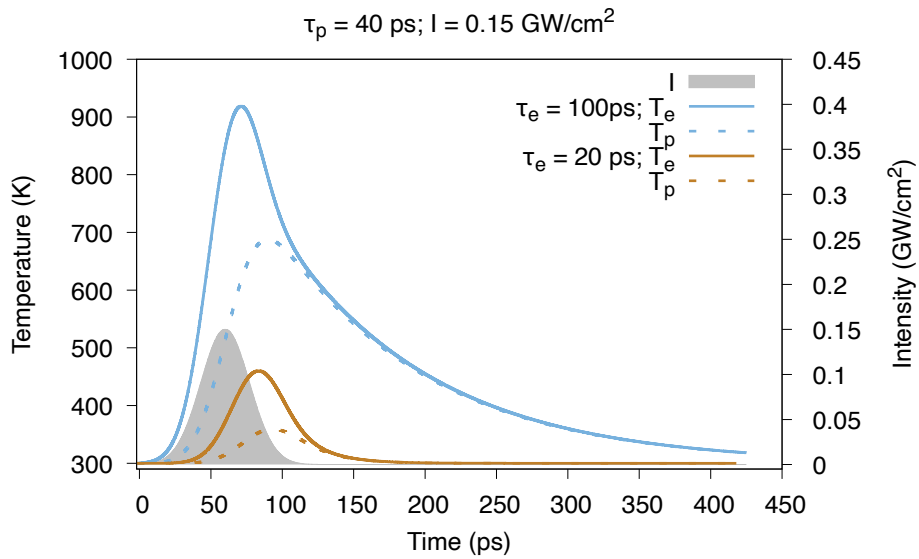


FIGURE B.1: Ultrafast heating estimation during single pulse excitation. TTM of Gaussian laser-pulse heating for peak intensity of  $I = 0.15 \text{ GW/cm}^2$  and full width at half maximum of 40 ps. We consider two distinct cooling rates of 20 ps and 100 ps.

compared to a Si or  $\text{Al}_2\text{O}_3$  substrate melting temperature —the latter was recently used in Ref. [110] —and the Néel temperature of  $\text{Mn}_2\text{Au}$ .



## Appendix C

# Supporting information for Chapter 5

The additional information presented here corresponds to the results discussed in Chapter 5.

### C.1 Analysis of longitudinal/transverse magnetisation contributions to the static hysteresis cycles in the TMspin Tb/Co model

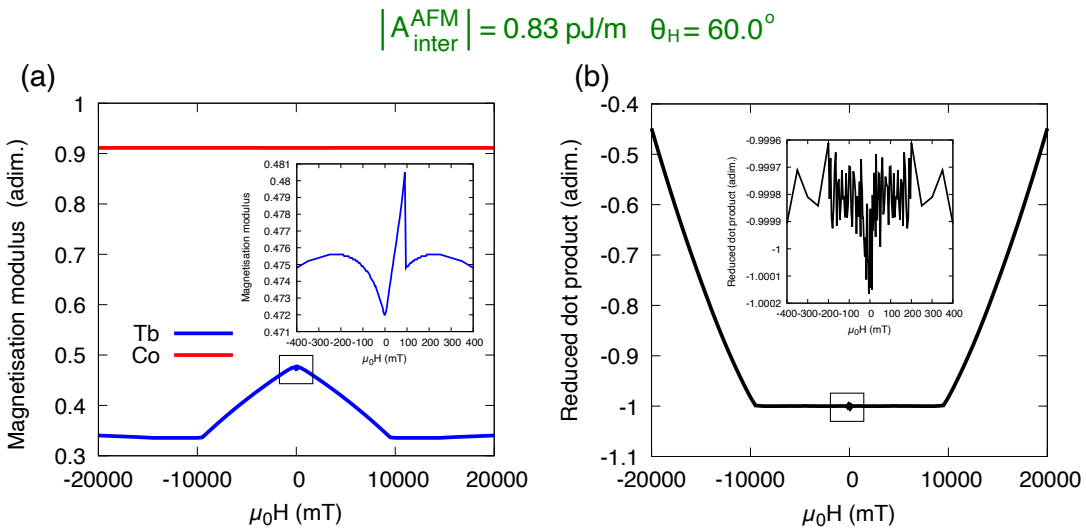


FIGURE C.1: Example of longitudinal contributions to the apparent non-coherent magnetisation reversal in Figure 5.4 for  $|A_{\text{inter}}^{\text{AFM}}| = 0.83 \text{ pJ/m}$  and  $\theta_H = 60^\circ$ . (a) Magnetisation modulus  $m_{\text{Co}}$  and  $m_{\text{Tb}}$  going from negative to positive field values along the hysteresis cycle. Interestingly, the Co magnetisation remains unaffected even for fields of up to  $\pm 20$  T while Tb exhibits clear longitudinal modifications due to the competition between the applied Zeeman field and the AFM coupling. (b) Reduced dot product  $(\vec{m}_{\text{Co}} \cdot \vec{m}_{\text{Tb}}) / (m_{\text{Co}} m_{\text{Tb}})$  between the Tb and Co macrospins which distinctly shows the deviations from the antiparallel alignment start to occur only for fields in the vicinity of  $\pm 10$  T. The insets correspond to a reduced magnetic field region of  $\pm 400$  mT.

In Figure 5.4 a series of static hysteresis cycles we obtain within the Tb/Co TM-spin model (and in particular subplots e and f) display an apparent non-coherent magnetisation reversal otherwise typical for two component magnetic systems. This shape in the hysteresis cycles does not appear however from a canting in between the antiferromagnetically coupled macrospins but rather from in-phase rotations of

the two subsystems and due to small longitudinal modifications of the macrospin vector lengths. Here we display this for the particular case of  $|A_{\text{inter}}^{\text{AFM}}| = 0.83 \text{ pJ/m}$  and  $\theta_H = 60^\circ$ . In Figure C.1 we analyse first of all the magnetisation modulus of Tb and Co for a wide range of applied magnetic field values in just one particular hysteresis branch (going from negative to positive field values). Interestingly, while the Co phase remains unaffected even for fields up to  $\pm 20 \text{ T}$ , the magnetisation of the Tb subsystem largely depends on the competition between the applied Zeeman field and the  $|A_{\text{inter}}^{\text{AFM}}|$  contribution. In subplot (b) we display on the other hand the reduced dot product  $(\vec{m}_{\text{Co}} \cdot \vec{m}_{\text{Tb}}) / (m_{\text{Co}} m_{\text{Tb}})$  for the same field range as in (a) which demonstrates the canting from the perfect antiparallel state between the macrospin vectors appears in the vicinity of  $\pm 10 \text{ T}$ . Thus, the magnetisation rotation of the Tb/Co macrospins in the range  $\pm 400 \text{ mT}$  displayed in subplot (e) of Figure 5.4 must be entirely coherent. Although not shown here, the same analysis was carried out for all other subplots in Figure 5.4 reaching similar conclusions.

## C.2 Short time-scale longitudinal fluctuations in the AOS dynamics of the Tb/Co bilayer

In Figure C.2 we display the short time-scale dynamics of the magenta, green and orange regions previously discussed in Figure 5.11 of the main text. In subplots (a),(c) and (e) we present the  $m_z$  magnetisation dynamics for both Tb and Co while in the subplots beneath (b), (d) and (f) we give the associated field amplitudes of the exchange, anisotropy and demagnetisation contributions. In all given situations, a residual transient ferromagnetic-like component fluctuates around the  $m_z = 0$  value in this near-complete demagnetised state. These fluctuations are in direct connection with the time variation of the interlayer exchange field contributions which we remind the reader are determined by a temperature-independent  $A_{\text{inter}}^{\text{AFM}}$  constant. Interestingly, the final  $m_z$  configuration during this fluctuating regime (just before the cooling process starts) seems to corresponds also with the switched/non-switched state hundreds of ps later as observed in Figure 5.11.

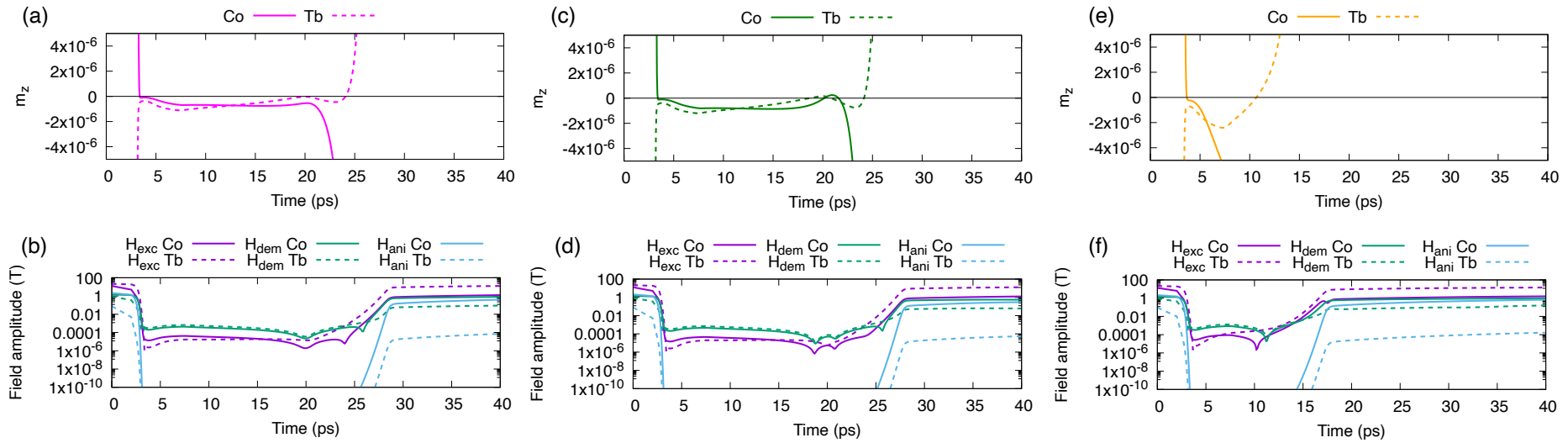


FIGURE C.2: Short time-scale longitudinal fluctuations in the AOS dynamics of the Tb/Co bilayer for the magenta, green and orange regions previously discussed in Figure 5.11 of the main text ( $F = 1.9 \text{ mJ/cm}^2$  and  $t_p = 1 \text{ ps}$ ). In (a), (c) and (e) we display the  $Oz$  magnetisation component for both Tb and Co while in (b), (d) and (f) we present the associated exchange, anisotropy and demagnetising field amplitudes. In the latter plots the y-axis is logarithmic for better visualisation.



# Bibliography

- <sup>1</sup>IDC, Statista, Various sources, “Volume of data/information created, captured, copied, and consumed worldwide from 2010 to 2023, with forecasts from 2024 to 2028 (in zettabytes) [Graph], May 31, 2024”, [Link accessed: 13/01/2025](#).
- <sup>2</sup>Patel, Sonal, “THE BIG PICTURE: How Much Power Will Data Centers Consume? (Infographic)”, [Link accessed: 15/01/2025](#).
- <sup>3</sup>Graham, Sean, “The Financial Impact of Increased Consumption and Rising Electricity Rates in Datacenter Facilities Spending”, [Link accessed: 15/01/2025](#).
- <sup>4</sup>IEA, “World Energy Outlook 2024”, [Link accessed: 15/01/2025](#).
- <sup>5</sup>imec, “Smaller, better, faster: imec presents chip scaling roadmap”, [Link accessed: 17/01/2025](#).
- <sup>6</sup>D. Kimovski, N. Saurabh, M. Jansen, A. Aral, A. Al-Dulaimy, A. B. Bondi, A. Galletta, A. V. Papadopoulos, A. Iosup, and R. Prodan, “Beyond Von Neumann in the computing continuum: architectures, applications, and future directions”, *IEEE Internet Computing* **28**, 6–16 (2024).
- <sup>7</sup>S. S. Parkin, M. Hayashi, and L. Thomas, “Magnetic domain-wall racetrack memory”, *Science* **320**, 190–194 (2008).
- <sup>8</sup>E. Beaurepaire, J. C. Merle, A. Daunois, and J. Y. Bigot, “Ultrafast Spin Dynamics in Ferromagnetic Nickel”, *Physical Review Letters* **76**, 4250 (1996).
- <sup>9</sup>B. Koopmans, M. Van Kampen, J. T. Kohlhepp, and W. J. De Jonge, “Ultrafast Magneto-Optics in Nickel: Magnetism or Optics?”, *Physical Review Letters* **85**, 844 (2000).
- <sup>10</sup>J. Hohlfeld, T. Gerrits, M. Bilderbeek, T. Rasing, H. Awano, and N. Ohta, “Fast magnetization reversal of GdFeCo induced by femtosecond laser pulses”, *Physical Review B* **65**, 012413 (2001).
- <sup>11</sup>C. D. Stanciu, A. V. Kimel, F. Hansteen, A. Tsukamoto, A. Itoh, A. Kirilyuk, and T. Rasing, “Ultrafast spin dynamics across compensation points in ferrimagnetic GdFeCo: The role of angular momentum compensation”, *Physical Review B* **73**, 220402(R) (2006).
- <sup>12</sup>C. D. Stanciu, F. Hansteen, A. V. Kimel, A. Kirilyuk, A. Tsukamoto, A. Itoh, and T. Rasing, “All-optical magnetic recording with circularly polarized light”, *Physical Review Letters* **99**, 047601 (2007).
- <sup>13</sup>I. Radu, K. Vahaplar, C. Stamm, T. Kachel, N. Pontius, H. A. Dürr, T. A. Ostler, J. Barker, R. F. Evans, R. W. Chantrell, A. Tsukamoto, A. Itoh, A. Kirilyuk, T. Rasing, and A. V. Kimel, “Transient ferromagnetic-like state mediating ultrafast reversal of antiferromagnetically coupled spins”, *Nature* **472**, 205–208 (2011).
- <sup>14</sup>A. Eschenlohr, M. Battiato, P. Maldonado, N. Pontius, T. Kachel, K. Holldack, R. Mitzner, A. Föhlisch, P. M. Oppeneer, and C. Stamm, “Ultrafast spin transport as key to femtosecond demagnetization”, *Nature Materials* **12**, 332–336 (2013).

- <sup>15</sup>R. John, M. Berritta, D. Hinzke, C. Müller, T. Santos, H. Ulrichs, P. Nieves, J. Walowski, R. Mondal, O. Chubykalo Fesenko, J. McCord, P. M. Oppeneer, U. Nowak, and M. Münzenberg, "Magnetisation switching of FePt nanoparticle recording medium by femtosecond laser pulses", *Scientific Reports* **7**, 4114 (2017).
- <sup>16</sup>A. V. Kimel, R. V. Pisarev, J. Hohlfeld, and T. Rasing, "Ultrafast Quenching of the Antiferromagnetic Order in [Formula presented]: Direct Optical Probing of the Phonon-Magnon Coupling", *Physical Review Letters* **89**, 287401 (2002).
- <sup>17</sup>F. Hansteen, A. Kimel, A. Kirilyuk, and T. Rasing, "Femtosecond photomagnetic switching of spins in ferrimagnetic garnet films", *Physical Review Letters* **95**, 047402 (2005).
- <sup>18</sup>F. Atoneche, A. M. Kalashnikova, A. V. Kimel, A. Stupakiewicz, A. Maziewski, A. Kirilyuk, and T. Rasing, "Large ultrafast photoinduced magnetic anisotropy in a cobalt-substituted yttrium iron garnet", *Physical Review B* **81**, 214440 (2010).
- <sup>19</sup>A. Stupakiewicz, K. Szerenos, D. Afanasiev, A. Kirilyuk, and A. V. Kimel, "Ultrafast nonthermal photo-magnetic recording in a transparent medium", *Nature* **542**, 71–74 (2017).
- <sup>20</sup>A. Stupakiewicz, K. Szerenos, M. D. Davydova, K. A. Zvezdin, A. K. Zvezdin, A. Kirilyuk, and A. V. Kimel, "Selection rules for all-optical magnetic recording in iron garnet", *Nature Communications* **10**, 612 (2019).
- <sup>21</sup>E. Kojima, R. Shimano, Y. Hashimoto, S. Katsumoto, Y. Iye, and M. Kuwata Gono-kami, "Observation of the spin-charge thermal isolation of ferromagnetic [Formula presented] by time-resolved magneto-optical measurements", *Physical Review B* **68**, 193203 (2003).
- <sup>22</sup>D. M. Wang, Y. H. Ren, X. Liu, J. K. Furdyna, M. Grimsditch, and R. Merlin, "Light-induced magnetic precession in (Ga,Mn)As slabs: Hybrid standing-wave Damon-Eshbach modes", *Physical Review B* **75**, 233308 (2007).
- <sup>23</sup>P. Němec, E. Rozkotová, N. Tesařová, F. Trojánek, E. De Ranieri, K. Olejník, J. Zemen, V. Novák, M. Cukr, P. Malý, and T. Jungwirth, "Experimental observation of the optical spin transfer torque", *Nature Physics* **8**, 411–415 (2012).
- <sup>24</sup>A. J. Ramsay, P. E. Roy, J. A. Haigh, R. M. Otxoa, A. C. Irvine, T. Janda, R. P. Campon, B. L. Gallagher, and J. Wunderlich, "Optical Spin-Transfer-Torque-Driven Domain-Wall Motion in a Ferromagnetic Semiconductor", *Physical Review Letters* **114**, 067202 (2015).
- <sup>25</sup>T. Ishii, H. Yamakawa, T. Kanaki, T. Miyamoto, N. Kida, H. Okamoto, M. Tanaka, and S. Ohya, "Ultrafast magnetization modulation induced by the electric field component of a terahertz pulse in a ferromagnetic-semiconductor thin film", *Scientific Reports* **8**, 6901 (2018).
- <sup>26</sup>A. Kirilyuk, A. V. Kimel, and T. Rasing, "Ultrafast optical manipulation of magnetic order", *Reviews of Modern Physics* **82**, 2731–2784 (2010).
- <sup>27</sup>T. A. Ostler, J. Barker, R. F. Evans, R. W. Chantrell, U. Atxitia, O. Chubykalo Fesenko, S. El Moussaoui, L. Le Guyader, E. Mengotti, L. J. Heyderman, F. Nolting, A. Tsukamoto, A. Itoh, D. Afanasiev, B. A. Ivanov, A. M. Kalashnikova, K. Vahaplar, J. Mentink, A. Kirilyuk, T. Rasing, and A. V. Kimel, "Ultrafast heating as a sufficient stimulus for magnetization reversal in a ferrimagnet", *Nature Communications* **3**, 666 (2012).

- <sup>28</sup>M. L. Lalieu, M. J. Peeters, S. R. Haenen, R. Lavrijsen, and B. Koopmans, "Deterministic all-optical switching of synthetic ferrimagnets using single femtosecond laser pulses", *Physical Review B* **96**, 220411(R) (2017).
- <sup>29</sup>C. Banerjee, N. Teichert, K. E. Siewierska, Z. Gercsi, G. Y. Atcheson, P. Stamenov, K. Rode, J. M. Coey, and J. Besbas, "Single pulse all-optical toggle switching of magnetization without gadolinium in the ferrimagnet Mn<sub>2</sub>RuxGa", *Nature Communications* **11**, 4444 (2020).
- <sup>30</sup>J. Wei, B. Zhang, M. Hehn, W. Zhang, G. Malinowski, Y. Xu, W. Zhao, and S. Mangin, "All-optical Helicity-Independent Switching State Diagram in Gd-Fe-Co Alloys", *Physical Review Applied* **15**, 054065 (2021).
- <sup>31</sup>A. Ceballos, A. Pattabi, A. El-Ghazaly, S. Ruta, C. P. Simon, R. F. L. Evans, T. Ostler, R. W. Chantrell, E. Kennedy, M. Scott, J. Bokor, and F. Hellman, "Role of element-specific damping in ultrafast, helicity-independent, all-optical switching dynamics in amorphous (Gd,Tb)Co thin films", *Physical Review B* **103**, 024438 (2021).
- <sup>32</sup>Y. Peng, D. Salomoni, G. Malinowski, W. Zhang, J. Hohlfeld, L. D. Buda-Prejbeanu, J. Gorchon, M. Vergès, J. X. Lin, D. Lacour, R. C. Sousa, I. L. Prejbeanu, S. Mangin, and M. Hehn, "In-plane reorientation induced single laser pulse magnetization reversal", *Nature Communications* **14**, 5000 (2023).
- <sup>33</sup>D. Salomoni, Y. Peng, L. Farcis, S. Auffret, M. Hehn, G. Malinowski, S. Mangin, B. Dieny, L. D. Buda-Prejbeanu, R. C. Sousa, and I. L. Prejbeanu, "Field-Free All-Optical Switching and Electrical Readout of Tb / Co -Based Magnetic Tunnel Junctions", *Physical Review Applied* **20**, 034070 (2023).
- <sup>34</sup>K. Mishra, T. G. Blank, C. S. Davies, L. Avilés-Félix, D. Salomoni, L. D. Buda-Prejbeanu, R. C. Sousa, I. L. Prejbeanu, B. Koopmans, T. Rasing, A. V. Kimel, and A. Kirilyuk, "Dynamics of all-optical single-shot switching of magnetization in tb/co multilayers", *Physical Review Research* **5**, 023163 (2023).
- <sup>35</sup>D. Hinzke and U. Nowak, "Domain wall motion by the magnonic spin seebeck effect", *Physical Review Letters* **107**, 027205 (2011).
- <sup>36</sup>F. Schlickeiser, U. Ritzmann, D. Hinzke, and U. Nowak, "Role of entropy in domain wall motion in thermal gradients", *Physical Review Letters* **113**, 097201 (2014).
- <sup>37</sup>S. Moretti, V. Raposo, E. Martinez, and L. Lopez-Diaz, "Domain wall motion by localized temperature gradients", *Physical Review B* **95**, 064419 (2017).
- <sup>38</sup>O. Sandig, Y. A. Shokr, J. Vogel, S. Valencia, F. Kronast, and W. Kuch, "Movement of magnetic domain walls induced by single femtosecond laser pulses", *Physical Review B* **94**, 054414 (2016).
- <sup>39</sup>Y. A. Shokr, O. Sandig, M. Erkovan, B. Zhang, M. Bernien, A. A. Ünal, F. Kronast, U. Parlak, J. Vogel, and W. Kuch, "Steering of magnetic domain walls by single ultrashort laser pulses", *Physical Review B* **99**, 214404 (2019).
- <sup>40</sup>K. H. Prabhakara, T. B. Shapaeva, M. D. Davydova, K. A. Zvezdin, A. K. Zvezdin, C. S. Davies, A. Kirilyuk, T. Rasing, and A. V. Kimel, "Controlling magnetic domain wall velocity by femtosecond laser pulses", *Journal of Physics: Condensed Matter* **33**, 075802 (2020).

- <sup>41</sup>C. A. Hassdenteufel, B. Hebler, C. Schubert, A. Liebig, M. Teich, M. Helm, M. Aeschlimann, M. Albrecht, R. Bratschitsch, A Hassdenteufel, B Hebler, C Schubert, A Liebig, M Albrecht, and R Bratschitsch, "Thermally assisted all-optical helicity dependent magnetic switching in amorphous fe100–xtbx alloy films", *Advanced Materials* **25**, 3122–3128 (2013).
- <sup>42</sup>U. Parlak, R. Adam, D. E. Bürgler, S. Gang, and C. M. Schneider, "Optically induced magnetization reversal in [Co/Pt]N multilayers: Role of domain wall dynamics", *Physical Review B* **98**, 214443 (2018).
- <sup>43</sup>J. Wei, "Magnetization manipulation induced by spin current and ultrafast laser", *PhD Thesis. Université de Lorraine ; Beihang university (Pékin)* (2021).
- <sup>44</sup>D. Salomoni, "All-optical switching of spintronic devices", *PhD Thesis. SPINTEC - SPINtronique et TEchnologie des Composants* (2024).
- <sup>45</sup>A. V. Kimel, A. Kirilyuk, P. A. Usachev, R. V. Pisarev, A. M. Balbashov, and T. Rasing, "Ultrafast non-thermal control of magnetization by instantaneous photomagnetic pulses", *Nature* **435**, 655–657 (2005).
- <sup>46</sup>S. I. Anisimov, B. L. Kapeliovich, T. L. Perelman, S. I. Anisimov, B. L. Kapeliovich, and T. L. Perelman, "Electron emission from metal surfaces exposed to ultrashort laser pulses", *Zhurnal Eksperimentalnoi i Teoreticheskoi Fiziki* **66**, 776–781 (1974).
- <sup>47</sup>O. Emile and J. Emile, "Energy, linear momentum, and angular momentum of light: what do we measure?", *Annalen der Physik* **530**, 1800111 (2018).
- <sup>48</sup>A. S. Disa, M. Fechner, T. F. Nova, B. Liu, M. Först, D. Prabhakaran, P. G. Radaelli, and A. Cavalleri, "Polarizing an antiferromagnet by optical engineering of the crystal field", *Nature Physics* **16**, 937–941 (2020).
- <sup>49</sup>D. Afanasiev, J. R. Hortensius, B. A. Ivanov, A. Sasani, E. Bousquet, Y. M. Blanter, R. V. Mikhaylovskiy, A. V. Kimel, and A. D. Caviglia, "Ultrafast control of magnetic interactions via light-driven phonons", *Nature Materials* **20**, 607–611 (2021).
- <sup>50</sup>F. Formisano, R. M. Dubrovin, R. V. Pisarev, A. M. Kalashnikova, and A. V. Kimel, "Laser-induced THz magnetism of antiferromagnetic CoF<sub>2</sub>", *Journal of Physics: Condensed Matter* **34**, 225801 (2022).
- <sup>51</sup>T. Janda, P. E. Roy, R. M. Otxoa, Z. Šobáň, A. Ramsay, A. C. Irvine, F. Trojanek, M. Surýnek, R. P. Campion, B. L. Gallagher, P. Němec, T. Jungwirth, and J. Wunderlich, "Inertial displacement of a domain wall excited by ultra-short circularly polarized laser pulses", *Nature Communications* **8**, 15226 (2017).
- <sup>52</sup>R. Medapalli, D. Afanasiev, D. K. Kim, Y. Quessab, S. Manna, S. A. Montoya, A. Kirilyuk, T. Rasing, A. V. Kimel, and E. E. Fullerton, "Multiscale dynamics of helicity-dependent all-optical magnetization reversal in ferromagnetic co/pt multilayers", *Physical Review B* **96**, 224421 (2017).
- <sup>53</sup>Y. Quessab, R. Medapalli, M. S. El Hadri, M. Hehn, G. Malinowski, E. E. Fullerton, and S. Mangin, "Helicity-dependent all-optical domain wall motion in ferromagnetic thin films", *Physical Review B* **97**, 054419 (2018).
- <sup>54</sup>B. Zhang, Y. Xu, W. Zhao, D. Zhu, X. Lin, M. Hehn, G. Malinowski, D. Ravelosona, and S. Mangin, "Energy-Efficient Domain-Wall Motion Governed by the Interplay of Helicity-Dependent Optical Effect and Spin-Orbit Torque", *Physical Review Applied* **11**, 034001 (2019).
- <sup>55</sup>Y. Quessab, M. Deb, J. Gorchon, M. Hehn, G. Malinowski, and S. Mangin, "Resolving the role of magnetic circular dichroism in multishot helicity-dependent all-optical switching", *Physical Review B* **100**, 024425 (2019).

- <sup>56</sup>K. T. Yamada, C. S. Davies, F. Ando, T. Li, T. Ono, T. Rasing, A. V. Kimel, and A. Kirilyuk, "Magnetization reversal of a ferromagnetic pt/co/pt film by helicity dependent absorption of visible to near-infrared laser pulses", *Physical Review B* **111**, L020406 (2025).
- <sup>57</sup>K. T. Yamada, S. Ruta, A. V. Kimel, K. H. Prabhakara, T. Li, F. Ando, S. Semin, T. Ono, A. Kirilyuk, R. W. Chantrell, and T. Rasing, "Ultrafast ferromagnetic spin switching by a single pair of optical pulses", *IEEE Transactions on Magnetics*, [10.1109/TMAG.2025.3535670](https://doi.org/10.1109/TMAG.2025.3535670) (2025).
- <sup>58</sup>C. H. Lambert, S. Mangin, B. S. S. Varaprasad, Y. K. Takahashi, M. Hehn, M. Cinchetti, G. Malinowski, K. Hono, Y. Fainman, M. Aeschlimann, and E. E. Fullerton, "All-optical control of ferromagnetic thin films and nanostructures", *Science* **345**, 1337–1340 (2014).
- <sup>59</sup>S. Mangin, M. Gottwald, C. H. Lambert, D. Steil, V. Uhlíř, L. Pang, M. Hehn, S. Alebrand, M. Cinchetti, G. Malinowski, Y. Fainman, M. Aeschlimann, and E. E. Fullerton, "Engineered materials for all-optical helicity-dependent magnetic switching", *Nature Materials* **13**, 286–292 (2014).
- <sup>60</sup>A. F. Kabychenkov, "Magnetic phase transitions in a light wave", *Zhurnal Eksperimentalnoi i Teoreticheskoi Fiziki* **100**, 1219–1237 (1991).
- <sup>61</sup>A. R. Khorsand, M. Savoini, A. Kirilyuk, A. V. Kimel, A. Tsukamoto, A. Itoh, and T. Rasing, "Role of magnetic circular dichroism in all-optical magnetic recording", *Physical Review Letters* **108**, 127205 (2012).
- <sup>62</sup>M. O. Ellis, E. E. Fullerton, and R. W. Chantrell, "All-optical switching in granular ferromagnets caused by magnetic circular dichroism", *Scientific Reports* **6**, 30522 (2016).
- <sup>63</sup>J. Gorchon, Y. Yang, and J. Bokor, "Model for multishot all-thermal all-optical switching in ferromagnets", *Physical Review B* **94**, 020409 (2016).
- <sup>64</sup>A. Fert, "Nobel lecture: origin, development, and future of spintronics", *Reviews of Modern Physics* **80**, 1517–1530 (2008).
- <sup>65</sup>A. Hirohata, K. Yamada, Y. Nakatani, L. Prejbeanu, B. Diény, P. Pirro, and B. Hillebrands, "Review on spintronics: principles and device applications", *Journal of Magnetism and Magnetic Materials* **509**, 166711 (2020).
- <sup>66</sup>B. Dieny, I. L. Prejbeanu, K. Garello, P. Gambardella, P. Freitas, R. Lehndorff, W. Raberg, U. Ebels, S. O. Demokritov, J. Akerman, A. Deac, P. Pirro, C. Adelmann, A. Anane, A. V. Chumak, A. Hirohata, S. Mangin, S. O. Valenzuela, M. C. Onbaşlı, M. d'Aquino, G. Prenat, G. Finocchio, L. Lopez-Diaz, R. Chantrell, O. Chubykalo-Fesenko, and P. Bortolotti, "Opportunities and challenges for spintronics in the microelectronics industry", *Nature Electronics* **3**, 446–459 (2020).
- <sup>67</sup>A. Manchon, H. C. Koo, J. Nitta, S. M. Frolov, and R. A. Duine, "New perspectives for rashba spin-orbit coupling", *Nature Materials* **14**, 871–882 (2015).
- <sup>68</sup>A. Manchon and A. Belabbes, "Spin-orbitronics at transition metal interfaces", *Solid State Physics* **68**, 1–89 (2017).
- <sup>69</sup>Y. Cao, G. Xing, H. Lin, N. Zhang, H. Zheng, and K. Wang, "Prospect of spin-orbitronic devices and their applications", *iScience* **23**, 101614 (2020).
- <sup>70</sup>F. Trier, P. Noël, J. V. Kim, J. P. Attané, L. Vila, and M. Bibes, "Oxide spin-orbitronics: spin-charge interconversion and topological spin textures", *Nature Reviews Materials* **7**, 258–274 (2022).

- <sup>71</sup>D. Go, D. Jo, H. W. Lee, M. Kläui, and Y. Mokrousov, "Orbitronics: orbital currents in solids", *Europhysics Letters* **135**, 37001 (2021).
- <sup>72</sup>D. Jo, D. Go, G.-M. Choi, and H.-W. Lee, "Spintronics meets orbitronics: emergence of orbital angular momentum in solids", *npj Spintronics* **2**, 19 (2024).
- <sup>73</sup>D. Go, Y. Mokrousov, and M. Kläui, "Non-equilibrium orbital angular momentum for orbitronics", *Europhysics News* **55**, 28–31 (2024).
- <sup>74</sup>P. Němec, M. Fiebig, T. Kampfrath, and A. V. Kimel, "Antiferromagnetic opto-spintronics", *Nature Physics* **14**, 229–241 (2018).
- <sup>75</sup>J. T. Gish, D. Lebedev, T. W. Song, V. K. Sangwan, and M. C. Hersam, "Van der waals opto-spintronics", *Nature Electronics* **7**, 336–347 (2024).
- <sup>76</sup>C. S. Davies and A. Kirilyuk, "Epsilon-near-zero regime for ultrafast opto-spintronics", *npj Spintronics* **2**, 1–6 (2024).
- <sup>77</sup>S. Parkin and S. H. Yang, "Memory on the racetrack", *Nature Nanotechnology* **10**, 195–198 (2015).
- <sup>78</sup>B. B. Vermeulen, B. Sorée, S. Couet, K. Temst, and V. D. Nguyen, "Progress in spin logic devices based on domain-wall motion", *Micromachines* **15**, 696 (2024).
- <sup>79</sup>A. Sengupta, Y. Shim, and K. Roy, "Proposal for an all-spin artificial neural network: emulating neural and synaptic functionalities through domain wall motion in ferromagnets", *IEEE Transactions on Biomedical Circuits and Systems* **10**, 1152–1160 (2016).
- <sup>80</sup>B. H. Rimmler, B. Pal, and S. S. Parkin, "Non-collinear antiferromagnetic spintronics", *Nature Reviews Materials* **10**, 109–127 (2025).
- <sup>81</sup>V. Baltz, A. Manchon, M. Tsoi, T. Moriyama, T. Ono, and Y. Tserkovnyak, "Anti-ferromagnetic spintronics", *Reviews of Modern Physics* **90**, 015005 (2018).
- <sup>82</sup>S. K. Kim, G. S. Beach, K. J. Lee, T. Ono, T. Rasing, and H. Yang, "Ferrimagnetic spintronics", *Nature Materials* **21**, 24–34 (2022).
- <sup>83</sup>D. O. Smith, "Proposal for magnetic domain-wall storage and logic", *IRE Transactions on Electronic Computers EC-10*, 708–711 (1961).
- <sup>84</sup>S. S. Parkin, "Shiftable magnetic shift register and method of using the same.", Google Patents **US6834005B1** (2004).
- <sup>85</sup>K. S. Ryu, S. H. Yang, L. Thomas, and S. S. Parkin, "Chiral spin torque arising from proximity-induced magnetization", *Nature Communications* **5**, 3910 (2014).
- <sup>86</sup>E. Raymenants, O. Bultynck, D. Wan, T. Devolder, K. Garello, L. Souriau, A. Thiam, D. Tsvetanova, Y. Canvel, D. E. Nikonov, I. A. Young, M. Heyns, B. Soree, I. Asselberghs, I. Radu, S. Couet, and V. D. Nguyen, "Nanoscale domain wall devices with magnetic tunnel junction read and write", *Nature Electronics* **4**, 392–398 (2021).
- <sup>87</sup>R. Blasing, A. A. Khan, P. C. Filippou, C. Garg, F. Hameed, J. Castrillon, and S. S. Parkin, "Magnetic racetrack memory: from physics to the cusp of applications within a decade", *Proceedings of the IEEE* **108**, 1303–1321 (2020).
- <sup>88</sup>C. M. Compagnoni, A. Goda, A. S. Spinelli, P. Feeley, A. L. Lacaita, and A. Visconti, "Reviewing the evolution of the nand flash technology", *Proceedings of the IEEE* **105**, 1609–1633 (2017).
- <sup>89</sup>D. H. Smith, "A magnetic shift register employing controlled domain wall motion", *IEEE Transactions on Magnetics* **1**, 281–284 (1965).

- <sup>90</sup>D. A. Allwood, G. Xiong, C. C. Faulkner, D. Atkinson, D. Petit, and R. P. Cowburn, "Magnetic domain-wall logic", *Science* **309**, 1688–1692 (2005).
- <sup>91</sup>J. Curriyan-Incorvia, S. Siddiqui, S. Dutta, E. Evarts, J. Zhang, D. Bono, C. Ross, and M. Baldo, "Logic circuit prototypes for three-terminal magnetic tunnel junctions with mobile domain walls", *Nature Communications* **7**, 10275 (2016).
- <sup>92</sup>X. Zheng, J. Wang, G. Li, X. Lu, W. Li, Y. Wang, L. Chen, H. Yin, J. Wu, and Y. Xu, "Paradigm of magnetic domain wall-based in-memory computing", *ACS Applied Electronic Materials* **2**, 2375–2382 (2020).
- <sup>93</sup>Z. Luo, A. Hrabec, T. P. Dao, G. Sala, S. Finizio, J. Feng, S. Mayr, J. Raabe, P. Gambardella, and L. J. Heyderman, "Current-driven magnetic domain-wall logic", *Nature* **579**, 214–218 (2020).
- <sup>94</sup>M. Alamdar, T. Leonard, C. Cui, B. P. Rimal, L. Xue, O. G. Akinola, T. P. Xiao, J. S. Friedman, C. H. Bennett, M. J. Marinella, and J. A. C. Incorvia, "Domain wall-magnetic tunnel junction spin-orbit torque devices and circuits for in-memory computing", *Applied Physics Letters* **118**, 112401 (2021).
- <sup>95</sup>H. Lin, N. Xu, D. Wang, L. Liu, X. Zhao, Y. Zhou, X. Luo, C. Song, G. Yu, and G. Xing, "Implementation of highly reliable and energy-efficient nonvolatile in-memory computing using multistate domain wall spin-orbit torque device", *Advanced Intelligent Systems* **4**, 2200028 (2022).
- <sup>96</sup>G. Venkat, D. A. Allwood, and T. J. Hayward, "Magnetic domain walls: types, processes and applications", *Journal of Physics D: Applied Physics* **57**, 063001 (2024).
- <sup>97</sup>G. Bourianoff, D. Pinna, M. Sitte, and K. Everschor-Sitte, "Potential implementation of reservoir computing models based on magnetic skyrmions", *AIP Advances* **8**, 055602 (2018).
- <sup>98</sup>N. Hassan, X. Hu, L. Jiang-Wei, W. H. Brigner, O. G. Akinola, F. Garcia-Sanchez, M. Pasquale, C. H. Bennett, J. A. C. Incorvia, and J. S. Friedman, "Magnetic domain wall neuron with lateral inhibition", *Journal of Applied Physics* **124**, 152127 (2018).
- <sup>99</sup>R. V. Ababei, M. O. Ellis, I. T. Vidamour, D. S. Devadasan, D. A. Allwood, E. Vasilaki, and T. J. Hayward, "Neuromorphic computation with a single magnetic domain wall", *Scientific Reports* **11**, 15587 (2021).
- <sup>100</sup>R. W. Dawidek, T. J. Hayward, I. T. Vidamour, T. J. Broomhall, G. Venkat, M. A. Mamoori, A. Mullen, S. J. Kyle, P. W. Fry, N.-J. Steinke, J. F. K. Cooper, F. Maccherozzi, S. S. Dhesi, L. Aballe, M. Foerster, J. Prat, E. Vasilaki, M. O. A. Ellis, D. A. Allwood, R. W. Dawidek, T. J. Hayward, I. T. Vidamour, T. J. Broomhall, G. Venkat, M. A. Mamoori, A. Mullen, S. J. Kyle, D. A. Allwood, P. W. Fry, N. J. Steinke, J. F. K. Cooper, F. Maccherozzi, S. S. Dhesi, L. Aballe, M. Foerster, J. Prat, E. Vasilaki, and M. O. A. Ellis, "Dynamically driven emergence in a nanomagnetic system", *Advanced Functional Materials* **31**, 2008389 (2021).
- <sup>101</sup>T. Leonard, S. Liu, M. Alamdar, H. Jin, C. Cui, O. G. Akinola, L. Xue, T. P. Xiao, J. S. Friedman, M. J. Marinella, C. H. Bennett, and J. A. C. Incorvia, "Shape dependent multi-weight magnetic artificial synapses for neuromorphic computing", *Advanced Electronic Materials* **8**, 2200563 (2022).
- <sup>102</sup>J. A. Vélez, M.-K. Lee, G. Tatara, P.-I. Gavriloaea, J. Ross, D. Laroze, U. Atxitia, R. F. L. Evans, R. W. Chantrell, M. Mochizuki, and R. M. Otxoa, "Chaotic proliferation of relativistic domain walls for reservoir computing", *npj Spintronics* **3**, 1–9 (2025).

- <sup>103</sup>R. A. Duine, K. J. Lee, S. S. Parkin, and M. D. Stiles, "Synthetic antiferromagnetic spintronics", [Nature Physics](#) **14**, 217–219 (2018).
- <sup>104</sup>D. Xiong, Y. Jiang, K. Shi, A. Du, Y. Yao, Z. Guo, D. Zhu, K. Cao, S. Peng, W. Cai, D. Zhu, and W. Zhao, "Antiferromagnetic spintronics: an overview and outlook", [Fundamental Research](#) **2**, 522–534 (2022).
- <sup>105</sup>J. Han, R. Cheng, L. Liu, H. Ohno, and S. Fukami, "Coherent antiferromagnetic spintronics", [Nature Materials](#) **22**, 684–695 (2023).
- <sup>106</sup>P. Wadley, B. Howells, J. Železný, C. Andrews, V. Hills, R. P. Campion, V. Novák, K. Olejník, F. Maccherozzi, S. S. Dhesi, S. Y. Martin, T. Wagner, J. Wunderlich, F. Freimuth, Y. Mokrousov, J. Kuneš, J. S. Chauhan, M. J. Grzybowski, A. W. Rushforth, K. W. Edmonds, B. L. Gallagher, and T. Jungwirth, "Electrical switching of an antiferromagnet", [Science](#) **351**, 587–590.
- <sup>107</sup>S. Y. Bodnar, L. Šmejkal, I. Turek, T. Jungwirth, O. Gomonay, J. Sinova, A. A. Sapozhnik, H. J. Elmers, M. Kläui, and M. Jourdan, "Writing and reading antiferromagnetic Mn<sub>2</sub>Au by Néel spin-orbit torques and large anisotropic magnetoresistance", [Nature Communications](#) **9**, 348 (2018).
- <sup>108</sup>H. Tsai, T. Higo, K. Kondou, T. Nomoto, A. Sakai, A. Kobayashi, T. Nakano, K. Yakushiji, R. Arita, S. Miwa, Y. Otani, and S. Nakatsuji, "Electrical manipulation of a topological antiferromagnetic state", [Nature](#) **580**, 608–613 (2020).
- <sup>109</sup>T. Higo, K. Kondou, T. Nomoto, M. Shiga, S. Sakamoto, X. Chen, D. Nishio-Hamane, R. Arita, Y. Otani, S. Miwa, and S. Nakatsuji, "Perpendicular full switching of chiral antiferromagnetic order by current", [Nature](#) **607**, 474–479 (2022).
- <sup>110</sup>Y. Behovits, A. L. Chekhov, S. Y. Bodnar, O. Gueckstock, S. Reimers, Y. Lytvynenko, Y. Skourski, M. Wolf, T. S. Seifert, O. Gomonay, M. Kläui, M. Jourdan, and T. Kampfrath, "Terahertz Néel spin-orbit torques drive nonlinear magnon dynamics in antiferromagnetic Mn<sub>2</sub>Au", [Nature Communications](#) **14**, 6038 (2023).
- <sup>111</sup>J. Godinho, H. Reichlová, D. Kriegner, V. Novák, K. Olejník, Z. Kašpar, Z. Šobáň, P. Wadley, R. P. Campion, R. M. Otxoa, P. E. Roy, J. Železný, T. Jungwirth, and J. Wunderlich, "Electrically induced and detected Néel vector reversal in a collinear antiferromagnet", [Nature Communications](#) **9**, 4686 (2018).
- <sup>112</sup>T. Moriyama, K. Oda, T. Ohkochi, M. Kimata, and T. Ono, "Spin torque control of antiferromagnetic moments in NiO", [Scientific Reports](#) **8**, 14167 (2018).
- <sup>113</sup>X. Z. Chen, R. Zarzuela, J. Zhang, C. Song, X. F. Zhou, G. Y. Shi, F. Li, H. A. Zhou, W. J. Jiang, F. Pan, and Y. Tserkovnyak, "Antidamping-torque-induced switching in biaxial antiferromagnetic insulators", [Physical Review Letters](#) **120**, 207204 (2018).
- <sup>114</sup>A. D. Din, O. J. Amin, P. Wadley, and K. W. Edmonds, "Antiferromagnetic spintronics and beyond", [npj Spintronics](#) **2**, 25 (2024).
- <sup>115</sup>P. Qin, H. Yan, X. Wang, H. Chen, Z. Meng, J. Dong, M. Zhu, J. Cai, Z. Feng, X. Zhou, L. Liu, T. Zhang, Z. Zeng, J. Zhang, C. Jiang, and Z. Liu, "Room-temperature magnetoresistance in an all-antiferromagnetic tunnel junction", [Nature](#) **613**, 485–489 (2023).
- <sup>116</sup>X. Chen, T. Higo, K. Tanaka, T. Nomoto, H. Tsai, H. Idzuchi, M. Shiga, S. Sakamoto, R. Ando, H. Kosaki, T. Matsuo, D. Nishio-Hamane, R. Arita, S. Miwa, and S. Nakatsuji, "Octupole-driven magnetoresistance in an antiferromagnetic tunnel junction", [Nature](#) **613**, 490–495 (2023).

- <sup>117</sup>S. W. Cheong, M. Fiebig, W. Wu, L. Chapon, and V. Kiryukhin, "Seeing is believing: visualization of antiferromagnetic domains", *npj Quantum Materials* **5**, 3 (2020).
- <sup>118</sup>Y. Yamasaki, H. Nakao, and T. H. Arima, "Augmented magnetic octupole in kagomé 120-degree antiferromagnets detectable via x-ray magnetic circular dichroism", *Journal of the Physical Society of Japan* **89**, 8 (2020).
- <sup>119</sup>N. L. Schryer and L. R. Walker, "The motion of 180° domain walls in uniform dc magnetic fields", *Journal of Applied Physics* **45**, 5406–5421 (1974).
- <sup>120</sup>G. Tatara and H. Kohno, "Theory of Current-Driven Domain Wall Motion: Spin Transfer versus Momentum Transfer", *Physical Review Letters* **92**, 086601 (2004).
- <sup>121</sup>N. Akhmediev and M. Karlsson, "Cherenkov radiation emitted by solitons in optical fibers", *Physical Review A* **51**, 2602 (1995).
- <sup>122</sup>M. Yan, A. Kákay, C. Andreas, and R. Hertel, "Spin-Cherenkov effect and magnonic Mach cones", *Physical Review B* **88**, 220412 (2013).
- <sup>123</sup>O. Gomonay, T. Jungwirth, and J. Sinova, "High Antiferromagnetic Domain Wall Velocity Induced by Néel Spin-Orbit Torques", *Physical Review Letters* **117**, 017202 (2016).
- <sup>124</sup>R. M. Otxoa, P. E. Roy, R. Rama-Eiroa, J. Godinho, K. Y. Guslienko, and J. Wunderlich, "Walker-like domain wall breakdown in layered antiferromagnets driven by staggered spin-orbit fields", *Communications Physics* **3**, 190 (2020).
- <sup>125</sup>I. Baryakhtar and B. Ivanov, "Effective equation of motion for an antiferromagnet in weak magnetic fields", *Fizika Nizkikh Temperatur* **5**, 759–768 (1979).
- <sup>126</sup>B. A. Ivanov and A. K. Kolezhuk, "Solitons with internal degrees of freedom in 1d heisenberg antiferromagnets", *Physical Review Letters* **74**, 1859 (1995).
- <sup>127</sup>A. Zvezdin, "Dynamics of domain walls in weak ferromagnets", *Journal of Experimental and Theoretical Physics Letters* **29**, 605–610 (1979).
- <sup>128</sup>I. V. Bar'yakhtar and B. A. Ivanov, "Nonlinear waves in antiferromagnets", *Solid State Communications* **34**, 545–547 (1980).
- <sup>129</sup>N. Papanicolaou, "Antiferromagnetic domain walls", *Physical Review B* **51**, 15062 (1995).
- <sup>130</sup>E. G. Tveten, T. Müller, J. Linder, and A. Brataas, "Intrinsic magnetization of antiferromagnetic textures", *Physical Review B* **93**, 104408 (2016).
- <sup>131</sup>R. Rama-Eiroa, P. E. Roy, J. M. González, K. Y. Guslienko, J. Wunderlich, and R. M. Otxoa, "Inertial domain wall characterization in layered multisublattice antiferromagnets", *Journal of Magnetism and Magnetic Materials* **560**, 169566 (2022).
- <sup>132</sup>O. Gomonay, M. Kläui, and J. Sinova, "Manipulating antiferromagnets with magnetic fields: ratchet motion of multiple domain walls induced by asymmetric field pulses", *Applied Physics Letters* **109**, 142404 (2016).
- <sup>133</sup>T. Janda, J. Godinho, T. Ostatnický, E. Pfitzner, G. Ulrich, A. Hoehl, S. Reimers, Z. Šobáň, T. Metzger, H. Reichlová, V. Novák, R. P. Campion, J. Heberle, P. Wadley, K. W. Edmonds, O. J. Amin, J. S. Chauhan, S. S. Dhesi, F. Maccherozzi, R. M. Otxoa, P. E. Roy, K. Olejník, P. Němec, T. Jungwirth, B. Kaestner, and J. Wunderlich, "Magneto-Seebeck microscopy of domain switching in collinear antiferromagnet CuMnAs", *Physical Review Materials* **4**, 094413 (2020).

- <sup>134</sup>S. H. Yang, K. S. Ryu, and S. Parkin, "Domain-wall velocities of up to 750ms<sup>-1</sup> driven by exchange-coupling torque in synthetic antiferromagnets", *Nature Nanotechnology* **10**, 221–226 (2015).
- <sup>135</sup>N. Hedrich, K. Wagner, O. V. Pylypovskiy, B. J. Shields, T. Kosub, D. D. Sheka, D. Makarov, and P. Maletinsky, "Nanoscale mechanics of antiferromagnetic domain walls", *Nature Physics* **17**, 574–577 (2021).
- <sup>136</sup>T. Okuno, D. H. Kim, S. H. Oh, S. K. Kim, Y. Hirata, T. Nishimura, W. S. Ham, Y. Futakawa, H. Yoshikawa, A. Tsukamoto, Y. Tserkovnyak, Y. Shiota, T. Moriyama, K. J. Kim, K. J. Lee, and T. Ono, "Spin-transfer torques for domain wall motion in antiferromagnetically coupled ferrimagnets", *Nature Electronics* **2**, 389–393 (2019).
- <sup>137</sup>L. Caretta, M. Mann, F. Büttner, K. Ueda, B. Pfau, C. M. Günther, P. Hessing, A. Churikova, C. Klose, M. Schneider, D. Engel, C. Marcus, D. Bono, K. Bagschik, S. Eisebitt, and G. S. Beach, "Fast current-driven domain walls and small skyrmions in a compensated ferrimagnet", *Nature Nanotechnology* **13**, 1154–1160 (2018).
- <sup>138</sup>K. J. Kim, S. K. Kim, Y. Hirata, S. H. Oh, T. Tono, D. H. Kim, T. Okuno, W. S. Ham, S. Kim, G. Go, Y. Tserkovnyak, A. Tsukamoto, T. Moriyama, K. J. Lee, and T. Ono, "Fast domain wall motion in the vicinity of the angular momentum compensation temperature of ferrimagnets", *Nature Materials* **16**, 1187–1192 (2017).
- <sup>139</sup>T. H. Pham, S. G. Je, P. Vallobra, T. Fache, D. Lacour, G. Malinowski, M. C. Cyrille, G. Gaudin, O. Boulle, M. Hehn, J. C. Rojas-Sánchez, and S. Mangin, "Thermal contribution to the spin-orbit torque in metallic-ferrimagnetic systems", *Physical Review Applied* **9**, 064032 (2018).
- <sup>140</sup>K. Cai, Z. Zhu, J. M. Lee, R. Mishra, L. Ren, S. D. Pollard, P. He, G. Liang, K. L. Teo, and H. Yang, "Ultrafast and energy-efficient spin-orbit torque switching in compensated ferrimagnets", *Nature Electronics* **3**, 37–42 (2020).
- <sup>141</sup>A. Donges, N. Grimm, F. Jakobs, S. Selzer, U. Ritzmann, U. Atxitia, and U. Nowak, "Unveiling domain wall dynamics of ferrimagnets in thermal magnon currents: competition of angular momentum transfer and entropic torque", *Physical Review Research* **2**, 013293 (2020).
- <sup>142</sup>C. D. Stanciu, F. Hansteen, A. V. Kimel, A. Tsukamoto, A. Itoh, A. Kirilyuk, and T. Rasing, "Ultrafast interaction of the angular momentum of photons with spins in the metallic amorphous alloy GdFeCo", *Physical Review Letters* **98**, 207401 (2007).
- <sup>143</sup>A. V. Kimel and M. Li, "Writing magnetic memory with ultrashort light pulses", *Nature Reviews Materials* **4**, 189–200 (2019).
- <sup>144</sup>D. Bedau, H. Liu, J. J. Bouzaglou, A. D. Kent, J. Z. Sun, J. A. Katine, E. E. Fullerton, and S. Mangin, "Ultrafast spin-transfer switching in spin valve nanopillars with perpendicular anisotropy", *Applied Physics Letters* **96**, 022514 (2010).
- <sup>145</sup>M. Gajek, J. J. Nowak, J. Z. Sun, P. L. Trouilloud, E. J. O'Sullivan, D. W. Abraham, M. C. Gaidis, G. Hu, S. Brown, Y. Zhu, R. P. Robertazzi, W. J. Gallagher, and D. C. Worledge, "Spin torque switching of 20 nm magnetic tunnel junctions with perpendicular anisotropy", *Applied Physics Letters* **100**, 132408 (2012).
- <sup>146</sup>K. Garello, C. O. Avci, I. M. Miron, M. Baumgartner, A. Ghosh, S. Auffret, O. Boulle, G. Gaudin, and P. Gambardella, "Ultrafast magnetization switching by spin-orbit torques", *Applied Physics Letters* **105**, 212402 (2014).

- <sup>147</sup>S. Shi, Y. Ou, S. V. Aradhya, D. C. Ralph, and R. A. Buhrman, "Fast low-current spin-orbit-torque switching of magnetic tunnel junctions through atomic modifications of the free-layer interfaces", *Physical Review Applied* **9**, 011002 (2018).
- <sup>148</sup>D. Kumar, H. J. Chung, J. P. Chan, T. Jin, S. T. Lim, S. S. Parkin, R. Sbiaa, and S. N. Piramanayagam, "Ultralow energy domain wall device for spin-based neuromorphic computing", *ACS Nano* **17**, 6261–6274 (2023).
- <sup>149</sup>F. Hoveyda, E. Hohenstein, and S. Smadici, "Heat accumulation and all-optical switching by domain wall motion in co/pd superlattices", *Journal of Physics: Condensed Matter* **29**, 225801 (2017).
- <sup>150</sup>M. L. Lalieu, R. Lavrijsen, and B. Koopmans, "Integrating all-optical switching with spintronics", *Nature Communications* **10**, 110 (2019).
- <sup>151</sup>H. Pezeshki, P. Li, R. Lavrijsen, M. Heck, E. Bente, J. V. D. Tol, and B. Koopmans, "Integrated hybrid plasmonic-photonic device for all-optical switching and reading of spintronic memory", *Physical Review Applied* **19**, 054036 (2023).
- <sup>152</sup>A. K. Mondal, S. Mukhopadhyay, P. Heinig, R. Salikhov, O. Hellwig, and A. Barman, "Femtosecond laser-induced transient magnetization enhancement and ultrafast demagnetization mediated by domain wall origami", *ACS Nano* **18**, 16914–16922 (2024).
- <sup>153</sup>R. Jangid, N. Z. Hagström, M. Madhavi, K. Rockwell, J. M. Shaw, J. A. Brock, M. Pancaldi, D. De Angelis, F. Capotondi, E. Pedersoli, H. T. Nembach, M. W. Keller, S. Bonetti, E. E. Fullerton, E. Iacocca, R. Kukreja, and T. J. Silva, "Extreme domain wall speeds under ultrafast optical excitation", *Physical Review Letters* **131**, 256702 (2023).
- <sup>154</sup>A. V. Kimel, A. Kirilyuk, A. Tsvetkov, R. V. Pisarev, and T. Rasing, "Laser-induced ultrafast spin reorientation in the antiferromagnet TmFeO<sub>3</sub>", *Nature* **2004** **429**, 850–853 (2004).
- <sup>155</sup>T. Kampfrath, A. Sell, G. Klatt, A. Pashkin, S. Mährlein, T. Dekorsy, M. Wolf, M. Fiebig, A. Leitenstorfer, and R. Huber, "Coherent terahertz control of antiferromagnetic spin waves", *Nature Photonics* **5**, 31–34 (2010).
- <sup>156</sup>S. Wienholdt, D. Hinzke, and U. Nowak, "THz switching of antiferromagnets and ferrimagnets", *Physical Review Letters* **108**, 247207 (2012).
- <sup>157</sup>P. Li, T. J. Kools, B. Koopmans, R. Lavrijsen, P. Li, T. J. Kools, B. Koopmans, and R. Lavrijsen, "Ultrafast racetrack based on compensated co/gd-based synthetic ferrimagnet with all-optical switching", *Advanced Electronic Materials* **9**, 2200613 (2023).
- <sup>158</sup>B. Zhang, D. Zhu, Y. Xu, X. Lin, M. Hehn, G. Malinowski, W. Zhao, and S. Mangin, "Optoelectronic domain-wall motion for logic computing", *Applied Physics Letters* **116**, 252403 (2020).
- <sup>159</sup>M. Battiatto, G. Barbalinardo, and P. M. Oppeneer, "Quantum theory of the inverse Faraday effect", *Physical Review B* **89**, 014413 (2014).
- <sup>160</sup>M. Berritta, R. Mondal, K. Carva, and P. M. Oppeneer, "Ab Initio Theory of Coherent Laser-Induced Magnetization in Metals", *Physical Review Letters* **117**, 137203 (2016).
- <sup>161</sup>F. Freimuth, S. Blügel, and Y. Mokrousov, "Laser-induced torques in metallic ferromagnets", *Physical Review B* **94**, 144432 (2016).
- <sup>162</sup>F. Freimuth, S. Blügel, and Y. Mokrousov, "Laser-induced torques in metallic antiferromagnets", *Physical Review B* **103**, 174429 (2021).

- <sup>163</sup>S. Khmelevskyi and P. Mohn, "Layered antiferromagnetism with high Neel temperature in the intermetallic compound Mn<sub>2</sub>Au", *Applied Physics Letters* **93**, 162503 (2008).
- <sup>164</sup>A. B. Shick, S. Khmelevskyi, O. N. Mryasov, J. Wunderlich, and T. Jungwirth, "Spin-orbit coupling induced anisotropy effects in bimetallic antiferromagnets: A route towards antiferromagnetic spintronics", *Physical Review B* **81**, 212409 (2010).
- <sup>165</sup>H. N. Russell, F. A. Saunders, H. N. Russell, and F. A. Saunders, "New regularities in the spectra of the alkaline earths", *ApJ* **61**, 38 (1925).
- <sup>166</sup>D. Jiles, *Introduction to magnetism and magnetic materials, third edition* (CRC Press, Sept. 2015).
- <sup>167</sup>J. M. Coey, *Magnetism and magnetic materials*, Vol. 9780521816144 (Cambridge University Press, Jan. 2010), pp. 1–617.
- <sup>168</sup>F. Hund, *Linienspektren und periodisches system der elemente* (Springer Vienna, 1927).
- <sup>169</sup>J. Stöhr and H. C. Siegmann, *Magnetism: from fundamentals to nanoscale dynamics* (Springer Berlin Heidelberg, 2006).
- <sup>170</sup>R. Skomski, *Simple models of magnetism* (Oxford University Press, Jan. 2008).
- <sup>171</sup>W. Heitler and F. London, "Wechselwirkung neutraler atome und homöopolare bindung nach der quantenmechanik", *Zeitschrift für Physik* **44**, 455–472 (1927).
- <sup>172</sup>W. Heisenberg, "Zur theorie des ferromagnetismus", *Zeitschrift für Physik* **49**, 619–636 (1928).
- <sup>173</sup>R. F. L. Evans, W. J. Fan, P Chureemart, T. A. Ostler, M. O. A. Ellis, and R. W. Chantrell, "Atomistic spin model simulations of magnetic nanomaterials", *Journal of Physics: Condensed Matter* **26**, 103202 (2014).
- <sup>174</sup>I. Žutić, J. Fabian, and S. D. Sarma, "Spintronics: fundamentals and applications", *Reviews of Modern Physics* **76**, 323 (2004).
- <sup>175</sup>C. J. Ballhausen, *Introduction to ligand field theory* (McGraw-Hill, New York, 1962).
- <sup>176</sup>S. Blundell, *Magnetism in condensed matter* (Oxford University Press, 2001).
- <sup>177</sup>I. Dzyaloshinsky, "A thermodynamic theory of "weak" ferromagnetism of anti-ferromagnetics", *Journal of Physics and Chemistry of Solids* **4**, 241–255 (1958).
- <sup>178</sup>T. Moriya, "Anisotropic Superexchange Interaction and Weak Ferromagnetism", *Physical Review* **120**, 91 (1960).
- <sup>179</sup>K. Vahaplar, A. M. Kalashnikova, A. V. Kimel, D. Hinzke, U. Nowak, R. Chantrell, A. Tsukamoto, A. Itoh, A. Kirilyuk, and T. Rasing, "Ultrafast Path for Optical Magnetization Reversal via a Strongly Nonequilibrium State", *Physical Review Letters* **103**, 117201 (2009).
- <sup>180</sup>K. Vahaplar, A. M. Kalashnikova, A. V. Kimel, S. Gerlach, D. Hinzke, U. Nowak, R. Chantrell, A. Tsukamoto, A. Itoh, A. Kirilyuk, and T. Rasing, "All-optical magnetization reversal by circularly polarized laser pulses: Experiment and multiscale modeling", *Physical Review B* **85**, 104402 (2012).
- <sup>181</sup>V. Raposo, R. Guedas, F. García Sánchez, M. A. Hernández, M. Zazo, and E. Martínez, "Micromagnetic Modeling of All Optical Switching of Ferromagnetic Thin Films: The Role of Inverse Faraday Effect and Magnetic Circular Dichroism", *Applied Sciences* **10**, 1307 (2020).

- <sup>182</sup>A. Longman and R. Fedosejevs, "Kilo-Tesla axial magnetic field generation with high intensity spin and orbital angular momentum beams", *Physical Review Research* **3**, 043180 (2021).
- <sup>183</sup>E. Martinez, L. Torres, and L. Lopez-Diaz, "Oscillator based on pinned domain walls driven by direct current", *Physical Review B* **83**, 174444 (2011).
- <sup>184</sup>A. Thiaville, S. Rohart, E. Jué, V. Cros, and A. Fert, "Dynamics of Dzyaloshinskii domain walls in ultrathin magnetic films", *Europhysics Letters* **100**, 57002 (2012).
- <sup>185</sup>A. Hubert and R. Schäfer, *Magnetic domains* (Springer International Publishing, Jan. 2021).
- <sup>186</sup>A. I. Mitsek, P. F. Gaidanskii, and V. N. Pushkar, "Domain structure of uniaxial antiferromagnets. the problem of nucleation", *physica status solidi (b)* **38**, 69–79 (1970).
- <sup>187</sup>V. Grigorev, M. Filianina, Y. Lytvynenko, S. Sobolev, A. R. Pokharel, A. P. Lanz, A. Sapozhnik, A. Kleibert, S. Bodnar, P. Grigorev, Y. Skourski, M. Kläui, H. J. Elmers, M. Jourdan, and J. Demsar, "Optically Triggered Néel Vector Manipulation of a Metallic Antiferromagnet Mn<sub>2</sub>Au under Strain", *ACS Nano* **16**, 20589–20597 (2022).
- <sup>188</sup>P. Hohenberg and W. Kohn, "Inhomogeneous electron gas", *Physical Review* **136**, B864 (1964).
- <sup>189</sup>F. Giustino, *Materials modelling using density functional theory : properties and predictions* (Oxford University Press, 2014).
- <sup>190</sup>P. Elliott, M. Stamenova, J. Simoni, S. Sharma, S. Sanvito, and E. K. U. Gross, "Time-dependent density functional theory for spin dynamics", *Handbook of Materials Modeling*, 841–866 (2020).
- <sup>191</sup>W. F. Brown, "Micromagnetics, domains, and resonance", *Journal of Applied Physics* **30**, S62–S69 (1959).
- <sup>192</sup>W. F. Brown, *Micromagnetics* (John Wiley Sons, New York, 1963).
- <sup>193</sup>W. F. Brown, "Thermal fluctuations of a single-domain particle", *Physical Review* **130**, 1677 (1963).
- <sup>194</sup>A. Lyberatos and R. W. Chantrell, "Thermal fluctuations in a pair of magnetostatically coupled particles", *Journal of Applied Physics* **73**, 6501–6503 (1993).
- <sup>195</sup>O. Chubykalo, J. D. Hannay, M. Wongsam, R. W. Chantrell, and J. M. Gonzalez, "Langevin dynamic simulation of spin waves in a micromagnetic model", *Physical Review B* **65**, 184428 (2002).
- <sup>196</sup>O. Chubykalo, R. Smirnov-Rueda, J. M. Gonzalez, M. A. Wongsam, R. W. Chantrell, and U. Nowak, "Brownian dynamics approach to interacting magnetic moments", *Journal of Magnetism and Magnetic Materials* **266**, 28–35 (2003).
- <sup>197</sup>O. Chubykalo-Fesenko, U. Nowak, R. W. Chantrell, and D. Garanin, "Dynamic approach for micromagnetics close to the Curie temperature", *Physical Review B* **74**, 094436 (2006).
- <sup>198</sup>U. Atxitia, O. Chubykalo-Fesenko, N. Kazantseva, D. Hinzke, U. Nowak, and R. W. Chantrell, "Micromagnetic modeling of laser-induced magnetization dynamics using the Landau-Lifshitz-Bloch equation", *Applied Physics Letters* **91**, 232507 (2007).

- <sup>199</sup>N. Kazantseva, U. Nowak, R. W. Chantrell, J. Hohlfeld, and A. Rebei, "Slow recovery of the magnetisation after a sub-picosecond heat pulse", *Europhysics Letters* **81**, 27004 (2007).
- <sup>200</sup>J. H. Mentink, J. Hellsvik, D. V. Afanasiev, B. A. Ivanov, A. Kirilyuk, A. V. Kimel, O. Eriksson, M. I. Katsnelson, and T. Rasing, "Ultrafast spin dynamics in multi-sublattice magnets", *Physical Review Letters* **108**, 057202 (2012).
- <sup>201</sup>F. Jakobs and U. Atxitia, "Bridging atomistic spin dynamics methods and phenomenological models of single-pulse ultrafast switching in ferrimagnets", *Physical Review B* **106**, 134414 (2022).
- <sup>202</sup>D. Hinzke, U. Nowak, R. W. Chantrell, and O. N. Mryasov, "Orientation and temperature dependence of domain wall properties in fept", *Applied Physics Letters* **90**, 082507 (2007).
- <sup>203</sup>N. Kazantseva, D. Hinzke, U. Nowak, R. W. Chantrell, U. Atxitia, and O. C. Fesenko, "Towards multiscale modeling of magnetic materials: simulations of fept", *Physical Review B* **77**, 184428 (2008).
- <sup>204</sup>R. Moreno, R. F. Evans, S. Khmelevskyi, M. C. Muñoz, R. W. Chantrell, and O. Chubykalo-Fesenko, "Temperature dependent exchange stiffness and domain wall width in Co", *Physical Review B* **94**, 104433 (2016).
- <sup>205</sup>O. Eriksson, A. Bergman, L. Bergqvist, and J. Hellsvik, *Atomistic spin dynamics: foundations and applications* (Oxford University Press, May 2017).
- <sup>206</sup>H. B. Callen and E. Callen, "The present status of the temperature dependence of magnetocrystalline anisotropy, and the  $l(l+1)2$  power law", *Journal of Physics and Chemistry of Solids* **27**, 1271–1285 (1966).
- <sup>207</sup>G. Grinstein and R. H. Koch, "Coarse graining in micromagnetics", *Physical Review Letters* **90**, 4 (2003).
- <sup>208</sup>D. Garanin, "Fokker-Planck and Landau-Lifshitz-Bloch equations for classical ferromagnets", *Physical Review B* **55**, 3050 (1997).
- <sup>209</sup>D. A. Garanin, "Generalized equation of motion for a ferromagnet", *Physica A: Statistical Mechanics and its Applications* **172**, 470–491 (1991).
- <sup>210</sup>A. J. Newell, W. Williams, and D. J. Dunlop, "A generalization of the demagnetizing tensor for nonuniform magnetization", *Journal of Geophysical Research: Solid Earth* **98**, 9551–9555 (1993).
- <sup>211</sup>N. Singh, "Two-temperature model of nonequilibrium electron relaxation: a review", *International Journal of Modern Physics B* **24**, 1141–1158 (2010).
- <sup>212</sup>S. Sadasivam, M. K. Chan, and P. Darancet, "Theory of thermal relaxation of electrons in semiconductors", *Physical Review Letters* **119**, 136602 (2017).
- <sup>213</sup>A. M. Brown, R. Sundararaman, P. Narang, W. A. Goddard, and H. A. Atwater, "Ab initio phonon coupling and optical response of hot electrons in plasmonic metals", *Physical Review B* **94**, 075120 (2016).
- <sup>214</sup>M. An, Q. Song, X. Yu, H. Meng, D. Ma, R. Li, Z. Jin, B. Huang, and N. Yang, "Generalized two-temperature model for coupled phonons in nanosized graphene", *Nano letters* **17**, 5805–5810 (2017).
- <sup>215</sup>L. Jiang and H. L. Tsai, "Improved two-temperature model and its application in ultrashort laser heating of metal films", *Journal of Heat Transfer* **127**, 1167–1173 (2005).

- <sup>216</sup>S. D. Brorson, A. Kazeroonian, J. S. Moodera, D. W. Face, T. K. Cheng, E. P. Ippen, M. S. Dresselhaus, and G. Dresselhaus, "Femtosecond room-temperature measurement of the electron-phonon coupling constant in metallic superconductors", *Physical Review Letters* **64**, 2172 (1990).
- <sup>217</sup>P. B. Corkum, F. Brunel, N. K. Sherman, and T. Srinivasan-Rao, "Thermal response of metals to ultrashort-pulse laser excitation", *Physical Review Letters* **61**, 2886 (1988).
- <sup>218</sup>M. Kaganov, I. Lifshitz, and L. Tanatarov, "Relaxation between Electrons and the Crystalline Lattice", *Journal of Experimental and Theoretical Physics* **4**, 173–178 (1957).
- <sup>219</sup>I. M. Lifshits, M. I. Kaganov, and L. V. Tanatarov, "On the theory of the changes produced in metals by radiation", *The Soviet Journal of Atomic Energy* **6**, 261–270 (1960).
- <sup>220</sup>V. L. Ginzburg and V. P. Shabanskii, "Kineticeskaya temperatura elektronov v metallakh i anomalnaya elektronnaya emissiya", *Doklady Akademii Nauk SSSR* **100**, 445–448 (1955).
- <sup>221</sup>D. Zahn, F. Jakobs, Y. W. Windsor, H. Seiler, T. Vasileiadis, T. A. Butcher, Y. Qi, D. Engel, U. Atxitia, J. Vorberger, and R. Ernststorfer, "Lattice dynamics and ultrafast energy flow between electrons, spins, and phonons in a 3d ferromagnet", *Physical Review Research* **3**, 023032 (2021).
- <sup>222</sup>M. Pankratova, I. P. Miranda, D. Thonig, M. Pereiro, E. Sjöqvist, A. Delin, O. Eriksson, and A. Bergman, "Heat-conserving three-temperature model for ultrafast demagnetization in nickel", *Physical Review B* **106**, 174407 (2022).
- <sup>223</sup>S. Pan, F. Ganss, S. Panda, G. Sellge, C. Banerjee, J. Sinha, O. Hellwig, and A. Barman, "Mechanism of femtosecond laser induced ultrafast demagnetization in ultrathin film magnetic multilayers", *Journal of Materials Science* **57**, 6212–6222 (2022).
- <sup>224</sup>T. Roth, A. J. Schellekens, S. Alebrand, O. Schmitt, D. Steil, B. Koopmans, M. Cinchetti, and M. Aeschlimann, "Temperature dependence of laser-induced demagnetization in Ni: A key for identifying the underlying mechanism", *Physical Review X* **2**, 021006 (2012).
- <sup>225</sup>J. Mendil, P. Nieves, O. Chubykalo-Fesenko, J. Walowski, T. Santos, S. Pisana, and M. Münzenberg, "Resolving the role of femtosecond heated electrons in ultrafast spin dynamics", *Scientific Reports* **4**, 3980 (2014).
- <sup>226</sup>R. Hertel, "Theory of the inverse Faraday effect in metals", *Journal of Magnetism and Magnetic Materials* **303**, L1–L4 (2006).
- <sup>227</sup>M. I. Kurkin, N. B. Bakulina, and R. V. Pisarev, "Transient inverse Faraday effect and ultrafast optical switching of magnetization", *Physical Review B* **78**, 134430 (2008).
- <sup>228</sup>D. Popova, A. Bringer, and S. Blügel, "Theory of the inverse Faraday effect in view of ultrafast magnetization experiments", *Physical Review B* **84**, 214421 (2011).
- <sup>229</sup>I. I. Smolyaninov, C. C. Davis, V. N. Smolyaninova, D. Schaefer, J. Elliott, and A. V. Zayats, "Plasmon-Induced magnetization of metallic nanostructures", *Physical Review B* **71**, 035425 (2005).
- <sup>230</sup>J. Hurst, P. M. Oppeneer, G. Manfredi, and P. A. Hervieux, "Magnetic moment generation in small gold nanoparticles via the plasmonic inverse Faraday effect", *Physical Review B* **94**, 134439 (2018).

- <sup>231</sup>I. D. Tokman and A. V. Shvetsov, "Inverse Faraday effect in crystals of molecular magnets", *Bulletin of the Russian Academy of Sciences: Physics* **73**, 28–31 (2009).
- <sup>232</sup>Z. Jin, H. Ma, D. Li, G. Ma, M. Wang, and C. Zhao, "Femtosecond inverse Faraday effect in magnetic ionic liquid [bmim]FeCl<sub>4</sub>", *Journal of Applied Physics* **109**, 073109 (2011).
- <sup>233</sup>P. Scheid, G. Malinowski, S. Mangin, and S. Lebègue, "Ab initio theory of magnetization induced by light absorption in ferromagnets", *Physical Review B* **100**, 214402 (2019).
- <sup>234</sup>P. Scheid, S. Sharma, G. Malinowski, S. Mangin, and S. Lebègue, "Ab Initio Study of Helicity-Dependent Light-Induced Demagnetization: From the Optical Regime to the Extreme Ultraviolet Regime", *Nano Letters* **21**, 1943–1947 (2021).
- <sup>235</sup>A. Frisk Kockum, A. Miranowicz, S. De Liberato, S. Savasta, and F. Nori, "Ultrastrong coupling between light and matter", *Nature Reviews Physics* **1**, 19–40 (2019).
- <sup>236</sup>H. Hübener, U. De Giovannini, C. Schäfer, J. Andberger, M. Ruggenthaler, J. Faist, and A. Rubio, "Engineering quantum materials with chiral optical cavities", *Nature Materials* **20**, 438–442 (2021).
- <sup>237</sup>A. Barman et al., "The 2021 Magnonics Roadmap", *Journal of Physics: Condensed Matter* **33**, 413001 (2021).
- <sup>238</sup>J. Li, C. J. Yang, R. Mondal, C. Tzschaschel, and S. Pal, "A perspective on nonlinearities in coherent magnetization dynamics", *Applied Physics Letters* **120**, 050501 (2022).
- <sup>239</sup>L. N. Bulaevsky and V. L. Ginzburg, "Temperature dependence of the shape of the domain wall in ferromagnetics and ferroelectrics", *Zhurnal Eksperimentalnoi i Teoreticheskoi Fiziki* **45**, 772–779 (1963).
- <sup>240</sup>V. G. Bar'yakhtar, "Phenomenological description of relaxation processes in magnetic materials", *Zhurnal Eksperimentalnoi i Teoreticheskoi Fiziki* **87**, 1501–1508 (1984).
- <sup>241</sup>V. G. Bar'yakhtar, B. A. Ivanov, T. K. Soboleva, and A. L. Sukstanskii, "Theory of dynamical-soliton relaxation in ferromagnets", *Zhurnal Eksperimentalnoi i Teoreticheskoi Fiziki* **91**, 1454–1465 (1986).
- <sup>242</sup>V. G. Bar'yakhtar, B. A. Ivanov, and K. A. Safaryan, "On the phenomenological description of the damping of the domain walls in ferrite-garnets", *Solid State Communications* **72**, 1117–1121 (1989).
- <sup>243</sup>I. A. Yastremsky, P. M. Oppeneer, and B. A. Ivanov, "Theory of fast time evolution of nonequilibrium spin states in magnetic heterostructures", *Physical Review B* **90**, 024409 (2014).
- <sup>244</sup>I. A. Yastremsky, J. Fassbender, B. A. Ivanov, and D. Makarov, "Enhanced longitudinal relaxation of magnetic solitons in ultrathin films", *Physical Review Applied* **17**, L061002 (2022).
- <sup>245</sup>T. J. Huisman, R. V. Mikhaylovskiy, J. D. Costa, F. Freimuth, E. Paz, J. Ventura, P. P. Freitas, S. Blügel, Y. Mokrousov, T. Rasing, and A. V. Kimel, "Femtosecond control of electric currents in metallic ferromagnetic heterostructures", *Nature Nanotechnology* **11**, 455–458 (2016).
- <sup>246</sup>G. M. Choi, A. Schleife, and D. G. Cahill, "Optical-helicity-driven magnetization dynamics in metallic ferromagnets", *Nature Communications* **8**, 15085 (2017).

- <sup>247</sup>N. Kazantseva, D. Hinzke, R. W. Chantrell, and U. Nowak, "Linear and elliptical magnetization reversal close to the Curie temperature", *Europhysics Letters* **86**, 27006 (2009).
- <sup>248</sup>S. Selzer, L. Salemi, A. Deák, E. Simon, L. Szunyogh, P. M. Oppeneer, and U. Nowak, "Current-induced switching of antiferromagnetic order in Mn<sub>2</sub>Au from first principles", *Physical Review B* **105**, 174416 (2022).
- <sup>249</sup>U. Atxitia and O. Chubykalo-Fesenko, "Ultrafast magnetization dynamics rates within the landau-lifshitz-bloch model", *Physical Review B* **84**, 144414 (2011).
- <sup>250</sup>B. Koopmans, G. Malinowski, F. Dalla Longa, D. Steiauf, M. Fähnle, T. Roth, M. Cinchetti, and M. Aeschlimann, "Explaining the paradoxical diversity of ultrafast laser-induced demagnetization", *Nature Materials* **9**, 259–265 (2009).
- <sup>251</sup>B. Heinrich, J. F. Cochran, M. Kowalewski, J. Kirschner, Z. Celinski, A. S. Arrott, and K. Myrtle, "Magnetic anisotropies and exchange coupling in ultrathin fcc co(001) structures", *Physical Review B* **44**, 9348–9361 (1991).
- <sup>252</sup>J. Lindner, I. Barsukov, C. Raeder, C. Hassel, O. Posth, R. Meckenstock, P. Landeros, and D. L. Mills, "Two-magnon damping in thin films in case of canted magnetization: theory versus experiment", *Physical Review B* **80**, 224421 (2009).
- <sup>253</sup>Y. P. Ivanov, A. Chuvalin, L. G. Vivas, J. Kosel, O. Chubykalo-Fesenko, and M. Vázquez, "Single crystalline cylindrical nanowires – toward dense 3D arrays of magnetic vortices", *Scientific Reports* **6**, 23844 (2016).
- <sup>254</sup>Z. Y. Chen, Z. R. Yan, M. H. Qin, and J. M. Liu, "Landau-Lifshitz-Bloch equation for domain wall motion in antiferromagnets", *Physical Review B* **99**, 214436 (2019).
- <sup>255</sup>G. Tatara and R. M. Otxoa De Zuazola, "Collective coordinate study of spin-wave emission from a dynamic domain wall", *Physical Review B* **101**, 224425 (2020).
- <sup>256</sup>P. Nieves, D. Serantes, U. Atxitia, and O. Chubykalo-Fesenko, "Quantum Landau-Lifshitz-Bloch equation and its comparison with the classical case", *Physical Review B* **90**, 104428 (2014).
- <sup>257</sup>K. Chen and D. P. Landau, "Spin-dynamics study of the dynamic critical behavior of the three-dimensional classical Heisenberg ferromagnet", *Physical Review B* **49**, 3266 (1994).
- <sup>258</sup>R. Chimata, A. Bergman, L. Bergqvist, B. Sanyal, and O. Eriksson, "Microscopic model for ultrafast remagnetization dynamics", *Physical Review Letters* **109**, 157201 (2012).
- <sup>259</sup>J. Brandão, S. Azzawi, A. T. Hindmarch, and D. Atkinson, "Understanding the role of damping and Dzyaloshinskii-Moriya interaction on dynamic domain wall behaviour in platinum-ferromagnet nanowires", *Scientific Reports* **7**, 4569 (2017).
- <sup>260</sup>Y. Yoshimura, K. J. Kim, T. Taniguchi, T. Tono, K. Ueda, R. Hiramatsu, T. Moriyama, K. Yamada, Y. Nakatani, and T. Ono, "Soliton-like magnetic domain wall motion induced by the interfacial Dzyaloshinskii–Moriya interaction", *Nature Physics* **12**, 157–161 (2016).
- <sup>261</sup>W. Wang, M. Albert, M. Beg, M. A. Bisotti, D. Chernyshenko, D. Cortés Ortuño, I. Hawke, and H. Fangohr, "Magnon driven domain wall motion with the Dzyaloshinskii–Moriya interaction", *Physical Review Letters* **114**, 087203 (2015).

- <sup>262</sup>D. Cortés-Ortuño, M. Beg, V. Nehruji, L. Breth, R. Pepper, T. Kluyver, G. Downing, T. Hesjedal, P. Hatton, T. Lancaster, R. Hertel, O. Hovorka, and H. Fangohr, "Proposal for a micromagnetic standard problem for materials with Dzyaloshinskii–Moriya interaction", *New Journal of Physics* **20**, 113015 (2018).
- <sup>263</sup>S. Lepadatu, "Emergence of transient domain wall skyrmions after ultrafast demagnetization", *Physical Review B* **102**, 094402 (2020).
- <sup>264</sup>P. S. Pershan, J. P. Van Der Ziel, and L. D. Malmstrom, "Theoretical Discussion of the Inverse Faraday Effect, Raman Scattering, and Related Phenomena", *Physical Review* **143**, 574 (1966).
- <sup>265</sup>V. I. Belotelov, E. A. Bezus, L. L. Doskolovich, A. N. Kalish, and A. K. Zvezdin, "Inverse Faraday effect in plasmonic heterostructures", *Journal of Physics: Conference Series* **200**, 092003 (2010).
- <sup>266</sup>F. Freimuth, S. Blügel, and Y. Mokrousov, "Laser-induced torques in spin spirals", *Physical Review B* **103**, 054403 (2021).
- <sup>267</sup>T. Jungwirth, X. Marti, P. Wadley, and J. Wunderlich, "Antiferromagnetic spintronics", *Nature Nanotechnology* **11**, 231–241 (2016).
- <sup>268</sup>T. Jungwirth, J. Sinova, A. Manchon, X. Marti, J. Wunderlich, and C. Felser, "The multiple directions of antiferromagnetic spintronics", *Nature Physics* **14**, 200–203 (2018).
- <sup>269</sup>S. H. Yang, K. S. Ryu, and S. Parkin, "Domain-wall velocities of up to 750ms<sup>-1</sup> driven by exchange-coupling torque in synthetic antiferromagnets", *Nature Nanotechnology* **10**, 221–226 (2015).
- <sup>270</sup>J. Lan, W. Yu, and J. Xiao, "Antiferromagnetic domain wall as spin wave polarizer and retarder", *Nature Communications* **8**, 178 (2017).
- <sup>271</sup>S. Zhang and Y. Tserkovnyak, "Antiferromagnet-Based Neuromorphics Using Dynamics of Topological Charges", *Physical Review Letters* **125**, 207202 (2020).
- <sup>272</sup>R. M. Otxoa, G. Tatara, P. E. Roy, and O. Chubykalo-Fesenko, "Tailoring Elastic Scattering of Relativistic Antiferromagnetic Domain Walls", *Scientific Reports* **13**, 21153 (2023).
- <sup>273</sup>J. Železný, H. Gao, K. Výborný, J. Zemen, J. Mašek, A. Manchon, J. Wunderlich, J. Sinova, and T. Jungwirth, "Relativistic néel-order fields induced by electrical current in antiferromagnets", *Physical Review Letters* **113**, 157201 (2014).
- <sup>274</sup>P. Wadley, B. Howells, J. Železný, C. Andrews, V. Hills, R. P. Campion, V. Novák, K. Olejník, F. Maccherozzi, S. S. Dhesi, S. Y. Martin, T. Wagner, J. Wunderlich, F. Freimuth, Y. Mokrousov, J. Kuneš, J. S. Chauhan, M. J. Grzybowski, A. W. Rushforth, K. Edmond, B. L. Gallagher, and T. Jungwirth, "Spintronics: Electrical switching of an antiferromagnet", *Science* **351**, 587–590 (2016).
- <sup>275</sup>P. E. Roy, R. M. Otxoa, and J. Wunderlich, "Robust picosecond writing of a layered antiferromagnet by staggered spin-orbit fields", *Physical Review B* **94**, 014439 (2016).
- <sup>276</sup>K. Olejník, T. Seifert, Z. Kašpar, V. Novák, P. Wadley, R. P. Campion, M. Baumgartner, P. Gambardella, P. Nemec, J. Wunderlich, J. Sinova, P. Kužel, M. Müller, T. Kampfrath, and T. Jungwirth, "Terahertz electrical writing speed in an antiferromagnetic memory", *Science Advances* **4**, eaar3566 (2018).
- <sup>277</sup>R. M. Otxoa, U. Atxitia, P. E. Roy, and O. Chubykalo-Fesenko, "Giant localised spin-Peltier effect due to ultrafast domain wall motion in antiferromagnetic metals", *Communications Physics* **3**, 31 (2020).

- <sup>278</sup>T. Dannegger, M. Berritta, K. Carva, S. Selzer, U. Ritzmann, P. M. Oppeneer, and U. Nowak, "Ultrafast coherent all-optical switching of an antiferromagnet with the inverse Faraday effect", *Physical Review B* **104**, L060413 (2021).
- <sup>279</sup>M. Weissenhofer, F. Foggetti, U. Nowak, and P. M. Oppeneer, "Néel vector switching and terahertz spin-wave excitation in Mn<sub>2</sub>Au due to femtosecond spin-transfer torques", *Physical Review B* **107**, 174424 (2023).
- <sup>280</sup>M. Merte, F. Freimuth, D. Go, T. Adamantopoulos, F. R. Lux, L. Plucinski, O. Gomonay, S. Blügel, and Y. Mokrousov, "Photocurrents, inverse Faraday effect, and photospin Hall effect in Mn<sub>2</sub>Au", *APL Materials* **11**, 71106 (2023).
- <sup>281</sup>J. L. Ross, P.-I. Gavriloaea, F. Freimuth, T. Adamantopoulos, Y. Mokrousov, R. F. L. Evans, R. Chantrell, R. M. Otxoa, and O. Chubykalo-Fesenko, "Ultrafast antiferromagnetic switching of mn<sub>2</sub>au with laser-induced optical torques", *npj Computational Materials* **10**, 234 (2024).
- <sup>282</sup>A. A. Sapozhnik, M. Filianina, S. Y. Bodnar, A. Lamirand, M. A. Mawass, Y. Skourski, H. J. Elmers, H. Zabel, M. Kläui, and M. Jourdan, "Direct imaging of anti-ferromagnetic domains in Mn<sub>2</sub>Au manipulated by high magnetic fields", *Physical Review B* **97**, 134429 (2018).
- <sup>283</sup>S. Jenkins, T. Wagner, O. Gomonay, and K. Everschor-Sitte, "Revealing the ultra-fast domain wall motion in manganese gold through permalloy capping", *Physical Review B* **109**, 224431 (2024).
- <sup>284</sup>M. Gell-Mann and M. Lévy, "The axial vector current in beta decay", *Il Nuovo Cimento* **16**, 705–726 (1960).
- <sup>285</sup>S. J. Orfanidis, "σ models of nonlinear evolution equations", *Physical Review D* **21**, 1513 (1980).
- <sup>286</sup>E. Infeld and G. Rowlands, *Nonlinear waves, solitons and chaos* (Cambridge University Press, July 2000).
- <sup>287</sup>K. Pohlmeyer, "Integrable hamiltonian systems and interactions through quadratic constraints", *Communications in Mathematical Physics* **46**, 207–221 (1976).
- <sup>288</sup>F. D. Haldane, "Nonlinear field theory of large-spin heisenberg antiferromagnets: semiclassically quantized solitons of the one-dimensional easy-axis néel state", *Physical Review Letters* **50**, 1153 (1983).
- <sup>289</sup>F. D. Haldane, "Continuum dynamics of the 1-d heisenberg antiferromagnet: identification with the o(3) nonlinear sigma model", *Physics Letters A* **93**, 464–468 (1983).
- <sup>290</sup>F. D. Haldane, "O(3) nonlinear σ model and the topological distinction between integer- and half-integer-spin antiferromagnets in two dimensions", *Physical Review Letters* **61**, 1029 (1988).
- <sup>291</sup>H. J. Mikeska and M. Steiner, "Solitary excitations in one-dimensional magnets", *Advances in Physics* **40**, 191–356 (1991).
- <sup>292</sup>A. M. Tsvelik, *Quantum field theory in condensed matter physics* (Cambridge University Press, 2003).
- <sup>293</sup>Y. M. Shnir, *Topological and non-topological solitons in scalar field theories* (Cambridge University Press, 2018).
- <sup>294</sup>V. G. Bar'Yakhtar, B. A. Ivanov, and M. V. Chetkin, "Dynamics of domain walls in weak ferromagnets", *Soviet Physics - Uspekhi* **28**, 563–588 (1985).

- <sup>295</sup>A. M. Kosevich, B. A. Ivanov, and A. S. Kovalev, "Magnetic solitons", *Physics Reports* **194**, 117–238 (1990).
- <sup>296</sup>H. J. Mikeska, "Non-linear dynamics of classical one-dimensional antiferromagnets", *Journal of Physics C: Solid State Physics* **13**, 2913 (1980).
- <sup>297</sup>A. F. Andreev, "Macroscopic magnetic fields of antiferromagnets", *JETP Letters* **63**, 758–762 (1996).
- <sup>298</sup>E. G. Galkina, A. Y. Galkin, and B. A. Ivanov, "Solitons in isotropic antiferromagnets: beyond the sigma model", *Low Temperature Physics* **34**, 522–527 (2008).
- <sup>299</sup>N. Manton and P. Sutcliffe, *Topological solitons* (Cambridge University Press, 2004).
- <sup>300</sup>T. Vachaspati, *Kinks and domain walls* (Cambridge University Press, 2006).
- <sup>301</sup>E. G. Galkina and B. A. Ivanov, "Dynamic solitons in antiferromagnets (review article)", *Low Temperature Physics* **44**, 618–633 (2018).
- <sup>302</sup>A. Mougin, M. Cormier, J. P. Adam, P. J. Metaxas, and J. Ferré, "Domain wall mobility, stability and walker breakdown in magnetic nanowires", *Europhysics Letters* **78**, 57007 (2007).
- <sup>303</sup>H. Yang, H. Y. Yuan, M. Yan, H. W. Zhang, and P. Yan, "Atomic antiferromagnetic domain wall propagation beyond the relativistic limit", *Physical Review B* **100**, 024407 (2019).
- <sup>304</sup>G. Tatara, C. A. Akosa, and R. M. O. De Zuazola, "Magnon pair emission from a relativistic domain wall in antiferromagnets", *Physical Review Research* **2**, 043226 (2020).
- <sup>305</sup>A. N. Stroh, "Steady state problems in anisotropic elasticity", *Journal of Mathematics and Physics* **41**, 77–103 (1962).
- <sup>306</sup>F. C. Frank and J. H. van der Merwe, "One-dimensional dislocations. I. Static theory", *Proceedings of the Royal Society of London. Series A. Mathematical and Physical Sciences* **198**, 205–216 (1949).
- <sup>307</sup>B. Wolba, O. Gomonay, and V. P. Kravchuk, "Chaotic antiferromagnetic nano-oscillator driven by spin torque", *Physical Review B* **104**, 024407 (2021).
- <sup>308</sup>R. Ovcharov, E. Galkina, B. Ivanov, and R. Khymyn, "Spin hall nano-oscillator based on an antiferromagnetic domain wall", *Physical Review Applied* **18**, 024047 (2022).
- <sup>309</sup>A. Kurenkov, S. Fukami, and H. Ohno, "Neuromorphic computing with antiferromagnetic spintronics", *Journal of Applied Physics* **128**, 010902 (2020).
- <sup>310</sup>V. G. Bar'yakhtar, B. A. Ivanov, and M. V. Chetkin, "Dynamics of domain walls in weak ferromagnets", *Usp. Fiz. Nauk* **146**, 417–458 (1985).
- <sup>311</sup>L. Šmejkal, J. Sinova, and T. Jungwirth, "Emerging Research Landscape of Alternagnetism", *Physical Review X* **12**, 040501 (2022).
- <sup>312</sup>L. Avilés-Félix, L. Álvaro Gómez, G. Li, C. S. Davies, A. Olivier, M. Rubio-Roy, S. Auffret, A. Kirilyuk, A. V. Kimel, T. Rasing, L. D. Buda-Prejbeanu, R. C. Sousa, B. Dieny, and I. L. Prejbeanu, "Integration of Tb/Co multilayers within optically switchable perpendicular magnetic tunnel junctions", *AIP Advances* **9**, 125328 (2019).
- <sup>313</sup>L. Avilés-Félix, A. Olivier, G. Li, C. S. Davies, L. Álvaro Gómez, M. Rubio-Roy, S. Auffret, A. Kirilyuk, A. V. Kimel, T. Rasing, L. D. Buda-Prejbeanu, R. C. Sousa, B. Dieny, and I. L. Prejbeanu, "Single-shot all-optical switching of magnetization in tb/co multilayer-based electrodes", *Scientific Reports* **10**, 5211 (2020).

- <sup>314</sup>R. Lizárraga, F. Pan, L. Bergqvist, E. Holmström, Z. Gercsi, and L. Vitos, "First Principles Theory of the hcp-fcc Phase Transition in Cobalt", *Scientific Reports* **7**, 3778 (2017).
- <sup>315</sup>W. C. Thoburn, S. Legvold, and F. H. Spedding, "Magnetic properties of terbium metal", *Physical Review* **112**, 56 (1958).
- <sup>316</sup>M. S. E. Hadri, V. Polewczyk, Y. Xiao, S. Mangin, and E. Fullerton, "Large anisotropic magnetocaloric effect in all sputtered epitaxial terbium thin films", *Physical Review Materials* **4**, 124404 (2020).
- <sup>317</sup>R.J. Elliott (Editor), *Magnetic Properties of Rare Earth Metals* (Springer New York, 1972).
- <sup>318</sup>Royal Society of Chemistry, "Terbium", [Link accessed: 10/12/2024](#).
- <sup>319</sup>V. Puliafito, R. Khymyn, M. Carpentieri, B. Azzerboni, V. Tiberkevich, A. Slavin, and G. Finocchio, "Micromagnetic modeling of terahertz oscillations in an antiferromagnetic material driven by the spin hall effect", *Physical Review B* **99**, 024405 (2019).
- <sup>320</sup>L. Sanchez-Tejerina, R. Tomasello, V. Puliafito, B. Azzerboni, M. Carpentieri, and G. Finocchio, "Unified framework for micromagnetic modeling of ferro-, ferrimagnetic, and antiferromagnetic materials at mesoscopic scale: domain wall dynamics as a case study", *IEEE Magnetics Letters* **11**, 1–5 (2020).
- <sup>321</sup>L. Sánchez-Tejerina, V. Puliafito, P. Khalili Amiri, M. Carpentieri, and G. Finocchio, "Dynamics of domain-wall motion driven by spin-orbit torque in antiferromagnets", *Physical Review B* **101**, 014433 (2020).
- <sup>322</sup>W. Schmidt, "Influence of antiferromagnetic interlayer exchange interactions in a double ferromagnetic film on the hysteresis curve", *Journal of Magnetism and Magnetic Materials* **84**, 119–126 (1990).
- <sup>323</sup>C. Stamm, I. Tudosa, H. C. Siegmann, J. Stöhr, A. Y. Dobin, G. Woltersdorf, B. Heinrich, and A. Vaterlaus, "Dissipation of spin angular momentum in magnetic switching", *Physical Review Letters* **94**, 197603 (2005).
- <sup>324</sup>C. S. Davies, K. H. Prabhakara, M. D. Davydova, K. A. Zvezdin, T. B. Shapaeva, S. Wang, A. K. Zvezdin, A. Kirilyuk, T. Rasing, and A. V. Kimel, "Anomalously damped heat-assisted route for precessional magnetization reversal in an iron garnet", *Physical Review Letters* **122**, 027202 (2019).
- <sup>325</sup>R. Moreno, T. A. Ostler, R. W. Chantrell, and O. Chubykalo-Fesenko, "Conditions for thermally induced all-optical switching in ferrimagnetic alloys: Modeling of TbCo", *Physical Review B* **96**, 014409 (2017).
- <sup>326</sup>C. Kooy and U. Enz, "Experimental and theoretical study of the domain configuration in thin layers of bafeo", *Philips Research Reports* **15**, 7–29 (1960).
- <sup>327</sup>M. S. E. Hadri, M. Hehn, P. Pirro, C. H. Lambert, G. Malinowski, E. E. Fullerton, and S. Mangin, "Domain size criterion for the observation of all-optical helicity-dependent switching in magnetic thin films", *Physical Review B* **94**, 064419 (2016).



# List of publications

## Concerning this thesis

1. **P.-I. Gavriloaea**, E. Saugar, R. Otxoa and O. Chubykalo-Fesenko, "Domain wall dynamics driven by a transient laser-induced magnetization", [Physical Review B 111, 054411 \(2025\)](#).
2. **P.-I. Gavriloaea**, J. L Ross, F. Freimuth, Y. Mokrousov, R.F.L Evans, R. Chantrell, O. Chubykalo-Fesenko and R. Otxoa, "Efficient motion of 90° domain walls in Mn<sub>2</sub>Au via pure optical torques", [npj Spintronics 3, 11 \(2025\)](#).
3. J. L. Ross, **P.-I. Gavriloaea**, F. Freimuth, T. Adamantopoulos, Y. Mokrousov, R. F. L. Evans, R. Chantrell, R. M. Otxoa and O. Chubykalo-Fesenko, "Ultrafast antiferromagnetic switching of Mn<sub>2</sub>Au with laser-induced optical torques", [npj Computational Materials 10, 234 \(2024\)](#).

## Beyond the scope of this thesis

1. P. Olleros-Rodríguez, M. Strungaru, S. Ruta, **P.-I. Gavriloaea**, A. Gudín, P. Perna, R. Chantrell and O. Chubykalo-Fesenko, "Non-equilibrium heating path for the laser-induced nucleation of metastable skyrmion lattices", [Nanoscale 14, 15701-15712 \(2022\)](#).
2. J. A. Vélez, M.-K. Lee, G. Tatara, **P.-I. Gavriloaea**, J. Ross, D. Laroze, U. Atxitia, R. F. L. Evans, R. W. Chantrell, M. Mochizuki, R. M. Otxoa, "Chaotic Proliferation of Relativistic Domain Walls for Reservoir Computing", [npj Spintronics 3, 14 \(2025\)](#).
3. J. A. Vélez, R. Rama-Eiroa, **P.-I. Gavriloaea**, J. L. Ross, D. Laroze, O. Chubykalo-Fesenko, U. Atxitia, and R. M. Otxoa, "Topological and relativistic hierarchies for spin-orbit field-induced antiferromagnetic 90° domain wall dynamics in Mn<sub>2</sub>Au", In preparation.
4. J. L. Ross, S. Jenkins, R. Rama-Eiroa, **P.-I. Gavriloaea**, J. Collings, U. Atxitia, O. Chubykalo-Fesenko, K. Everschor-Sitte, R. M. Otxoa, R. Chantrell and R. F. L. Evans "Micromagnetic temperature-dependent parameters using atomistic-scale dynamics in the antiferromagnet Mn<sub>2</sub>Au", In preparation.